

DISSERTATION

FROM FABRICATION TO APPLICATION: DEVELOPING
HIGH-PERFORMANCE GOLD NANOPARTICLE-BASED
SENSORS USING MIXED LIGAND/LINKER SYSTEMS

in conformity with the requirements for the degree of
Doctor rerum naturalium (Dr. rer. nat)

Faculty of Mathematics, Informatics, and Natural Sciences
Department of Chemistry
University of Hamburg

submitted by
Chih-Yin Liu

Hamburg
2024

Dissertation

Titel:	From Fabrication to Application: Developing High-Performance Gold Nanoparticle-Based Sensors Using Mixed Ligand/Linker Systems
Titel (deu.):	Von der Herstellung zur Anwendung: Entwicklung von hochleistungsfähigen Gold Nanopartikel-basierten Sensoren unter Verwendung von gemischten Ligand/Linker-Systemen
Eingereicht von:	Chih-Yin Liu
Matrikelnummer:	7228302
Email:	liunancy122579@gmail.com
Arbeitsgruppe:	Prof. Dr. Horst Weller
Institut:	Institut für Physikalische Chemie
Universität:	Universität Hamburg
Datum der Einreichung:	25.October.2024
Erstgutachter:	PD Dr. Tobias Vossmeier
Zweitgutachter:	Prof. Dr. Alf Mews
Datum der Disputation:	27.November.2024
Prüfungskommission:	PD Dr. Tobias Vossmeier Prof. Dr. Carmen Herrmann Prof. Dr. Ying-Chih Liao

This dissertation was prepared under the supervision of PD Dr. Tobias Vossmeier, in the group of Prof. Dr. Horst Weller at the Institute of Physical Chemistry (Department of Chemistry, Faculty of Mathematics, Informatics, and Natural Sciences) of the University of Hamburg. The work began in September 2018, and the dissertation was submitted in October 2024. Additionally, a part of the work presented herein was conducted in the Precision Printing Technology Laboratory Group at National Taiwan University in collaboration with Prof. Dr. Ying-Chih Liao during a research visit from February to April 2020.

List of Publications

The following list is chronologically ordered and includes peer-reviewed journal articles published within the framework of this research project.

1. Karen Schaefer, Chih-Yin Liu, Andreas Meyer, Hendrik Schlicke, Tobias Vossmeier, and Carmen Herrmann, "Cross-Linked Gold Nanoparticle Assemblies: What Can We Learn from Single Flat Interfaces?", *J. Phys. Chem. C* **2024**, 128, 3994–4008.[1]
2. Chih-Yin Liu, Sophia C. Bittinger, Ahir Bose, Andreas Meyer, Hendrik Schlicke, and Tobias Vossmeier, "Tuning the Interfacial Chemistry of Nanoparticle Assemblies via Spin-Coating: From Single Sensors to Monolithic Sensor Arrays", *Adv. Mater. Interfaces* **2024**, 2301058.[2]

Acknowledgements

Completing my PhD study and thesis has been a long journey, and I could not have done it without the support and encouragement of many individuals.

First and foremost, I would like to express my greatest appreciation to PD Dr. Tobias Vossmeier and Prof. Dr. Horst Weller for welcoming me into the research group, and especially to my supervisor, PD Dr. Tobias Vossmeier, for his guidance and help during my doctoral project. He was always willing to spend his time discussing with me and providing insightful ideas on my scientific research. Meanwhile, he also gave me sufficient freedom to explore my own ideas. Beyond the scientific field, he showed care and fully understood my struggles as a foreigner in Germany. I would also like to thank Prof. Dr. Alf Mews for his numerous valuable suggestions regarding my research project and for the stimulating discussions we had in the GRK program.

I would like to extend my special thanks to Prof. Dr. Ying-Chih Liao for giving me the chance to have a research stay abroad at National Taiwan University (Taiwan). He allowed me to access all lab equipment and provided valuable feedback to advance my research. I would also like to thank Dr. Shiuan-Ying Peng, who assisted me with all lab equipment and offered significant mental support. Moreover, I gratefully acknowledge the funding source, Hamburg Global, for financially supporting my research stay in Taiwan.

I also want to thank everyone from AK Weller. Without you all, I could not have worked in such a motivated and enjoyable environment. I also enjoyed the activities we did together outside of work. Particularly, I would like to thank all members of the sensor group: Dr. Sophia C. Bitteringer, Dr. Hendrik Schlicke, Dr. Bendix Ketelsen, Svenja Kunze, Shin-Da Wu, Jana Struck, Hauke Hartmann, Finn Dobschall, and Ahir Bose, for their collaboration, friendship, inspiring discussions, and for creating a fun environment in which I have learned so much. Moreover, I would like to express my gratitude to Svenja Kunze for providing all the instructions and help at the beginning of my PhD study.

Special thanks go to my office mate, Jana Struck. We had a lot of fun talks and great times during our office hours. I also enjoy our time together after work, playing frisbee, watching movies, cooking, and much more. Thanks for making me feel more at home in Hamburg.

I am grateful to all members of the Graduate School GRK Nanohybrid for inspiring talks, workshops, discussions, and collaborations. I would like to thank Prof. Dr. Carmen Herrmann and her research group, especially Karen Schaefer, for the collaboration.

I thank Robert Schön and Dr. Charlotte Ruhmlieb for performing SEM measurements and the helpful discussions afterwards. I also thank Stefan Werner for conducting TEM measurements and Dr. Andreas Meyer for conducting and analyzing SAXS and GISAXS measurements.

Additionally, I am thankful to Marion Manin and Sigrid Zeckert for their help with administrative matters.

I also thank Karen Schaefer, Jana Struck, and Dr. Sophia C. Bittinger for reviewing this thesis and providing helpful advice.

Lastly, I would like to express my deepest gratitude to my parents for their unwavering support and love. Even though we live 9000 km apart, they cared for me all the time and were always there for me through all the ups and downs. Additionally, I would also like to thank my dear friends, both near and far, for their constant companionship, support and encouragement. To CK Pay, Tim Kauschke, and Ginger Cheng, thank you for always being there for me, sharing my worries and celebrating my successes. Your friendship gave me the strength and joy to walk through this difficult journey.

Contents

1	Abstract	1
2	Zusammenfassung	3
3	Introduction	7
4	Objectives	11
5	Theoretical Background	15
5.1	Gold Nanoparticle	15
5.1.1	Optical Properties of Gold Nanoparticles	15
5.1.2	Synthesis of Gold Nanoparticles	17
5.1.3	Gold Nanoparticle Composite Films	18
5.2	Electrical Properties	24
5.3	Gold Nanoparticle-Based Films and Sensors	27
5.3.1	Resistive Chemical Sensors	27
5.3.2	Gravimetric Sensors	28
5.3.3	Response Isotherm and Sorption Behavior	32
5.3.4	Stability of Gold Nanoparticle Films and Sensors	33
5.3.5	Sensor Arrays and Pattern Recognition	36
6	Experimental Part	39
6.1	Colloidal Gold Nanoparticles	39
6.1.1	Materials and Apparatus	39
6.1.2	Synthesis	39
6.1.3	TEM-Sample Preparation and Analysis	40
6.1.4	Determination of Particle Concentration Using UV/vis Spectroscopy	40
6.1.5	Regular Small Angle X-Ray Scattering (SAXS)	41
6.2	Fabrication of Fully Printed Gold Nanoparticle-Based Chemiresistors	42
6.2.1	Materials and Apparatus	42
6.2.2	Fabrication of Interdigitated Electrodes	42
6.2.3	Fabrication of Gold Nanoparticle Films via Inkjet Printing	42
6.3	Glass-Supported Gold Nanoparticle-Based Chemiresistors	44
6.3.1	Materials and Apparatus	44
6.3.2	Fabrication of Gold Nanoparticle Films via Layer-by-Layer Spin-Coating	44

6.4	Silicon-Supported Gold Nanoparticle Chemiresistor Arrays	46
6.4.1	Materials and Apparatus	46
6.4.2	Fabrication of Interdigitated Electrodes Using Lithography	46
6.4.3	Lithographic Patterning of Gold Nanoparticle Films	47
6.5	Characterizations of Gold Nanoparticle Films	48
6.5.1	UV/vis Spectroscopy	48
6.5.2	Atomic Force Microscopy (AFM)	48
6.5.3	Scanning Electron Microscopy (SEM)	48
6.5.4	Grazing Incidence Small Angle X-Ray Scattering (GISAXS)	48
6.5.5	Charge Transport Measurements	49
6.6	Vapor-Dosing Experiments	50
6.6.1	Materials	50
6.6.2	Vapor Dosing System Setup	50
6.6.3	Chemiresistor Measurements	51
6.6.4	Quartz Crystal Microbalance (QCM) Measurements	52
6.6.5	In situ GISAXS Measurements	53
7	Results and Discussion	55
7.1	Colloidal Gold Nanoparticles	55
7.2	Fully Printed Gold Nanoparticle-Based Chemiresistors on Flexible Substrates	57
7.2.1	Fabrication of Fully Printed Gold Nanoparticle Chemiresistors	58
7.2.2	Electrical Properties	61
7.2.3	Reproducibility, Repeatability, and Stability	62
7.2.4	Chemiresistor Measurements	65
7.2.5	Amine Sensing	70
7.2.6	Summary and Outlook	73
7.3	Gold Nanoparticle Films with a Mixed Organic Matrix	75
7.3.1	Fabrication of Gold Nanoparticle-Based Sensors with Mixed Organic Matrix	75
7.3.2	Conductivity and UV/vis Absorbance of Gold Nanoparticle Films, and GISAXS Measurements	80
7.3.3	Chemiresistor Screening Tests	83
7.3.4	Response Isotherms and Sorption Characteristics	87
7.3.5	Summary and Outlook	94
7.4	Gold Nanoparticle Films Composed of Mixed Organic Composites: Experimental Data vs. Simulation Data	96
7.4.1	Molecular Dynamics Simulations	97
7.4.2	Fabrication of Gold Nanoparticle Films	98
7.4.3	Experimental Results	99
7.4.4	Molecular Dynamics Simulation Results	107
7.4.5	Summary and Outlook	111
7.5	Chemiresistor Array	113
7.5.1	Fabrication of Monolithic Chemiresistor Arrays	113
7.5.2	Array Consisting of Four Types of Gold Nanoparticle Chemiresistors	117
7.5.3	Array Consisting of Eight Types of Gold Nanoparticle Chemiresistors	126

7.5.4	Summary and Outlook	131
8	Bibliography	133
A	Supplementary Data	143
A.1	Printed Gold Nanoparticle-Based Sensors	143
A.2	Glass-Supported Gold Nanoparticle Films via Layer-by-Layer Spin-Coating	151
A.2.1	Characterizations of Gold Nanoparticle Films	151
A.2.2	Chemiresistor Screening Tests	156
A.2.3	Aging of Gold Nanoparticle Films	160
A.3	Glass-Supported Gold Nanoparticle Films for Comparison with Simulation Data	162
A.3.1	Characterizations of Gold Nanoparticle Films	162
A.3.2	Chemiresistor Measurements	163
A.3.3	Molecular Dynamics Simulations	164
A.4	Gold Nanoparticle-Based Chemiresistor Arrays	166
A.4.1	4-Sensor Array	166
A.4.2	8-Sensor Array	177
B	Safety	192
C	Declaration On Oath	196

Abbreviations

10T 1-decaenthiol

11MUA 11-mercaptoundecanoic acid

11MUO 11-mercapto-1-undecanol

11T 1-undecanethiol

12A 1-dodecylamine

12DT 1,12-dodecanethiol

12T 1-dodecanethiol

14T 1-tetradecanethiol

16MHDA 16-mercaptohexadecanoic acid

20DT 1,20-icosanedithiol

2ATP 2-aminothiophenol

2D 2-dimensional

3D 3-dimensional

3MPA 3-mercaptopropionic acid

4M2P 4-methyl-2-pentanone

4MBA 4-mercaptobenzoic acid

4MPO 4-mercaptophenol

4NTP 4-nitrothiophenol

4TBT 4-tert-butylbenzenethiol

6DT 1,6-hexanedithiol

6MHA 6-mercaptohexanoic acid

6MNA 6-mercapto-3-pyridinecarboxylic acid

6T 1-hexanethiol

8MOA 8-mercaptooctanoic acid

8MOO 8-mercapto-1-octanol

8T 1-octanethiol

9DT 1,9-nonanedithiol

AC alternating current

AFM atomic force microscopy

AG analyte gas

ANNs artificial neural networks

AO atomic orbital

AT alkanethiol

BVD Butterworth-Van Dyke

CIJ continuous inkjet

CVs coefficient of variations

DC direct current

DI deionized

DT dithiol

DOD drop-on-demand

DUV deep-ultraviolet

e.g. for example

e-nose electronic nose

FCC face-centered-cubic

GISAXS grazing incidence small angle X-ray scattering

EtOH ethanol

GNP gold nanoparticle

HOMO highest occupied molecular orbital

IDE interdigitated electrode

I-V current voltage

LbL layer-by-layer

LDA linear discriminant analysis

LSPR localized surface plasmon resonance

LUMO lowest unoccupied molecular orbital

MD molecular dynamics

MNP metal nanoparticle

MO molecular orbital

MOP metal oxide nanoparticle

MT monothiol

NND near neighbor distance

PCA principal component analysis

PCB printed circuit board

PI polyimide

PMMA poly(methyl methacrylate)

ppb part per billion

ppm parts-per-million

PTFE polytetrafluoroethylene

PVD physical vapor deposition

QCM quartz crystal microbalance

SA self-assembly

SAM self-assembled monolayer

SAXS small angle X-ray scattering

SC spin-coating

SDs standard deviations

SEM scanning electron microscopy

SF4 [4]-staffane-3,3''-dithiol

SMD surface mount device

SMU source measurement unit

TBAB tert-butylamine borane

TEM transmission electron microscopy

TG 1-thioglycerol

TOAB tetraoctylammonium bromide

UV ultraviolet

UV/vis ultraviolet/visible

VOC volatile organic compound

XPS X-ray photoelectron spectroscopy

XRD X-ray diffraction

ZG zero gas

Chapter 1

Abstract

This thesis explores the fabrication and application of composites of organically capped gold nanoparticles (GNPs) for gas sensing. These GNPs are encapsulated within an organic matrix, typically consisting of functionalized monothiol (MT) ligands and dithiol (DT) linkers. The study investigates the incorporation of mixed functionalized MTs and 1,9-nonanedithiol (9DT) in the organic matrix. The aim is to combine the robust cross-linking properties offered by 9DT with compatibility with layer-by-layer (LbL) deposition methods, while also leveraging the chemical tunability of the MT ligand.

The first project presents the development of flexible substrate-supported GNP-based chemiresistors using printing technologies. The fabrication process involves two key steps: printing interdigitated electrodes (IDEs) via a dispensing technique and LbL deposition of GNP films using a precise inkjet printing machine. The MT ligands functionalized with hydroxyl, carboxylic acid, and amino groups are mixed with the 9DT linker. These functionalized MT ligands enhance chemiresistive sensitivity towards polar vapors, with characteristic transient response kinetics serving as potential additional features. Furthermore, the response patterns to six different analyte vapors exhibit consistent results at two different vapor concentrations, rendering the sensors suitable for analyte recognition. Notably, the GNP films containing carboxylic acid-functionalized MT ligands exhibit high sensitivity and selectivity towards Lewis base compounds, making them promising for amine sensing applications, especially in the field of food quality control.

The second project systematically investigates how the chain length and fraction of MT ligands impact GNP film's characteristics. This study demonstrates a facile fabrication route of GNP films via a layer-by-layer spin-coating (LbL-SC) process. By adjusting the length and structure of MT ligands, along with the mixing ratio between MT and 9DT molecules, the conductivity and optical properties of the films can be tailored. These modifications correspond to changes in their sensing behavior. Generally, increasing the length and fraction of MT ligands significantly enhances the sensor's sensitivity, with resistive response isotherms transitioning from Langmuir-Henry to Henry type. Electrical, optical and grazing incidence small angle X-ray scattering (GISAXS) measurements elucidate this increase in sensitivity and change in isotherm type, attributed to variations in interparticle distance and swelling ability. Moreover, quartz crystal microbalance (QCM) measurements reveal distinct response patterns, which differ from the

chemiresistor data, revealing the potential of these GNP films with different organic matrix compositions to enable the fabrication of a combined sensor array with two different transducers. This offers a more reliable and precise fingerprint for each analyte, enhancing the sensor’s capabilities in diverse sensing applications.

The third project addresses molecular dynamics (MD) simulations, which were performed by Karen Schaefer in the research group of Prof. Dr. Carmen Herrmann (University of Hamburg, Department of Chemistry), to investigate GNP films prepared with MT/9DT mixtures at the atomic level. To this end, three alkanethiol (AT) ligands with varying chain lengths are combined with 9DT in four different ratios. On the experimental side, GNP films are prepared using the LbL-SC procedure as described in the second project. To ensure data reliability, four GNP films for each composition are produced. When the length of the added AT ligand is shorter than that of 9DT, the conductivity of the resulting films increases gradually with the increasing AT fraction and surpasses that of pure 9DT films, which is consistent with the findings of the second project. However, the localized surface plasmon resonance (LSPR) bands are positioned at similar wavelength as those of GNP films cross-linked with pure 9DT. In contrast, when using AT ligands longer than 9DT, the conductivity of the resulting films decreases, especially at high AT molar fractions, while the LSPR bands of the resulting GNP films show strong blueshifts. GISAXS data indicate slightly shorter interparticle distances within the GNP films prepared with short AT/9DT mixtures, and longer interparticle distances for those prepared with long AT/9DT mixtures. Chemiresistor measurements further reveal a low degree of cross-linking in films consisting of high fractions of long AT ligands. Overall, the addition of short AT ligands maintains a high degree of cross-linking in the film, preserving more space for closer cross-linking by the 9DT molecules and resulting in shorter interparticle distances. Conversely, the addition of long AT ligands leads to the presence of two different domains: one dominated mainly by the 9DT linkers and the other mainly dominated by the long AT ligands. The MD simulation data are in agreement with the experimental results, indirectly supporting the disruption of cross-linking and the "two-domain" hypothesis when using high fractions of long AT ligands. In the future, MD simulations can further assist in screening film compositions and predicting the resulting film’s sensing performance, potentially saving time and resources.

Finally, the fourth project explores the fabrication and utilization of monolithic chemiresistor arrays. Beside selecting GNP films based on the previous projects, three additional functionalized MT ligands are incorporated into the sensor array. Through the cross-linking of GNPs by 9DT molecules, the resulting films are robust enough to be patterned via deep-ultraviolet (DUV) photolithography. In this process, poly(methyl methacrylate) (PMMA) acts as a sacrificial layer for a lift-off procedure, complementing the LbL-SC method for deposition of GNP films. The diverse nanostructure and chemical composition arising from different organic matrices allow the chemiresistive response amplitudes and kinetics of transient responses to serve as features for analyte recognition. Upon normalization, some of these features are related to the molecular size and dielectric constant of analytes, while remaining largely unaffected by the analyte’s vapor pressure and concentration. The chemiresistor arrays are exposed to nearly 20 different volatile compounds, with the resulting features of the response transients utilized as input data for a linear discriminant analysis (LDA). The analysis reveals the array’s capability to discriminate very similar analytes, even when applied at different concentrations. Furthermore, the sensor array, comprising eight different GNP films, demonstrates stable electrical properties and sensing performance two weeks after fabrication, highlighting its robustness and ability to provide consistent and reliable results.

Chapter 2

Zusammenfassung

In dieser Arbeit wurde die Herstellung und Anwendung von Kompositen aus organisch funktionalisierten Goldnanopartikeln (GNPn) für die Gassensoren untersucht. Diese GNPn sind in eine organische Matrix eingebettet, die typischerweise aus funktionalisierten Monothiol (MT)-Liganden und Dithiol (DT)-Quervernetzer besteht. In dieser Arbeit wurde der Einbau von gemischten funktionalisierten MTs und 1,9-Nonandithiol (9DT) in die organische Matrix untersucht. Ziel ist es, die robusten Vernetzungseigenschaften von 9DT mit Layer-by-Layer (LbL)-Abscheidungsverfahren zu kombinieren und gleichzeitig die chemische Steuerbarkeit des MT-Liganden zu nutzen.

Das erste Projekt beschreibt die Entwicklung von GNP-basierten Chemiresistoren auf flexiblen Substraten unter Verwendung von Drucktechnologien. Der Herstellungsprozess umfasst zwei Hauptschritte: das Drucken von Interdigitalelektroden (IDEn) mit Hilfe einer Dosiertechnik und die LbL-Abscheidung von GNP-Filmen mit einer präzisen Tintenstrahl Druckmaschine. Die MT-Liganden, die mit Hydroxyl-, Carbonsäure- und Aminogruppen-funktionalisiert sind, werden mit dem 9DT-Quervernetzer gemischt. Diese funktionalisierten MT-Liganden erhöhen die chemiresistive Sensitivität für polare Analyten, wobei die charakteristische Antwortkinetik des Transienten als potentiell zusätzliches Merkmal dient. Darüber hinaus zeigen die Antwortmuster für sechs verschiedenen Analytengase konsistente Ergebnisse bei zwei verschiedenen Dampfkonzentrationen, wodurch sich die Sensoren für die Identifizierung von Analyten eignen. Bemerkenswerterweise zeigen die GNP-Filme mit Carboxylsäure funktionalisierten MT-Liganden eine hohe Sensitivität und Selektivität für Lewis-Base-Analyten. Dies macht diese Filme vielversprechend für die Anwendung zur Amindetektion, insbesondere im Bereich der Lebensmittelqualitätskontrolle.

Das zweite Projekt untersucht systematisch, wie sich die Kettenlänge und der Anteil der MT-Liganden auf die Eigenschaften der GNP-Filme auswirken. Diese Studie zeigt einen einfachen Herstellungsweg für GNP-Filme über einen LbL-Spin-Coating-Prozess (LbL-SC). Durch Anpassung der Länge und Struktur der MT-Liganden, sowie des Mischungsverhältnisses der MT- und 9DT-Molekülen, können die Leitfähigkeit und die optischen Eigenschaften der Filme gezielt angepasst werden. Diese Anpassungen resultieren in Veränderungen der Sensoreigenschaften. Im Allgemeinen erhöht die Verlängerung und der höhere Anteil der MT-Liganden signifikant die Sensitivität des Sensor, wobei sich die resistiven Antwortisothermen von Langmuir-Henry- zu Henry-Typ-Isothermen ändern. Elektrische, optische und

Grazing-Incidence-Small-Angle-X-Ray-Scattering (GISAXS) Messungen verdeutlichen den Anstieg der Sensitivität und den Wechsel des Isotherm-Typs, der auf Variationen in den Partikelabständen und der Quellfähigkeit zurückzuführen sind. Zudem zeigen Messungen mit der Quarzkristall-Mikrowaage unterschiedliche Antwortmuster im Vergleich zu den Chemiresistordaten, was das Potenzial dieser GNP-Filme mit unterschiedlichen organischen Matrixzusammensetzungen zur Herstellung eines kombinierten Sensor-Arrays mit zwei verschiedenen Transducern aufzeigt. Dies ermöglicht eine zuverlässigere und präzisere Identifizierung einzelner Analyten und verbessert die Sensorleistung in vielfältigen Anwendungsbereichen der Sensorik.

Das dritte Projekt befasst sich mit Molekulardynamik (MD)-Simulationen, die von Karen Schaefer in der Forschungsgruppe von Prof. Dr. Carmen Herrmann (Universität Hamburg, Fachbereich Chemie) durchgeführt wurden, um GNP-Filme, die mit MT/9DT-Gemischen hergestellt wurden, auf atomarer Ebene zu untersuchen. Zu diesem Zweck werden drei Alkanthiol (AT)-Liganden mit unterschiedlichen Kettenlängen mit 9DT in vier verschiedenen Verhältnissen kombiniert. Auf der experimentellen Seite wurden GNP-Filme mithilfe des im zweiten Projekt beschriebenen LbL-SC-Verfahrens hergestellt. Um die Zuverlässigkeit der Daten zu gewährleisten, wurden für jede Zusammensetzung vier GNP-Filme produziert. Wenn die Länge des hinzugefügten AT-Liganden kürzer ist als die von 9DT, nimmt die Leitfähigkeit der Filme mit zunehmendem AT-Anteil allmählich zu und übertrifft die Leitfähigkeit reiner 9DT-Filme, was mit den Ergebnissen des zweiten Projekts übereinstimmt. Die Bänder der lokalisierten Oberflächenplasmonenresonanz (LSPR) liegen jedoch bei ähnlichen Wellenlängen wie die von GNP-Filmen, die mit reinem 9DT vernetzt sind. Im Gegensatz dazu nimmt die Leitfähigkeit der resultierenden Filme bei Verwendung von AT-Liganden, die länger als 9DT sind, insbesondere bei hohen AT-Molverhältnissen ab, während die LSPR-Bänder der GNP-Filme starke Blauverschiebungen aufweisen. Die GISAXS-Daten zeigen geringfügig kürzere Partikelabstände in GNP-Filmen, die mit kurzen AT/9DT-Gemischen hergestellt wurden, und längere Partikelabstände in solchen, die mit langen AT/9DT-Gemischen hergestellt wurden. Chemiresistor Messungen zeigen zudem einen geringen Vernetzungsgrad in Filmen mit hohem Anteil an langen AT-Liganden. Insgesamt resultiert die Zugabe kurzer AT-Liganden in einem hohen Vernetzungsgrad im Film, sodass mehr Raum für eine engere Vernetzung durch die 9DT-Moleküle vorliegt, was zu kürzeren Partikelabständen führt. Die Zugabe langer AT-Liganden hingegen führt zur Bildung von zwei unterschiedlichen Domänen: eine, die hauptsächlich von 9DT-Quervernetzern dominiert wird und eine, die hauptsächlich von den langen AT-Liganden dominiert wird. Die MD-Simulationsdaten stimmen mit den experimentellen Ergebnissen überein und stützen indirekt die Hypothese einer Störung der Vernetzung und der "Zwei-Domänen"-Bildung bei Verwendung hoher Anteile langer AT-Liganden. Zukünftig können MD-Simulationen die Auswahl geeigneter Filmzusammensetzungen weiter unterstützen und die Sensoreigenschaften der Filme vorhersagen, was potenziell Zeit und Ressourcen spart.

Das vierte Projekt dieser Arbeit untersucht die Herstellung und Nutzung von monolithischen Chemiresistor-Arrays. Neben der Auswahl von GNP-Filmen basierend auf den vorhergehenden Projekten werden drei weitere funktionalisierte MT-Liganden in das Sensor-Array integriert. Durch die Vernetzung der GNPs mittels 9DT-Molekülen sind die Filme robust genug, um mit Hilfe von tiefer Ultraviolette-Photolithografie strukturiert zu werden. In diesem Prozess dient Poly(methylmethacrylat) als Opferschicht für ein Lift-off-Verfahren, das die LbL-SC-Methode zur Abscheidung der GNP-Filme ergänzt. Die vielfältige Nanostruktur und chemische Zusammensetzung, die aus den verschiedenen organischen Matrizen resultieren, ermöglichen es, die Amplituden der chemiresistiven Antwort und die Kinetik der

transienten Antworten als Merkmale zur Analyt-Erkennung zu nutzen. Nach der Normalisierung ist erkennbar, dass einige dieser Merkmale in Beziehung zur Molekülgröße und der Dielektrizitätskonstante der Analyten stehen, während sie weitgehend unbeeinflusst von dem Dampfdruck und der Konzentration der Analyte bleiben. Das Chemiresistor-Array wird nahezu 20 verschiedenen flüchtigen Verbindungen ausgesetzt, wobei die Merkmale, extrahiert aus den Antwort-Transienten, als Eingabedaten für eine lineare Diskriminanzanalyse verwendet werden. Die Analyse zeigt, dass das Array in der Lage ist sehr ähnliche Analyte zu unterscheiden, selbst bei unterschiedlichen Konzentrationen. Zudem weist das Sensor-Array, bestehend aus acht verschiedenen GNP-Filmen, stabile elektrische Eigenschaften und Sensoreigenschaften zwei Wochen nach der Herstellung auf, was seine Robustheit und Fähigkeit zur Bereitstellung konsistenter und zuverlässiger Ergebnisse unterstreicht.

Chapter 3

Introduction

Nowadays, the field of gas sensing has garnered significant interest due to its applications in non-invasive and real-time health monitoring, medical diagnosis, environmental detection, food safety control, and explosives detection. Over recent decades, extensive research has focused on exploring various sensing materials, including metal oxides, polymers, metal organic frameworks, and metal nanoparticles. Among these, gold nanoparticles (GNPs) stand out as promising sensing materials due to their unique optical properties, biocompatibility, and high stability. Additionally, the synthesis of GNPs is well studied, allowing precise control over their size and shape. Furthermore, the surfaces of GNPs can be easily modified, facilitating straightforward functionalization and tuning their chemical and physical properties.

Thin films of organically capped GNPs can be prepared using either non-cross-linking ligands (e.g., monothiols, MTs) or cross-linkers (e.g., dithiols, DTs). These films have been extensively studied regarding their distinct optical[3–6], electrical[7–9], and mechanical[10–12] properties, which can be finely tuned by adjusting the composition of their organic matrix. The first GNP-based chemiresistors were demonstrated by Wohltjen and Snow in 1998, exhibiting sensitivity to volatile organic compounds (VOCs) through a resistance increase triggered by sorption-induced swelling of the organic matrix.[13] This swelling of the organic matrix leads to an increase in tunneling distances between neighboring GNPs.[14] Besides their high sensitivity towards analyte vapors, these sensors offer rapid response/recovery times, room temperature operation, low power consumption, and they can be miniaturized and integrated. Moreover, their chemical selectivity can be tuned by surface functionalization with a wide range of commercially available ligand and linker molecules.

Thin films of MT ligands-stabilized GNPs are widely used due to their chemical versatility and flexibility in the resulting organic matrix. These films show distinct responses to various analyte vapors with high sensitivity, and can be fabricated using diverse methods such as drop-casting, spray-coating, spin-coating, and so on. However, the surface functionalization of GNPs often involves laborious handling of colloidal solutions, as it is usually the case during GNP synthesis or during the ligand exchange after GNP synthesis.

In contrast, films prepared with DT cross-linkers allow for in situ ligand exchange during the deposition of

GNP films.[15, 16] By using different structures[17, 18] and chemically functionalized linkers[19–21], the physical properties and sensing characteristics of the resulting films can easily be tuned. Moreover, the cross-linked network provides stability to the films[22], enabling post-fabrication steps such as lithographic patterning and further functionalization[23]. However, despite their advantages, commercially available cross-linkers are much less versatile compared to MT ligands, which potentially limits the selectivity-tuning of the resulting GNP films. In addition, a high degree of cross-linking in GNP films also leads to a low amplitude of sensor responses.[22]

Recent research efforts have explored hybrid approaches, combining MT ligands and cross-linkers to leverage the benefits of both components, which also enable a straightforward film fabrication process.[24, 25] Particularly, Ketelsen et al. demonstrated that MT ligands terminated with various functional groups can modify the sensor’s chemical selectivity. Additionally, mixing MT and DT molecules in different ratios results in GNP films with varying response characteristics.[24] Such semi-selective sensors, when integrated into arrays and combined with multivariate data analysis methods, hold promise for a wide range of applications. Previous studies have shown that features extracted from the responses of these arrays together with multivariate data analysis methods allow for the non-invasive diagnosis of various diseases through the detection of volatile compounds in breath and body fluids[26, 27], including Alzheimer’s and Parkinson’s disease[28], ovarian carcinoma[29], lung cancer[30–33], and COVID-19[34]. Furthermore, GNP chemiresistor arrays are effective for the detection and classification of bacteria[35], explosives[36, 37], food products[38, 39], and solvent vapors[18, 24, 25]. Although the maximum response amplitude is commonly used as input data for discriminant analyses, it captures only a single point in time and overlooks the dynamics of transient responses. This limitation may lead to poor discrimination and imprecise classification. Some studies have shown that the dynamics of the transient responses are influenced by the nanostructures of GNP films.[18, 25, 40] For instance, Schlicke et al. demonstrated significant improvements by including kinetic response features to discriminate ten different volatile compounds at varying concentrations.[18]

However, the optimal selection of ligands for specific applications often requires extensive screening tests, which is time-consuming and labor-intensive. Hubble et al. screened 132 different MT ligands to detect aryl compounds in water. Finally, only 8 out of 132 functionalized MT ligands were selected for a further use in sensor array.[41] To simplify this ligand-selection process, molecular dynamics (MD) simulations offer a promising approach. For instance, GNPs are widely used as strain sensors, and Yeh et al. employed MD simulations to model assemblies of cross-linked GNPs, successfully reproducing their mechanical properties in accordance with experimental data.[42] Schaefer et al. developed a model to investigate the nanostructures of assemblies of cross-linked and non-cross-linked GNPs, with the simulation model accurately estimating interparticle distances and charge transport properties consistent with experimental results.[1] By providing insights into the atomic-level behavior of GNP assemblies, MD simulations offer a deeper understanding of their nanostructures and sensing behavior. This could potentially facilitate the design of GNP-based sensors with significantly improved performance tailored to specific applications.

The aim of this work is the development of GNP-based sensors and sensor arrays using a mixed ligand/linker system. Eco-friendly fabrication methods such as LbL inkjet printing and layer-by-layer spin-coating (LbL-SC) are employed to fabricate GNP chemiresistors with tunable chemical selectivity. The research covers comprehensive investigations into interparticle distances and sensing performances influ-

enced by the added MT ligands' structures and chemical properties. Experimental techniques including current voltage (I-V), UV/vis, GISAXS, chemiresistor, and quartz crystal microbalance (QCM) measurements are conducted. Based on findings obtained from experiments and MD simulations, selected GNP films are integrated as monolithic arrays and exposed to various volatile compounds to explore potential applications.

Chapter 4

Objectives

Gold nanoparticle (GNP) composites with an organic matrix are promising candidates for applications as chemiresistors due to their electrical properties, which are based on a thermally activated tunneling mechanism. The organic matrix surrounding the GNPs sorbs the target analytes from the gas phase, causing swelling and a change in the dielectric properties of the charge transport environment. This can be detected as an electrical signal. The chemical selectivity strongly depends on the nature of the organic matrix's composition. Monothiols (MTs) tailored with different types of functional groups are commonly used for chemical selectivity-tuning. On the other hand, cross-linker molecules, such as dithiols (DTs), enable the formation of a robust network by cross-linking the GNPs and, thereby, enable layer-by-layer (LbL) film deposition procedures involving in situ ligand exchange. 1,9-Nonanedithiol (9DT) molecules have been widely used as the cross-linker. Their flexible alkyl chain leads to good vapor sensitivity and their thiol-bifunctional ends enable the formation of robust GNP films.

The aim of this thesis was to produce an array of GNP sensors, which exhibit a broad variety of signal responses, utilizing cost-effective and time-saving fabrication approaches. To combine the advantages of both, MT ligands and DT cross-linkers, this thesis employs the mixed ligand/linker strategy, where 9DT serves as the standard the cross-linker, facilitating the LbL deposition process. Additionally, MTs functionalized with methyl, hydroxyl, carboxylic acid, amine, and nitro groups are used to deliberately adjust the chemical selectivity toward target vapors. Figure 4.1 provides an overview of the projects presented in this thesis.

1. The first project in this thesis aims at the fabrication of flexible chemiresistors using different printing technologies. The interdigitated electrodes (IDEs) are produced using a dispenser robot. A colloidal batch of 1-dodecylamine-stabilized GNPs is used as the GNP ink. MTs with different functional groups, structures, and lengths are mixed with 9DT cross-linker molecules and used as the organic inks. The LbL deposition of GNP films is carried out using a precise inkjet printer. The resulting GNP films are expected to exhibit characteristic responses towards various volatile organic compounds (VOCs) and humidity.
2. The second project builds on the successful achievement of the mixed ligand/linker strategy, which

enables the fabrication of chemiresistors with characteristic responses to different VOCs and humidity. To further advance these findings, a more comprehensive systematic investigation is conducted to understand how the length and molar ratio of MTs impact on the GNP films' optical and electrical properties, their chemiresistive responses, as well as their sorption behavior. In this project, all GNP films are fabricated using a LbL spin-coating (SC) procedure. The optimal MT/9DT mixing ratios and the appropriate lengths of applied MTs are explored to improve both sensitivity and selectivity of the resulting sensors.

3. Based on the findings from the systematic investigation of GNP films prepared using ligand/linker mixtures, the third project is conducted as a collaboration between our research group and Prof. Dr. Carmen Herrmann's group. Karen Schaefer from the Herrmann's group developed a molecular dynamics (MD) simulation model. This model consists of a sandwich structure, where MT and DT molecules are intercalated between two Au(111) surfaces. This MD simulation model aims to explain the conformation of the organic molecules within the organic matrix as well as the distance between two gold surfaces of the system. According to the second project, the different lengths and molar fractions of MTs mixed with DT molecules result in changes of their respective GNP films' optical, electrical, and chemiresistive properties. On the other hand, the experimental part was performed by the author to further validate the findings of the second project. For each ligand/linker composition, four GNP films were fabricated via the LbL-SC procedure with MT molar fractions adjusted between 50% to 90%. The electrical, optical, and sensing properties of these films were investigated. Additionally, some of the selected GNP films were characterized using grazing incidence small angle X-ray scattering (GISAXS) measurements by Dr. Andreas Meyer to evaluate the interparticle distances of the GNPs in the films. These experimental data were then compared with the MD simulation data to gain a more comprehensive understanding of how the length and fraction of the added MT ligands affect the film's properties.
4. The last project focuses on sensor arrays combined with a supervised learning algorithm. GNP films prepared with selected mixtures of MT/DT are fabricated via the same facile LbL-SC procedure used in the second project, followed by deep UV lithographic patterning of the GNP films. Two monolithic sensor arrays composed of 4 and 8 different types of GNP-based chemiresistors are fabricated and exposed to various analyte vapors. Linear discriminant analysis (LDA) is employed for the classification of analyte vapors. Finally, the LDA prediction algorithm is used to identify unknown analyte vapors at unknown concentrations.

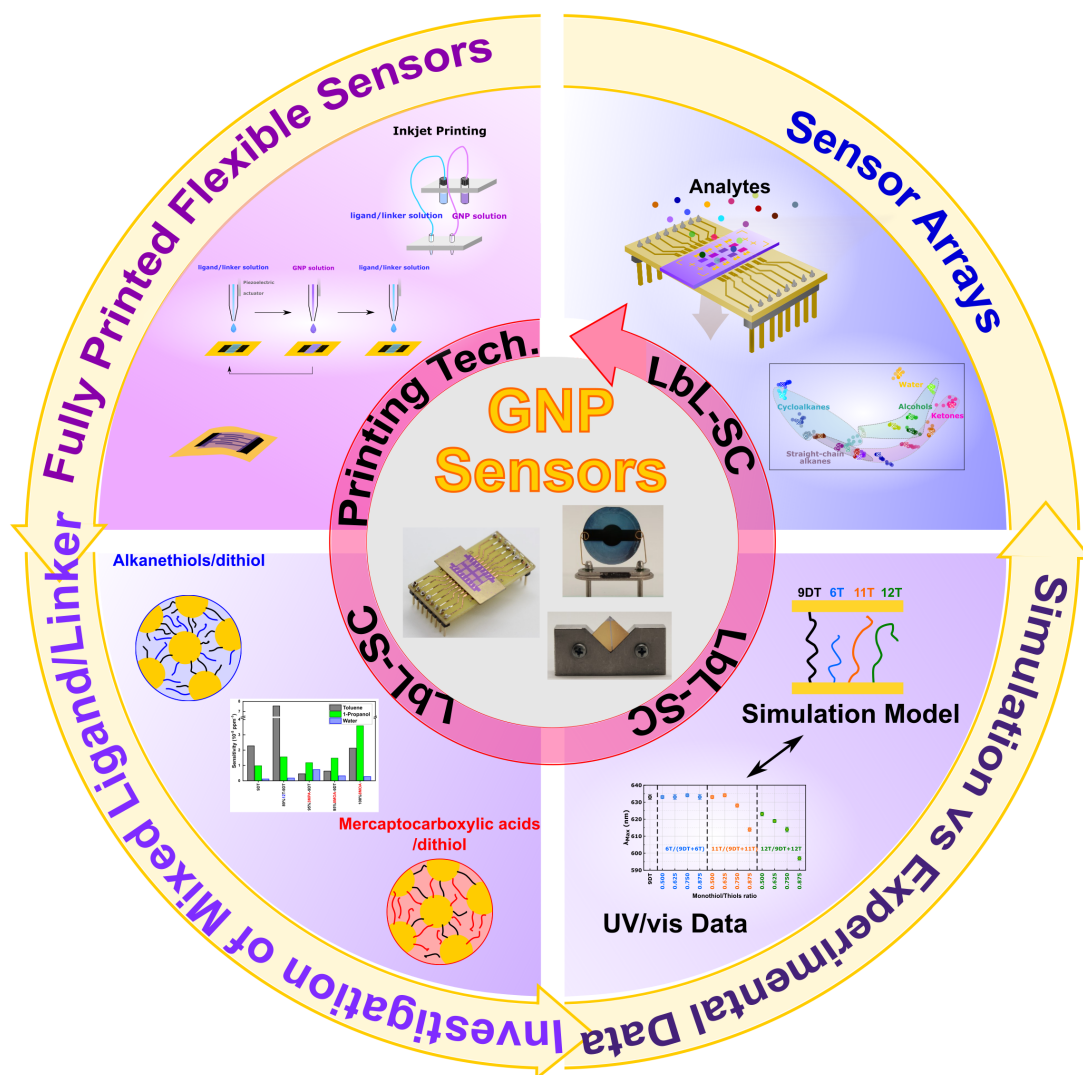


Figure 4.1: Graphic table of contents as an overview of the projects presented in this thesis.

Chapter 5

Theoretical Background

5.1 Gold Nanoparticle

5.1.1 Optical Properties of Gold Nanoparticles

Gold nanoparticles (GNPs) have a long history of utilization, dating back to ancient times, due to their remarkable optical properties. The earliest known applications of GNPs include their use in stained glass during the Roman period. Notably, artifacts like the Lycurgus Cup, dating back to the 4th century A.D., exemplify the intriguing optical effects achieved with GNPs. This cup, manufactured with gold-silver nanocrystals embedded in glass, exhibits a unique color-change phenomenon, where transmitted light appears red, while reflected light appears green. The dispersion of nanocrystals throughout the glass matrix is responsible for this remarkable optical property.[43, 44] In subsequent centuries, nanoparticles found application in pottery, where colloidal nanoparticle glazes were applied as decorations on ceramics. However, the systematic scientific evaluation of colloidal nanoparticles began in the mid-19th century when Michael Faraday accidentally produced a red solution containing GNPs in 1850.[45] Faraday's subsequent experiments with phosphorus as a reducing agent for AuCl_4^- further highlighted the intriguing optical properties of GNPs. This colloidal GNP solution maintained its optical properties for a long period. The discovery that the particle size governs the optical performance of GNPs, marked a significant milestone in the field of colloid science.

Since the 20th century, significant advancements have been made in the synthesis of stable GNPs using various wet-chemical routes in aqueous media.[46, 47] These methods have provided researchers with precise control over the size, shape, and stability of GNPs, thereby laying the foundation for their widespread use in modern scientific research and technological applications. The detailed synthesis methods for GNPs will be discussed in the following subsection, Section 5.1.2.

Typically, GNP colloids present a ruby red color, in contrast to bulk gold, which shines golden. This distinct red-color of GNPs is attributed to the so-called localized surface plasmon resonance (LSPR) effect. Figure 5.1 schematically illustrates the LSPR effect, a key optical phenomenon exhibited by

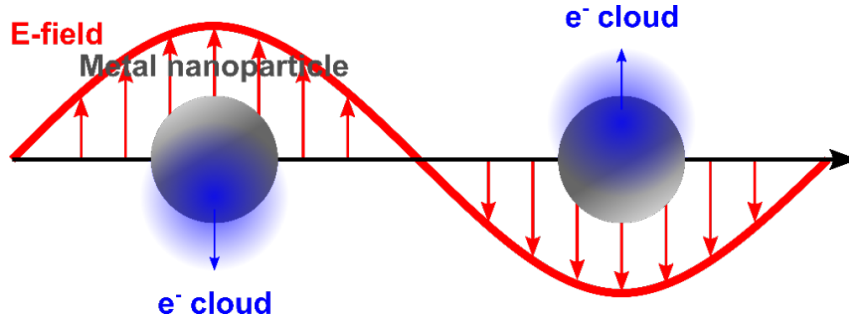


Figure 5.1: Schematic illustration of the LSPR effect. The electron cloud of the particle oscillates with the electric field (E-field) of the incident light.

GNPs. When light propagates through a colloidal particle, the oscillating electric field induces the free electron cloud of the particle to oscillate along with the incident electromagnetic wave. The oscillation causes electron displacement and polarization with a resonant frequency. When the resonant frequency matches the wavelength of the incident light, strong absorption of the incident light is observed. The energy level of d-d transitions in GNPs causes the LSPR to occur within the visible light spectrum.

Richard Zsigmondy was one of the pioneers, who observed light scattering by GNPs and proved their presence in the Purple of Cassius using an "ultramicroscope" instrument.[48, 49] At about the same time, Gustav Mie proposed the Mie theory, which describes the scattering of light by spherical particles through the solution of Maxwell's equations. This theory is often used to model and understand the optical properties of spherical particles where LSPR may occur. For small particles, specially those much smaller than the wavelength of the incident light, the Mie theory can be simplified using the dipolar approximation.[50–54] As shown in Figure 5.1, if the particle is much smaller than the wavelength of incident light, the electric field is almost constant over the dimension of the particle.

The extinction coefficient, as shown in Equation 5.1[51, 54], is a crucial parameter related to the LSPR effect. It is influenced by various factors such as the volume of the particle (V_m), the wavelength of incident light (λ), the dielectric constant of the surrounding medium (ϵ_m), and the real (ϵ_{Re}) and imaginary (ϵ_{Im}) parts of the dielectric function of the metal nanoparticle.

$$\epsilon(M^{-1} \cdot cm^{-1}) = \frac{18\pi \cdot V_m \cdot 10^4}{2.303 \cdot \lambda} \cdot \frac{\epsilon_m^{3/2} \cdot \epsilon_{Im}(\lambda)}{(\epsilon_{Re}(\lambda) + 2 \cdot \epsilon_m)^2 + \epsilon_{Im}(\lambda)^2} \quad (5.1)$$

In contrast to isolated particles, densely packed GNPs, such as those found in thin GNP films, exhibit unique optical properties, which are described by theories like the Maxwell-Garnett theory.[55, 56] In such films, interactions between adjacent particles lead to the observation of plasmon coupling. This interaction results in a redshift of the plasmon band, and the extent of this redshift varies depending on the interparticle distances. For example, Ung et al. deposited GNP films with varying lengths of ligands and different thicknesses of silica shells encapsulating the GNPs. They observed differently strong redshifts in their experiments, which aligns well with predictions from the Maxwell-Garnett theory.[57] Furthermore, the color of resulting GNP colloids or films is highly dependent on factors such as particle size, shape, concentration, and the medium surrounding the GNPs. By exploiting these properties, GNPs can be modified to exhibit specific optical responses to analytes, making them valuable tools for detecting

and quantifying various substances in a range of fields, including biomedical diagnostics, environmental monitoring, and chemical analysis.

5.1.2 Synthesis of Gold Nanoparticles

The synthesis of GNPs has been a subject of extensive research since Michael Faraday’s systematic demonstration in 1857, when he synthesized GNPs in an aqueous medium using a phosphorus-based reducing agent.[45] Since Faraday’s pioneering work, researchers have pursued various methods to achieve precise control over the size, shape, and a narrow size distribution of synthesized GNPs by using different capping agents, reducing agents, Au precursors, and reaction conditions.

One of the most prominent synthesis methods was introduced by Turkevich et al. in 1951.[46] This method, although slightly modified over time, is still utilized in some recent researches. In this approach, sodium citrate serves as both a stabilizer and reducing agent. Gold salts are dissolved in heated water, and sodium citrate is added to induce the formation of GNPs. The resulting GNPs typically have a diameter of around 20 nm with a relatively narrow size distribution. However, achieving batch-to-batch reproducibility has remained a challenge. About twenty years later, Frens conducted a more systematic study using a modified Turkevich method with a higher concentration of sodium citrate.[58] In this study, the size of the GNPs was controlled by adjusting the amount of the added citrate solution, resulting in particle diameters ranging from 16 to 147 nm. Subsequent developments in the Turkevich method led to variations such as the inverse Turkevich method, which offers better pH control during synthesis, and facilitates faster nucleation and homogeneous growth.[59, 60]

In the early 1990s, Brust and Schiffrin described another synthesis method that enables the rapid production of highly stable GNPs in an organic phase.[47] This breakthrough synthesis, known as the Brust-Schiffrin method, produces spherical GNPs with controlled sizes and surface functionalizations. The method involves a two-phase one-pot synthesis, where HAuCl_4 is transferred from an aqueous phase to an organic phase (e.g., toluene) with the assistance of tetraoctylammonium bromide (TOAB) as a phase-transfer agent. Alkanethiol (AT) molecules serve as stabilizing agent to prevent aggregation and maintain dispersion stability of the GNPs. Following the transfer of the gold salts into the organic phase and the addition of the AT capping ligands, sodium borohydride acts as reducing agent to form GNPs with a core diameter typically ranging from 1 to 3 nm.

Later, Leff et al. reported another two-phase synthesis route derived from the Brust-Schiffrin protocol, where 1-dodecylamine (12A) replaces 1-dodecanethiol (12T) as the stabilizing agent in the reaction.[61] The resulting GNPs have sizes ranging from 2.5 to 7 nm with a more controllable size distribution. The use of amine ligands opens up more possibilities for subsequent GNP-surface functionalization, due to the weaker N-Au covalent bond compared to the S-Au bond. These advancements in synthetic methods have greatly expanded the range of techniques that can be used to produce GNPs with tunable properties for a variety of applications.

Another modified Brust-Schiffrin method was reported by Zheng et al.[62], with a simplified one-phase and one-step synthesis, where the gold precursor, stabilizing agent, and reducing agent are all dissolved homogeneously in nonpolar solvents. Following the protocol, the gold precursor,

chloro(triphenylphosphine)gold(I) (AuPPh_3Cl) is reduced by tert-butylamine borane (TBAB). Unlike the Brust-Schiffrin method, which employs TOAB as the reducing agent, the amine-borane complex used in Zheng's method is weaker, resulting in a slower reduction rate of gold cations. This slower reduction rate leads to a narrower size distribution of synthesized GNPs. Similarly, Peng et al. demonstrated another one-phase and one-step synthesis method. In this method, HAuCl_4 serves as the gold precursor, stabilized by oleylamine, and is then reduced by TBAB. Moreover, tetralin is employed as the solvent. The resulting GNPs have core diameters ranging from 2.5 to 10 nm with a narrow size distribution, where the size of GNPs is modulated by the reaction temperature. Lower reaction temperatures result in larger GNPs. In our research group, we adapted a modified version of Peng's synthesis with slight adjustments to obtain GNPs with an average core diameter ranging from 5 to 8 nm.[18, 24] In this modified approach, 12A and n-hexane were used as the stabilizing agent and solvent, respectively, instead of oleylamine and tetralin. Interestingly, unlike the original Peng synthesis, the GNPs grew slightly larger at higher reaction temperatures. The syntheses conducted in this thesis at room temperature resulted in particles with an average core diameter of approximately 6 nm. However, raising the reaction temperature to around 32 °C led to an increase in the core diameter of the GNPs to roughly 7.5 nm.

The choice of the solvent in the wet-chemical synthesis may significantly influence the formation of nanoparticles, such as their temperature-dependent size evolution. Different solvents have different dielectric constants, viscosity, and solvation ability. Moreover, the use of different stabilizing agents may also result in different nucleation and growth mechanisms. In the original Peng synthesis, the higher temperature may increase the solubility of reactants, promoting the formation of smaller nanoparticles. Meanwhile, in the modified Peng synthesis, the higher temperature potentially results in increasing rates of nucleation and particle growth. This difference underlines the importance of reaction conditions in controlling the GNP size and morphology.

5.1.3 Gold Nanoparticle Composite Films

With the increasing interest in GNPs, numerous relevant application fields have emerged, including drug delivery[63], diagnostics[64], catalysts[65], probes[66, 67], electronics[68], and sensors[13, 69, 70]. This work particularly focuses on the application of GNP-based sensors. GNPs have the ability to self-assemble into ordered structures to varying degrees. Figure 5.2 illustrates two exemplary arrangements of GNPs using colloids of 12T capped GNPs. In Figure 5.2a, a thin film prepared by Olichwer et al.[14] via the drop-casting is shown. Van der Waals interactions between the long alkyl chains of 12T molecules promote a highly ordered arrangement of GNPs, known as a superlattice structure. Similarly, Huang's group also proposed the formation of long-range ordered self-assembled GNPs via the Langmuir-Blodgett method, cf. Figure 5.2b.[71] By adjusting parameters such as surface pressure during the Langmuir-Blodgett procedure, the voids and defects within the GNP film can be significantly reduced, resulting in a long-range ordered GNP assembly. Both of these examples of GNP assemblies are highly ordered, and their resulting GNP films are a few nanometers to tens of nanometers thick. In addition, even thicker GNP films are also of great interest, particularly for sensing applications. In 1998, Wohltjen and Snow reported the first chemiresistor based on organically capped GNP assemblies (with films hundreds of nanometers thick)[13], which sparked a rapid increase in related studies.

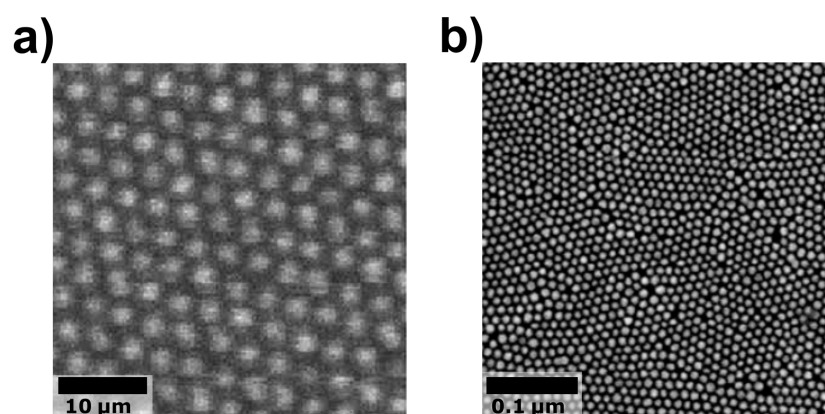


Figure 5.2: SEM images of two types of GNP assemblies. a) A colloidal solution of 1-dodecanethiol (12T) capped GNPs with an average core diameter of 3.7 nm was drop-casted on a silicon wafer. Reprinted with permission from Ref. [14]. ©2016 Royal Society of Chemistry. b) 12T capped GNPs with an average core diameter of 8.5 nm were deposited onto a hydrophobic hexamethyldisilazane modified silicon substrate via a Langmuir-Blodgett method. Reprinted with permission from Ref. [71]. ©2004 American Chemical Society.

For the applications of chemiresistors, 2-dimensional (2D) and 3-dimensional (3D) assemblies of organically capped GNPs or GNP films can be generated with different organic non-cross-linking ligands or cross-linker molecules through different fabrication approaches. Currently, three major approaches are applied for the fabrication of GNP-based chemiresistors with tunable selectivity, as illustrated in Figure 5.3.

Following Route A, multiple GNP syntheses are conducted in the presence of various ligands.[34, 72–75] Thus, the surface functionalization of GNPs occurs in situ during the formation of the GNPs. Given that the solubility and colloidal stability of the GNPs are determined by their surface functionalization, selecting appropriate solvents and adjusting reaction conditions for each type of ligand are crucial. However, due to the use of different ligands, the resulting GNP sizes vary from batch to batch. For example, Lu's group demonstrated GNP-based sensors with four kinds of terminal-functionalized thiol ligands. The GNPs were synthesized in the presence of the different ligands resulting in core diameters ranging between 2.5 to 3.7 nm.[74] After purification, the GNPs are deposited onto substrates. However, prior to sensor fabrication, each batch of GNP dispersion requires individual purification to eliminate excess ligands and reaction by-products. Consequently, preparing GNP-based chemiresistor arrays through Route A is laborious and requires substantial use of chemicals and solvents.

In comparison to Route A, Route B simplifies the procedure[39, 76]. In Route B, the same GNP batch is used to prepare all chemiresistors, avoiding variations in GNP size of different batches. To modulate the chemical selectivity, the GNP surface is initially coordinated with weakly binding ligands, such as amines. Due to the weak bonding between amine ligands and GNP surface, these ligands can be exchanged for functionalized ligands of interest, which bind more strongly to the GNP surface. Similar to Route A, adjustments of conditions for ligand-exchange reactions and selection of appropriate solvents for each ligand-exchange system are necessary. These steps ensure the colloidal stability of the resulting GNPs before their deposition as thin films. Furthermore, individual purification steps for different GNP batches are essential to remove excess ligands. Afterwards, the GNPs are deposited onto substrates via similar approaches as Route A. Therefore, while Route B simplifies the procedure, its advantages over Route A

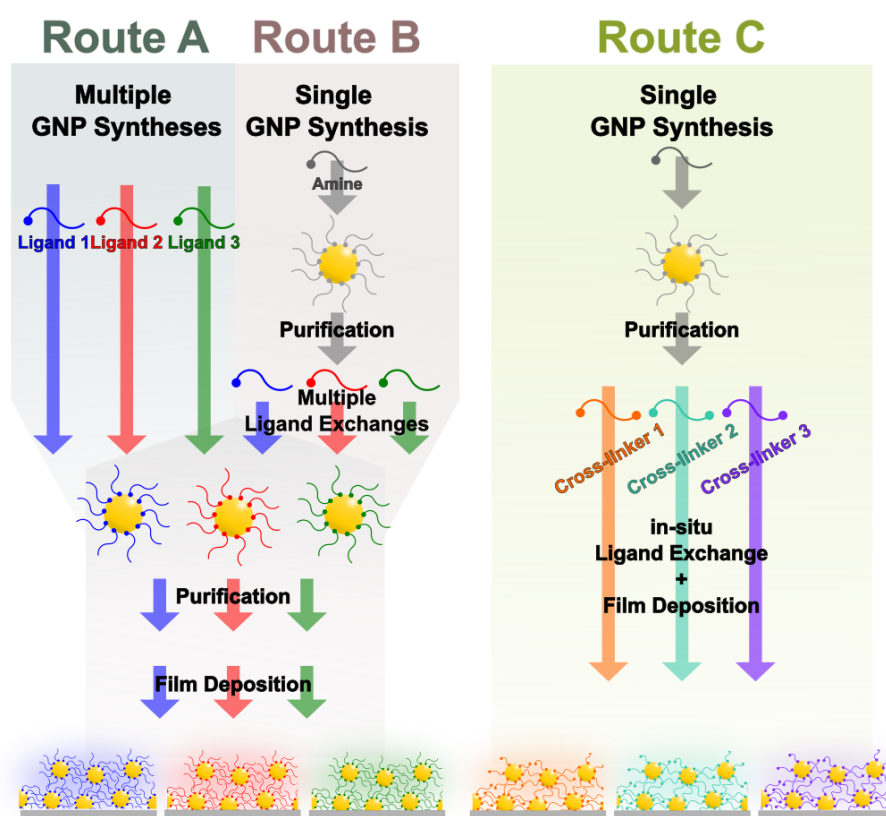


Figure 5.3: Different approaches to deposit GNP films as resistive transducing elements in chemical sensors. Routes A and B involve the preparation of GNPs in the liquid phase with different ligand shells to fine-tune the sensor's chemical selectivity before depositing the particles onto a suitable substrate. In Route C, surface modification of the GNPs and film preparation occur simultaneously through cross-linking the GNPs with various pure linker or ligand/linker mixtures. Reprinted with permission from Ref. [2]. ©2024 The Authors. Advanced Materials Interfaces published by Wiley-VCH GmbH.

are limited.

Route C involves the fabrication of GNP films using the same GNP stock solution as in Route B. However, in contrast, surface modification of GNPs and film deposition occur simultaneously through the formation of a cross-linked network of GNPs using different cross-linker molecules or ligand/linker mixtures.[15, 18, 20, 21, 24, 25, 31, 77–79] Consequently, the structure and chemical nature of the applied cross-linker and functionalized ligand molecules dominate the chemical selectivity of resulting GNP chemiresistors. The cross-linked network provides robustness to the GNP assembly, allowing for washing with arbitrary solvents and patterning the GNP film using lithographic methods.[23] Furthermore, this robustness also enables post-preparative tuning of the selectivity through a solid-state ligand/linker exchange.[23]

In summary, Routes A and B involve intricate handling of GNP colloidal batches to produce diverse surface-modified GNPs for film fabrication. Conversely, Route C streamlines the process by forming GNP films as a cross-linked network of GNPs without the need for a pre-surface-modification of the GNPs. These fabricated films can easily be washed with any solvent and re-functionalized as needed. Furthermore, cross-linking enhances the mechanical properties and durability of the film. Additionally, cross-linking can reduce baseline drifts associated with electromigration of non-cross-linked GNPs.[13]

Presently, Routes A and B are widely employed for the fabrication of GNP chemiresistors, while Route C is less commonly used, despite its potential advantages. Several variations of Route C have been reported. For example, Zhong and co-workers introduced a one-step exchange-cross-linking-precipitation method.[25, 32, 78] In another study, Mol’s group advanced a preparation process reported by Martin et al.[80], where GNPs in aqueous solution were first partially covered with different thiol ligands dissolved in a mixed solvent of n-hexane and chloroform. By adding ethanol into the solution, the GNPs were destabilised and migrated toward the water–organic interface, where their surfaces were partially coated by the thiol ligand. Simultaneously, GNPs assembled at the water–air interface forming a thin layer.[77] In a different experiment, Zamborini et al. used GNPs with mixed ligand shells comprising AT and ω -mercaptocarboxylic acid molecules to fabricate chemiresistors.[81] Following a layer-by-layer self-assembly (LbL-SA) approach, the terminal carboxylic acid groups complexed with Cu^{2+} ions form cross-linking bridges between adjacent GNPs. Further, vapor phase thiol place-exchange reactions were applied to produce differently functionalized GNP films, which were then used to fabricate chemiresistor arrays, as reported by Yang et al.[82]. Adapting Bethell et al.’s LbL-SA method[83], chemiresistors were fabricated by cross-linking amine-stabilized GNPs. The stabilizing amine ligands were replaced by a variety of dithiols (DTs)[16] and dendrimers[15–17, 20, 21, 84]. The LbL-SA process generally involves multiple assembly and washing steps. Therefore, the more economic and efficient layer-by-layer spin-coating (LbL-SC) method[18, 23, 85] was proposed to simplify the laborious LbL-SA process. Additionally, the LbL-SC approach is compatible with industrial fabrication routines, including standard photolithographic patterning[23]. Another simple LbL deposition method is LbL inkjet printing, where the GNP-based chemiresistors’ chemical selectivity can be tuned with functionalized ligand and cross-linker molecules.[24]

In the three discussed fabrication routes, Routes A and B typically utilize non-cross-linking and terminal-functionalized ligands (e.g., monothiols (MTs), amines), while Route C applies cross-linking molecules (e.g., DTs, disulfides). Commercially available functionalized ligands, with their diverse molecular structures, lengths, and functional groups, are preferably used as they enable a straightforward tuning of the chemical selectivity. For instance, Haick’s group developed a GNP chemiresistor array using various

lengths of straight and branched ATs, as well as functionalized MTs. This chemiresistor array enabled the diagnosis of lung cancer[32] and the detection of COVID-19[34]. Similarly, Willis' group employed commercially available functionalized MTs and amines for the fabrication of a chemiresistor array. Such sensor array successfully classified tea aromas[39], and detected explosives[37]. The selection of commercially available ligands for sensor preparation is more diverse than that of cross-linkers. Additionally, non-cross-linked GNP-based chemiresistors generally exhibit higher sensitivity than their cross-linked counterparts, attributed to the reduced swelling ability of cross-linked GNP films during analyte sorption.[14, 16, 22] Non-cross-linking ligands provide a broad diversity of functional groups for easy selectivity tuning and high sensitivity, while cross-linking molecules offer high stability of resulting GNP films and a straightforward fabrication route (Route C).

To complement the benefits of both non-cross-linking ligand and linker molecules, a mixed ligand/linker system may be effective. Few early studies on mixed ligand systems were reported. Zamborini et al. deliberately mixed different lengths of ATs and ω -mercaptocarboxylic acids. Different combinations of non-cross-linking and cross-linking molecules resulted in changes in the microstructures and the electron tunneling pathways within the organic matrix, leading to distinct swelling behavior in the resulting GNP assemblies.[81] Chow et al. described GNP films with tunable chemical selectivity using a mixture of 1-hexanethiol (6T) (with nonpolar tail) and 4-mercaptophenol (4MPO) (with polar functional group).[86] Three different ratios of 6T mixed with 4MPO were embedded into the organic matrices, impacting their hydrophilic-lipophilic balance, which also influenced the vapor sensing selectivity. Additionally, the ligand shell packing density can be modified by using a mixture of two types of MTs. Lu's group combined 1-octanethiol (8T) and 4-tert-butylbenzenethiol (4TBT) molecules, resulting in a looser ligand shell structure and slightly larger initial interparticle distance compared to a pure 8T ligand shell-coated GNP film, enhancing chemiresistive sensitivity.[87] In a recent development, our research group successfully fabricated GNP-based chemiresistors using the cross-linker 1,9-nonanedithiol (9DT) in combination with various functionalized MTs.[24] The cross-linker facilitated the layer-by-layer deposition of GNPs, while the incorporation of functionalized MTs resulted in versatile chemiresistive response patterns. This achievement with a mixed ligand/linker system demonstrates the potential to advance the field of GNP-based sensors.

In the previous paragraphs, a brief introduction to the three main fabrication routes and the application of ligands, linkers, and a mixed ligand/linker system was described. Generally, GNP films can be fabricated via various deposition methods onto the desired substrates. Some of the most common methods are spray-coating[13, 74], drop-casting[32, 37, 39, 88], Langmuir-Blodgett[71], LbL-SA[16, 17, 20, 81, 89], LbL-SC[18, 23, 85], and inkjet printing[24, 72, 90]. This work focuses on developing the facile fabrication of GNP-based sensors via Route C using a mixed ligand/linker system.

In the first part of this study, the LbL inkjet printing approach was applied. Inkjet printers fall into two main categories: continuous inkjet (CIJ) and drop-on-demand (DOD). In the early 1950s, CIJ was introduced to the market and remains popular up to date.[91] The concept of DOD was later introduced, allowing the controlled deposition of a single droplet onto a specific substrate location. DOD printers hold the advantages of reducing the use of ink and providing more precise deposition. DOD printers use either piezoelectric or thermal actuators.[92] Most consumer inkjet printers typically use thermal DOD printing, where heating elements on the printhead rapidly vaporize the ink in the chamber, forming a

bubble. Then, the increasing pressure in the chamber propels a droplet onto a substrate. Alternatively, a piezo-driven element deforms when voltage is applied, changing the volume of the ink chamber, and ejecting a droplet through the nozzle. The applied voltage pulse influences the droplet characteristics during the printing process.[92, 93] Figure 5.4 schematically illustrates unipolar pulse and bipolar pulse waveforms. A trapezoidal unipolar pulse waveform has three phases—rise time (t_{rise}), dwell time (t_{dwell}), and fall time (t_{fall}). A bipolar pulse waveform consists of a double trapezoidal waveform: a positive phase (highest voltage point: V_1) and a negative one (lowest voltage point: V_2). A positive trapezoidal pulse enables the jetting of a droplet efficiently, however, it generates residual vibrations. To dampen any of these residual vibrations, a positive pulse is followed by a negative trapezoidal pulse, as shown in Figure 5.4b.[94, 95] The parameters, such as applied voltages (V_1 and V_2) and jetting pulse periods (t_{rise} , t_{dwell} , t_{fall} , t_{echo} , and $t_{\text{finalrise}}$), must be carefully adjusted for reliable printing conditions. In this work, the GNP films were fabricated using a MicroFab inkjet printer with a bipolar pulse waveform. Further details on adjusted printing parameters and results will be presented in the Experimental Part and Results and Discussion chapters.

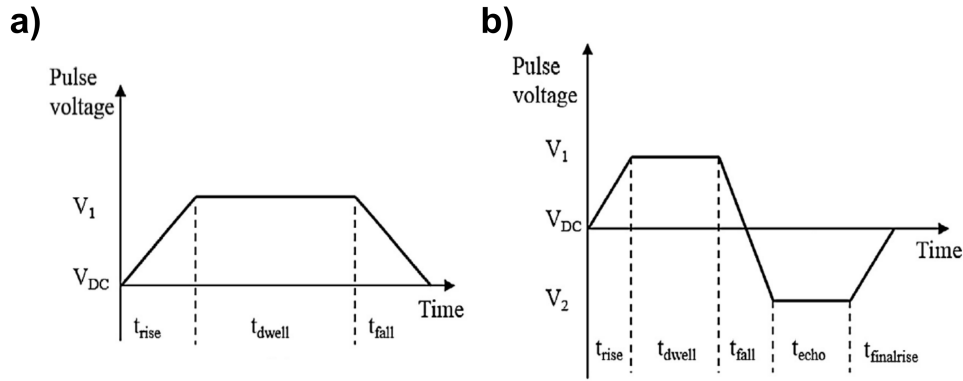


Figure 5.4: Schematic diagrams show a) a unipolar pulse waveform, and b) a bipolar pulse waveform. Reprinted with permission from Ref. [95]. ©2015 Elsevier.

In addition to inkjet printing, the LbL-SC approach was employed to prepare GNP films, which was well-established in 2011 by our research group.[85] In this approach, colloidal amine-stabilized GNPs and cross-linker (e.g., DTs) solutions are alternately deposited onto rotating substrates. The amine molecules used to stabilize the GNPs are rapidly replaced by the DT molecules. Each deposition cycle involves one droplet of GNP colloid and two droplets of linker solution. The thickness of the resulting GNP films is determined by the number of deposition cycles. To ensure compatibility with the LbL-SC method, we selected 9DT as the standard cross-linker for the mixed ligand/linker system used in this work. This choice allowed for effective LbL deposition.

5.2 Electrical Properties

Electrical conductivity is a crucial property of metals that finds application across various fields. Bulk metals are known for their high conductivity, a characteristic that can be explained by two prominent models: "electron sea model" and "molecular orbital (MO) and band theory". In 1900, Drude first proposed a simple model, explaining the electron transport in the solid state of metals.[96, 97] This model was further developed by Lorentz as the Drude-Lorentz model, or a more well-known name, the electron sea model.[98] In bulk metals, numerous atoms arrange themselves into a crystal-lattice structure, and their valence electrons are delocalized, creating a sea of electrons. Moreover, these electrons move freely across the metal lattice, obeying the Maxwell-Boltzmann distribution of velocities. Another model is the MO and band theory, which is rooted in chemical bonding models. The neighboring atomic orbitals (AOs) overlap with each other, forming MOs with discrete energies. In bulk metals, the large number of atoms results in an infinite number of overlapped AOs, generating a continuum of MOs. Consequently, the energy gap between these orbitals becomes negligible, forming a continuous band. However, with increasing temperature, the atoms in the lattice vibrate, which restricts the movement of free valence electrons, causing a decrease in electrical conductivity.[99]

Unlike bulk metals, the electrical properties of metals at the nanometer scale undergo changes due to quantum confinement effects. When the dimensions of a metal are reduced to the nanoscale, the finite number of atoms results in a breakdown of the band structure into discrete energy levels.[100] Granular metals, composite materials composed of both metals and insulators, exhibit non-metallic behavior in their electrical properties. The electrical conductivity increases with increasing temperature. Neugebauer and Webb proposed a model to describe the charge transport in such granular metals.[101] In the experiments, thin metal films were evaporated onto glass substrates, forming multiple metal islands (several tens of Ångströms) separated by small distances. The charge transport process involves two key steps: i) creation of thermally activated charge carriers, where electrons are transferred between initially neutral particles (resulting in the formation of charged particles), and ii) drifting of charge carriers in the presence of an electric field, leading to electron transfer between charged and neutral particles. Experimental data confirmed a linear correlation between the logarithm of conductivity and the reciprocal temperature (T^{-1}), following Arrhenius behavior. The fabricated thin films also displayed ohmic behavior while applying low bias voltage. Conclusively, the authors suggested a thermally activated tunneling mechanism within these granular materials, taking into account Coulomb charging energy of the particles. (cf. Equation 5.2)

$$\sigma = \sigma_0^* e^{-\frac{E_a^*}{kT}} \quad (5.2)$$

Here, σ_0^* is a pre-exponential factor, E_a^* is the thermal activation energy, k is the Boltzmann constant, and T is the absolute temperature in Kelvin. Several subsequent studies evidenced such Arrhenius-type model, showing a temperature dependent electrical conductivity $\ln \sigma \propto T^{-1}$ in metal composites.[102–106] However, other studies demonstrated a deviation from this inverse temperature relationship. Instead, a linear correlation between $T^{-\frac{1}{2}}$ and the logarithm of conductivity was observed.[107, 108]

For sensor applications, assemblies of organically capped GNPs are of particular interest. The charge transport in such granular materials can be described by a model proposed by Terrill et al., which is based on previously established charge transport models. This model accounts for thermally activated

charge tunneling processes according to the following Equation 5.3.[105, 109]

$$\sigma = \sigma_0 e^{-\beta\delta} e^{-\frac{E_a}{kT}} \quad (5.3)$$

Here, σ_0 is a pre-exponential factor, β is the tunneling decay constant, δ is the edge-to-edge distance between neighboring GNPs, and E_a is the activation energy.

The first term of the equation describes the tunneling process. From a quantum mechanical perspective, in a metal-insulator-metal junction, the potential barrier (insulator) has a finite height, which is much smaller than the typical barrier height. The typical barrier height is effected by the work function of the metal and the properties of the insulator. For gold, the work function is approximately 5.1 eV.[7, 110] Therefore, electrons can tunnel through the barrier. The probability of electron tunneling through the barrier can be expressed by the transmission probability, $|T|^2$.

$$|T|^2 \approx e^{-2KL} \quad (5.4)$$

Here, K is the tunneling decay constant, and L is the thickness of the barrier. The decay constant K depends on the height of the barrier (\bar{U}), as shown in Equation 5.5.

$$K = \frac{\sqrt{2m\bar{U}}}{\hbar} \quad (5.5)$$

Here, m is the mass of the electron and \hbar is the Planck's constant. Using Fermi's golden rule, the net rate of electron tunneling from one electrode to another can be calculated and translated into a net tunneling current I flowing from one electrode to the other.[7]

When considering the organic matrix capped GNP assemblies, the organic matrix consists of ligand or linker molecules (e.g., MTs or DTs) and acts as an electrical barrier. Compared to the previously mentioned tunneling process, such metal nanoparticle (MNP)-organic matrix-MNP configurations vary the effective potential barrier height. This is based on the alignment of the Fermi-level of the MNPs with the applied ligand or linker molecule's highest occupied molecular orbital (HOMO) and lowest unoccupied molecular orbital (LUMO). Within the ligand or linker molecule, the electrons tunnel through a superexchange pathway provided by the side orbitals.[7, 111] The tunneling efficiency shows an exponential dependence on the length of the molecules.[112] Similarly, Wuelfing et al. reported that GNP assemblies show an exponential dependence of electrical conductivity on the chain-length of the ligand molecules within GNP assemblies.[106] Further, when using conjugated molecules containing double-bonds or delocalized π -electrons, the charge can be transported more efficiently, leading to a smaller decay constant value. This is attributed to a narrower HOMO-LUMO gap or the positioning of the Fermi level of metal NPs closer to the HOMO or LUMO level of the molecule.[112] In experiments, the decay constant β can be determined by plotting $\ln \sigma$ against T^{-1} , where the obtained y-intercept represents the infinite temperature conductivity, which is equal to $\sigma_0 e^{-\beta\delta}$. The decay constant, β , is obtained from the slope of the $\ln(\sigma_0 e^{-\beta\delta})$ versus δ plot. For DT-crosslinked GNP assemblies, a tunneling decay constant of $\beta_N \sim 0.61$ [16] was obtained, where β_N is the decay constant per methylene unit of the alkyl chain of the DT molecule. This experimentally determined value is in good agreement with the values provided by Cui et al., where β_N is approximately 0.57 at zero bias.[113] In their measurements, DT molecules

comprised of different numbers of methylene units were co-assembled within a MT-coated gold surface, and the outer free thiol groups were contacted to a gold nanocrystal probe.

The second term in Equation 5.3 describes the activation energy for charge transport. Different approaches have been used to determine the charging energy of nanoparticle assemblies. The activation energy can theoretically be expressed based on Abeles's electrostatic model in granular metals.[114] This model takes into account the contribution of inter-particle capacitance to the charging energy by considering the surrounding particles as a concentric metal layer. The expression of the Coulomb charging energy is given as:

$$E_{A,GM} = \frac{e^2}{8\pi\epsilon\epsilon_0} \left(\frac{1}{r} - \frac{1}{r+\delta} \right) \quad (5.6)$$

Here, e is the electron charge, ϵ the relative permittivity of the surrounding medium, ϵ_0 the vacuum permittivity, r the radius of the particle, and δ the interparticle distance. Brust et al. prepared 3D pellets of DT-crosslinked GNPs, utilizing DT molecules of varying lengths and two different sizes of GNPs. The experimentally determined activation energy values were consistent with the theoretically estimated values.[103] The self-assembled films of MT-stabilized GNPs prepared by Terrill et al. were used to determine their activation energy, where the experimentally determined and theoretically estimated values were also consistent.[105] In accordance with this model, a larger particle size and a smaller interparticle distance lead to a smaller activation energy, resulting in higher electrical conductivity. Therefore, below a certain particle size, the typical linear I-V characteristic observed in MNP films may transition into a nonlinear I-V characteristic. Very small particles exhibit very low electrical capacitance. As a result, the electron transfer between the MNPs remains blocked until the energy provided by the applied electric field is high enough to overcome this barrier, which is known as the Coulomb blockade.[100]

Another model to describe the activation energy for electron transfer was developed by Marcus[115, 116], which can be expressed as follows:

$$\Delta G^* = \frac{\lambda}{4} = \frac{e^2}{16\pi\epsilon_0} \left(\frac{1}{2r_1} + \frac{1}{2r_2} - \frac{1}{r} \right) \left(\frac{1}{\epsilon_{op}} - \frac{1}{\epsilon_s} \right) \quad (5.7)$$

Here, ΔG^* is the free energy of activation based on the repolarization of the organic matrix, λ is the outer sphere reorganizational energy, r_1 and r_2 are the radii of neighboring NPs, r is the nanoparticles' center-to-center distance, and ϵ_{op} and ϵ_s are the medium optical and static dielectric constants.

Abele's model, based on electrostatic interactions and tunneling, describes the electrostatic potential energy and the work required to move charges within an electrostatic field. Marcus theory, on the other hand, is based on quantum mechanics and thermodynamics, focusing on the changes in the Gibbs free energy and the reorganization energy related to the electron transfer process. Nevertheless, both models can be used to describe electron transfer, with the activation energy being a key factor in determining transfer rates.

5.3 Gold Nanoparticle-Based Films and Sensors

5.3.1 Resistive Chemical Sensors

Composite films composed of organically capped GNPs possess unique physical and chemical properties, making them highly versatile for various applications, particularly in sensing. These properties are strongly influenced by factors such as particle size, shape, and the composition of the organic matrix surrounding the GNPs. As discussed in the previous section, GNPs have been extensively studied, and their synthesis methods allow for precise control over their size, shape and size distribution. Additionally, the selection of ligand or linker molecules for capping GNPs is highly versatile, enabling deliberate tuning of their chemical nature. These aforementioned advantages make GNP composite films excellent candidates for sensing applications. These composite films can generate electrical signals in response to chemical or physical stimuli, making them suitable for use in gas sensors[13–15], ion-sensing in liquid phase[117, 118], and strain sensors[90, 119–121]. The observed electrical signals are caused by the controllable aggregation of GNPs or swelling of the organic matrix surrounding the GNPs, which in turn, varies the grain size and the interparticle distance of the GNPs, respectively.

A chemiresistor is a type of sensor, which exhibits changes in resistance upon exposure to an analyte. For GNP composite films, when exposed to analyte vapor, the organic matrix sorbs the analyte molecules from the gas phase, resulting in swelling. This swelling effect enlarges the interparticle distance of GNPs. The vapor-induced resistive signal can be expressed by the following equation, which is derived from Equation 5.3.

$$\frac{\Delta R}{R_0} = e^{\beta \Delta \delta} \cdot e^{\Delta E_a / kT} - 1 \quad (5.8)$$

Here, R_0 is the baseline resistance of the sensor, ΔR is the relative change in resistance due to sorption of analyte by the film, β is the tunneling decay constant, $\Delta \delta$ is the change in the interparticle distance between neighboring GNPs, ΔE_a is the change in the activation energy, k is the Boltzmann constant, and T is the absolute temperature. The chemiresistive signal is considered as the relative resistance change normalized by the baseline resistance $\frac{\Delta R}{R_0}$.

In 1998, Wohltjen and Snow pioneered the development of the first GNP-based chemiresistors.[13] The chemiresistor they fabricated, which consisted of GNPs capped with 1-octanethiol (8T) ligands, exhibited a notable change in resistance upon exposure to different types of analyte vapors. Specifically, they observed a positive change in resistance (positive signal) when exposed to less polar or nonpolar vapors such as toluene and tetrachloroethylene. In contrast, exposure to polar vapors like 1-propanol and water resulted in a negative change in resistance (negative signal). The directional disparity in signals is attributed to two opposing effects acting on the charge transport mechanism, as described by Equation 5.8. Based on Equation 5.8, two factors influence the resistive response, which can be referred to as the "swelling effect" (first term) and the "permittivity effect" (second term). The swelling effect results in increased interparticle distances, leading to a positive signal. In contrast, the permittivity effect results from an increase in permittivity within the organic matrix during analyte sorption. As described

by Equation 5.6, exposure to analytes with a higher dielectric constant (higher polarity) increases the permittivity of the environment of the GNPs. Consequently, this lowers the activation energy, thereby increasing the electrical conductivity and resulting in a negative resistive response. These two effects are acting simultaneously, and the dominance of one over the other determines the direction of the signal. When the swelling effect dominates over the permittivity effect, a positive signal is observed, and vice versa. This interplay between the swelling and permittivity effects provides valuable insights into the underlying mechanisms governing the response of GNP-based chemiresistors to different analyte vapors.

The vapor-induced swelling of GNP films is significantly influenced by the amount of analyte sorbed by the GNP film from the vapor phase, which is primarily determined by the match of the solubility properties of the analyte and the film's organic matrix. Olichwer et al. conducted a study in which they combined chemiresistor and microgravimetric measurements with small angle X-ray scattering (SAXS) to establish a direct link between the swelling ability, the analyte sorption and the resistive response of the GNP films.[14] In their investigation, they found that the organic matrix consisting of 1-dodecanethiol (12T) molecules (with 12T possessing a long nonpolar alkyl tail) exhibited varying vapor uptake. Remarkably, when exposed to the analyte with the highest polarity, namely 1-propanol, the GNP films showed the lowest analyte uptake. Conversely, when exposed to the analyte with the lowest polarity, e.g., toluene vapor, the GNP films exhibited the highest uptake of analyte. This selective vapor-sorption behavior of the GNP films had a significant impact on their swelling extent. Specifically, the enhanced uptake of toluene vapor led to the largest interparticle distance change and highest amplitude of the resistive response observed in these films.

Vossmeier and coworkers[19] investigated DT cross-linked GNP chemiresistors. They provided indirect evidence of how the flexibility and the number of sorption sites impact the swelling ability. They reported that the longest DT molecule, 1,20-icosanedithiol (20DT), with a larger number of sorption sites, demonstrated enhanced flexibility in the organic matrix due to its long alkyl backbone. Additionally, Joseph et al.[16] reported more explicit evidence by preparing GNP films using both flexible 1,12-dodecanethiol (12DT) and rigid [4]-staffane-3,3''-dithiol (SF4) linker molecules. The 12DT cross-linked GNP films exhibited positive signals when exposed to various vapors, indicating a dominant swelling effect. In contrast, SF4-cross-linked GNP films showed negative responses to all vapors, indicating their restricted swelling ability, which allowed the permittivity effect to predominate.

In summary, for 3D GNP films, the swelling effect generally dominates, resulting in positive chemiresistive responses. However, the use of shorter and rigid cross-linker molecules weakens the swelling ability of GNP films, leading to negative responses or reduced response amplitudes. This highlights the potential for designing the organic matrix to achieve a wide range of desired responses.

5.3.2 Gravimetric Sensors

In addition to chemiresistors, gravimetric sensors serve as another type of transducer for detection of analytes in the gas phase. These sensors operate on the principle that the resonance frequency of mass-sensitive devices decreases upon the increase of mass by sorption of the analyte. Renowned for their remarkable sensitivity, stability, rapid response and recovery times, as well as cost-effectiveness, such

sensors hold immense promise. Among these, the quartz crystal microbalance (QCM) emerges as the most prevalent choice in this field.

The piezoelectric effect, first discovered by the Curie brothers[122, 123] in 1880, enables the functionality of such sensors. When a physical stress is applied to a piezoelectric material (for example, a quartz crystal), a voltage is generated on the surface of this material. In contrast, when an electrical field is applied to a piezoelectric material, a mechanical distortion in this material is induced (inverse piezoelectric effect). Quartz crystals, being anisotropic materials, exhibit piezoelectric coefficients that depend on crystal orientation. This dependency categorizes quartz crystals based on cutting angles relative to crystallographic axes, such as AT-cut, BT-cut, and FC-cut. Among them, the AT-cut crystal, with a cutting angle of $35^{\circ}15'$, shows exceptional frequency stability across temperatures ranging from -40 to 85°C . [124] AT-cut crystals operate in a pure thickness-shear-mode vibration configuration, making them more suitable for gravimetric sensing applications.

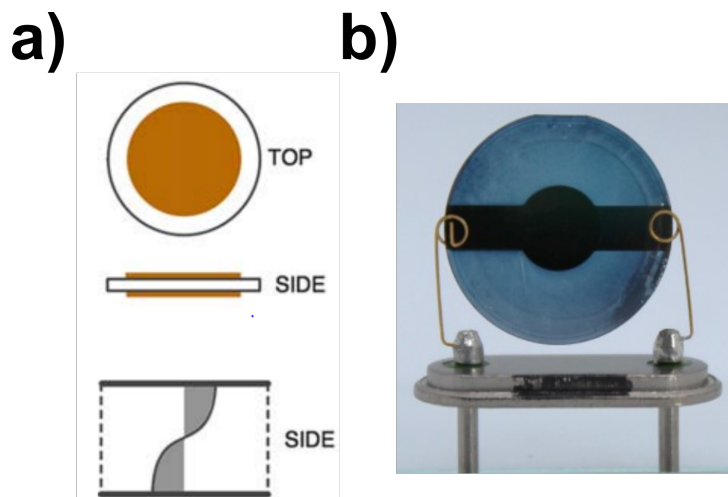


Figure 5.5: a) Scheme of a quartz crystal microbalance (QCM) from both top and side views. The bottom scheme shows the resonance of a QCM in the thickness shear mode. Reprinted with permission from Ref. [124]. ©2009 Springer Nature. b) Photograph of a GNP film-coated QCM serving as a mass sensitive sensor.

The QCM typically consists of a disc-shaped quartz plate sandwiched between two electrodes, known as the top and bottom electrodes (depicted in brown in Figure 5.5 a). When an alternating current (AC) voltage is applied, the quartz crystal undergoes mechanical oscillations, generating standing waves at its resonance frequency. This resonance frequency (f_0) depends on the thickness of the crystal; thinner crystals exhibit higher f_0 values, which are correlated with increased sensitivity. Typically, the resonance frequency of quartz crystals falls within the low MHz range ($\sim 1 - 10$ MHz). Even the smallest frequency shifts, as small as 1 Hz, are easily measurable, enabling the detection of sorbed masses as small as a few nanograms. However, bare QCMs lack selectivity towards target analytes. To enable chemical selectivity, sensitizing materials such as polymers[125–127], graphene[128, 129], and metal nanoparticle composites[130, 131], are deposited onto QCMs. The utilization of QCMs as mass-sensitive sensor dates back to the late 1950s, based on the pioneering work of Sauerbrey. In 1959, Sauerbrey reported a linear relationship between the frequency change (Δf) of an oscillating quartz and its mass change (Δm),

formulated by the Sauerbrey equation[132]:

$$\Delta f = \frac{2f_0^2}{\sqrt{\rho_q \mu_q}} \cdot \frac{\Delta m}{A} \quad (5.9)$$

Here, Δm denotes the mass change due to analyte sorption or the deposition of the sensitizing material, ρ_q and μ_q represent the density and shear modulus of the quartz crystal, respectively, and A is the active sensing area. Note, it is assumed that the sensitizing material is uniformly coated onto the QCM and behaves acoustically rigid like the quartz crystal. For very thin and rigidly coated films, the limit of applicability of the Sauerbrey equation is usually specified as $\Delta f/f_0 < 0.02$, known as the "Sauerbrey limit".

When a QCM resonates, both electrical current and mass oscillate simultaneously. Therefore, the QCM device can be represented by either a mechanical layout (cf. Figure 5.6a) or an equivalent circuit model (cf. Figure 5.6b). Here, the mechanical model consists of a spring, a mass (M), and a piston. The spring represents the restoring force through the elastic deformation of the quartz crystal, and the piston represents the dissipation of energy by the internal friction. On the other hand, the equivalent circuit model can be referred to as the Butterworth-Van Dyke (BVD) electrical model, which is useful for predicting the frequency shifts and losses of an AT-cut quartz crystal in QCM applications. It contains four elements, the static capacitance C_0 , the motional capacitance C_1 , the motional inductance L_1 , and the motional resistance R_1 . Comparing the mechanical and equivalent circuit models, L_1 corresponds to the oscillating mass, C_1 represents the elasticity (spring), and R_1 is the piston, reflecting the losses of the energy in the system. Another common method used to describe the electromechanical equivalent circuit is Mason's model, which takes into account the acoustic characteristics of the crystal. This model is based on transmission line theory and acoustic wave theory. The Mason's Model provides a more detailed and complex description of the acoustic wave behavior and piezoelectric effects, resulting in a more precise estimation of the QCM's performance.[133] However, due to the simplicity of the BVD model, it is more widely used for general QCM applications.

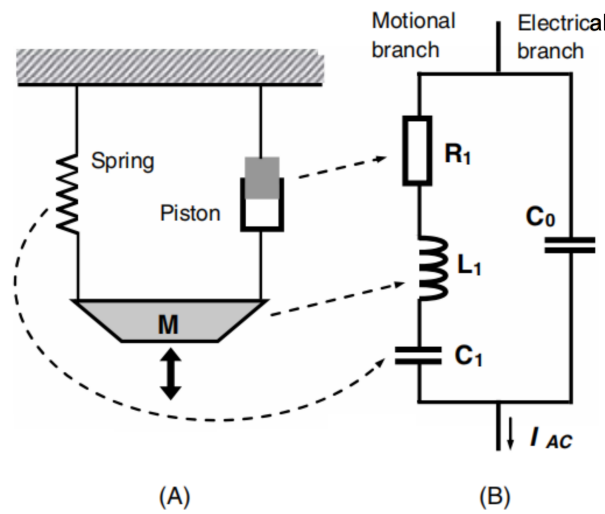


Figure 5.6: Schematic diagrams of a) the mechanical layout, and b) the equivalent circuit of an unloaded QCM sensor. The Butterworth-Van Dyke (BVD) equivalent circuit is widely used to model the electro-acoustic behavior of QCM devices. Reprinted with permission from Ref. [133]. ©2012 John Wiley and Sons.

According to Figure 5.6b, the impedance $Z(\omega)$ of QCM devices based on the BVD model is determined by the parallel combination of the impedance $Z_0(\omega)$ of the static (electrical) branch and the impedance $Z_1(\omega)$ of the motional branch. The analytical expression of impedance $Z(\omega)$ for the BVD model is given by the following equation:

$$Z(\omega) = \frac{Z_0(\omega)Z_1(\omega)}{Z_0(\omega) + Z_1(\omega)} \quad (5.10)$$

Furthermore, the impedance of the motional branch is expressed as:

$$Z_1(\omega) = R_1 + j\omega L_1 - \frac{j}{\omega C_1} \quad (5.11)$$

Here, j is the imaginary unit and ω is the angular frequency. When the QCM is at the resonance frequency, the inductive and capacitive components cancel each other out, leaving only the resistive component R_1 . Therefore, the impedance $Z_1(\omega)$ is minimized at this point and is equal to R_1 . In this scenario, the current reaches a maximum and the phase shift between the excited and measured oscillations equals zero.

For QCM measurements, a network analyzer applies an AC voltage, and the current is measured as a function of the applied frequency. The measured data is then analyzed by the network analyzer, presenting Bode plots showing impedance and phase shift versus frequency. Figure 5.7 shows exemplary Bode plots. In the upper plot, the static capacitance C_0 in the electrical branch causes signal splitting, resulting in resonance (left) and anti-resonance (right) peaks, corresponding to frequencies where the phase shift (φ) equals zero degree in the lower plot. Increasing the resistance (R_1) in the motional branch, corresponding to damping of the QCM's oscillation, leads to broader resonance and anti-resonance peaks, as well as to a flattened rectangular phase response.

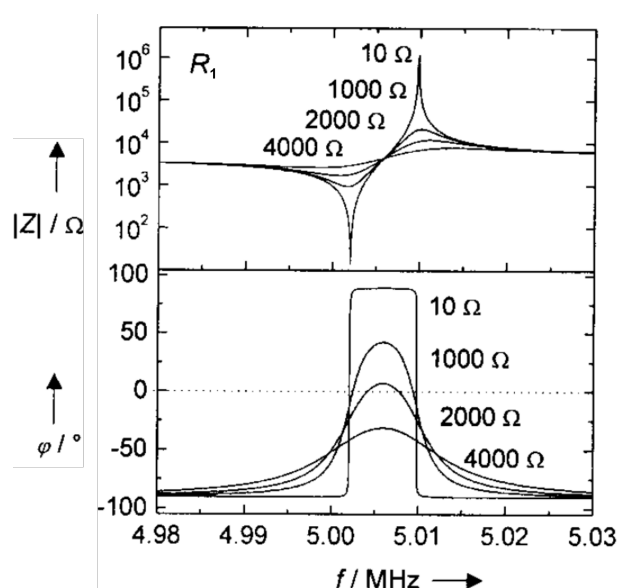


Figure 5.7: Simulated Bode plots of QCM devices using the BVD model. R_1 represents the resistance in the motional branch of the BVD model, cf. Figure 5.6b. The upper plot illustrates the effect of increasing R_1 on the resonance (left) and anti-resonance (right) peaks. The lower plot shows the impact of increasing R_1 on the phase response. Reprinted and adapted with permission from Ref. [134]. ©2000 Wiley-VCH.

5.3.3 Response Isotherm and Sorption Behavior

The resistive responses induced in GNP films by analyte sorption are often assumed to be directly proportional to the quantity of sorbed analyte in the film. The concentration of sorbed analyte in the film (C_f) depends on the concentration of analyte in the gas phase (C_g), and is related to the partition coefficient K , as described in Equation 5.12. This partition coefficient is related to two key factors: the vapor pressure of the analyte and the affinity between the analyte and the analyte sorption sites in the GNP films. Analytes with lower vapor pressures tend to be more favorably sorbed on sorption sites rather than remaining in the gas phase. Notably, the chemical nature of the organic matrix in GNP films influences analyte sorption preference; for instance, employing a more hydrophilic organic matrix tends to enhance the uptake of polar analytes. Generally, QCM measurements are used to investigate the sorption behavior of GNP films.

$$K = \frac{C_f}{C_g} \quad (5.12)$$

Figure 5.8 schematically illustrates three different sorption characteristics. The grey line represents nonselective adsorption, which obeys Henry's law with a linear dependence. When GNP films are prepared with extremely long and flexible cross-linkers, their resistive responses increase nearly linearly with increasing vapor concentration within certain concentration range.[78] Similarly, some MT ligand-stabilized GNP films also exhibit comparable behavior, such as films from MT-capped GNPs prepared using a spray-coating approach.[135, 136] However, due to the different film fabrication approaches, the variation in their nano- and micro-structures may also influence their resistive response isotherms as well as their sorption characteristics. For example, 12T-stabilized GNP films fabricated via a spray-

coating method exhibited a linear correlation[136], while other 12T-capped GNP films prepared via a drop-casting method by Olichwer et al.[14] exhibited a monoexponential increase in response amplitudes with increasing analyte concentration. This exponential behavior was attributed to the high flexibility of the MT-constructed organic matrices, where the sorbed analyte triggers a linear or exponential increase in interparticle distance between GNPs.

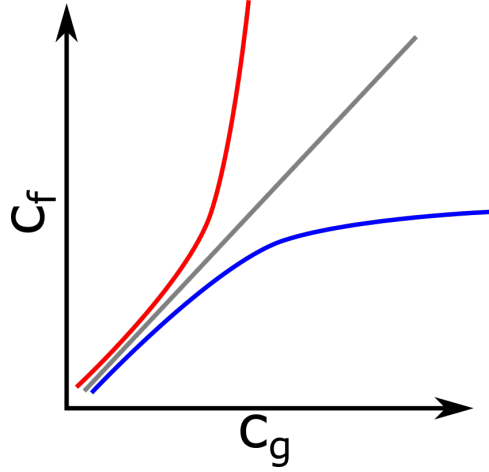


Figure 5.8: Schematic illustration of sorption isotherms, showing linear (grey line), positively curved (red line), and negatively curved (blue line) characteristics.

Selective monolayer adsorption is described by the Langmuir model (cf. Equation 5.13). At low concentration ranges, a quasi-linear correlation between the resistive response and vapor concentration is observed. When the analyte covers all binding sites, the resistive response reaches a plateau. Generally, for cross-linked GNP films, the resistive response isotherms can be described using either the Langmuir model[84, 137] or a combination of the Langmuir and Henry model.[15, 24] Equation 5.14 describes the combination of these two models, which considers both selective sorption and bulk partitioning.

$$\frac{\Delta R}{R_0} = \left(\frac{\Delta R}{R_0}\right)_{\text{sat}} \frac{K_L C_g}{1 + K_L C_g} \quad (5.13)$$

$$\frac{\Delta R}{R_0} = \left(\frac{\Delta R}{R_0}\right)_{\text{sat}} \frac{K_L C_g}{1 + K_L C_g} + K_H C_g \quad (5.14)$$

In these equations, $\left(\frac{\Delta R}{R_0}\right)_{\text{sat}}$ denotes the Langmuir saturation response, K_L is the Langmuir binding constant, and K_H is the bulk partitioning constant of Henry's law.

5.3.4 Stability of Gold Nanoparticle Films and Sensors

GNP composites are promising candidates for applications as sensing materials, e.g., as chemiresistors and gravimetric sensors. While significant progress has been made in developing fabrication methods for GNP-based sensor devices, and understanding their electrical and mechanical properties, challenges remain in translating these findings from the laboratory to practical market applications.

One critical obstacle is the stability of GNP composites. The stability of a sensor ensures the accuracy and reliability of electrical signals over a period of time, which can be classified into the short-term and the long-term stability. The short-term stability can be defined as the consistency of sensor performance on the same stimulus in the time frame of seconds to minutes. Factors such as electronic noise, vapor-induced aggregation and rearrangement of GNPs, and environmental fluctuations can influence the short-term stability. This aspect is particularly crucial for real-time monitoring applications, where precise and reliable sensing information is essential. On the other hand, the long-term stability refers to the ability of electronic devices to maintain their sensing capability without significant deviations over weeks, months, or even years of usage. Aging of GNP composites is the primary factor affecting the long-term stability. Ensuring the long-term stability is critical for practical applications, allowing continuous detection over extended periods without frequent maintenance requirements.

Since GNP assemblies are often prepared with MT or DT molecules, several studies have focused on investigating the degradation of these molecules, providing insights into the aging processes they induce. In 1992, Li et al. used laser desorption Fourier-transform mass spectrometry to characterize self-assembled AT molecules on a gold film. This study revealed the oxidation of thiolate upon air exposure, resulting in the generation of sulfonate. Interestingly, the intensity of the detected sulfonate signal increased when a shorter chain length of AT molecules was used.[138] Later, Huang et al.[139] also detected sulfonate signals using the same measuring approach, where the self-assembled monolayer (SAM) of two types of MTs was irradiated with UV-light. The same finding of chain-length dependent oxidation rate was reported by Hutt and Leggett[140], where different lengths of straight ATs were employed and exposed to UV-light. The oxidation rate strongly depends on the chain length of ATs, and correlates with the degree of order in the SAM of ATs. When the ATs contain less than 8 methylene units, the resulting SAM on the gold surface is less ordered and shows much faster oxidation, compared to those containing more than 8 methylene units. At a similar time, some studies also investigated the oxidation phenomenon under different conditions, such as ambient conditions, under oxygen-poor conditions, under exposure to light, or in darkness. Under different ozone levels, Schoenfisch and Pemberton reported that ozone is the primary oxidant responsible for sulfur oxidation.[141] Brewer et al.[142] applied UV light to oxidize 11-mercaptoundecanoic acid (11MUA) SAMs. The oxidized thiolate also partially desorbed from the gold surface. A more comprehensive investigation on storage conditions was performed by Willey et al.[143], where 12T SAMs on gold substrates were kept under four conditions: oxygen-poor and in darkness, oxygen-poor and under light, oxygen-enriched in darkness, and oxygen-enriched under light. In the absence of oxygen, both samples in the dark and light still contained a high amount of sulfur-gold bonds, losing only a few molecules. Conversely, both samples under oxygen-enriched conditions oxidized rapidly, leading to a less orientational order of the SAM. In a more recent study, Maciel et al. demonstrated that the terminal group of SAM significantly impacts the oxidation rate. Methyl-terminated SAMs showed the highest stability over 9 weeks of storage in an oxygen-free and dark environment. In contrast, hydroxyl-terminated SAMs showed the lowest stability. Even under the same storage conditions, hydroxyl-terminated thiol oxidized after two weeks.[144]

The oxidation phenomenon discussed above were primarily studied using thiol-based SAMs on planar gold surfaces. In practical sensing applications, 3D GNP assemblies are more often used than 2D SAMs. Zamborini's group reported GNP-based chemiresistors with varying degrees of cross-linking. Initially, 6T molecules were used to encapsulate the GNPs, that were later partially substituted with 1,6-hexanedithiol

(6DT) molecules. The introduction of 6DT molecules establishes a cross-linked network within the organic matrix, enhancing the stability. The organic matrices with a high ratio of 6DT exhibited repeatable resistive responses to the same analyte vapor under identical conditions, indicating a good short-term stability. In contrast, the organic matrices with a high ratio of 6T showed different responses under the same measuring conditions.[22] The same research group also investigated the influence of different capping ligands used in GNP films, such as tetraoctylammonium bromide (TOAB) and 6T. After 12 months, the resistive response amplitude of the GNP films prepared with the 6T ligands to analyte vapors decreased dramatically by as much as 60%, and the baseline current of these films reduced by nearly 50%. Conversely, GNP chemiresistors prepared with TOAB ligands showed only minimal changes in the baseline current, with a reduction in resistive response amplitude of less than 20% after 16 months of fabrication. This emphasizes a more pronounced oxidation of sulfurs compared to amines.[8] Consistent with experiments using thiol-based SAMs on flat gold surfaces, different terminal groups strongly influence the oxidation rate. For instance, Im et al. reported that GNP sensors prepared with aryl-terminated molecules exhibited high stability, whereas those prepared with hydroxyl-terminated molecules showed low stability.[145] X-ray photoelectron spectroscopy (XPS) data also revealed partial desorption of oxidized thiol molecules, suggesting that continuous exposure to analyte vapors may accelerate the degradation of thiol monolayer. Additionally, Garg et al.[146] used trithiol instead of monothiol molecules to enhance the stability of fabricated GNP chemiresistors. The structure of trithiol efficiently prevents oxygen from penetrating the ligand shell and reaching the sulfur-gold bond. More comprehensive oxidation conditions were studied by Joseph et al.[147], where GNP chemiresistors consisting of alkanedithiol cross-linked networks were stored under four different conditions. These four storage conditions were the same as those used in Willey's study[143] using 12T-based SAM on gold substrates (under ambient conditions in the light, under ambient conditions in the dark, under inert atmosphere in the light, and under inert atmosphere in the dark). Similar results were observed, with XPS data demonstrating neglectable degradation of thiolates for the samples stored under inert atmosphere. However, changes in chemiresistor behavior suggested alterations in their microstructures.

In summary, both 2D MT-based SAMs on gold surfaces and 3D organically capped GNP films demonstrated similar results, indicating that chain length, terminal functional group, and storage conditions are the main factors impacting the rate of degradation. In our research group, we observed a drift in the baseline resistance of the fabricated sensors, highlighting the critical need to address both the short-term and the long-term stability concerns. Recently, Ketelsen[148] began investigating the aging behavior of alkanedithiol cross-linked GNP films. Sensors were prepared using three different sizes of GNPs cross-linked by 9DT molecules and subjected to various storage conditions: in a nitrogen chamber, or artificially aged in a climate chamber under heating and humid conditions. Interestingly, a significant increase in conductance was observed in samples exposed to heating and humid conditions, particularly those prepared with larger GNPs. This phenomenon may be attributed to a lower degree of cross-linking in GNP films prepared with larger particles, which leads to faster degradation of 9DT molecules. Apart from changes in their electrical properties, their strain sensing characteristics also varied accordingly. However, X-ray diffraction (XRD) and XPS measurements showed only minor changes, suggesting a low degree of degradation of thiolates. A slight decrease in the activation energies for electron transfer in these GNP films was observed, implying potential growth of GNPs due to the Ostwald ripening mechanism. The aging behavior of GNP composites is complex, and further characterization methods are required to gain a deeper understanding of this phenomenon. Nevertheless, it is crucial to consider the influence of aging

when using GNP composites as sensors. Such sensors should be stored under appropriate conditions.

Based on the findings from pioneering works, all fabricated sensors in this study were stored in a light-shielded nitrogen chamber to minimize degradation of ligands and linkers and to prolong the sensors' stability. To evaluate the sensors' stability, current-voltage (I-V) curves and chemiresistor characteristics of GNP-based sensors were periodically recorded.

5.3.5 Sensor Arrays and Pattern Recognition

As the development of GNP-based sensors continues to advance, their potential applications under real-world conditions are rapidly expanding, including areas such as real-time health diagnosis, environmental monitoring, and quality control in the food industry. Conventional approaches to detect target analytes often rely on the lock-and-key principle, where sensors must exhibit high selectivity or specificity to certain chemical compounds. For example, recent studies have linked acetone concentration in breath to blood plasma glucose levels, making acetone sensing from exhaled breath a promising approach for real-time, noninvasive monitoring of diabetes patients. However, acetone has a high vapor pressure and is only present in the part per billion (ppb) range of human breath, making its detection a major challenge. To address this, Xie et al. synthesized urea-structured thiol molecules specifically designed for detecting acetone vapor. These urea-functionalized thiol GNP sensors exhibited high selectivity for acetone over other chemical vapors, such as ethylbenzene, ethanol, and water, due to the hydrogen bonding of carbonyl-urea.[149, 150] However, it's worth noting that such binding moieties may not be limited to acetone alone but could potentially interact with other compounds containing carbonyl groups, emphasizing the complexity of designing specific molecules for target analytes.

In 1982, Persaud and Dodd[151] proposed an alternative approach inspired by the mammalian senses of taste and smell. Instead of using highly specific sensors, they proposed the use of "differential" or "generalized" sensors. An array of broadly cross-reactive sensors, coupled with pattern recognition methods, enables the classification of a variety of chemical compounds either in the gas phase (resembling an electronic nose) or in the liquid phase (resembling an electronic tongue).[152] This approach is particularly useful when dealing with complex backgrounds, such as high humidity and a broad variety of volatile organic compounds (VOCs) present in human breath. Moreover, since most diseases cannot be detected by a single VOC such cross-sensitive sensor arrays successfully overcome this limitation and are capable of sensing multiple analytes simultaneously. Numerous studies have demonstrated the remarkable achievements of GNP-based chemiresistor arrays in this field. For instance, Cooper et al. developed eight GNP films composed of various functionalized MT and DT molecules to discriminate between mixtures of alcohols and mixtures of hydrocarbons in liquid phases.[153] Moreover, in the past decades, more research groups reported GNP-based chemiresistors in conjunction with pattern recognition algorithms for sensing in the gas phase. Haick's group developed a wide variety of thiol-capped GNP-based chemiresistors, allowing for the detection of lung cancer.[32] Later, these sensors have been further expanded to diagnose multiple types of cancer in a single breath test.[33] Beyond cancer detection, GNP-based chemiresistors have also been employed in the diagnosis of chronic kidney disease.[154] Further, during the COVID-19 outbreak, these sensors were even utilized to differentiate between infected patients and healthy controls, highlighting their adaptability to real-world demands.[34]

The remarkable achievements of sensor arrays have been extensively documented across various applications, including plant health monitoring[155], explosives detection[37], pollutant identification[41], and differentiation of tea aromas[39]. However, none of these applications could be enabled without the assistance of pattern recognition approaches. In pattern recognition, features are extracted from each signal response of individual sensors. Commonly, "steady-state" features such as the highest relative resistance change over baseline resistance are extracted as input data for classification.[32, 33] In addition to "steady-state" features, "transient-state" features provide further information, such as response and recovery times of signals.[18] Different pattern recognition algorithms have been applied, including principal component analysis (PCA), linear discriminant analysis (LDA), artificial neural networks (ANNs), and so on.

Sensor arrays with a large number of extracted features possess high dimensionality. In order to reduce the dimensionality of datasets and still preserve their information, PCA is widely employed in many studies.[32, 33, 88, 155, 156] PCA aims to find a rotated coordinate system, where the variance of the projected data is maximized. The data processing begins by shifting the origin of the coordinate system to the center of gravity of the data (mean of the dataset) and then calculating the eigenvectors and eigenvalues of the covariance matrix. The eigenvectors represent the directions of the maximum variance, while the eigenvalues indicate the magnitude of the variance spread on each eigenvector. Subsequently, the eigenvectors are used to transform the data into a lower-dimensional space, known as the principal subspace.[157, 158]

Another technique for dimensionality reduction is LDA. Firstly, the mean of all data points and the mean of the data points within the same classes are determined. Subsequently, the scatter between different classes (between-class matrix) and the scatter within the same classes (within-class matrix) are calculated. The aim is to construct a lower dimensional space that maximizes the ratio of the between-class matrix to the within-class matrix. Finally, all data points are projected into the lower dimensional space for classification.[157–159] The supervised learning method, LDA, is often considered a better way to separate different classes of analytes than the unsupervised learning method, PCA, which focuses on reducing the dimensionality of the data by capturing the direction with the maximum variance in a dataset, regardless of any class labels. This means that PCA is not always effective in separating different classes. On the other hand, with LDA, the user has provided the computer with labeled data, and LDA attempts to maximize the separation between different classes by finding the linear combinations of features that best distinguishes them. Because LDA uses class labels in its computations, it is better suited for tasks such as classification and pattern recognition, which results in more efficient separation of different classes of analytes.

In conclusion, sensor arrays coupled with pattern recognition algorithms are powerful tools that mimic biological systems such as electronic noses or electronic tongues. In this dissertation, organic matrices composed of a diverse mixture of functionalized MT/DT molecules were selected for the preparation of GNP-based chemiresistor arrays. Combined with LDA, these sensor arrays could be used to classify different VOCs such as alcohols, ketones, n-alkanes, and cycloalkanes.

Chapter 6

Experimental Part

6.1 Colloidal Gold Nanoparticles

In total, five batches of colloidal gold nanoparticles (GNPs) were synthesized following the approach proposed by Peng et al.[160] with slight modifications. The resulting GNPs were stabilized by 1-dodecylamine ligands in n-heptane. Subsequently, these particle batches were analyzed using transmission electron microscopy (TEM), UV/vis spectroscopy, and small angle X-ray scattering (SAXS).

6.1.1 Materials and Apparatus

(*Materials*) 1-Dodecylamine (12A, 98%), tert-butylamine borane complex (TBAB, 98%), tetrachloroauric(III) acid (HAuCl_4 , 99.99%), 1-hexadecanethiol (16T, 99%), ethanol (EtOH, 99.8%), 2-propanol ($\geq 99.5\%$), n-hexane ($\geq 99\%$), n-heptane (99%), and toluene (99.5%) were purchased from Sigma Aldrich, Alfa Aesar, and VWR. All chemicals were used as received without further purification. Deionized water ($18.2 \text{ M}\Omega\cdot\text{cm}$) was purified using a water purification system (ELGA LabWater). Polytetrafluoroethylene (PTFE) syringe filters (pore size of $0.2 \text{ }\mu\text{m}$) were purchased from Carl Roth. (*Apparatus*) A centrifuge (Sigma 3-18K) was used for the purification process of the GNP synthesis.

6.1.2 Synthesis

The synthesis of GNPs was conducted using a three-neck flask. Initially, 5.6 g (30.21 mmol) of 12A was dissolved in 10 mL of n-hexane, and the solution was stirred continuously until it became clear. Subsequently, 110 mg of tetrachloroauric(III) acid (0.28 mmol) was added to the 12A solution until the solution turned a light orange color, indicating complete dissolution. Simultaneously, the reducing agent, 0.044 g (0.51 mmol) of TBAB, was pre-dissolved in a 12A/n-hexane solution (0.56g 12A, 3.02 mmol, in 1 mL of n-hexane). Using a syringe, the TBAB solution was injected into the three-neck flask, resulting in

a rapid color change of the solution to dark red. The reaction was carried out at 25 °C for the synthesis of batch GNP1 and at 32 °C for the syntheses of batches GNP2-5, all at 900 rpm for an hour. To terminate the reaction, 50 mL of EtOH was added to the flask and cooled to room temperature. The solution was gently shaken by hand and then stored in the fridge overnight.

On the following day, the transparent supernatant was removed from the solution, and the remaining solution was divided into two 45 mL centrifuge tubes for centrifugation (10000 G for 5 min at 0 °C). After centrifugation, the supernatant was discarded, and the precipitate was re-dispersed in 4 mL of n-heptane. The GNPs were precipitated again with 12 mL of 2-propanol, followed by centrifugation (15,000 G) for 10 minutes at 0°C. This purification process was repeated twice to eliminate excess 12A and unreacted TBAB. Finally, the GNPs were re-dispersed in 2 or 4 mL of n-heptane, and the GNP colloid was filtered through a PTFE syringe filter.

6.1.3 TEM-Sample Preparation and Analysis

To prevent the aggregation of GNPs during the measurements, GNP colloids underwent a ligand exchange process.[85] To enhance the stability of GNPs, the 12A ligands were replaced by the 16T ligands. For this purpose, 25 μ L of 16T was dissolved in 500 μ L of n-heptane, followed by the addition of 25 μ L of GNP solution. The solution was agitated on a shaking tray for one hour. Subsequently, 1 mL of EtOH was added to the solution, and it was centrifuged at 8000 G for 10 min at room temperature. After centrifugation, the supernatant was discarded, and the GNPs were blown by using a nitrogen gun. The dried GNPs were re-dispersed in toluene and diluted until the colloid exhibited a light pink color.

Next, 7 μ L of the diluted GNP colloid was dripped onto a carbon-coated TEM grid, and the solvent of the TEM-sample was evaporated under ambient conditions for at least one hour. TEM measurements were performed using a JEOL JEM-1011 microscope equipped with a LaB₆ filament and operated at an acceleration voltage of 100 kV. TEM imaging was conducted by Stefan Werner at the department service center of the electron microscopy of the Institute of Physical Chemistry (University of Hamburg). To determine the average sizes of the GNPs, the cross-sectional areas of at least approximately 400 GNPs were extracted from the TEM images using the software *ImageJ*. The average core diameters of the synthesized GNPs ranged from 6.0 to 7.5 nm.

6.1.4 Determination of Particle Concentration Using UV/vis Spectroscopy

The GNP colloidal solutions were diluted with n-heptane at dilution factors ranging from 300 to 600 to achieve a UV/vis absorbance of at least 0.3. Subsequently, the diluted GNP solutions were transferred into a quartz cuvette with an optical path of 10 mm, and analyzed using a Cary50 spectrophotometer. During the measurements, light illuminated the sample at wavelengths ranging from UV to visible, from 300 to 900 nm. All recorded spectra were corrected with n-heptane background absorbance. The particle concentration of the GNP colloids was calculated following the method reported by Haiss et al.[161], which considers the UV/vis absorbance at 450 nm, the dilution factor, and the average GNP size determined by TEM.

6.1.5 Regular Small Angle X-Ray Scattering (SAXS)

To further determine the particle size and size distribution of a GNP colloid, a small angle X-ray scattering (SAXS) measurement was conducted under ambient conditions by Dr. Andreas Meyer at the Institute of Physical Chemistry, University of Hamburg. An in-house SAXS apparatus was used, equipped with an Incoatec—X-ray source I_μS and Quazar Montel optics. The wavelength of X-ray beam was 0.154 nm and was directed at the sample with a focal spot size of 0.6 mm². The undiluted GNP colloid was filled into a quartz capillary, and measured in transmission geometry. The SAXS sample was placed at a distance of 1.2 m from a Rayonix SX165 CCD detector, and the accumulation period of each measurement was set to 10 min. The analysis and fitting of the SAXS data were conducted by Dr. Andreas Meyer using the software *Scatter*.^[162, 163]

6.2 Fabrication of Fully Printed Gold Nanoparticle-Based Chemiresistors

The GNP batch, GNP1, was used to fabricate the fully printed sensors. The fabrication process of a fully printed GNP chemiresistor consists of two main parts: i) electrode printing, and ii) deposition of GNP films.

6.2.1 Materials and Apparatus

(*Materials*) 1,9-Nonanedithiol (9DT, 95%), 11-mercapto-1-undecanol (11MUO, 97%), 4-mercaptobenzoic acid (4MBA, 90%), and 4-mercaptophenol (4MPO, 97%), 11-mercaptopundecanoic acid (11MUA, 95%), 1-thioglycerol (TG, $\geq 97\%$), 2-aminothiophenol (2ATP, 90%), 2-propanol ($\geq 90\%$), acetone ($\geq 99.8\%$), and n-octane ($\geq 98\%$) were purchased from Alfa Aesar, Sigma Aldrich, and Merck. These chemicals were used as received without further purification. The nylon filter membranes (pore size: $0.45\ \mu\text{m}$) were purchased from Finetech. The graphene-doped carbon paste was purchased from Euflex. Polyimide (PI) foil was purchased from Shinmax Technology Ltd. (*Apparatus*) Robotic dispensing system (DT-200F, Dispenser Tech Co., Ltd.), inkjet printing system (JetLab 4, MicroFab Technologies Inc.), homogenizer (Kennesaw, Omni Ruptor 4000), and plasma system (Delta, TP04) were employed in the fabrication process.

6.2.2 Fabrication of Interdigitated Electrodes

Prior to the printing process, the conductive carbon paste was homogenized for 3 minutes, and the PI substrate was cleaned with acetone. A robotic dispensing system equipped with a stainless steel nozzle with an inner diameter of $110\ \mu\text{m}$ was used to print the interdigitated electrode (IDE) structures onto the PI substrates. The printed IDE structure comprised 5 pairs of fingers with a finger width of $\sim 195\ \mu\text{m}$, a spacing of $\sim 160\ \mu\text{m}$ between the fingers, and an overlapping length of $\sim 5\ \text{mm}$, accompanied by two $5 \times 2.5\ \text{mm}^2$ pads on each side. To dry the freshly printed IDE structures, the substrate was placed on a hot plate heated to $60\ ^\circ\text{C}$ for one hour.

6.2.3 Fabrication of Gold Nanoparticle Films via Inkjet Printing

The GNP ink was prepared using the diluted GNP batch, GNP1. To ensure optimum printing conditions, the original GNP1 colloid was diluted by a factor of four using n-octane to create a more stable ink, which was more suited to the printing procedure. Furthermore, the diluted GNP colloid was filtered through a nylon syringe filter to remove larger GNPs induced by aggregation. In parallel, the organic inks were prepared using either pure cross-linker (9DT) or mixtures of monothiol (MT)/9DT solutions. Initially, the stock solutions of MT and 9DT were prepared in 2-propanol at a concentration of $7.4\ \text{mM}$. The 9DT stock solution directly served as the 9DT ink. The MT/9DT solutions were prepared by combining MT and 9DT stock solutions in a volume ratio of 1:3. For pre-printing preparation, both GNP and organic

(9DT or MT/9DT) inks were filled into two separate small vials, each connected to an individual printing nozzle. Prior to film deposition, the IDE-mounted PI substrate was treated with plasma cleaning for 5 minutes. For the inkjet printer, the purge pressure of the device was set to 10 psi, which supplied a constant flow to mechanically impulse printing ink. On the other hand, the back pressure of the device was adjusted between -15 to 0 psi to counter the purge pressure, yielding a steady flow to transfer the ink from the vial to the nozzle. The inkjet printer utilized the piezo-driven printing nozzles with an inner diameter of 50 μm , actuated by a bipolar pulse, both positive and negative. When applying voltage, the piezoelectric transducer inside the printing nozzles deforms, inducing pressure inside the inner wall of the nozzles. This generated forces, therefore, enable either the acceleration or ejection of droplets from the inks. Moreover, different ink compositions require adjustments to the parameters of the piezo-actuator, such as rise-, dwell-, fall-, echo- and finalrise-times as well as the voltages of the bipolar driving pulse.

During the printing process, a constant ejection frequency of 700 Hz was maintained and the droplets were continuously monitored by an integrated CCD camera. The droplet diameter was controlled within the range of 35 to 65 μm . The specific parameters for the GNP and organic (the pure 9DT or the mixtures of MT/9DT) inks are presented in Table 6.1. Depending on the printing environment and the ink composition, these parameters were slightly adjusted to achieve stable droplet formation.

For the deposition of the GNP film, the printing procedure began with using the 9DT ink to establish an adhesive layer between the substrate and the GNPs. Subsequently, the GNP ink was applied to form a homogeneous coating, followed by one coating of organic ink to create an organic matrix. This sequential deposition of GNP and organic inks represented one complete deposition cycle. In total, three deposition cycles were used to fabricate the printed GNP-based chemiresistors.

Table 6.1: Adjusted parameters for the piezo-driven printing nozzle during the printing procedure. The notation for these adjusted printing parameters refers to those shown in the exemplary bipolar pulse waveform in Figure 5.4b.

Ink	t_{rise} [μs]	t_{dwell} [μs]	t_{fall} [μs]	t_{echo} [μs]	$t_{\text{finalrise}}$ [μs]	Dwell voltage [V]	Echo voltage [V]
GNP	6	3	5	4	2	20	-20
Organic	3	4	3	3	3	30	-35

6.3 Glass-Supported Gold Nanoparticle-Based Chemiresistors

The GNP batches GNP2, GNP3 and, GNP4, were utilized to fabricate GNP-based chemiresistors on glass substrates via a layer-by-layer spin-coating (LbL-SC)[85] procedure. Additionally, a strategy utilizing monothiol (MT) ligand/dithiol linker mixtures was employed to modify the chemical and physical properties of the organic matrix surrounding the GNPs.

6.3.1 Materials and Apparatus

(*Materials*) 1,9-Nonanedithiol (9DT, 95%), 1-hexanethiol (6T, 95%), 1-octanethiol (8T, $\geq 98.5\%$), 1-decanethiol (10T, 96%), 1-undecanethiol (11T, $\geq 96\%$), 1-dodecanethiol (12T, 98%), 1-tetradecanethiol (14T, $\geq 97\%$), 3-mercaptopropionic acid (3MPA, $\geq 99\%$), 6-mercaptophexanoic acid (6MHA, 90%), 8-mercaptooctanoic acid (8MOA, 95%), 11-mercaptoundecanoic acid (11MUA, 95%), 4-mercaptobenzoic acid (4MBA, 90%), methanol ($\geq 99.8\%$), acetone (99.5%), toluene (99.5%), and 3-aminopropyldimethylethoxysilane (95%) were purchased from Sigma Aldrich, VWR, Th. Geyer, abcr, Alfa Aesar, Grüssing, and Acros Organics, and used as received. Glass slides (size: 2.2×2.2 cm², thickness: 0.2 mm) were purchased from Carl Roth. Deionized (DI) water was purified using a purification system (18.2 M Ω ×cm, flex3, Purelab). (*Apparatus*) Equipment including an ultrasonic cleaner (PTIC-3-ES, Palsson), high-power expanded plasma cleaner (PDC-002, Harrick Plasma), spin-coater (table-top Labspin6, Süß MicroTec), precision hotplates (PZ 28-2 SR, Harry Gestigkeit GmbH), and vacuum evaporator (Classic 250, Pfeiffer) were used during the fabrication procedure.

6.3.2 Fabrication of Gold Nanoparticle Films via Layer-by-Layer Spin-Coating

Prior to the deposition of GNP films, the glass slides were cleaned with acetone in an ultrasonic cleaner for 15 min, followed by rinsing with DI water. The glass substrates were dried under a nitrogen flow and then treated with air-oxygen plasma for 2 min to enhance the surface hydrophilicity. For the GNP films prepared with the mixtures of 89% 12T/9DT, 95% 12T/9DT, 95% 8MOA/9DT, and pure 8MOA, pre-surface modification of the substrates was required in advance. The substrates were immersed in a 3-aminopropyldimethylethoxysilane solution (50 μ L in 5 mL toluene) and heated to 50 °C on a hotplate for 30 min. After pre-silanization, the substrates were rinsed with toluene and acetone to remove excess 3-aminopropyldimethylethoxysilane. The 9DT stock solution was prepared at a concentration of 7.4 mM in methanol. The monothiol (MT) stock solutions were prepared at a concentration of 14.8 mM in methanol to maintain the same thiol concentration as the 9DT stock solution. Three different volume ratios of MT and 9DT stock solutions were mixed to prepare solutions of MT/9DT mixtures. The mixing ratios were 50/50, 80/20, and 90/10 (MT/9DT v/v), corresponding to 67%, 89%, and 95% molar fractions of MTs.

During the deposition of GNP films onto glass substrates, the substrates without pre-silanization required two initial deposition steps of 100 μ L of 9DT stock solution to form an adhesion layer between the substrate and the GNPs. One deposition cycle of the GNP films began with 1×10 μ L of the GNP batch

followed by 2×10 μL of the MT/9DT or pure 9DT solution. This process was repeated several times to achieve the desired thickness of GNP films on the glass substrates. The GNP films used for the systematic investigation in Section 7.3 were prepared from the GNP batches, GNP2 and GNP3, with five to six LbL-SC deposition cycles. For those used in Section 7.4, the GNP films were prepared using the batch GNP4 with four LbL-SC deposition cycles. Subsequently, gold electrodes with a thickness of ~ 100 nm were deposited onto the resulting GNP films using a cannula (diameter: 0.4 mm) as a shadow mask in a vacuum evaporator.

6.4 Silicon-Supported Gold Nanoparticle Chemiresistor Arrays

GNP-based chemiresistor arrays were produced using the GNP batch, GNP5. The fabrication process includes two main parts: i) the preparation of interdigitated electrode (IDE) structures via the lithographic method, and ii) lithographic patterning of GNP films onto silicon wafers based on deep-UV (DUV) photolithography.

6.4.1 Materials and Apparatus

(Materials) 1,9-Nonanedithiol (9DT, 95%), 1-dodecanethiol (12T, 98%), 3-mercaptopropionic acid (3MPA, $\geq 99\%$), 8-mercaptooctanoic acid (8MOA, 95%), 6-mercapto-3-pyridinecarboxylic acid (6MNA, 90%), 4-nitrothiophenol (4NTP, 80%), 8-mercapto-1-octanol (8MOO, 98%), methanol ($\geq 99.8\%$), 2-propanol ($\geq 99.5\%$), toluene (99.5%), acetone (99.5%), 4-methylpentan-2-one (4M2P, 98.5%), poly(methyl methacrylate) (PMMA, average molecular weight: ~ 996 kDa), chlorobenzene (99.8%), and 3-aminopropyldimethylethoxysilane (95%), hydrogen peroxide (30%), triammonium citrate (99.5%), potassium iodide (KI, 99.5%), AZ351B (developer, buffered NaOH and typically used in 1:4 dilution), TechniStrip555 (remover for negative photoresist), and AZ ECI 3000 (negative photoresist) were purchased from Sigma Aldrich, Chemsolute, Merck, VWR, Th. Geyer, abcr, Alfa Aesar, Grüssing, Acros Organics, and MicroChemicals, and used as received. Iodine (I_2 , 100%) was self-filled. Deionized (DI) water was purified using a purification system (18.2 M Ω ×cm, flex3, Purelab). Thermally oxidized silicon wafers (orientation $\langle 100 \rangle$, 500 nm SiO₂) and unoxidized silicon wafers (orientation $\langle 100 \rangle$, thickness: 380 ± 20 m, 8-25 Ω cm) were purchased from Si-Mat. *(Apparatus)* Ultrasonic cleaner (PTIC-3-ES, Palsson), high-power expanded plasma cleaner (PDC-002, Harrick Plasma), spin-coater (table-top Labspin6, Süß MicroTec), precision hotplate (PZ 28-2 SR, Harry Gestigkeit GmbH), vacuum evaporation system (UNIVEX 350G, Oerlikon Leybold Vacuum), mask aligner equipped with a Hg lamp (Karl Süß MJB-3), and hot plate (Präzitherm) were utilized for the fabrication of the GNP chemiresistor arrays. A custom-built DUV lamp was also used to lithographically pattern GNP films. This light source has a main emission peak at 254 nm with an irradiance of 520 mW/cm².

6.4.2 Fabrication of Interdigitated Electrodes Using Lithography

A 10 nm thick titanium layer was deposited onto a thermally oxidized silicon wafer as an adhesion layer, followed by the deposition of a 40 nm thick gold layer using a vacuum evaporation system. Subsequently, a negative photoresist was applied to the Ti/Au coated substrate to cover the entire surface. The substrate was then spun at 3000 rpm for 60 s using a spin-coater to obtain a uniform layer. The substrate was then soft-baked on a hot plate at 90 °C for 90 s. In the next step, a photomask, previously fabricated by our group[23] and equipped with an array of eight IDEs on a quartz substrate, was used. The Ti/Au and photoresist coated substrate was exposed to UV light for 8 s through the photomask using a mask aligner. After exposure, the substrate was post-baked at 110 °C for 90 s, and then developed in a mixture of AZ351B developer and DI water in a volume ratio of 1:4 for 60 s. Subsequently, the substrate was rinsed with water and dried under a nitrogen flow.

To remove the unwanted areas of the gold layer on the silicon substrate, the substrate was immersed in a solution of KI, I₂, and water (a mass ratio of 4:1:200) under agitation for 2 to 3 minutes, and then rinsed with water. The remaining photoresist was dissolved in TechniStrip555 at room temperature for 30 minutes under gentle stirring conditions, and the substrate was then rinsed with water. Afterwards, the substrate was immersed in a 5 wt% aqueous solution of triammonium citrate for 9 min to remove the unwanted areas of Ti layer. This process resulted in the fabrication of a silicon substrate featuring an array of eight IDEs. Each IDE structure consisted of 10 fingers featuring 50 μm in width, 50 μm in finger spacing, and an overlap distance of 800 μm . These IDEs were built from a 10/40 nm thick layer of Ti/Au.

6.4.3 Lithographic Patterning of Gold Nanoparticle Films

Two quartz-supported photomasks were fabricated by our group. The photomask depicted in Figure 6.1a features a pair of rectangular openings corresponding to the positions on the sides of the IDE structures, while the one shown in Figure 6.1b has a pair of openings corresponding to the central positions of the IDEs.

A solution of PMMA dispersed in chlorobenzene (approximately 33 mg/mL) was deposited on the silicon wafer containing the priorly fabricated IDEs. The substrate was then placed on a spin-coater and rotated at 4000 rpm for 60 s, followed by soft-baking on a heating plate at 60 °C for 10 min. Subsequently, a custom-built DUV lamp was utilized to irradiate the PMMA-coated substrate through the photomasks (see Figure 6.1a and b) for 130 minutes. The PMMA layer was then developed by immersing the PMMA coated-substrate in a mixture of 4M2P and 2-propanol (1:3, V:V) for 70 s under gentle agitation, followed by rinsing with 2-propanol. This process resulted in the production of patterned PMMA with two rectangular openings on the substrate, as shown in Figure 6.1c.

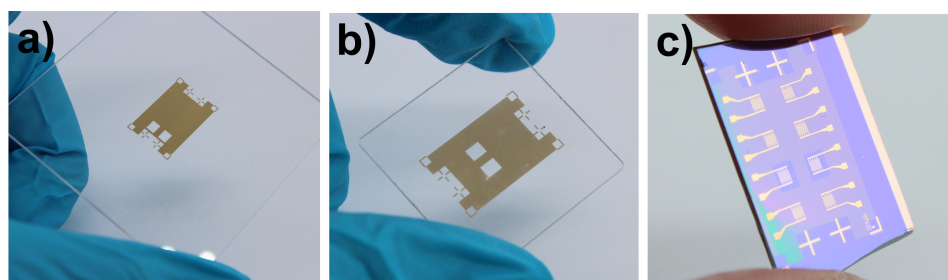


Figure 6.1: Photograph of the quartz-supported photomasks with a pair of rectangular openings a) positioned on the sides and b) positioned in the center. c) A PMMA-coated silicon substrate (featuring an array of 8 IDEs) with a pair of openings at the central position, achieved through lithography using the photomask shown in b.

Afterwards, the PMMA-coated silicon substrate underwent a pre-silanization step, and the selected GNP films were deposited onto it via the LbL-SC procedure as described in Section 6.3.2. Next, a lift-off step was conducted by dissolving the PMMA layer in acetone, resulting in a patterned GNP film on top of a pair of IDEs. The lithographic process was repeated four times to deposit four kinds of GNP films on top of all 8 IDEs.

6.5 Characterizations of Gold Nanoparticle Films

The fabricated GNP films were thoroughly characterized to evaluate their optical and electrical properties, film thickness, surface morphology, nanostructure of their corresponding GNP assemblies, and the average interparticle distance of the GNPs within the films. This section provides a detailed discussion of these analyses.

6.5.1 UV/vis Spectroscopy

To analyze the optical properties of the glass-supported GNP films, ultraviolet/visible (UV/vis) spectroscopy was conducted using a Cary 50 spectrophotometer (Varian) over a wavelength range of 300 to 900 nm. The glass-supported GNP films were positioned in a custom-built sample holder, oriented such that the film's surface was perpendicular to the incident beam. The spectra were recorded at four distinct spots on the GNP films to ensure representative measurements.

6.5.2 Atomic Force Microscopy (AFM)

The thickness of a GNP film was measured by atomic force microscopy (AFM) using a Digital Instruments Multimode AFM (JPK Nanowizard) equipped with a NanoScope IV controller. The glass-supported GNP film, $\sim 1.1 \times 1.1$ cm² in size, was affixed to a magnetic sample plate using double-sided tape. To prepare the sample, the GNP film was gently scraped multiple times with a cannula and any residue was subsequently removed under a nitrogen flow. AFM imaging was performed using an ACTA probe in tapping mode to capture a 20×5 μm^2 image of the topography of the scratch edge on the film. The recorded AFM data were subsequently analyzed using the software *Gwyddion* (version 2.61) to determine the average film thickness.

6.5.3 Scanning Electron Microscopy (SEM)

To analyze the morphology and nanostructure of the GNP assemblies, scanning electron microscopy (SEM) measurements were conducted. The GNP films were deposited onto unoxidized silicon substrates via the LbL-SC procedure as described in Section 6.3.2, approximately two days before the measurements. The SEM measurements were performed by Robert Schön at the Institute of Physical Chemistry, University of Hamburg, using a field emission scanning electron microscope (LEO 1550 Gemini, Carl Zeiss). The operating voltage in the range between 10 to 20 kV was applied during the imaging process.

6.5.4 Grazing Incidence Small Angle X-Ray Scattering (GISAXS)

The grazing incidence small angle X-ray scattering (GISAXS) measurements were performed by Dr. Andreas Meyer at the Institute of Physical Chemistry, University of Hamburg, under ambient conditions.

An in-house SAXS apparatus was used for GISAXS measurements, with the apparatus setup details as described in Section 6.1.5. For GISAXS measurements, selected GNP films were deposited onto unoxidized silicon substrates via the LbL-SC procedure, and mounted on a motorized stage with the samples positioned at an incidence angle of 0.3° . The GISAXS samples were positioned 1.2 m away from a Rayonix SX165 CCD detector, and each measurement accumulated data over a period of 30 minutes. The analysis and fitting of the GISAXS data were performed by Dr. Andreas Meyer using the software *Scatter*.^[162, 163]

6.5.5 Charge Transport Measurements

For the charge transport measurements, a parameter analyzer (4156C, Agilent) was used to characterize the charge transport properties of the fabricated GNP films. The fully printed GNP films deposited on flexible substrates with IDE structures, as described in Section 6.2, consisted of two electrode pads, each with a size of approximately $2.5 \times 5 \text{ mm}^2$. This configuration gave challenges for achieving optimal contact with the conductive pins in the test cell. To facilitate electrical measurements on these fully printed sensors, the electrode pad area was manually enlarged using conductive carbon paste to improve contact with the conductive pins. The glass-supported GNP films consisted of a $\sim 100 \text{ nm}$ thick gold electrode, with a sensing channel being approximately $400 \text{ }\mu\text{m}$ long (l) and 1.1 cm wide (w). Both the flexible substrate-supported GNP films and glass-supported GNP films were placed in a custom-built aluminum test-cell ($\sim 20 \text{ mL}$) equipped with conductive pins. The GNP-based sensor arrays fabricated on silicon wafers with the IDE structures, as detailed in Section 6.4.2, were placed on a custom-built probe station and electrically contacted using gold-coated microprobes connected to the parameter analyzer. Current-voltage (I-V) curves were measured over a range between -5 to $+5 \text{ V}$ at room temperature. The conductance (G) of the GNP films was determined from the slopes of the I-V curves using a linear function. The conductivity (σ) of glass-supported GNP films was calculated using Equation 6.1, taking into account the electrode geometry and film thickness (t).

$$\sigma = G \cdot \frac{l}{w \cdot t} \quad (6.1)$$

6.6 Vapor-Dosing Experiments

To investigate the sensing characteristics of GNP films, the fabricated GNP films, the GNP-based chemiresistors, and the GNP-film coated QCMs were exposed to different analyte vapors at defined concentrations ranging from 5 to 10000 ppm. Detailed experimental setups for each device, including chemiresistor, QCM, and in situ vapor/GISAXS measurements, are described in the following sections.

6.6.1 Materials

Ethanol (99.8%), 1-propanol (99.5%), 2-propanol ($\geq 99.5\%$), n-butanol (99.8%), isobutanol (99%), n-hexane ($\geq 97\%$), n-heptane (99%), n-octane (99%), isooctane ($\geq 99\%$), cyclopentane (98%), cyclohexane ($\geq 99.5\%$), methylcyclohexane ($\geq 99\%$), cyclooctane ($\geq 99\%$), toluene (99.5%), acetone (99.5%), 4-methylpentan-2-one (4M2P, 98.5%), 2-pentanone (99.8%), ethyl acetate (99.8%), and n-butylamine (99.5%) were purchased from Sigma Aldrich, Merck, VWR, Th. Geyer, Alfa Aesar, Fluka, Grüssing, Honeywell, and Acros Organics. All chemicals were used as received without further purification. DI water was purified using a purification system (18.2 M Ω ×cm, flex3, Purelab). Nitrogen 5.0 (Linde) was used as the carrier gas and zero gas (ZG) in the vapor dosing measurements.

6.6.2 Vapor Dosing System Setup

Different analyte vapors at various concentrations were generated using a gas calibration system (CGM2000, MCZ Umwelttechnik). The measurements were all conducted under ambient conditions. Figure 6.2 presents schematically the flow plan of the gas calibration system. Nitrogen served as both the carrier gas and zero gas (ZG). During measurements, each exposure cycle comprised 2 minutes of analyte vapor followed by a 4-minute purging phase with ZG. The system received ZG from an in-house gas supply, which then split into two lines regulated by mass flow controllers (MFCs). One line provided pure ZG, while the other line generated the analyte gas (AG) by passing a gas flow through a vessel containing the target analyte in liquid form (heated up to 30 °C to vaporize the analyte solvent). Nitrogen, serving as the carrier gas, transported the generated analyte vapors into a condenser set to 20 °C. The concentration of the saturated analyte vapors was quantified using the Antoine equation (cf. Equation 6.2). After exiting the condenser, the saturated analyte vapors were mixed with ZG in a mixing chamber. ZG was used to dilute the saturated analyte vapors to achieve the desired vapor concentration. The test cell was positioned between a valve and a pump. The valve controlled the flow of either ZG or AG into the test cell. The pump, consisting of an MFC, maintained a constant gas flow of 500 mL/min into the test cell.

$$\log_{10} P = A - \frac{B}{T + C} \quad (6.2)$$

Where, T is the temperature in degrees Celsius, and A , B , and C are substance-specific constants.

While the basic setup was adequate for most measurements, the second dilution unit shown in the brown

dashed box in Figure 6.2 was necessary to generate relatively low vapor concentrations or handle analytes with high vapor pressures. The second dilution unit was positioned after the mixing chamber (in the basic setup, grey dashed box), which further diluted the AG generated from the vapor saturation system to achieve the desired vapor concentration.

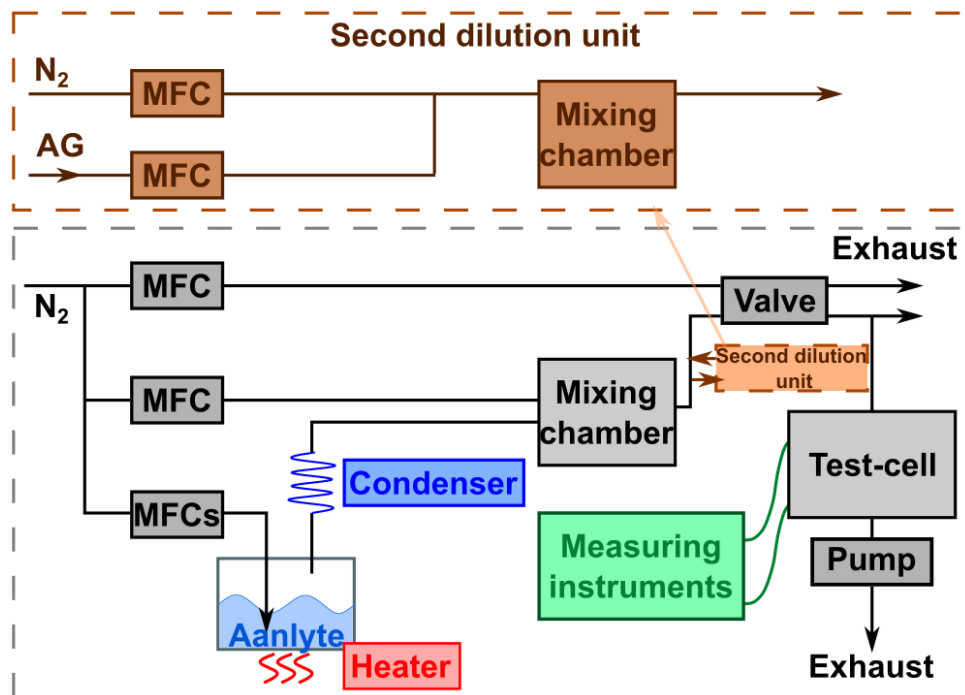


Figure 6.2: Schematic illustration of the setup of the gas calibration system for the vapor dosing measurements. The grey dashed box represents the basic setup of the vapor saturation system, containing three MFCs controlling different flow-rate ranges to direct the carrier gas into the vessel containing liquid analytes. The second dilution unit, enclosed within the brown dashed line box, is only necessary for generating extremely low vapor concentrations or when dealing with high-vapor-pressure analytes.

6.6.3 Chemiresistor Measurements

Chemiresistor measurements were conducted using two types of test cells, as illustrated in Figure 6.3. Both flexible substrate-supported and glass-supported GNP chemiresistors were placed in a polytetrafluoroethylene (PTFE) test cell (Figure 6.3a), with a capacity of approximately 20 mL. Two pairs of conductive pins mounted on the test cell lid contacted the electrode pads of the GNP chemiresistors when the test cell was sealed. These GNP chemiresistors were connected to a parameter analyzer (4156C, Agilent), which supplied a constant bias of 5 V to the chemiresistors and recorded current changes throughout the measurement to determine the resistive responses. The device recorded data points at one-second intervals. The chemiresistive signal was quantified as the relative change in resistance $\Delta R/R_0$, where ΔR is $(R_{\max} - R_0)$. Here, R_{\max} represents the maximum response, calculated as the average resistance during exposure to analyte gas (AG) between the 110th and 115th seconds, while R_0 is the baseline resistance during exposure to zero gas (ZG).

In a separate setup (cf. Figure 6.3b), GNP chemiresistor arrays were attached to a printed circuit board (PCB) using wire bonding. Each sensor in the array was connected to the PCB, which was then mounted

with stacking header pins. This assembly was put into an aluminum test cell (approximately 16 mL). Each sensor was linked to a commercial surface mount device (SMD) shunt resistor in series via a ribbon cable. The resistances of these shunt resistors were ~ 1 to 10% of the baseline resistance of the corresponding sensor. A sourcemeter (2601A, Keithley) provided a constant bias of 5 V to all sensor/shunt pairs. The voltage drop across each shunt resistor was measured using a multimeter (2002, Keithley). Multi-signal readouts were processed using a custom-designed multiplexer, based on reed relays, with a measurement frequency of ~ 0.5 Hz. The resistance of each sensor in the array was determined using Equation 6.3. The resistive responses of the sensor array were extracted using the same approach used to define the relative responses of the the glass-supported GNP sensors.

$$R_{\text{Sensor}} = \frac{V_{\text{Source}} - V_{\text{Shunt}}}{V_{\text{Shunt}}/R_{\text{Shunt}}} \quad (6.3)$$

Here, R_{Sensor} denotes the resistance of the sensor, V_{Source} the applied bias (a constant 5 V) by the sourcemeter, V_{Shunt} the measured voltage at the shunt resistor by the multimeter, and R_{Shunt} is the resistance of the shunt resistor.

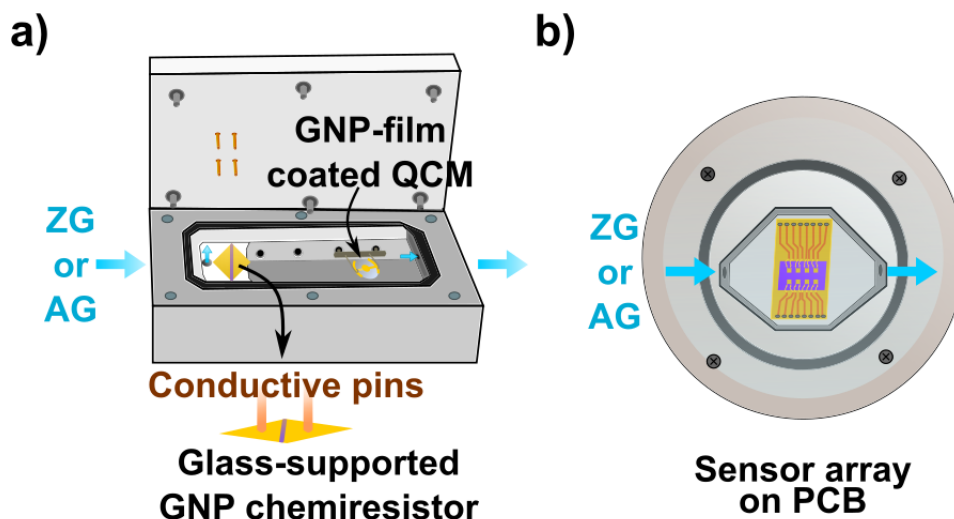


Figure 6.3: a) Schematic of the PTFE test cell with a capacity of ~ 20 mL. Both flexible substrate-supported and glass-supported GNP chemiresistors were placed on the left plane, with the conductive pins (on the test cell lid) making contact with each side of the electrode pads (as illustrated below the test cell). On the right side, the test cell was equipped with two pairs of metal-encased apertures. For quartz crystal microbalance (QCM) measurements, the QCM was first mounted onto a wire holder and then plugged into two of the apertures. b) Schematic of the aluminum test cell with a capacity of ~ 16 mL. The PCB-supported chemiresistor array was plugged into the mating socket. This test cell was sealed with an optical glass with an O-ring to prevent leaking.

6.6.4 Quartz Crystal Microbalance (QCM) Measurements

To determine the uptake mass of the analytes in GNP films, QCM measurements were conducted. The GNP films with various organic compositions were deposited onto QCMs (resonant frequency: 10.00 MHz, diameter: 14 mm, Ti/Au electrodes, QuartzPro) via the LbL-SC procedure as described in Section 6.3.2. Each electrode on the QCM was attached to a wire holder, with conductive pins (as shown in Figure 5.5b). The QCM was plugged into the hole inside the test cell (~ 20 mL) as shown in Figure 6.3a. Gravimetric

measurements were performed using a network analyzer (E5100A, Agilent).

Initially, the blank QCM was measured to obtain its reference resonance frequency under nitrogen conditions. Subsequently, the GNP film was deposited onto one side of the QCM, while the other side was gently cleaned with acetone to remove any residues. The GNP-film coated QCM was then placed in the test cell under nitrogen conditions, and its resonance frequency was measured. The mass of the GNP film can be determined from the change in resonance frequency after the deposition of the GNP film. During the measurements, the resonance frequency of the QCM was recorded using the network analyzer. A Python script, developed by Dr. Hendrik Schlicke (Dresden University of Technology), controlled the recorded parameters (anti-resonance frequency, resonance frequency, anti-resonance impedance, and resonance impedance) using the "OUTPRES0?" command.[164]

6.6.5 In situ GISAXS Measurements

To evaluate the differences in the swelling behavior of the selected GNP films, in situ saturated analyte vapor/GISAXS measurements were conducted. The different GNP films were deposited onto unoxidized silicon substrates via the LbL-SC procedure as detailed in Section 6.3.2. The measurement setup was consistent with the general GISAXS measurements as described in Section 6.5.4.

After positioning the wafer-supported GNP films, two droplets of toluene were dispensed near the samples without making direct contact. The measurement environment was then sealed with a lid to ensure saturation with toluene vapor. Scattering patterns were recorded after a 10-minute equilibration period in the saturated vapor, with a 30-minute accumulation period for each measurement.

Chapter 7

Results and Discussion

7.1 Colloidal Gold Nanoparticles

The investigations detailed in this thesis focused on gold nanoparticle (GNP)-based films prepared with mixtures of monothiol (MT) ligands and dithiol (DT) cross-linkers following various fabrication routes. In order to obtain monodisperse colloidal GNPs, a synthesis method reported by Peng et al.[160] was employed with minor modifications. Five colloidal batches of 1-dodecylamine (12A) stabilized GNPs were synthesized and used for composite film fabrication. The average sizes of GNPs determined by transmission electron microscopy (TEM) ranged from 6.0 to 7.5 nm (cf. Figure 7.1). The synthesized GNPs exhibited the localized surface plasmon resonance (LSPR) at approximately 520 nm, consistent with previous findings[23, 24]. The UV/vis absorbance spectra of diluted GNP stock solutions (dilution factors ranging from 1/300 to 1/600) are shown in Figure 7.1. These UV/vis data were also utilized to calculate the particle concentration of the GNP batches (c_{GNP}) using Haiss' method, as expressed by Equation 7.1.[161]

$$c_{\text{GNP}} = \frac{A_{450} \cdot 10^{17}}{d^2[-0.295 + 1.36 \exp -(\frac{d-96.8}{78.2})^2]} \cdot \frac{1}{N_A \cdot f_d} \quad (7.1)$$

Here, A_{450} is the absorbance measured at a wavelength of 450 nm, d the average diameter of GNPs (in nm) determined by TEM, N_A the Avogadro constant, and f_d is the dilution factor of the GNP colloids for UV/vis measurements. The calculated particle concentrations for GNP1 to GNP5 were approximately 11.3, 4.1, 4.5, 4.2, and 11.8 μM , respectively.

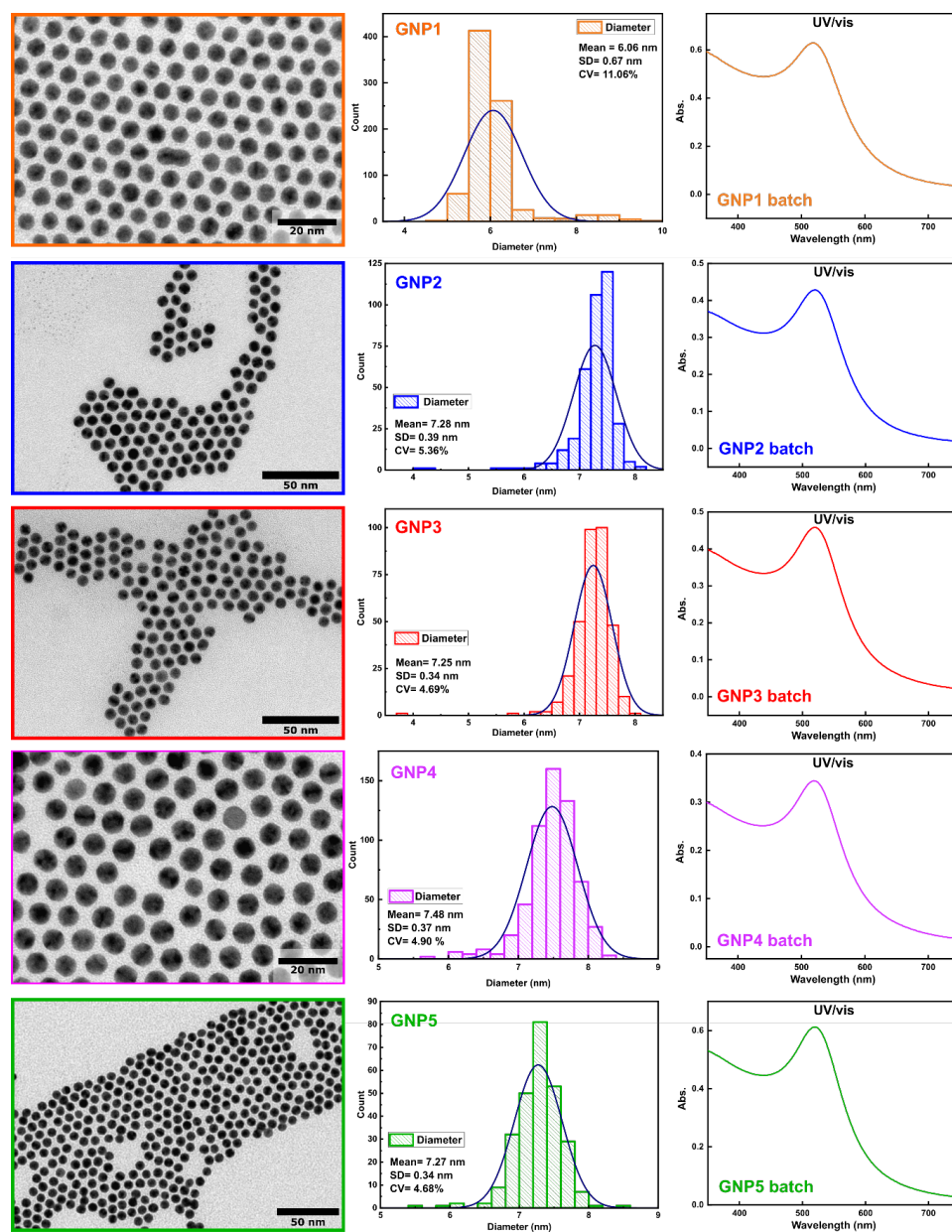


Figure 7.1: TEM images of five GNP batches (scale bar: 20, 50, 50, 20, and 50 nm from top to bottom), the corresponding histograms of the GNP diameters fitted with normal distribution curves (with mean core diameter value, standard deviations (SDs), and coefficient of variations (CVs)), and the respective UV/vis absorbance spectra (optical path length = 10 mm). Adapted and reproduced with permission from the Supporting Information of Ref. [2] ©2024 The Authors. Advanced Materials Interfaces published by Wiley-VCH GmbH.

7.2 Fully Printed Gold Nanoparticle-Based Chemiresistors on Flexible Substrates

Wearable electronics have gained significant attention due to the growing demands for real-time health monitoring. These devices require user-friendly systems with a simplified signal read-out, light weight, small volume, and biocompatibility. GNPs possess properties that meet these requirements—they are small in size, stable across varying conditions, nontoxic, facile to synthesize, and their surfaces can easily be modified. Tailoring the surface of GNPs with functionalized molecules enables selective interactions with target molecules or compounds. This surface modification can occur during GNP synthesis or through post-synthesis ligand exchange processes. Due to their exceptional properties, GNPs are ideal sensing materials for wearable electronic devices. Over the past decade, considerable efforts have been devoted to developing GNP-based wearable sensors for healthcare applications. These sensors can convert physical motions (such as compression, bending, tension, shear stress, and strain)[90, 120, 121, 165], as well as the presence of biomarkers[166], volatile organic compounds (VOCs)[24] and humidity[167], into electrical signals. While GNPs have demonstrated the potential for wearable sensor applications, challenges such as complicated fabrication procedures and the generation of chemical wastes remain.

This section focuses on the development of GNP-based chemiresistors on flexible substrates using a cost-effective fabrication approach to meet the requirements for wearable sensors. Printing technology provides an efficient tool for fabricating wearable electronics. Polyimide (PI) was selected as substrate for the preparation of flexible wearable GNP-based chemiresistors due to its exceptional properties. PI can withstand high temperatures up to 400 °C and is resistant to a wide range of chemicals, making it highly convenient in the manufacturing process. Additionally, it is lightweight, highly flexible, and mechanically strong, which are essential qualities for ensuring the durability and comfort of wearable electronics. To systematically adjust the selectivity, a combination of cross-linker and functionalized ligand molecules were employed. Notably, our research group recently reported the successful fabrication of fully printed GNP-based chemiresistors for gas/vapor sensing. This involved incorporating hydroxyl and carboxylic acid functionalized MT ligands in conjunction with a cross-linker.[24] The present work follows a similar fabrication route, with an emphasis on diversifying the functional groups of the MT ligand and exploring MTs with various structures. This approach aims to broaden the chemical selectivity of the chemiresistors, enabling a more comprehensive response to different vapors when employing arrays of such selectivity-tuned sensors.

This study represents an international collaborative project with Prof. Dr. Ying-Chih Liao's group at National Taiwan University in Taiwan. The fabrication of all GNP-based chemiresistors was carried out by the author (C.-Y.L.) in Prof. Dr. Liao's lab, with Prof. Liao's group providing assistance and access to laboratory equipment. On the other hand, all chemiresistor measurements were conducted in our lab at the University of Hamburg.

7.2.1 Fabrication of Fully Printed Gold Nanoparticle Chemiresistors

GNP-based chemiresistors were fabricated using printing technologies, comprising three main steps. Firstly, electrode structures were fabricated by printing interdigitated electrode (IDE) structures onto PI foil using a tabletop dispensing machine with a commercial graphene-doped conductive carbon ink, cf. Figure 7.2a. The IDE structures consisted of 5 finger pairs with a finger width of 195 μm , 5 mm overlapping, and approximately 160 μm finger spacing, as shown in Figure 7.2b. This design flexibility was facilitated by controlling the speed, position, and motion of the robot. Secondly, GNP and organic inks were prepared to be used in the subsequent printing processes. Finally, inkjet printing was employed to deposit the prepared inks onto the IDE structures on PI substrates. The resulting fully printed GNP-based chemiresistor is shown in Figure 7.2c. Notably, this fabrication route obviates the need for conventional lithographic processes. Furthermore, compared to conventional lithographic methods, this printing technology offers efficient production of electrode structures, providing flexibility in design, high productivity, and a significant reduction in chemical waste.

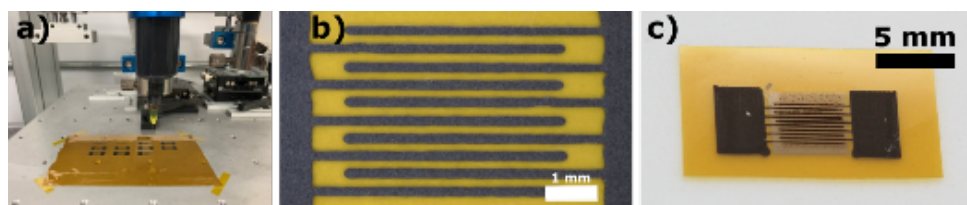


Figure 7.2: a) Photograph of the deposition of graphene ink onto a PI substrate by a tabletop dispensing robot (fabrication of IDEs on PI substrate). b) Optical microscopic image of the printed IDE structure on a PI substrate. (scale bar: 1 mm) c) Photograph of the fully printed flexible GNP chemiresistor. (scale bar: 5 mm)

The fabrication procedure started with the preparation of the IDE structures, where printing parameters such as dispensing speed and nozzle positioning were carefully controlled to ensure the printing quality. The graphene-based ink offers good electrical conductivity, mechanical flexibility and high stability, essential for wearable electronic applications.

Next, the GNP and organic inks were formulated. The successful fabrication of GNP-based chemiresistors via printing technologies, employing a mixed ligand/linker system, was demonstrated in an earlier publication from our research group.[24] This approach effectively combined various functionalized MT ligands with the 1,9-nonanedithiol (9DT) linker within the organic matrix, allowing for chemical selectivity tuning. While this method yielded diverse compositions of GNP films, resulting in a variety of response patterns to different chemical vapors, achieving higher sensitivities and more pronounced distinct response characteristics beyond those of GNP films prepared with the pure 9DT linker remained a priority. In this study, a broader variety of MT ligands featuring different lengths and functional groups were used to refine and expand the capabilities of the sensing platform, aiming to gain a more comprehensive understanding of printed GNP sensors comprising mixtures of ligand/linker and to improve their sensing characteristics.

In this section, the GNP colloid, batch GNP1, with a particle size of ~ 6 nm and a particle concentration of ~ 11.3 μM was used, diluted by a factor of four using n-octane. This choice was made due to n-octane's higher boiling point (n-heptane: ~ 98.4 $^{\circ}\text{C}$ and n-octane: ~ 125.6 $^{\circ}\text{C}$ at ambient pressure), which contributes to the formation of more stable droplets during the inkjet printing process. To ensure

comparability with previously reported 9DT cross-linked GNP films, 9DT was selected as the standard linker molecule. Moreover, 9DT being commercially available and widely used for GNP sensors preparation[12, 15, 24], was considered especially suitable for this purpose.

To investigate the influence of the structure and size of MT ligands on the physical properties and sensing characteristics of the resulting GNP films, various MTs were employed. These included MTs longer than the 9DT molecule, such as 11-mercapto-1-undecanol (11MUO) and 11-mercapto-1-undecanoic acid (11MUA), as well as MTs with aromatic ring structures, such as 4-mercaptophenol (4MPO), 4-mercaptobenzoic acid (4MBA), and 2-aminothiophenol (2ATP). 1-Thioglycerol (TG) was included for result comparison with previous studies.[24] The selected MT ligands were functionalized with hydroxyl, carboxylic acid (Lewis acid), and amino (Lewis base) groups, respectively (listed in Table 7.1). Both 9DT (in 2-propanol) and MT (in 2-propanol) stock solutions were prepared at a concentration of ~ 7.4 mM, consistent with the standard concentration used for the layer-by-layer spin-coating (LbL-SC) procedure previously reported by our research group[85]. The 9DT stock solution was used directly as the organic ink, while the mixtures of MT/9DT inks were prepared by mixing the 9DT and MT stock solutions in a 3:1 volume ratio. In a previous study by our research group, two different ratios of 9DT linker and functionalized MT ligand were investigated, 1:1 and 3:1, respectively.[24] However, no significant differences between the resulting chemiresistors prepared with these two different ratios of 9DT and MT ligand were observed. The high fraction of 9DT in the film is expected to prevent the aging phenomenon and preserve the stability of the sensor's performance. Therefore, in this preliminary study, we selected a 25% molar fraction of MT ligand in the organic ink.

Table 7.1: Dithiol cross-linker and monothiol ligands used in this study, their structural formulas, and sensor notations.

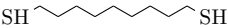
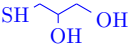

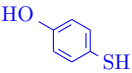
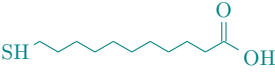
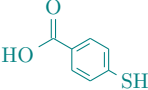
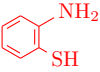
Thiols	Structural Formula	Sensor
1,9-Nonanedithiol (9DT)		9DT
1-Thioglycerol (TG)		TG-9DT
11-Mercapto-1-undecanol (11MUO)		11MUO-9DT
4-Mercaptophenol (4MPO)		4MPO-9DT
11-Mercapto-1-undecanoic acid (11MUA)		11MUA-9DT
4-Mercaptobenzoic acid (4MBA)		4MBA-9DT
2-Aminothiophenol (2ATP)		2ATP-9DT

Figure 7.3 provides a schematic overview of the precise inkjet printing device and outlines the printing procedures employed in this study. Throughout the printing process, the platform was heated to 40 °C to facilitate solvent evaporation, which is important for achieving uniform film formation. The deposition

of GNP films followed a LbL-inkjet printing method, as detailed in the Experimental Section. Before depositing the GNP film, a 9DT coating is deposited on the PI substrate to form an adhesive layer between the PI substrate and the GNPs. As shown in Figure 7.3, the GNP films were fabricated using the LbL-inkjet printing with three deposition cycles. Each deposition cycle consisted of one coating of GNP ink and one coating of organic ink, and each ink coating composed of four printing layers. The first printing layer started with a 0-degree printing direction, followed by subsequent printing layers with 90-degree printing shifts. This strategy ensured a uniform coverage on substrates and minimized the formation of void defects within the GNP films. For the first and second layers, the droplet spacing was set at 0.05 mm, and the platform moved at a velocity of 35 mm/s, synchronized with a droplet dropping frequency of 700 Hz. To avoid uncovered void defects, the platform velocity and droplet spacing were slightly reduced for the third and fourth layers, with the platform velocity set to 28 mm/s and 21 mm/s, respectively. Previous studies[24, 167] have noted a decrease in the resistance of GNP films with an increasing number of deposited coatings. In accordance, after three LbL-inkjet deposition cycles, the resistance of the resulting GNP film fell within the low megaohm range. Consequently, in this study, all printed GNP films consisted of three GNP ink coatings, and four organic ink coatings in a sandwich structure.

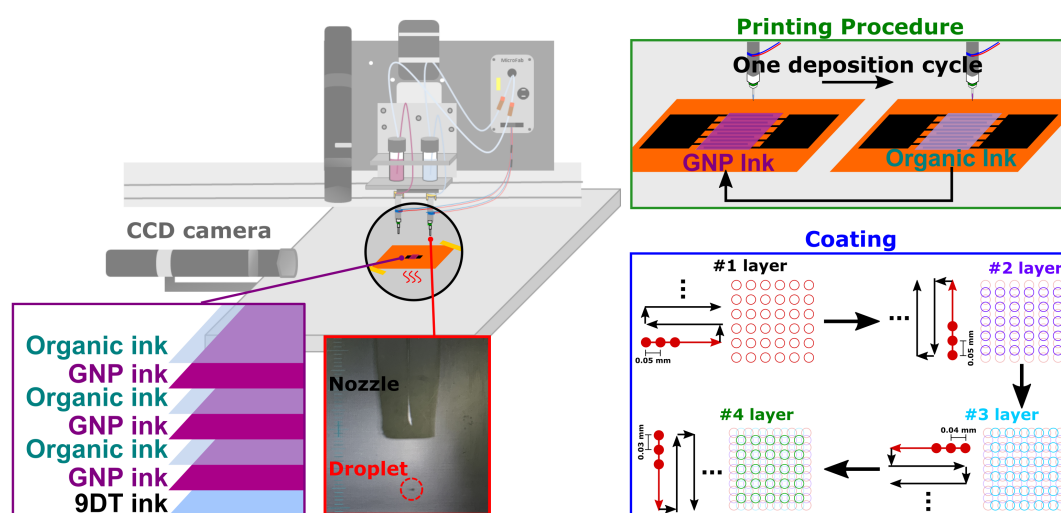


Figure 7.3: Schematic of the deposition of GNP films via the inkjet printing procedure. The droplet emerging from the nozzle was continuously monitored by an integrated CCD camera positioned on the left side of the platform. Organic and GNP inks were each connected to separate printheads. During the printing process, GNP and organic inks were alternatively deposited onto the PI substrate in one deposition cycle. Each printed coating comprised 4 printing layers. For each layer, the deposition began at a different position with a distinct printing direction. The deposition cycle was repeated three times. The film deposition process began with a coating of 9DT ink and ended with a coating of organic ink, with coatings of GNP ink sandwiched between the organic ink coatings.

This mixed ligand/linker strategy aims to systematically tune the selectivity and sensitivity of the chemiresistors by adjusting the functional groups and chain lengths of the added MT ligands, thereby tuning the interaction between GNP films and different volatile compounds. This approach is expected to improve sensing performance as well as offer a deeper understanding of the role of the MT ligand structure in the electronic properties of GNP-based chemiresistors.

7.2.2 Electrical Properties

The electrical properties of the fabricated GNP-based chemiresistors were characterized to evaluate their performance as sensing elements. Current-voltage (I-V) characteristics of the chemiresistors were measured using a parameter analyzer connected to the electrodes, with a voltage sweep range from -5 to +5 V. The results are depicted in Figure 7.4. The I-V curves of all GNP-based chemiresistors exhibited linearity, indicating Ohmic behavior. This observation suggests that the printed GNP films establish an efficient percolation pathway for charge transport.

The fabricated pure 9DT cross-linked GNP chemiresistor exhibited a baseline resistance of $0.72\text{ M}\Omega$, consistent with the literature value[24]. However, except for the GNP films prepared with the TG/9DT mixture, all chemiresistors prepared with MT/9DT mixtures showed significantly higher resistance than the one prepared with the pure 9DT linker, corroborating previous findings[24]. This increase in resistance is hypothesized to be due to a reduction in the degree of cross-linking within the organic matrix, resulting in lower charge transport efficiency. MT ligands with longer molecular lengths than the 9DT molecule, such as 11MUO and 11MUA, have functional end groups that may form hydrogen bonds, which can potentially hinder the bonding between the 9DT's sulfur functional groups and the GNP surface. Additionally, MT ligands with a larger size of the organic residue with the functional group, such as aromatic rings (4MPO, 4MBA, and 2ATP), may also reduce the degree of cross-linking via 9DT linker due to steric hindrance. In contrast, the TG ligand, which is shorter than the 9DT molecule, does not suppress cross-linking efficiently. Consequently, the resistance of the TG-9DT chemiresistor was only slightly lower than that of the pure 9DT sensor. These resistance measurements not only reflect the charge transport properties of the fabricated films but also provide evidence that ligand/linker mixtures alter the composition of the organic matrix within the film, thereby influencing its characteristics.

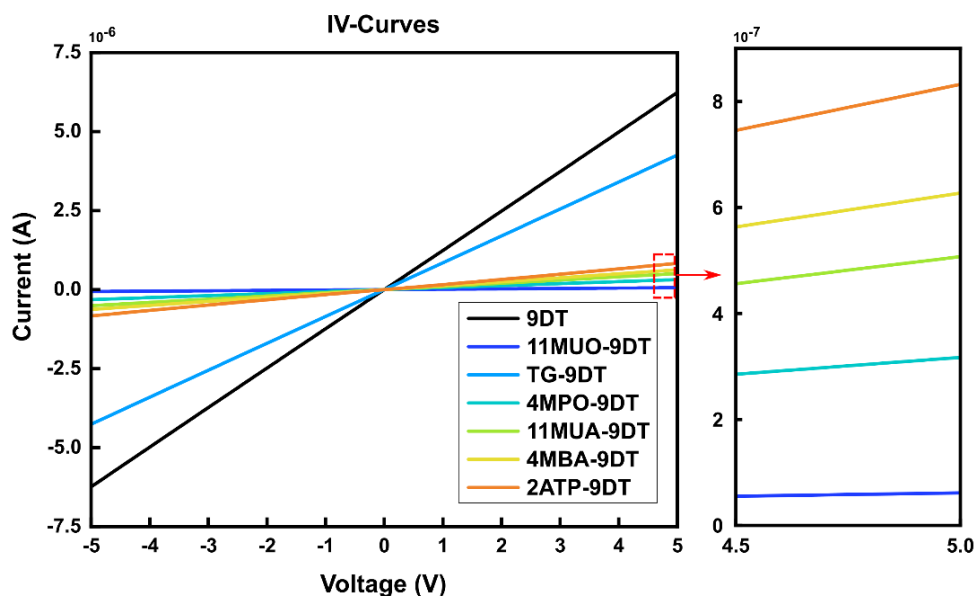


Figure 7.4: I-V curves of the printed GNP-based chemiresistors, which were all measured under nitrogen atmosphere at ambient temperature. These chemiresistors were fabricated using mixtures of 1,9-nonanedithiol (9DT) linker combined with various functionalized MT ligands, as indicated by the legend. The right plot is a zoomed-in view of the left plot, as marked by the red box.

7.2.3 Reproducibility, Repeatability, and Stability

Ensuring reproducibility is critical for sensor applications as it guarantees reliability, quality, and comparability from sensor to sensor. The coffee ring effect, a common issue during the printing process is caused by unequal evaporation rates at the edges of and inside the droplets. This effect can lead to a non-uniform distribution of GNPs and ligand/linker components, potentially resulting in inconsistent sensor performance.[168, 169] In addition, minor variations in droplet size during the inkjet printing process can further lead to deviations in sensor’s characteristics and sensing performance.

In order to examine sensor-to-sensor variations in this study, in addition to the 9DT sensor (as Sensor 1) mentioned in the previous section, two other sensors (Sensor 2 and Sensor 3) were fabricated with the pure 9DT linker molecules at different dates to account for variations in printing conditions (e.g., humidity, temperature) and printing device. The electrical properties of the resulting GNP chemiresistors were characterized by I-V measurements. The resistance values extracted as the inverse slope of the I-V curves were within the same order of magnitude: 0.72, 0.39, and 0.80 M Ω for Sensor 1, Sensor 2, and Sensor 3, respectively. The deviation in the baseline resistance of Sensor 2 compared to the others may be attributed to uncontrolled variations of the printing conditions, resulting in smaller droplets ejected from the inkjet printer and thereby leading to a thinner GNP film.

The conductivity of GNP films, as described by Equation 5.3, exhibits an exponential dependence on both the interparticle distances of GNPs (δ) and the activation energy of the GNP film (E_a). Consequently, even slight perturbations in these parameters can result in easily detectable electrical signals. When analyte molecules are sorbed within the film, the organic matrix swells, leading to an increase in the tunneling distance. As a result, an increase in resistance with a positive signal can be observed. Simultaneously, the analyte-adsorbed organic matrix provides a higher permittivity environment, typically leading to a negative signal due to a reduction in the activation energy. However, in most cases, the swelling effect of a 3D GNP film outbalances the permittivity effect, resulting in a positive signal. To quantify these electrical signals (response amplitudes), the relative change in resistance ($\Delta R/R_0$) was utilized, where ΔR represents the difference between the maximum change in response (the average of resistance when exposed to an analyte vapor at 110-115 s) and the baseline resistance R_0 (the resistance when exposed to zero gas).

Chemiresistors measurements were conducted to further examine variations in sensing performance from sensor to sensor. Three GNP sensors (Sensor 1 to 3) were exposed to nonpolar and polar vapors (toluene and ethanol (EtOH)) at concentrations ranging from 50 to 1000 ppm. Figure 7.5a and b show the baseline-corrected time traces of transient responses of Sensor 1 to 3 under exposures to the analytes vapors. The response amplitudes showed very good reproducibility across all three sensors for both vapors throughout the entire concentration range of the analyte. Moreover, the kinetics of their chemiresistive responses were also consistent. Despite slight deviations in film resistance, all three chemiresistors responded similarly to the vapors. These data clearly confirm that the printing parameters were well-suitable for the fabrication of GNP sensors with a high degree of sensor-to-sensor reproducibility. Compared to the fully printed 9DT chemiresistors prepared by Ketelsen et al.[24], the 9DT chemiresistors in this study exhibited smaller overall response amplitudes. However, the relative response amplitudes between toluene and EtOH remained similar. This deviation in sensitivity may be attributed to differences in film

thickness and the use of different GNP batches.

Further, repeatability and stability of each individual sensor are also essential attributes of sensors that complement reproducibility to ensure consistent, accurate, and reliable measurements in a variety of applications. Figure 7.5c shows the result of repeatability tests. Sensor 1 was exposed to toluene vapor at 500 ppm for 2 min, followed by 4 min of zero gas (pure nitrogen). The exposure was repeated 9 times. All response amplitudes were identical with the same shape of transient response. Moreover, the resistance recovered to its baseline resistance (resistance in a nitrogen atmosphere) after each exposure to the test gas, indicating reversible interactions between the GNP film and the analyte. Figure 7.5d illustrates the results of an aging test. The transient responses were recorded again after storing the sensor for one week in a nitrogen cabinet at ambient temperature. Not only the response amplitudes remained the same, but also the shape of transient response. Such a high level of repeatability and good stability confirms that the fabricated sensors provide accurate measurements consistently over time and under varying conditions.

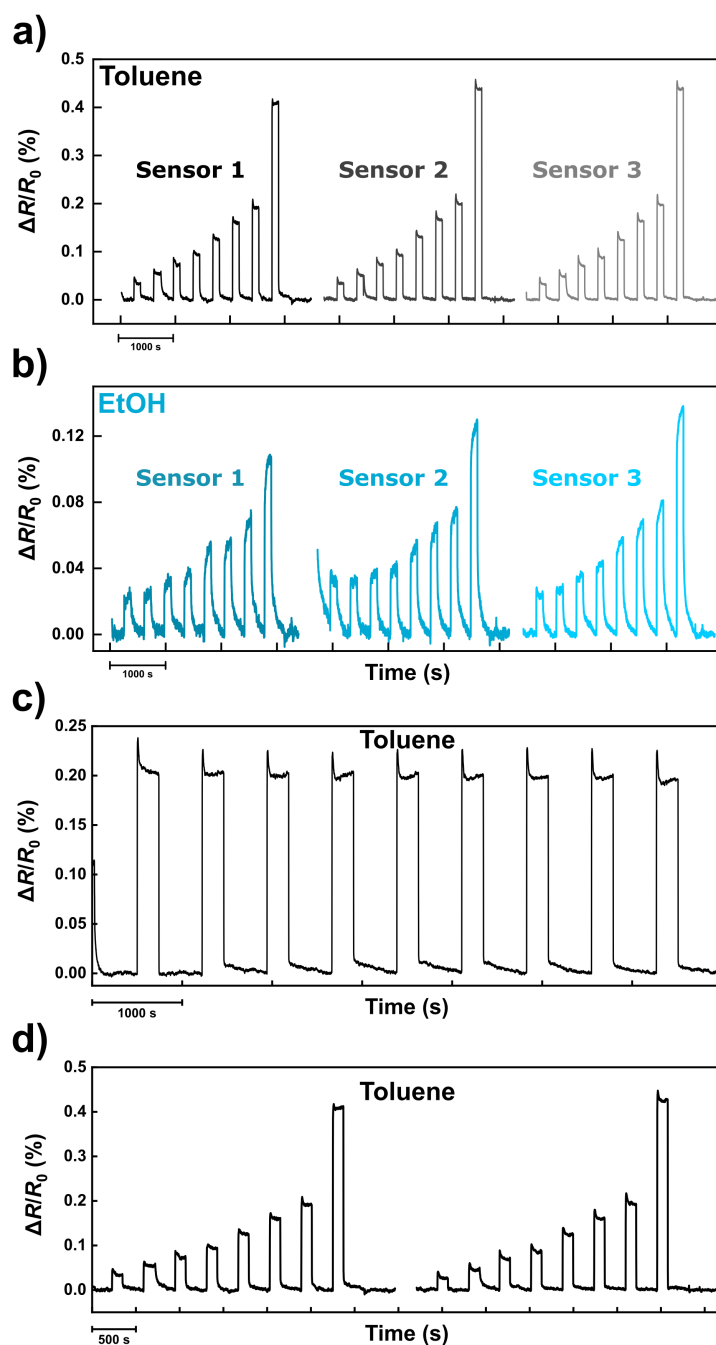


Figure 7.5: Reproducibility tests of three 9DT chemiresistors (Sensor 1-3), fabricated on different days. These chemiresistors were exposed to a) toluene and b) ethanol vapors at concentrations ranging from 50 to 1000 ppm in nitrogen (concentration profile: 50, 100, 150, 200, 300, 400, 500, 1000 ppm). c) Repeatability tests of Sensor 1 from panels a and b. Sensor 1 was exposed to toluene vapor at 500 ppm in nitrogen and pure nitrogen alternatively, and the exposure was repeated nine times. d) Aging test of Sensor 1. Sensor 1 was exposed to toluene vapors with the same analyte concentration profile as in panel a) on two different days. The time trace of transient responses on the left side was recorded first, and the one on the right side was recorded one week later.

7.2.4 Chemiresistor Measurements

The GNP films produced by the printing process exhibited variations in electrical properties, confirming the modification of their respective organic matrices. Preliminary experiments showed exceptional reproducibility, repeatability, and stability of their chemiresistor characteristics, indicating their potential for sensor applications. To fully evaluate their performance, chemiresistor measurements were conducted. To this end, seven GNP films with different organic compositions were fabricated, and their chemiresistive responses were tested against six types of analyte vapors: 1-propanol, 4-methyl-2-pentanone (4M2P), toluene, water, ethanol (EtOH), and acetone. With the exception of acetone and EtOH, the remaining analytes, 1-propanol, 4M2P, water and toluene, represent analytes with different polarities, but with similar vapor pressures (~ 25 , ~ 17 , ~ 24 , and ~ 29 mmHg at 25°C , respectively[170]). In this case, the partition coefficients for analytes sorbed by a GNP film depend strongly on their distinct chemical nature. In addition to screening the chemical nature of the analytes to test each GNP film individually, two other analyte vapors were also of great interest: EtOH and acetone. EtOH is known for its effects on cerebral function and is found in many beverages, while acetone is considered as a biomarker. During ketosis, acetone is generated as byproduct and exhaled through the lung.[171–174] Moreover, studies have shown that the concentration of acetone in breath correlates with blood sugar levels, making a real-time acetone monitor beneficial for diabetes patient[173, 174] and individuals on ketogenic diets[171, 172]. Compared to the first four mentioned vapors, EtOH has a higher vapor pressure (~ 66 mmHg[170]), while acetone has a significantly higher vapor pressure (~ 230 mmHg[170]). These differences in vapor pressure may result in a lower partition coefficient for analyte uptake by the films, thus affecting the sensitivity and selectivity of the chemiresistors.

The seven GNP chemiresistors were exposed to the analyte vapors over the concentration range of 50 to 1000 ppm (50, 100, 150, 200, 300, 400, 500, 1000 ppm), and they exhibited linear response characteristics within the range between 50 to 500 ppm. The sensitivities were determined by the slopes of linear fits to the response isotherms within this concentration range of 50 to 500 ppm, without forcing the lines to pass through the origin, as shown in Figures A8 to A14 in the Appendix (extracted from the responses presented in Figures A1 to A7). Figure 7.6 presents the transient responses of these GNP chemiresistors exposed to six different analyte vapors at a concentration of 500 ppm, as well as the sensitivities of these chemiresistors exposed to six different analyte vapors. The transient responses of all printed GNP-based chemiresistors are shown in Figures A1 to A7 in the Appendix.

The sensitivity of the printed pure 9DT cross-linked GNP chemiresistor to analyte vapors was an order of magnitude lower than reported in previous studies[15, 24]. This decrease can be attributed to the different fabrication process. Due to the long hydrophobic alkyl chain of the 9DT linker, the 9DT chemiresistor possessed a highly hydrophobic organic matrix, resulting in sensitivities following the order: 4M2P > toluene > 1-propanol > water > EtOH > acetone. This sensitivity order is consistent with the 9DT films prepared via the LbL-SC method[23], the LbL self-assembly method[15], and the LbL-inkjet printing method[24]. Except for the sensitivity to 4M2P, the sensitivity order closely reflects the polarity of the analytes. The slightly higher sensitivity to 4M2P compared to toluene is likely due to the lower vapor pressure of 4M2P. Moreover, the low sensitivity towards EtOH and acetone vapors is primarily attributed to the high vapor pressures of these analytes, leading to a lower mass uptake by the film. Additionally, the transient responses of the 9DT chemiresistor to all analyte vapors exhibited quasi-rectangular shapes,

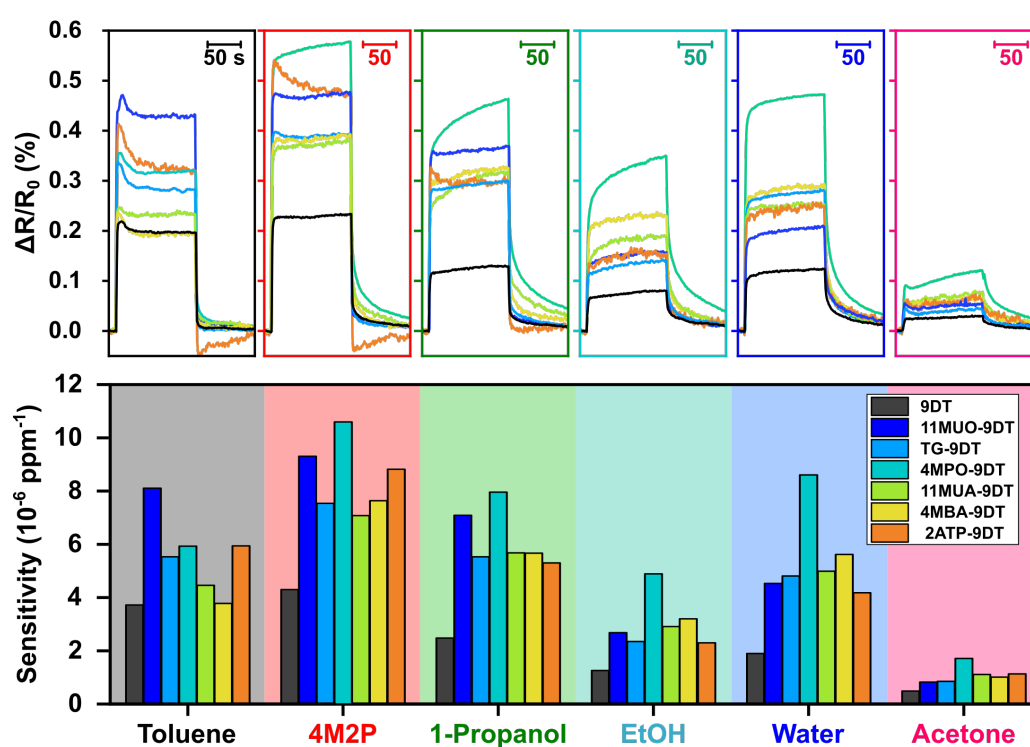


Figure 7.6: Transient responses of seven GNP-based chemiresistors upon exposure to six different analyte vapors at 500 ppm in nitrogen (top). Sensitivities of these chemiresistors towards the six analyte vapors (bottom). Sensitivities were determined from the slopes of linear functions to the response isotherms in the concentration range of 50 to 500 ppm (as shown in Figures A8 to A14 in the Appendix). The colors of the bars represent different GNP chemiresistors prepared with varying organic matrix compositions, as indicated by the legend.

indicating rapid response and recovery times.

The chemical selectivity of GNP-based chemiresistors can be effectively tuned by manipulating the polarity of the ligand shell surrounding the GNPs or by incorporating different cross-linkers during the assembly of GNP films.[9, 15, 20, 24, 29, 41] These strategies enable the customization of sensor responses to specific analytes or classes of analytes, making GNPs a versatile platform for gas and vapor sensing applications. A previous investigation from our research group has demonstrated successful selectivity-tuning through the addition of short hydroxyl and carboxylic acid functionalized MTs.[24] However, the extent of selectivity change remained constrained, and the response kinetics were unaffected by the approach of employing a ligand/linker mixture strategy. To enhance selectivity tuning, various sizes and types of functionalized ligands were employed and investigated, aiming to detect analyte vapors of interest.

To gain insights into how the ligand structure affects sensing characteristics, three hydroxyl functionalized MTs with different structural characteristics were investigated: one possessing a long straight alkyl chain (11MUO), another with a short chain and branched functional groups (TG), and the third containing an aromatic ring (4MPO). As illustrated in Figure 7.6, the film prepared with the ligand containing an aromatic ring (4MPO-9DT) exhibited the highest sensitivity to polar vapors compared to the corresponding other two films (TG-9DT and 11MUO-9DT). The presence of the aromatic ring in the 4MPO ligand may occupy more space on the GNP surface, thus reducing the ligand coverage on GNPs and potentially increasing the analyte uptake or swelling efficiency of the organic matrix.

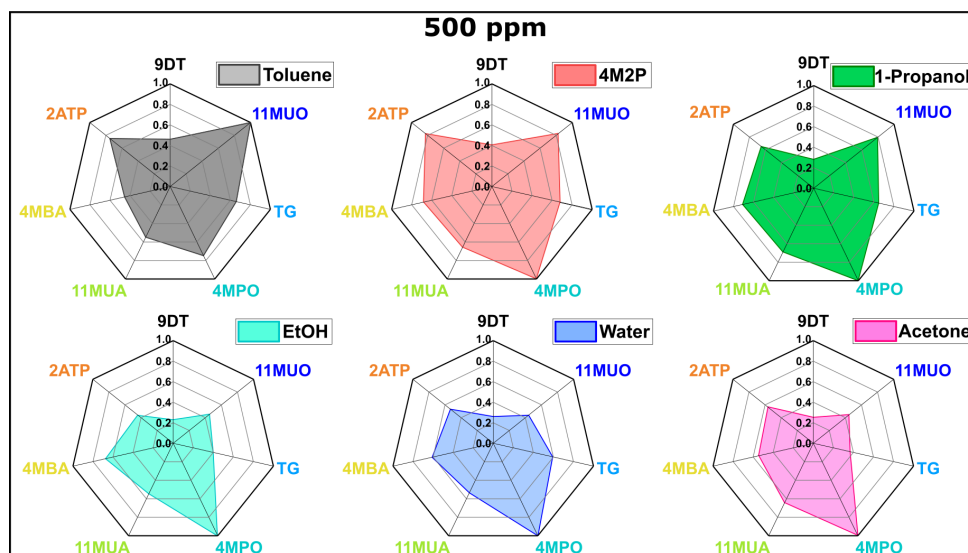
Moreover, according to the "like dissolves like" rule, the hydroxyl-functionalized MT composite organic matrix is expected to exhibit a higher affinity for alcohol vapors. On the other hand, for the detection of volatile compounds with carbonyl groups, amino-functionalized MT, such as 2ATP, was utilized. The carbonyl group has a partially positively charged carbon atom, which is an electrophilic center, whereas the nitrogen atom of the amino group has a partially negative charge, which makes it nucleophilic. Thus, the amino and carbonyl groups are capable of interacting with each other through nucleophilic reactions. Previous studies have highlighted the advantages of using amino-modified materials for acetone sensing.[175, 176] On the other hand, carboxylic acid functionalized ligands have also been widely used for vapor sensing due to their ability to engage in hydrogen bonding with compounds containing nitrogen, oxygen, or fluor atoms.[25, 39, 40, 78, 81, 177–181]

As expected, the resulting GNP chemiresistors prepared with functionalized MT ligands showed higher sensitivity towards polar vapors than the one prepared with the pure 9DT linker. Notably, among all fabricated chemiresistors, the one consisting of the 4MPO ligand exhibited the highest sensitivity towards the polar vapors. Despite the addition of various polar functional groups, the high vapor pressure of acetone still limited its partitioning into the films, resulting in low sensitivity across all chemiresistors. However, some improvements were observed. For instance, compared to the 9DT chemiresistor, the chemiresistor consisting of the amino-functionalized 2ATP ligand succeeded in doubling the sensitivity to acetone, likely due to interactions between the carbon (from the carbonyl of acetone) and nitrogen (from the amino of 2ATP) atoms. Moreover, for the chemiresistor prepared with the mixture of 4MPO/9DT, the sensitivity to acetone could be further increased more than three-fold. Apart from sensitivity enhancement, each chemiresistor exhibited different sensitivity orders towards the six analyte vapors, demonstrating the potential for tailoring sensor responses through careful selection of MT ligands and DT cross-linker.

In addition to tuning the sensor's selectivity, specific MT ligands can also modify the response kinetics of the chemiresistors. For instance, the 4MPO-9DT chemiresistor exhibited a fin-like shape in its transient responses when exposed to 1-propanol and EtOH vapors. This delayed response to alcohol vapors could be attributed to the shielding effect on the sorption site[147], possibly the hydroxyl functional group of the 4MPO ligand. Conversely, the chemiresistor prepared with the mixture of 2ATP/9DT displayed different response kinetics, with rapid responses observed when exposed to toluene, 4M2P, and 1-propanol vapors, followed by a decrease in response amplitude when exposed to the analyte vapors. This phenomenon may originate from the re-assembly of GNPs triggered by vapor sorption. Initially, the organic matrix swells significantly during analyte uptake, and the GNPs subsequently rearrange themselves, eventually settling into more stable positions. The use of functionalized ligand/linker mixtures provides the potential for modifying the response kinetics, which could serve as a feature for further analysis or as a unique fingerprint for specific vapor recognition. These unique characteristics of the response kinetics were later extracted as sensor response features for the GNP-based chemiresistor arrays. In Section 7.5, these features are combined with classification algorithms such as linear discriminant analysis (LDA), and used to distinguish between different volatile chemical compounds. However, a more detailed investigation is necessary to fully understand the influence of functionalized ligands on response kinetic variations.

As previously described, each chemiresistor prepared with a different organic matrix composite displayed distinct vapor sensitivities and selectivities. For the representation of characteristic response patterns produced by an array of different sensors for different analytes, it is necessary to handle significant differences in the values of the response amplitudes caused by variations in the vapor pressure of the analytes by normalizing the measured chemiresistive response amplitudes. For normalization, for each analyte, the highest resistive response amplitude among the seven sensors was used as a reference, allowing the deviation of the relative response magnitudes to be compared to this highest response. Figure 7.7 depicts the radar plots of the relative chemiresistive responses upon exposure to toluene, 4M2P, 1-propanol, EtOH, water, and acetone at vapor concentrations of 500 and 200 ppm. Once again, these radar plots confirm noticeable selectivity tuning when applying mixtures of functionalized MT ligands and the 9DT cross-linker for printing the sensors. The responses from these seven fully printed chemiresistors to each analyte vapor demonstrate unique patterns. Even among the alcohol group vapors, 1-propanol and EtOH, the response patterns were different. Importantly, these analyte specific patterns remained consistent despite variations in vapor concentration.

(a)



(b)

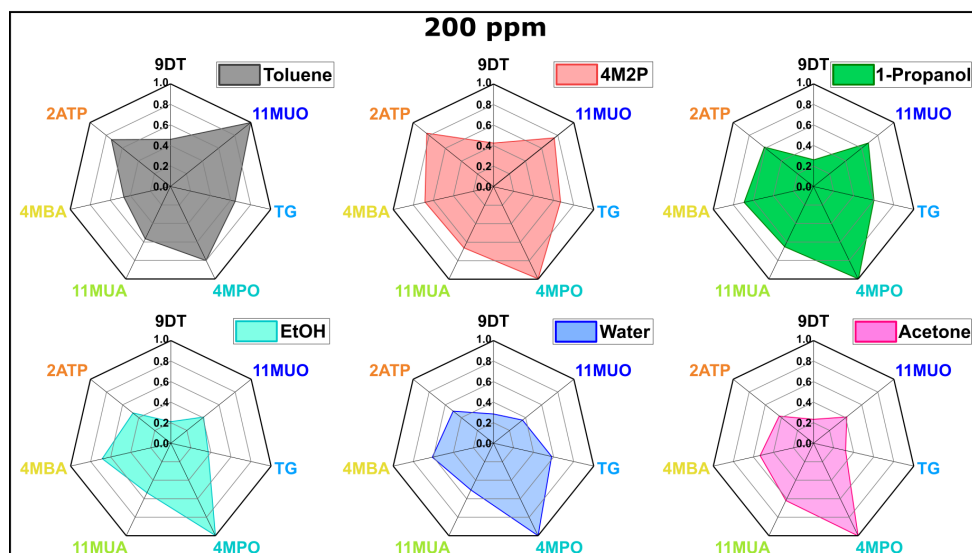


Figure 7.7: Radar plots of the relative chemiresistive response amplitudes of seven different GNP films upon exposure to six analyte vapors at concentrations of a) 500 and b) 200 ppm in nitrogen. The colors of the radar plots represent different analyte vapors as indicated by the legend. Consistency in response patterns is observed for both vapor concentrations.

7.2.5 Amine Sensing

Amine sensing has garnered increasing interest due to the significance of amines in food quality control[182, 183], environmental monitoring[184], and health detection[185]. Amines, as Lewis bases, have the ability to deprotonate Lewis acids such as carboxylic acids, forming carboxylates. Due to the strong interaction between amines and carboxylic acids, carboxylic acid-terminated molecules can serve as potential ligands for amine sensing. Snow et al. proposed GNP-based chemiresistors functionalized with ω -mercaptocarboxylic acid, showing pronounced and selective responses to amine vapors.[177] However, these sensors experienced significant baseline resistance drifts after exposure to amines, necessitating a heating process for the recovery of properties. Similarly, in our study, an ω -mercaptocarboxylic acid with a straight long alkyl chain was employed for the preparation of the fully printed chemiresistors. Compared to the sensor reported in the literature, our printed chemiresistor containing the 11MUA ligand has a much lower ω -mercaptocarboxylic acid fraction within the organic matrix, and the different fabrication method may also lead to variations in GNP assembly and film microstructure. Nevertheless, it is worthwhile to examine its capability as an amine sensor.

In the preliminary amine-sensing measurements, n-butylamine was used as the representative amine gas, possessing a vapor pressure of ~ 93 mmHg at 25°C [186]. The 11MUA-9DT chemiresistor was exposed to n-butylamine vapor at concentrations ranging from 50 to 1000 ppm, with the concentration profile set at 50, 100, 150, 200, 300, 400, 500, 1000 ppm. Figure 7.8 presents the baseline-corrected transient responses. Despite the higher vapor pressure of n-butylamine compared to the previously tested analytes, the response amplitude at the lowest concentration of 50 ppm still reached nearly a 5% increase in resistance. This notable increase in response amplitude of more than a factor of ten compared to the previously tested analyte vapors aligns well with previous findings[177], attributed to a strong Lewis acid-base interaction. However, as depicted in Figure 7.8, the response amplitude did not increase proportionally with increasing concentrations. The response amplitudes within the concentration range of 50 to 500 ppm remained similar, and increased only slightly when the vapor concentration was increased to 1000 ppm. This observation suggests that the organic matrix consisting of the 11MUA/9DT mixture may have reached its maximum swelling ability due to the strong interactions between the analyte and the sensing film. Consequently, even with an increased presence of n-butylamine molecules in the film, a higher degree of swelling is not possible and thereby, it cannot cause a significant increase in response amplitude.

Earlier, Joseph et al.[137] demonstrated that 9DT-cross-linked GNP films prepared via the LbL self-assembly method showed a modest increase in resistance ($\sim 0.2\%$) when exposed to 400 ppm toluene vapor, and an increase of $\sim 0.3\%$ in resistance when exposed to 400 ppm ammonia vapor. This higher sensitivity to ammonia than to toluene is due to the strong affinity between the amine molecules and the gold surfaces. In this case, the response amplitude to amine was 1.5 times higher than the response to toluene. However, in the case of the printed 11MUA-9DT chemiresistor, it showed an increase of $\sim 0.16\%$ in resistance to 400 ppm toluene but a significant increase of $\sim 5\%$ in resistance to 400 ppm n-butylamine, which is more than 30 times greater than the response to toluene. Therefore, although the interaction between the amines and the gold surfaces plays a role in the chemiresistive response, the addition of the 11MUA ligand significantly enhances the sensitivity of the films to the amine analyte.

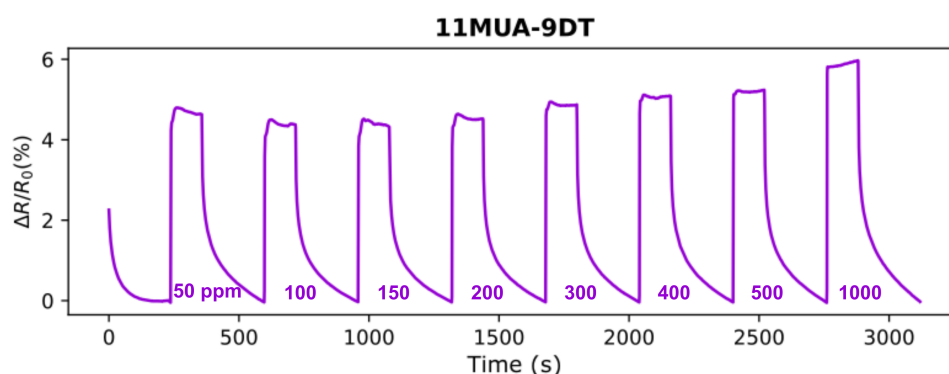


Figure 7.8: Baseline-corrected chemiresistive responses of the 11MUA-9DT sensor to n-butylamine vapor at concentrations of 50, 100, 150, 200, 300, 400, 500, and 1000 ppm in nitrogen.

To confirm the limited swelling of the 11MUA-constructed organic matrix, a second n-butylamine dosing measurement was conducted, starting from a lower concentration of 5 ppm. Figure 7.9 presents the time trace of resistance change upon exposure to amine vapor without baseline correction (top plot), and baseline-corrected resistive responses (bottom plot). In order to obtain lower concentrations of analyte vapor, this measurement was performed with the assistance of a second dilution unit integrated with the standard gas calibration system, as illustrated in Figure 6.2. As n-butylamine is considered to be a corrosive compound, the carrier gas flow rate into the vessel containing the n-butylamine solution was set to a low level. Additionally, it was observed that due to the corrosive nature of n-butylamine, slight degradation of the o-ring between the condenser and the analyte-containing vessel was observed, which could have resulted in analyte gas leakage. These two factors may have contributed to some technical errors during the measurements. Although some technical errors were observed, particularly at vapor exposures of 10 and 25 ppm, the response amplitude at the lowest vapor concentration of 5 ppm still reached a 5% change in resistance. This result suggests that even at 5 ppm of n-butylamine vapor, the 11MUA-9DT sensor is still operating at its maximum swelling ability. However, achieving even lower vapor concentrations becomes challenging, potentially leading to unstable and unreliable testing conditions. This instability is evident when dosing 5 ppm of amine vapor, as three repeated exposures resulted in varying response amplitudes and shapes of transient responses.

The structure of the 11MUA ligand includes a carboxylic acid group, which can react strongly with amines to form carboxylate compounds. This chemical interaction can lead to irreversible baseline drifts in the sensor's response when exposed to amine vapors. Such drifts arise from changes in the assembly of GNPs and the presence of amine residues in the organic matrix. A previous research by Snow and Ancona has reported the need of a heating step to restore sensor's performance and fully desorb amine molecules from the organic matrix.[177] To evaluate the reversibility of our sensor device after being exposed to amine analytes, I-V measurements of the 11MUA-9DT sensor were conducted before and after each amine-dosing experiment (cf. Figure 7.10). Initially, the baseline resistance was around 10 MΩ. After the first amine vapor dosing experiment, which involved vapor concentrations ranging from 50 to 1000 ppm, the resistance increased slightly. To ensure complete desorption of amine molecules within the organic matrix, a 30-minute pure nitrogen purging step was employed after the first experiment. Although the baseline resistance of the sensor dropped back slightly, it did not fully recover to its original value. Subsequently, a second n-butylamine vapor dosing experiment was conducted in a lower concentration range of 5 to 300

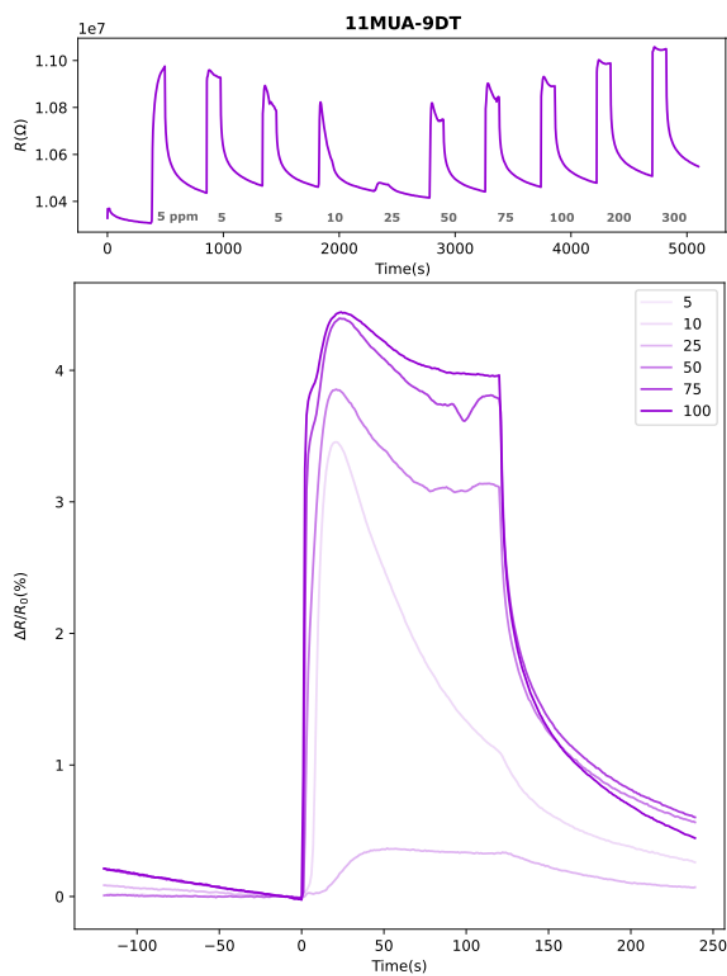


Figure 7.9: Time trace of non-baseline-corrected responses (top plot) and baseline-corrected resistive responses (bottom plot) under exposure to n-butylamine vapor at concentrations of 5, 5, 5, 10, 25, 50, 75, 100, 200, and 300 ppm in nitrogen.

ppm. Again, the baseline resistance of the sensor increased very slightly. However, over two vapor-dosing measurements, the baseline resistance of the 11MUA-9DT sensor eventually stabilized at approximately 10 M Ω . This observation suggests that this sensor not only demonstrates high sensitivity and selectivity towards amine compounds but also exhibits excellent recovery after exposure to amine analytes. The stability and repeatability underline the potential of the fully printed 11MUA-9DT sensor for reliable amine detection in practical applications.

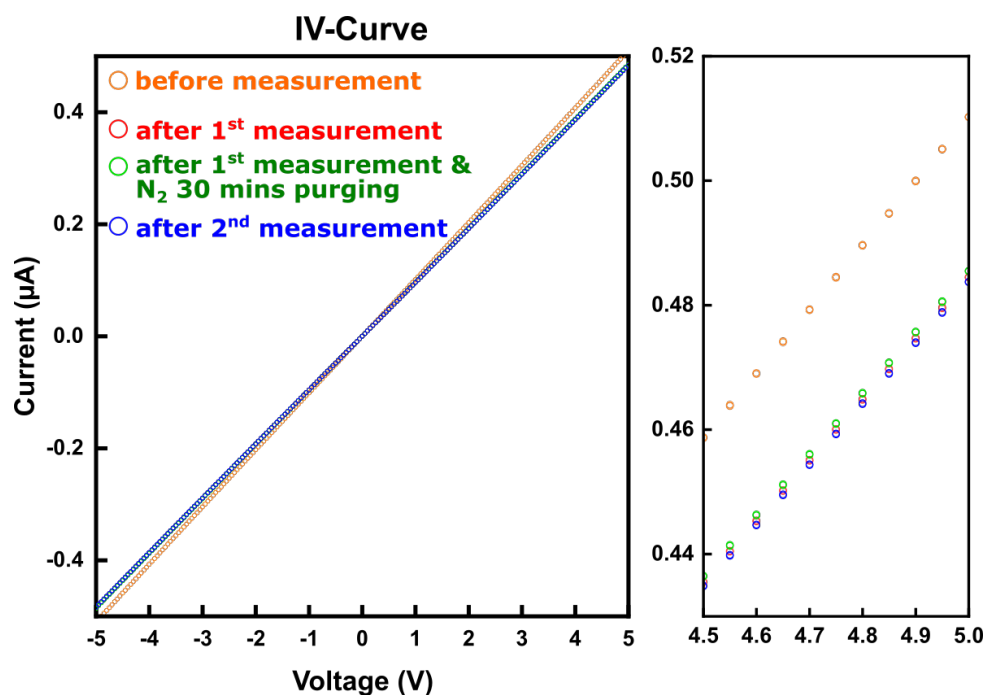


Figure 7.10: I-V curves of the 11MUA-9DT sensor measured before and after each amine-dosing experiment. The right plot is a zoomed-in view of the left plot in the voltage range of 4.5 to 5 V.

7.2.6 Summary and Outlook

In this section, we explored the use of printing approaches combined with a mixed ligand/linker strategy to fabricate GNP-based chemiresistors. This method offers flexible designs for sensors with potential for scale-up, while reducing chemical usage and waste production. Seven chemiresistors with differently functionalized MT ligands were successfully fabricated. We began by examining the electrical properties of the GNP sensors, observing variations of the baseline resistance, which indicates modifications in their organic matrix compositions. Subsequently, comprehensive chemiresistor measurements were conducted by exposing the resulting chemiresistors to various analyte vapors and analyzing their responses. The results reveal distinct sensitivity orders and response kinetics, indicating the potential for selective gas and vapor sensing applications, especially when combining the different sensors to form a sensor array. Furthermore, we investigated the sensors' performance of the 11MUA-9DT sensor for amine sensing, a critical area of interest in food quality control, environmental monitoring, and health detection. Despite encountering some challenges such as baseline drifts and limitation of our gas calibration system for generating even lower vapor concentrations, the sensor demonstrated promising sensitivity and selectivity towards n-butylamine.

Looking ahead, further research could focus on optimizing the organic matrix composition to improve sensitivity and selectivity, as well as exploring additionally functionalized ligands to expand the range of detectable analytes. Additionally, considering the promising results from the amine-dosing experiments, where high sensitivity and selectivity resulted from a Lewis base-acid interaction, further investigations into the response of sensors containing Lewis base functional groups to acidic analytes would be valuable. Specifically, the 2ATP-9DT chemiresistor, which contains the Lewis base functional group, may exhibit high sensitivity to acidic analytes. Conducting acid vapors-dosing experiments using this sensor could provide valuable insights into its performance and potential applications. In summary, the findings presented in this section lay a foundation for the development of advanced fully printed GNP-based chemiresistors for diverse sensing applications.

7.3 Gold Nanoparticle Films with a Mixed Organic Matrix

In Section 7.2, the utilization of a mixed ligand/linker system demonstrated effective selectivity tuning, resulting in GNP-based sensors with distinct response patterns to various analyte. However, these sensors showed relatively low sensitivities to all analyte vapors (with the exception of n-butylamine), and the selection of added ligands was not entirely based on a deep understanding of the underlying structure-property relationships. Therefore, in this section, the present study shifts its focus to a systematic investigation of GNP films prepared with different ligand/linker mixtures. Instead of employing printing technologies, this study adopts a time-saving and straightforward approach to prepare GNP films with different organic matrix compositions through a layer-by-layer spin-coating (LbL-SC) procedure[85], as previously reported by our research group.

Two types of functionalized monothiol (MT) ligands were studied: hydrophobic alkanethiols (ATs) and amphiphilic ω -mercaptocarboxylic acids. The functionalized MTs with varying alkyl chain lengths were mixed with the 9DT linker to determine the optimum mixing ratio and chain length of the MT ligand to achieve high sensitivity and selectivity. The resulting GNP films were analyzed by electrical and optical measurements, grazing incidence small angle X-ray scattering (GISAXS), scanning electron microscopy (SEM), chemiresistor measurements, and quartz crystal microbalance (QCM) measurements.

This section contains a summary of results that were published in the following journal article: C.-Y. Liu, S. C. Bittinger, A. Bose, A. Meyer, H. Schlicke, T. Vossmeier, "Tuning the Interfacial Chemistry of Nanoparticle Assemblies via Spin-Coating: From Single Sensors to Monolithic Sensor Arrays", *Advanced Materials Interfaces*, **2024**, 2301058.[2]

7.3.1 Fabrication of Gold Nanoparticle-Based Sensors with Mixed Organic Matrix

GNP films were prepared using the previously reported LbL-SC procedure[85], as depicted in Figure 7.11. To facilitate highly efficient ligand exchange reactions, amine molecules served as initial ligands to stabilize the GNPs in colloidal solution. Previous studies have demonstrated that these ligand exchange reactions can occur in situ during the LbL-SC procedure. 12A, which binds weakly to the gold surface compared to thiols, allows for efficient exchange for stronger binding linker and ligands such as 9DT and MT molecules during the LbL-SC procedure.[12]

For this study, two batches of GNPs, e.g., GNP2 and GNP3, were used. The particles of both batches had an average core diameter of ~ 7.3 nm, and similar particle concentrations of ~ 4.1 and ~ 4.5 μM , respectively. The characterizations of these batches, including UV/vis absorbance spectra and TEM images, are presented in Figure 7.1. For fundamental characterizations and screening tests of GNP films, batch GNP2 was mainly employed, while the 100%3MPA and 100%8MOA films were prepared using batch GNP3. To investigate the resistive response isotherms, sorption characteristics of different analytes, and vapor-induced swelling of selected GNP films, the GNP films were deposited onto glass substrates (resistive sensors), QCMs (mass sensors), and silicon wafers (GISAXS and SEM measurements) using GNP3 batch. Considering the similar particle sizes and concentrations of batches GNP2 and GNP3, we

assumed that the properties and sensing performances of the resulting GNP films prepared with these two batches are comparable. 12A-stabilized GNPs and various mixtures of functionalized MTs/9DT were alternatively deposited onto a rotating glass substrate, following the procedure detailed in the Experimental Section.[85] 9DT has been widely used as a cross-linker in chemiresistor applications[15, 24, 85, 137], and is commercially available. To ensure comparability with earlier publications and the previous section (Section 7.2), we intentionally chose to use 9DT as the standard cross-linker in the present study.

The 9DT linker was mixed with the hydrophobic ATs and amphiphilic ω -mercaptocarboxylic acids in different ratios aiming to adjust the cross-linking degree and polarity of the resulting organic matrix within the GNP films, as detailed in Table 7.2. In an earlier study conducted by our research group, GNP films were prepared using mixtures of MT/9DT, with the highest molar fraction of MT reaching 50%.[24] However, this previous investigation showed that this MT fraction did not significantly enhance neither sensitivity nor selectivity. Therefore, for the present study, high molar fractions of MT were deliberately chosen to explore GNP films with minimal covalent GNP cross-linking and to optimize the properties of the organic matrix. Consequently, three different MT molar fractions were investigated: 67%, 89%, and 95%. The MT ligands applied in this study can be categorized into three groups depending on their molecular lengths:

1. MTs with lengths shorter than that of 9DT, including 1-hexanethiol (6T), 1-octanethiol (8T), 3-mercaptopropionic acid (3MPA), 6-mercaptophexanoic acid (6MHA), and 4-mercaptobenzoic acid (4MBA).
2. MTs with lengths comparable to that of 9DT, such as 1-decanethiol (10T) and 8-mercaptooctanoic acid (8MOA).
3. MTs with lengths longer than that of 9DT, including 1-undecanethiol (11T), 1-dodecanethiol (12T), 1-tetradecanethiol (14T), and 11-mercaptoundecanoic acid (11MUA).

For the majority of GNP films prepared using mixtures of MT/9DT via the LbL-SC process, it remained feasible to fabricate films even with relatively low 9DT cross-linker molar fractions, as low as 5%. Firstly, experiments were conducted using pure MT ligand solutions to test their suitability for the LbL-SC film fabrication. In these tests, either the GNPs failed to form a film on the substrate during the LbL-SC procedure, or the resulting films were fragile and easily destroyed during the washing step (Figure 7.11a, step v). This observation leads to the conclusion that, regarding the AT ligands, a minor fraction of 9DT linker is necessary to enable the LbL deposition of GNP films via covalently cross-linking of GNPs. Conversely, when pure 3MPA and 8MOA ligand solutions were applied, GNPs were successfully deposited LbL. This result can be attributed to the formation of hydrogen bonds between the carboxylic acid end groups, a mechanism supported by previous studies.[25, 78, 177] The end groups of ω -mercaptocarboxylic acids act as alternative cross-linkers by bridging themselves, and the resulting hydrogen bonds are robust enough to support the LbL-SC fabrication process. However, with the relatively long 11MUA ligand, a molar fraction of 33% of 9DT was required to enable the LbL-SC film fabrication. This suggests that for ω -mercaptocarboxylic acids of such lengths, hydrogen bonds alone were insufficient to form a stable GNP network. Similarly, in the case of the long 14T ligand, the LbL-SC film fabrication was only feasible when a 33% molar fraction of 9DT was used; a lower fraction of 9DT mixed with 14T was insufficient to enable

the LbL-SC procedure. Moreover, the LbL-SC fabrication of the 67%14T-9DT film was challenging in that, as this material exhibited a tendency to detach from the substrate and resulted in the formation of an inhomogeneous film. These findings indicate that the long alkyl residue of 14T ligands sterically hinders the cross-linking ability of the much shorter 9DT linker. Therefore, when using the combination of very long ATs and the 9DT linker, a higher fraction of 9DT linker in the organic matrix appears essential to produce stable GNP networks during LbL-SC film fabrication.

For the fundamental characterization and the chemiresistor screening tests, a total of 32 GNP films (listed in Table 7.2) were prepared by applying five to six LbL-SC cycles (referred to as steps ii and iii in Figure 7.11a). Depending on the applied MT/9DT mixtures, the resulting GNP films exhibited colors ranging from bluish to purple. Exemplary photographs of the films are provided in Figure A16 in the Appendix. Film thicknesses determined by AFM measurements were in the range from ~ 34 to ~ 45 nm (cf. Table A1 in the Appendix). SEM and AFM images of exemplary films are shown in Figure A16 in the Appendix. The GNP chemiresistor fabrication was finished after the evaporation of approximately 100 nm thick gold electrodes onto the GNP films using physical vapor deposition (PVD) with a shadow mask (Figure 7.11a, step vi). The distance between gold electrodes was approximately 400 μm and the electrode width was approximately 11 nm, cf. Figure 7.11b.

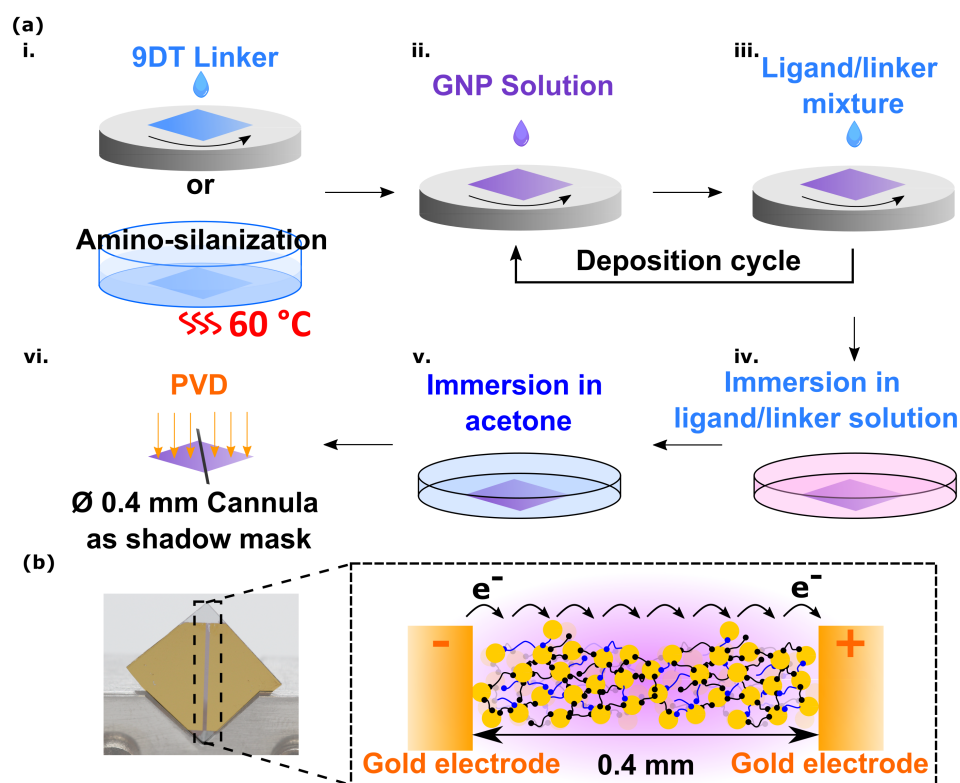
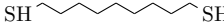






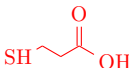
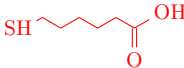
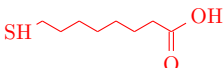

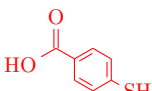


Figure 7.11: a) Overview of the fabrication process for GNP-based sensing films using the LbL-SC method. Initially, the glass substrate was double-coated with pure 9DT cross-linker solution or the surface of the substrate was modified with amino silanes to improve the adhesion between GNPs and the substrate (step i). Subsequently, GNP and MT/9DT solutions were cyclically deposited onto the substrate (steps ii and iii). This procedure was repeated 4 to 5 times. The substrate was then immersed in the ligand solution overnight (step iv), followed by washing in an acetone bath (step v). The resulting GNP film-coated substrate was divided into quarters, and gold electrodes were deposited using PVD with a cannula used as a shadow mask (step vi). b) Photograph of a fabricated GNP chemiresistor and a schematic representation of a partially cross-linked GNP film. Reprinted with permission from Ref. [2]. ©2024 The Authors. Advanced Materials Interfaces published by Wiley-VCH GmbH.

Table 7.2: Cross-linker and MT ligands used in this study, along with the MT molar fractions in MT/9DT mixtures used for GNP films fabrication, and corresponding sensor notations. Reprinted with permission from Ref. [2]. ©2024 The Authors. Advanced Materials Interfaces published by Wiley-VCH GmbH.

Thiols	Structural Formula	MT Molar Fraction [%]	Sensor
1,9-nonanedithiol (9DT)		0	9DT
		67	67% 6T -9DT
1-hexanethiol (6T)		89	89% 6T -9DT
		95	95% 6T -9DT
		67	67% 8T -9DT
1-octanethiol (8T)		89	89% 8T -9DT
		95	95% 8T -9DT
		67	67% 10T -9DT
1-decanethiol (10T)		89	89% 10T -9DT
		95	95% 10T -9DT
		67	67% 11T -9DT
1-undecanethiol (11T)		89	89% 11T -9DT
		95	95% 11T -9DT
		67	67% 12T -9DT
1-dodecanethiol (12T)		89	89% 12T -9DT
		95	95% 12T -9DT
		67	67% 14T -9DT
1-tetradecanethiol (14T)		67	67% 14T -9DT
		67	67% 3MPA -9DT
3-mercaptopropionic acid (3MPA)		89	89% 3MPA -9DT
		95	95% 3MPA -9DT
		100	100% 3MPA
		67	67% 6MHA -9DT
6-mercaptohexanoic acid (6MHA)		89	89% 6MHA -9DT
		95	95% 6MHA -9DT
		67	67% 8MOA -9DT
8-mercaptooctanoic acid (8MOA)		89	89% 8MOA -9DT
		95	95% 8MOA -9DT
		100	100% 8MOA
		67	67% 11MUA -9DT
11-mercaptoundecanoic acid (11MUA)		67	67% 11MUA -9DT
		67	67% 4MBA -9DT
4-mercaptobenzoic acid (4MBA)		89	89% 4MBA -9DT
		95	95% 4MBA -9DT

7.3.2 Conductivity and UV/vis Absorbance of Gold Nanoparticle Films, and GISAXS Measurements

As Equation 5.3 suggests, the conductivity of organically capped GNP films decreases exponentially with increasing interparticle distance. In other words, the conductivity of the film is strongly influenced by the tunneling distance between neighboring GNPs. However, it is important to note that the interparticle distance extracted from conductivity measurements only takes into account the percolation pathway of charge transport. On the other hand, according to the Maxwell-Garnett theory and confirmed by numerous experimental studies[57, 83, 187], the localized surface plasmon resonance (LSPR) band of the GNP films shows a blueshift in spectral position with increasing interparticle distance. In this scenario, changes in the interparticle distance observed in UV/vis data represent an average estimate across the spot size of the spectrometer. Similarly, the GISAXS measurements provide the information about the order of GNP assemblies as well as their interparticle distances based on the spot size of the instrument. By analyzing data from these three measurements, we can infer a correlation between the variation of interparticle distances and charge transport as a function of the composition of mixtures of MT/9DT within the GNP films.

In the electrical measurements, all the prepared GNP films exhibited linear current-voltage (I-V) curves within the voltage range of -5 to +5 V. The conductivities and the spectral positions of the LSPR bands of these GNP films were measured at room temperature as illustrated in Figure 7.12. The conductivity of the 9DT cross-linked GNP film in this study was $\sim 1 \cdot 10^{-2} \text{ S}\cdot\text{cm}^{-1}$, falling within the same order of magnitude as values reported in earlier publications.[12, 15, 23, 24] Interestingly, the GNP films formulated with mixtures of MT/9DT, which included short ligands such as 6T and 8T, showed similar conductivities as the film cross-linked with pure 9DT. This suggests that the presence of 6T and 8T in the organic matrix did not significantly affect the average interparticle distance along the percolating pathway. However, as the fraction of MT ligands increased, the LSPR band shifted slightly towards the blue, indicating a slight increase in the average interparticle distances across the spot size of the spectrometer, see the UV/vis absorbance spectra shown in Figure A17 in the Appendix.

When applying molar fractions of 89% and 95% of the 10T ligand mixed with the 9DT linker, the blueshift of the LSPR band became more obvious, cf. Figure A17 in the Appendix. In addition, a pronounced decrease in conductivity was observed for the GNP films prepared with a molar fraction of 10T at 95%. As the lengths of the MT ligands (11T, 12T, 14T) exceeded that of the 9DT molecule, an even more substantial blueshift was observed. For instance, when the molar fraction of 11T increased from 67% to 89%, the films' conductivity dropped by nearly two orders of magnitude, from $\sim 10^{-2}$ to $\sim 10^{-4} \text{ S}\cdot\text{cm}^{-1}$, while the LSPR band was blueshifted from ~ 615 to $\sim 590 \text{ nm}$. Similarly, but even more pronouncedly, the conductivity of the GNP films prepared with mixtures of 12T/9DT continuously dropped from $\sim 10^{-2}$ down to $\sim 10^{-5} \text{ S}\cdot\text{cm}^{-1}$ (roughly three orders of magnitude) when increasing the 12T molar fraction from 67% to 95%. Concomitantly, the LSPR band blueshifted from ~ 615 to 580 nm . Eventually, for the GNP films prepared with mixtures of 14T/9DT, the conductivity decreased by approximately three orders of magnitude compared with the pure 9DT cross-linked film, and a $\sim 50 \text{ nm}$ blueshift of the LSPR band was observed, despite the low 14T molar fraction of only 67%.

Overall, the GNP films comprising mixtures of ω -mercaptocarboxylic acid/9DT displayed consistent

trends. As the length of the MT ligands increased, the conductivity dropped, accompanied by a blueshift of the LSPR band, as shown in Figure A18 in the Appendix. Additionally, for the films prepared with mixtures of 6MHA/9DT and 8MOA/9DT, the conductivities decreased with higher molar fractions of the MT ligand, along with blueshifts of the LSPR bands (cf. Figure A18, Appendix). In contrast, when using the shorter-length MT, 3MPA, the resulting films showed increased conductivity with increasing 3MPA fractions, and the LSPR bands consistently shifted to the red, except for the film prepared with the pure 3MPA ligand. Similarly, when using the other short MT ligand, 4MBT, the conductivities of the resulting films followed the same trend, but the LSPR bands shifted inconsistently (cf. Figure A18, Appendix). This increase in conductivity and the red-shift of the LSPR can be attributed to the increasing permittivity of the organic matrix with an increasing fraction of polar ligands such as 3MPA or 4MBA molecules. It is noteworthy that for charge transport, the activation energy E_a decreases with the increasing permittivity (cf. equation 5.6).[105] However, for the long MTs, such as 6MHA, 8MOA and 11MUA, the increase in interparticle distance due to longer lengths of the ligands outweighs the permittivity effect. Consequently, with increasing MT fractions, the interparticle distance increased, leading to a decrease in film conductivity.

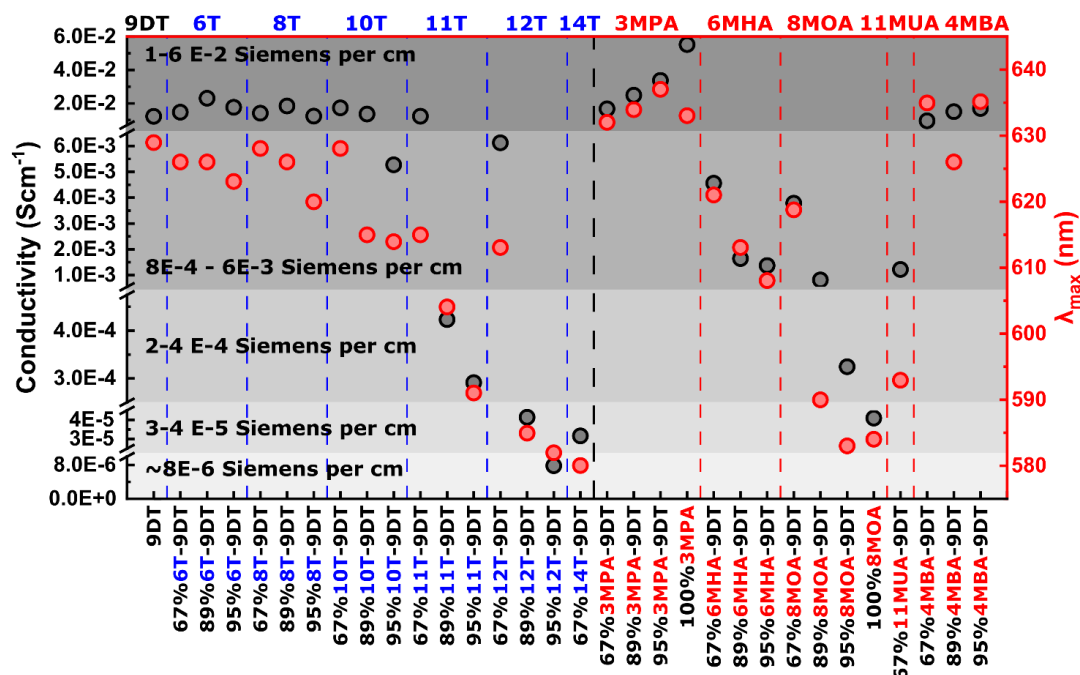


Figure 7.12: Room temperature conductivities and spectral positions of the LSPR band of GNP films assembled with different MT/9DT mixtures. Note, the 100%3MPA and 100%8MOA films were prepared using batch GNP3, while the remaining films were prepared using batch GNP2. Reprinted with permission from Ref. [2]. ©2024 The Authors. Advanced Materials Interfaces published by Wiley-VCH GmbH.

The conductivity and UV/vis data provided insights into the tunneling distance along the charge transport's percolation pathway and the interparticle distance within the spectrometer's spot size of the GNP films. To further validate these findings, GISAXS measurements were conducted on selected samples to confirm the average nearest neighbor distances (NNDs) of GNPs in films prepared using MT ligands of varying lengths and with different functional groups. For this purpose, the GNP films were deposited onto silicon wafers by applying three LbL-SC deposition cycles. Due to the size limitation of the sample stage, a maximum of three samples could be mounted and measured in one experimental run. The 9DT,

95%6T-9DT, and 89%12T-9DT films were measured on the same day, while the 95%3MPA-9DT and 95%8MOA-9DT films were measured on a separate day. Slight deviations in GISAXS measurements may occur due to errors caused by sample alignment. An exemplary GISAXS scattering pattern of the 95%3MPA-9DT film is shown in Figure 7.13a. The intensity profiles of five selected films were derived by applying line cuts from the center-to-edge of the pattern along the red arrow direction as indicated in Figure 7.13a. Intensity profiles were also extracted along the yellow arrow direction and fitted with a 2D hexagonal model to estimate the particle size, resulting in an average core diameter of approximately 7.9 nm. To obtain a more precise GNP size, the GNP colloid from batch GNP3 was subjected to a small angle X-ray scattering (SAXS) measurement in transmission geometry. The intensity profile extracted from the SAXS measurement was fitted with a core/shell spherical form-factor model, yielding an average particle core diameter of 7.44 nm (cf. Figure A15, Appendix), which is in reasonable agreement with the average core diameter of 7.25 nm determined by TEM analysis. The average edge-to-edge interparticle distances of GNPs in different films were calculated by subtracting the SAXS-determined core diameter from the GISAXS-determined NNDs (cf. Figure 7.13b). In qualitative agreement with our previous interpretation, GISAXS measurements revealed average edge-to-edge interparticle distances of approximately 1.2 nm, 0.9 nm, and 1.1 nm for the 9DT, 95%6T-9DT and 95%3MPA-9DT GNP films, respectively. As expected, significantly longer average edge-to-edge distances of approximately 1.9 nm and 1.7 nm were determined for the 89%12T-9DT and 95%8MOA-9DT GNP films, respectively. The interparticle distance of the film prepared with the mixture of 89% 12T/9DT is comparable to the film prepared with the pure 12T ligand reported by Olichwer et al.[14], indicating that the large content of 12T governs the films' properties.

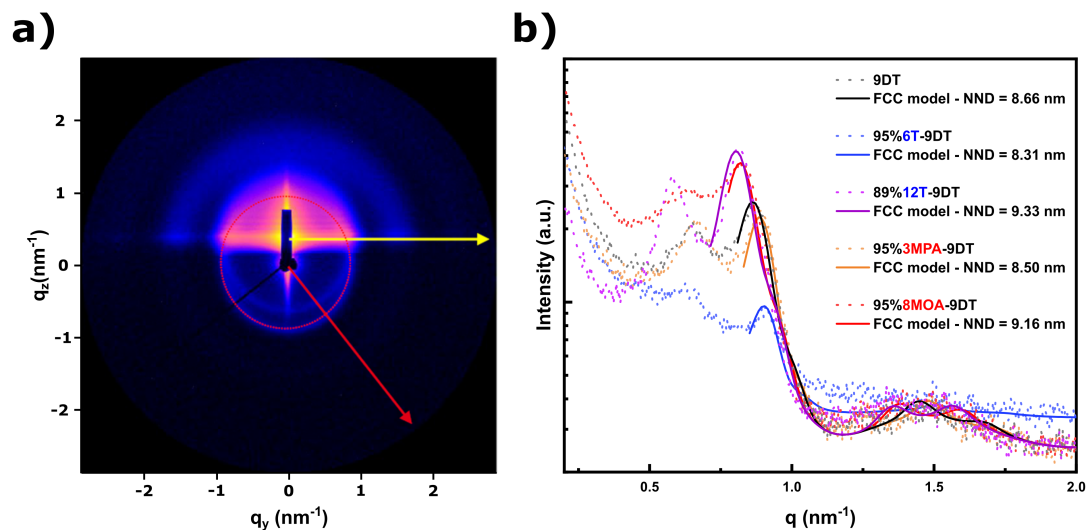


Figure 7.13: a) GISAXS pattern of the 95%3MPA-9DT film prepared using 3 LbL-SC cycles with GNP3 batch. The intensity profiles along yellow arrow direction were fitted with a 2D hexagonal lattice model, while the intensity profiles along red arrow direction were fitted with a 3D FCC model. b) Intensity profiles (data points) extracted along the red arrow of 5 selected samples, as indicated in the legend. The solid lines represent the fits with a 3D FCC model to calculate average NNDs of GNPs in different films. Reprinted with permission from the Supporting Information of Ref. [2]. ©2024 The Authors. Advanced Materials Interfaces published by Wiley-VCH GmbH.

In conclusion, the major trends observed in Figure 7.12 indicate a significant increases in interparticle distances when using AT/9DT mixtures, particularly when the length of the MT ligands (11T, 12T, 14T) exceeds that of the 9DT cross-linker and when the MT ligand fraction is sufficiently high within the

organic matrix. Conversely, with mixtures of ω -mercaptocarboxylic acid/9DT, an increase in interparticle distances is evident even for MT ligands (6MHA, 8MOA) that are somewhat shorter or of similar length to that of the 9DT cross-linker. Previous studies have suggested that ω -mercaptocarboxylic acid ligands enable cross-linking of GNPs via hydrogen bonds[25, 78, 177], which prevents the interdigitation of ligands from neighboring GNPs and requires more space than the interdigitating alkyl chains of AT ligands.[78] Such looser packing of GNPs may create more voids within the films, which is shown in SEM images of Figure A16 in the Appendix. In contrast, when using mixtures of AT/9DT, the highly interdigitated alkyl chains promote a higher GNP assembly order, as evidenced by the scattering patterns in GISAXS measurements and SEM images.

7.3.3 Chemiresistor Screening Tests

In chemiresistor screening tests, 32 GNP films were exposed to analyte vapors of toluene and 1-propanol, which represent nonpolar aprotic and polar protic VOCs, respectively. Due to the comparable vapor pressures of both analytes at 25 °C, approximately 29 and 25 mmHg[170], respectively, their distinct chemical nature predominantly controls the partition coefficients for analyte sorption. Each film was exposed to analyte vapor for 120 s, followed by 240 s of exposure to zero gas (nitrogen). Two different vapor concentrations, 200 and 2000 ppm, corresponding to low and moderate concentrations, were employed for the screening tests. The higher test concentration facilitated the observation of major trends with varying MT/9DT compositions in the GNP films. Consequently, Figures 7.14 and 7.15 solely depict the chemiresistive response amplitudes when exposed to analyte vapors at 2000 ppm. Figures A20 and A21 in the Appendix show the response amplitudes measured when dosing the films with analyte vapors at a concentration of 200 ppm, and, although not as pronounced, confirm a similar trend.

The relative change in resistance ($\Delta R/R_0$) was again used as chemiresistive signal, as described in Section 7.2, where ΔR is the difference between the maximum change in resistance (the average of resistance when exposed to the analyte vapor between 110 to 115 s) and the baseline resistance R_0 (the resistance when exposed to zero gas).

Figure 7.14a displays the results of the GNP films prepared with the pure 9DT linker and the hydrophobic AT/9DT mixtures, while Figure 7.14b shows the transient responses of two exemplary films, 9DT and 89%12T-9DT. The transient responses of the remaining films are presented in Figure A22 in the Appendix. Films prepared with the shorter ATs (6T, 8T, and 10T) exhibited similar response amplitudes to the pure 9DT cross-linked film upon exposure to both vapors. In contrast, compared to the pure 9DT film, films prepared with the longer ATs (11T, 12T, and 14T) exhibited enhanced signal amplitudes for toluene vapor but reduced signal amplitudes for 1-propanol vapor. Increasing the molar fraction of 11T from 67% to 95% led to significant changes in the LSPR band position and film conductivity, as discussed in the previous subsection. Similarly, the chemiresistor behavior changed significantly when a high fraction of long AT ligands was applied. At 95% molar fraction of 11T, the response amplitude for toluene vapor doubled. The same phenomenon was observed for the films prepared with the 12T/9DT mixtures, where the longer 12T molecules reduces the degree of cross-linking of GNPs. At high AT fractions, the LSPR bands showed strong blueshifts, and the conductivities of these films decreased, while the signal amplitude for toluene vapor increased nearly fivefold. It is noteworthy that despite the 95%12T-9DT film

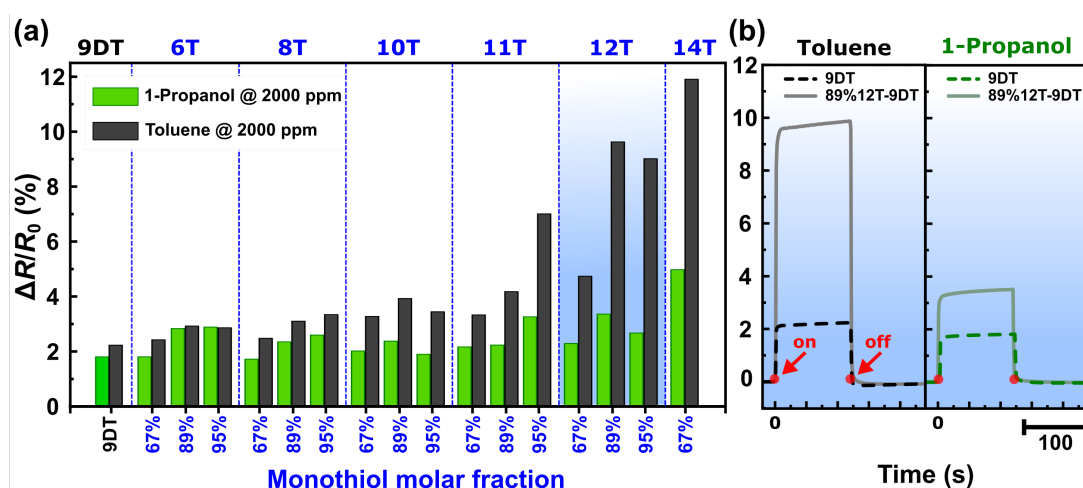


Figure 7.14: a) Chemiresistive responses of GNP films prepared with the pure 9DT cross-linker and AT/9DT mixtures. The films were dosed with toluene (black) and 1-propanol (green) vapors at the concentration of 2000 ppm in nitrogen. b) Response transients of the films prepared with pure 9DT (dark color) and with the 89% 12T/9DT mixture (light color). The films were exposed to the analyte vapors from $t = 0$ s (on) until $t = 120$ s (off). Both films responded and recovered rapidly. Reprinted with permission from Ref. [2]. ©2024 The Authors. Advanced Materials Interfaces published by Wiley-VCH GmbH.

possessing a higher 12T fraction compared to the 89%12T-9DT film, the response amplitude was slightly lower. This can be attributed to defects within this film, as the insufficient cross-linking resulted in an inhomogeneous film morphology, cf. Figure A19 in the Appendix. Nevertheless, the observed decrease in film conductivity and the shift in the LSPR band discussed in Section 7.3.2 qualitatively correlate with the major trends in enhancement of chemiresistive sensitivity to toluene vapor. Moreover, the quasi-rectangular shape of transients shown in Figure 7.14b for both the pure 9DT and 89%12T-9DT films demonstrate rapid response and recovery kinetics. In addition, the mixed AT/9DT strategy maintained the stability of the GNP films for sensing purposes, with the signal responses initially fluctuating, but stabilizing after a few days, cf. Figure A25a and b in the Appendix.

A previous study highlighted the crucial role of the hydrophilicity/hydrophobicity balance of the organic matrix in determining a sensor's vapor-sensing preference, emphasizing the importance of adjusting the mixing ratio of two types of ligands.[86] By utilizing a variety of functionalized ligands and cross-linkers, the chemical selectivity of GNP chemiresistors can be easily tailored.[9, 15, 20, 24, 29, 41] Moreover, several studies have demonstrated exceptional sensing behavior by functionalizing GNP surfaces with thiocarboxylic acids.[25, 40, 78, 177, 180, 181] Therefore, in this study, a polar carboxylic acid functional group was introduced into the organic matrix. Figure 7.15a illustrates a clear selectivity tuning towards more polar vapors compared to films prepared with pure 9DT and mixtures of ω -mercaptocarboxylic acids with 9DT.

For films composed of the shortest carboxylic acid functionalized MT ligand, 3MPA, the response amplitude to toluene vapor decreased with increasing MT fraction. Specifically, the signal direction switched from positive to negative when the molar fraction of 3MPA increases from 67% to 100%. Analogously, in the case of films containing the 4MBA ligand, increasing the MT molar fraction from 67% to 95% also resulted in a negative signal. Snow et al.[177] observed a similar phenomenon, where positive chemiresistive responses upon exposure to 1-propanol were attributed to an increase in interparticle distances

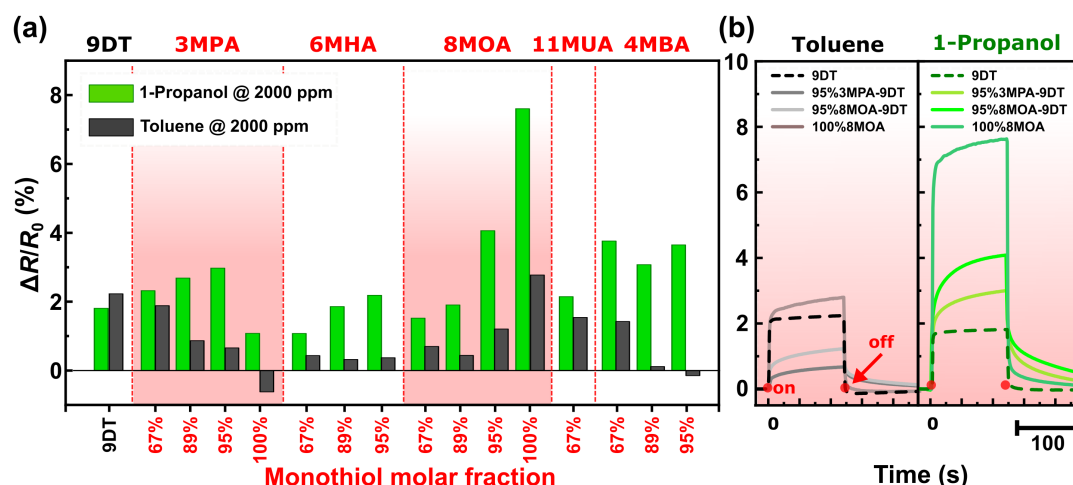


Figure 7.15: a) Chemiresistive responses of GNP films prepared with the pure 9DT cross-linker and ω -mercaptocarboxylic acid/9DT mixtures. The films were dosed with toluene (black) and 1-propanol (green) vapors at the concentration of 2000 ppm in nitrogen. b) Response transients of the films prepared with pure 9DT (black and olive dashed lines), the 95% 3MPA/9DT (grey and light green solid lines) and the 95% 8MOA/9DT (light grey and lime solid lines), and pure 8MOA (brown and green solid lines). The films were exposed to the analyte vapors from $t = 0$ s (on) until $t = 120$ s (off). Both films responded and recovered rapidly. Reprinted with permission from Ref. [2]. ©2024 The Authors. Advanced Materials Interfaces published by Wiley-VCH GmbH.

triggered by analyte molecules binding to the polar carboxylic acid groups between neighboring GNPs. In contrast, upon exposure to toluene, the films behaved more like rigid materials, leading to negative chemiresistive responses due to increased permittivity resulting from toluene molecule filling the free voids within the organic matrix.[17] Although films prepared with the pure 3MPA and mixtures of 4MBA/9DT exhibited distinctive sensing performances, the presence of random spikes and inconsistent shapes in the transient responses at different concentrations posed significant challenges for signal analysis (cf. Figures A23 and A26b in the Appendix). Additionally, the response isotherm changed dramatically due to rapid aging, disqualifying these GNP films for further sensing applications (cf. Figures A25c and A26 in the Appendix). Successful chemical selectivity-tuning was also observed for GNP chemiresistors prepared with mixtures of 6MHA/9DT, and the response to 1-propanol increased slightly with increasing 6MHA fraction. Overall, the use of shorter carboxylic acid functionalized MTs such as 3MPA, 6MHA, and 4MBA resulted in GNP chemiresistors showing preferable selectivity towards more polar vapors. However, the sensitivity to 1-propanol vapor remained similar to that of the 9DT films.

Given the significant sensitivity enhancement observed in chemiresistors consisting of long ATs, we also explored the use of long carboxylic acid functionalized MTs, 8MOA and 11MUA, to prepare GNP chemiresistors. As discussed earlier, film preparations with mixtures of 11MUA/9DT via the LbL-SC procedure were only feasible at a low MT fraction of 67%, due to the relatively weak hydrogen bonding bridge formed by the longer 11MUA ligand. The resulting 67%11MUA-9DT film showed similar response amplitudes to the pure 9DT film, although with reversed sensing selectivity, demonstrating a preference for 1-propanol vapor over toluene vapor. The longest carboxylic acid functionalized MT, 11MUA, did not provide further advantages to the performance as chemiresistor, possibly due to the low MT fraction employed. On the other hand, it was feasible to fabricate films with the pure 8MOA ligand via the LbL-SC procedure. GNP chemiresistors prepared with the 8MOA ligand exhibited higher responses to 1-propanol with increasing MT fraction, particularly showing strengthened signal enhancement with higher fractions of 8MOA. At

lower MT fractions (67% and 89%), the response amplitudes to 1-propanol were comparable to that of the 9DT film. However, at higher MT fractions (95% and 100%), significant changes in the position of the LSPR band and conductivity of these films were observed. These alterations were also accompanied by pronounced changes in their chemiresistor characteristics, resulting in twofold and threefold increases in response amplitudes to 1-propanol, respectively. The significant enhancement of response amplitudes to 1-propanol led to a notable difference in the relative responses to 1-propanol and toluene vapors. This indicates a much higher sensitivity to 1-propanol vapor in the films containing a high fraction of 8MOA ligands compared to the pure 9DT film.

For GNP films prepared with the ω -mercaptocarboxylic acid ligands, their response kinetics, such as response and recovery times, differed from the films prepared with the pure 9DT and mixtures of AT/9DT. As depicted in Figure 7.15b, chemiresistors prepared with ω -mercaptocarboxylic acid ligands exhibited slower response and recovery times to the analyte vapors, as indicated by their shapes of resistive signals. This delay in response and recovery kinetics could be attributed to the complexity of ω -mercaptocarboxylic acids-based organic matrix. This complexity may retard the sorption-induced swelling of the organic matrix and prolong the time required for the organic matrix to recover to its initial structure after the desorption of analyte molecules.

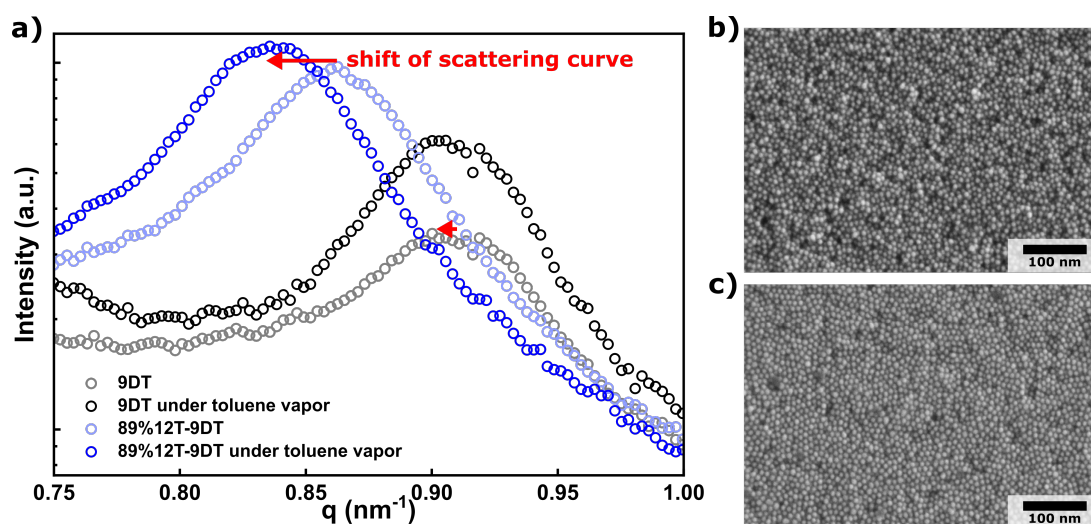


Figure 7.16: GISAXS scattering curves of GNP films at ambient conditions and during exposure to saturated toluene vapor in air. The data of the 9DT film measured at ambient conditions and under saturated toluene vapor are indicated by grey and black color, respectively. The data of the 89%12T-9DT film measured at ambient condition and under saturated toluene vapor are indicated by light blue and blue color, respectively. A clear shift of the scattering curves was only observed for the 89%12T-9DT film. b) SEM-image of the pure 9DT film used for in-situ GISAXS measurements. c) SEM-image of 89%12T-9DT film used for in-situ GISAXS measurements. Adapted and reproduced with permission from the Supporting Information of Ref. [2] ©2024 The Authors. Advanced Materials Interfaces published by Wiley-VCH GmbH.

In summary, the significant changes observed in the optical and electrical properties of GNP films prepared with different ligand/linker compositions reflected corresponding alterations in their chemiresistor characteristics compared to the 9DT film. Short ATs did obviously not affect significantly the cross-linking of 9DT within the organic matrix. Conversely, the use of appropriately longer MT ligands can decrease the degree of cross-linking. Moreover, the addition of long MT ligands such as 12T enhanced the assembly order of the resulting GNP films compared to the 9DT film (see Figure 7.16b vs. c), likely due to the Van der Waals interactions between the long alkyl chains of neighboring GNPs. GNP films

composed of 12T/9DT mixtures exhibited significant enhancement in response amplitudes to toluene. Notably, films prepared with high molar fractions (89% and 95%) of 12T displayed behavior similar to that of the non-cross-linked 12T-stabilized GNP films reported by Olichwer et al.[14]. The weakly cross-linked organic matrix provided high flexibility, granting for greater freedom for sorption-induced swelling. To qualitatively evaluate the swelling-ability, the 9DT and 89%12T-9DT GNP films were subjected to in situ GISAXS measurements under saturated toluene vapor. The scattering curve of the 9DT film shifted slightly upon exposure to toluene vapor, indicating a minor change in the interparticle distance; however, due to the broad signature of the GISAXS signal, the precise extent of swelling could not be quantified. In contrast, when exposed to toluene, the scattering curve of the 89%12T-9DT film shifted significantly, confirming the superior swelling ability (Figure 7.16a). Assuming that 1-propanol induces a comparable swelling distance in both hydrophobic organic matrices (composed of the pure 9DT and the mixture 89% 12T/9DT), the constrained maximum swelling distance of the 9DT cross-linked film results in only a small difference in swelling for the two different vapors. However, as shown by GISAXS measurements, the 89%12T-9DT film demonstrated a much greater ability for sorption-induced swelling, leading to a substantial difference in swelling-induced interparticle distance changes regarding the two vapors and, thus, a more pronounced selectivity towards nonpolar vapors can be observed. Similarly, implementation of the long ω -mercaptocarboxylic acid, 8MOA, increased the response amplitude significantly. These results indicate that MTs with longer chains improve the flexibility and swelling-ability of the organic matrix. Based on the screening test results, five GNP films of interest were selected for further investigations according to their response amplitude, vapor selectivity, and response kinetics. These included the 9DT, 89%12T-9DT, 95%3MPA-9DT, 95%8MOA-9DT, and 100%8MOA films.

7.3.4 Response Isotherms and Sorption Characteristics

Based on the exceptional response characteristics discussed above, we selected five samples for further investigations: 9DT, 89%12T-9DT, 95%3MPA-9DT, 95%8MOA-9DT, and 100%8MOA GNP films. These samples were deposited onto glass substrates and quartz crystal microbalances (QCMs) using batch GNP3 to examine their chemiresistive and sorption characteristics. The GNP film-coated QCMs showed frequency shifts of approximately 6-8 kHz, corresponding to masses of the films of approximately 5-7 μg calculated using the Sauerbrey equation (Equation 5.9). In situ chemiresistor/QCM measurements were conducted over a broad concentration range of analyte vapors, from 50 to 10000 ppm. Toluene, 1-propanol and water were selected as analyte vapors due to their significant differences in polarity but similar vapor pressure. The sensitivities of the sensors were determined by the slope of linear fits ($y = mx + b$) to the response isotherms in the concentration range of 50 to 500 ppm. To exam the sorption ability of the blank QCM, it was first exposed to all three vapors at concentrations ranging from 50 to 10000 ppm. Within this concentration range, the blank QCM showed nearly zero water molecule uptake. However, exposure to the toluene and 1-propanol vapors resulted in frequency shifts of approximately 7 and 8 Hz, respectively, at 10000 ppm. Assuming equal sorption abilities on both sides of the QCM, the effect of sorption on the non-coated side of the QCM on the general trend of all QCM data was negligible.

Figure 7.17 shows the transient responses of both chemiresistors and QCMs when dosed with toluene vapor at 2000 ppm during the in situ chemiresistor/QCM measurements. Consistent with the response kinetics observations discussed earlier, the hydrophobic organically capped GNP chemiresistors (9DT

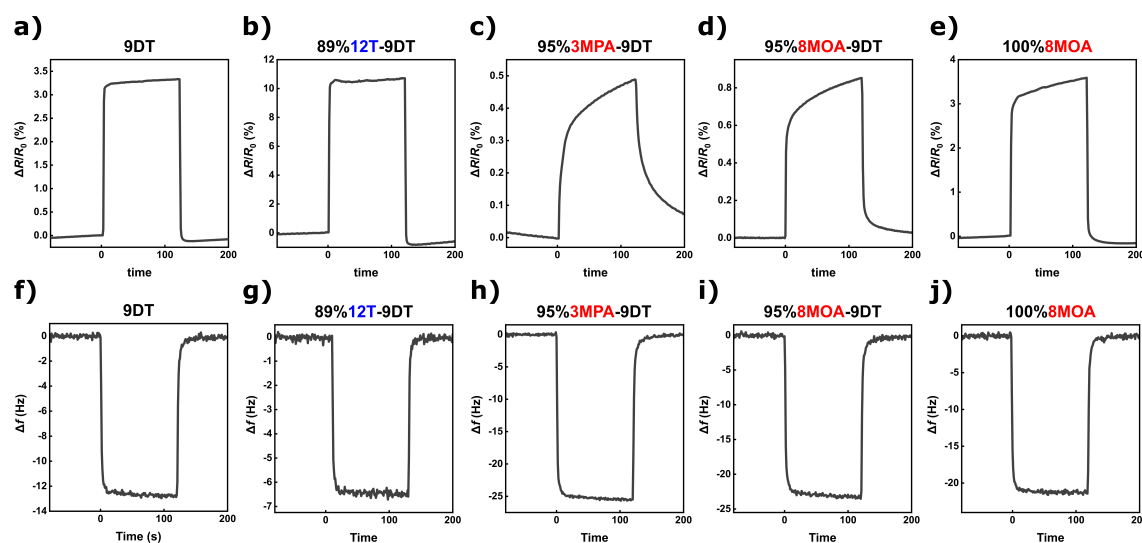


Figure 7.17: In situ chemiresistor/QCM measurements of five selected GNP films: 9DT (a and f), 89%12T-9DT (b and g), 95%3MPA-9DT (c and h), 95%8MOA-9DT (d and i), and 100%8MOA (e and j). The data show their corresponding chemiresistive (a-e) and QCM (f-j) responses under exposure to toluene vapor at 2000 ppm in nitrogen.

and 89%12T-9DT) exhibited rapid response and recovery. Moreover, although the results from the QCM measurements showed that the 9DT film sorbed a larger amount of toluene molecules than the 89%12T-9DT film, an enhancement in the chemiresistive response amplitude was observed in the case of the 89%12T-9DT sensor. This confirms that the high response amplitude is mainly due to the high swelling ability of the organic matrix. In contrast, the amphiphilic organically capped GNP chemiresistors (95%3MPA-9DT, 95%8MOA-9DT and 100%8MOA) exhibited delays in both response and recovery. However, the QCM data revealed rapid sorption and desorption for these three GNP films. This again confirms that the slow response and recovery were not due to slow partitioning of analytes into the films. Instead, the delays are attributed to the complexity of the ω -mercaptocarboxylic acids-based organic matrices, which impedes the diffusion of the analyte molecules within the film and the rearrangement of the film structure during analyte sorption.

Early studies have demonstrated that the response isotherms of DT cross-linked GNP films can be described by first-order Langmuir[24, 84] or Langmuir-Henry[15, 18] models. In line with these findings, the 9DT sensor exhibited a good fit with the Langmuir-Henry sorption model (cf. Equation 5.14). The binding constants (K_L) were in the order of $\sim 10^4$ L/mol, which is in good agreement with previously reported values[15, 18, 24] for 9DT cross-linked GNP films. The signal saturation observed in the isotherms can be attributed to the constrained swelling ability of the cross-linked organic matrix. Throughout the measured concentration range, the sensitivity for the three vapors followed the order of toluene $>$ 1-propanol \gg water (cf. Figure 7.18a and f). Specifically, the sensitivity for toluene ($\sim 2.2 \times 10^{-5}$ ppm $^{-1}$) was approximately two times higher than for 1-propanol ($\sim 9.8 \times 10^{-6}$ ppm $^{-1}$), and ten times higher for water ($\sim 1.2 \times 10^{-6}$ ppm $^{-1}$). The hydrophobic nature of the alkyl chains in 9DT molecules mainly accounts for this sensitivity order. These relative sensitivity values are also comparable to 9DT cross-linked GNP sensors fabricated on flexible substrates reported earlier (cf. Figure 7.19).[15, 24] Comparing with the data presented in Figure 7.14a, the relative sensitivities between toluene and 1-propanol vapors presented in Figure 7.19 showed deviations. This can be attributed to sensor-to-sensor and batch-to-batch variations,

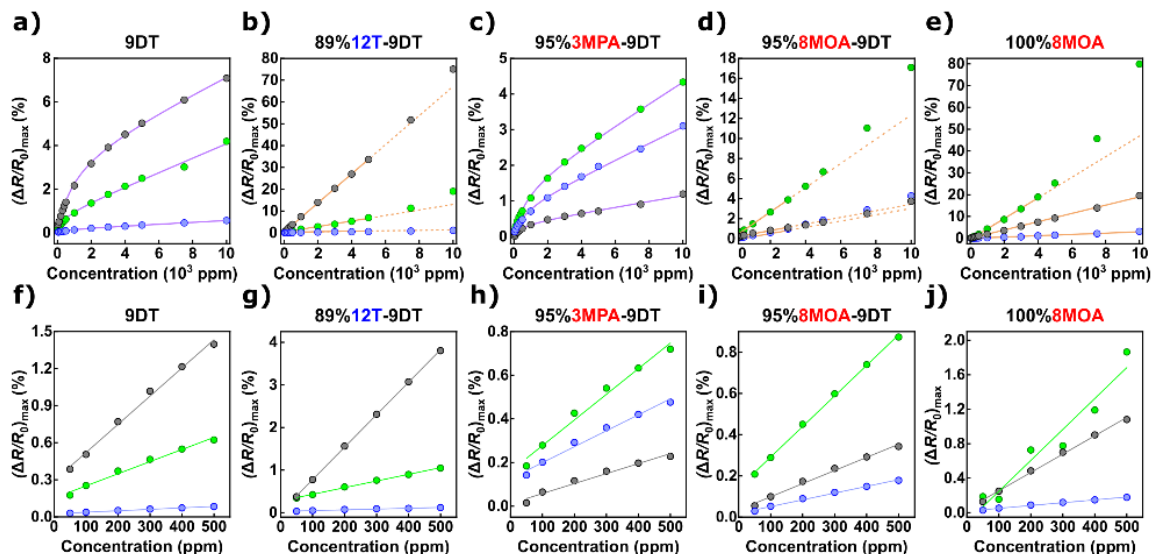


Figure 7.18: a-e) Chemiresistive response isotherms of five selected GNP films: a) 9DT, b) 89%12T-9DT, c) 95%3MPA-9DT, d) 95%8MOA-9DT, and e) 100%8MOA. These films were exposed to toluene (black), 1-propanol (green), and water (blue) vapors at concentrations ranging from 50 to 10000 ppm in nitrogen. Data points are the relative resistance changes ($\Delta R/R_0$). Solid purple lines represent the fits using a Langmuir-Henry model, while solid orange lines represent linear functions, with dashed orange lines showing extrapolations. f-j) Chemiresistive response isotherms at low concentrations ranging from 50 to 500 ppm of the same five selected GNP films. The response isotherms were fitted with linear functions to determine the sensitivity. Reprinted with permission from Ref. [2]. ©2024 The Authors. Advanced Materials Interfaces published by Wiley-VCH GmbH.

as illustrated in Figure A24 in the Appendix.

Films prepared with the 12T/9DT mixtures exhibited superior sensing capabilities compared to those prepared using pure 9DT. As evidenced by screening tests, these mixtures showed a remarkable improvement in sensitivity towards nonpolar vapors. A previous study employed a drop-casting method to fabricate assemblies of purely 12T stabilized GNPs, where the resulting GNP films demonstrated a sensitivity for toluene vapor of approximately $6 \times 10^{-5} \text{ ppm}^{-1}$. [14] In comparison, our partially cross-linked 89%12T-9DT film showed a similar sensitivity for toluene vapor of approximately $7.6 \times 10^{-5} \text{ ppm}^{-1}$. Moreover, the sensitivity towards 1-propanol vapor was more effectively suppressed by the 89%12T-9DT film, resulting in a pronounced disparity in response amplitudes of toluene and 1-propanol vapors. In addition, compared to the 9DT cross-linked film, the shape of isotherms transitioned from saturation-type to a more linear correlation, as depicted in Figure 7.18b. For all three vapors, the chemiresistive responses correlated linearly with the concentrations of analyte vapors up to 5000 ppm. Linear response isotherms are generally preferred for many applications as they simplify the evaluation of sensor array data using statistical methods, such as principal component analysis (PCA) and linear discriminant analysis (LDA), especially when the test analytes are evaluated at various concentrations. However, for toluene and 1-propanol vapors, concentrations above 5000 ppm led to deviations from linearity, exhibiting a slight positive curvature. This observation aligns with previous findings by Olichwer et al. [14], who attributed such isotherms with positive curvature to the exponentially increasing resistance associated with increasing interparticle distances induced by analyte sorption. Moreover, the addition of the 12T ligand led to an increase in the hydrophobicity of the organic matrix within the film, alongside a reduction in the degree of cross-linkage, thereby enhancing the flexibility of the organic matrix. The increased hydrophobicity due to the incorporation of the more hydrophobic ligand, 12T, made the organic matrix more favorable

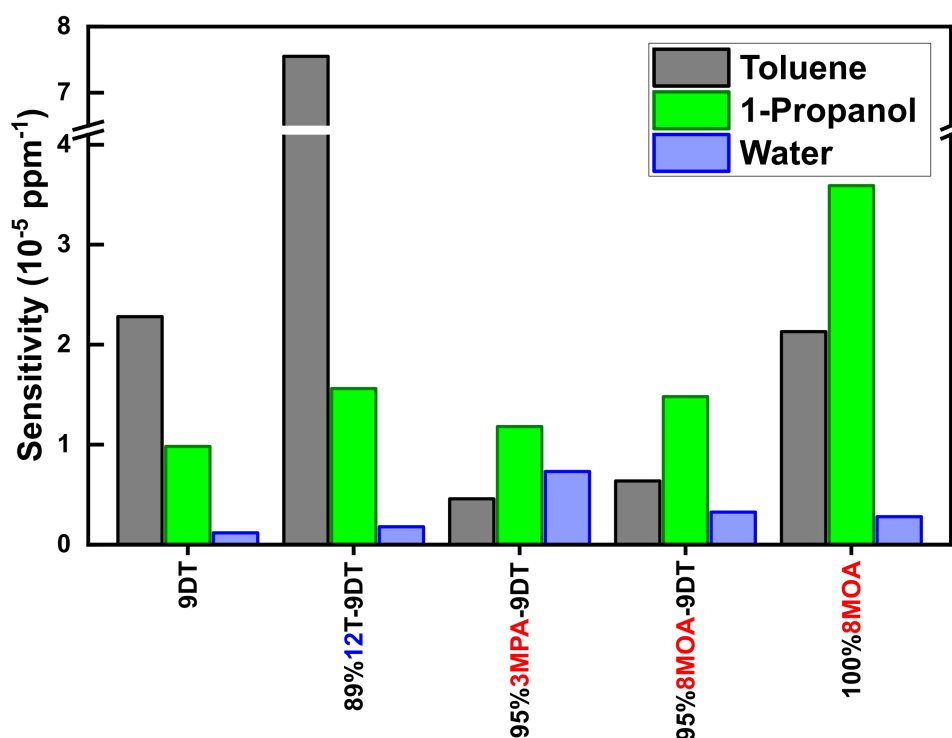


Figure 7.19: Sensitivities of the GNP chemiresistors prepared with the pure 9DT and MT/9DT mixtures to three different analyte vapors. The sensitivities were determined by extracting the slope of the respective response isotherms within the concentration range of 50 to 500 ppm, as shown in Figure 7.18f-j. Reprinted with permission from Ref. [2]. ©2024 The Authors. Advanced Materials Interfaces published by Wiley-VCH GmbH.

for sorption of nonpolar analytes. Qualitatively, compared to the 9DT film, the sensitivity for the three vapors followed the same order: toluene > 1-propanol \gg water. However, the sensitivity for toluene vapor was significantly enhanced, nearly falling in the range of 10^{-4} ppm^{-1} . Moreover, the low sensitivity towards water vapor was negligible across a broad concentration range, reducing the cross-sensitivity to humidity. In summary, these data demonstrate that using a mixture of the 9DT cross-linker with 12T for sensor fabrication offers several advantages: i) facile fabrication of the sensor via a LbL-SC procedure, ii) significant increase in sensitivity and selectivity, iii) linear response isotherms, and iv) low cross-sensitivity to humidity.

In contrast to the hydrophobic organic matrices in GNP films, using 3MPA/9DT mixtures for sensor application, compared to the pure 9DT film, significantly enhanced sensitivity towards water while decreasing sensitivity towards toluene, with the sensitivity towards 1-propanol remaining almost unchanged (see Figure 7.19). Unlike the 9DT film, the sensitivity order changed to 1-propanol > water > toluene for the 95%3MPA-9DT chemiresistor (Figure 7.19), resulting in a selectivity towards polar vapors. Furthermore, the resistive response isotherms of this sensor retained a negative curvature, indicating that the swelling ability was still limited by the high degree of cross-linking via 9DT linkers and/or hydrogen bonds between carboxylic acid groups. These response isotherms could once again be described by the Langmuir-Henry model (cf. Figure 7.18c), with the binding constants ($\sim 3 - 4 \times 10^4 \text{ L/mol}$) in the same order of magnitude as for the 9DT film.

When applying the longer ω -mercaptocarboxylic acid at a molar fraction of 95%, the 8MOA ligand

effectively disrupted the 9DT cross-linking network within the organic matrix. This improved the swelling ability of the resulting film and provided a significant enhancement in sensitivity towards 1-propanol, a moderate rise in sensitivity towards water, and a decrease in sensitivity towards toluene (cf. Figure 7.19). At 10000 ppm, the resistive response amplitudes for both polar vapors, 1-propanol and water, increased by more than four times, while it decreased by $\sim 50\%$ for the nonpolar vapor, toluene. In the higher concentration range (> 500 ppm), the isotherms exhibited a slight positive curvature, see Figure 7.18d. Conversely, in the lower concentration range (50-500 ppm), the response isotherms were linear, see Figure 7.18i. Overall, for all three analyte vapors, the response isotherms displayed linear behavior up to 3000 ppm, and above this concentration, the order of the sensitivity shifted from 1-propanol $>$ toluene $>$ water to 1-propanol $>$ water $>$ toluene.

Applying an even higher fraction of 8MOA in the organic matrix, the 100%8MOA GNP film exhibited increased sensitivity towards 1-propanol and toluene vapors (cf. Figure 7.18e) compared to the 95%8MOA-9DT film, particularly in the higher concentration range (> 500 ppm). This notable enhancement in sensitivity can be attributed to the cross-linked network formed by hydrogen bonding rather than the covalent bonding by the 9DT linker, which results in a more flexible film structure. For both toluene and water vapors, the 100%8MOA GNP film demonstrated linear correlations between the resistive response and concentration up to 10000 ppm, enabling quantification of both analytes over a wide concentration range. The response isotherm for 1-propanol showed a linear correlation up to 4000 ppm, followed by a pronounced positive curvature at higher vapor concentrations (> 7500 ppm). Notably, under exposure to 1-propanol vapor at 10000 ppm, the 100%8MOA film showed a resistance change of 80%, which was twenty times higher than that of the pure 9DT film. The significantly improved sensitivity of the 100%8MOA film towards 1-propanol highlights its potential for highly sensitive detection of polar vapors. The sensitivity order of this film followed the sequence 1-propanol $>$ toluene \gg water.

The results presented above demonstrate the capability of the LbL-SC method to fabricate GNP chemiresistors with tunable response characteristics. Through careful selection of ligand/linker mixtures and adjusted mixing ratios, it is feasible to tune the chemical selectivity, response isotherms, and sensitivity of the sensors. Remarkably, by reducing the fraction of DT linker, the sensitivity can be substantially enhanced, and the response isotherms can be tailored to exhibit desirable linear behavior over a wide range of analyte concentrations.

In the in situ chemiresistor/QCM measurements, alongside the chemiresistor measurements, microgravimetric measurements using 10 MHz QCMs were conducted to quantify the mass of sorbed analyte from the vapor phase. Figure 7.20 shows the relative mass uptake ($\Delta m/m_0$) of different GNP films, where Δm represents the change in mass upon exposure to analyte vapors, and m_0 is the initial mass of the GNP film. When the GNP films were prepared with the hydrophobic 9DT linker or 12T ligand, both their respective chemiresistors and QCM sensors exhibited consistent sensitivity patterns, showing decreasing sensitivity in the order of toluene $>$ 1-propanol \gg water. The shapes of the sorption isotherms closely resembled the resistive response isotherms (cf. Figure 7.18a and b vs. Figure 7.20a and b), with the exception of the response isotherms of the 9DT film sensor to 1-propanol. Similar observations were reported by Olichwer et al., who found that QCM data for superlattice films comprised of 12T-stabilized GNPs showed that at higher vapor concentrations, 1-propanol condensed on the film surface (multilayer sorption) and/or sorbed in the voids without causing swelling. Therefore, this phenomenon was not

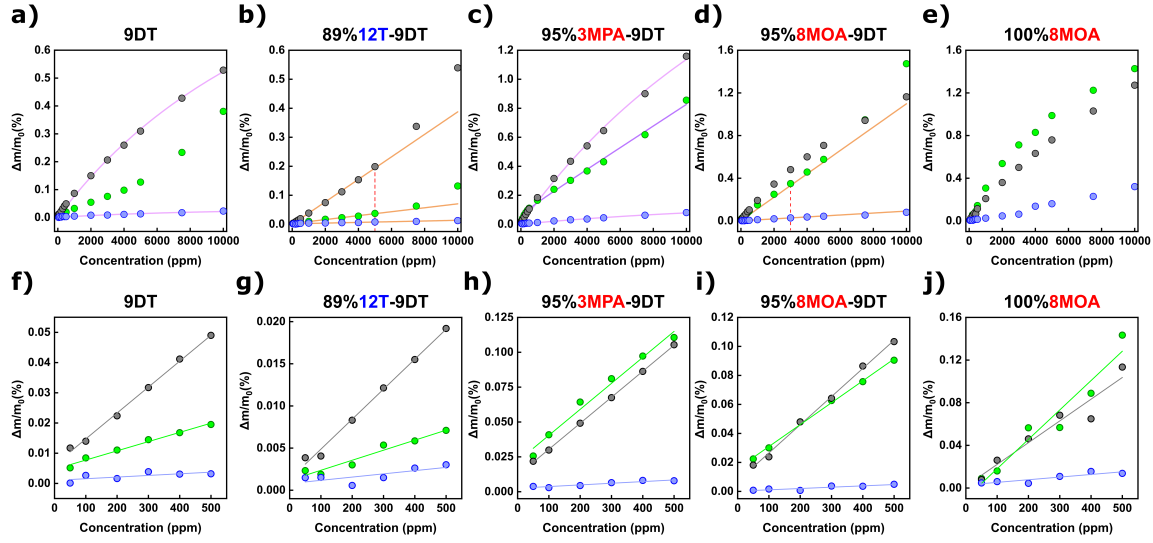


Figure 7.20: Sorption isotherms of five selected GNP films: a) 9DT, b) 89%12T-9DT, c) 95%3MPA-9DT, d) 95%8MOA-9DT, and e) 100%8MOA. These films were coated onto QCM substrates. The film-coated QCMs were exposed to toluene (black), 1-propanol (green), and water (blue) vapors at concentrations ranging from 50 to 10000 ppm in nitrogen. Data points are the relative mass uptake of the films ($\Delta m/m_0$). Solid purple lines represent the fits using the Langmuir-Henry model, while solid orange lines represent linear functions, with dashed orange lines showing extrapolations. f-j) Sorption isotherms at low concentrations ranging from 50 to 500 ppm of the same five selected GNP films. The sorption isotherms were fitted with linear functions.

detectable in the chemiresistor measurements.[14] Nevertheless, qualitatively, in the case of the 9DT film, its chemiresistor and QCM data demonstrated similar response characteristics, including analogous sensitivity patterns. Likewise, the 89%12T-9DT chemiresistor and the 89%12T-9DT GNP film-coated QCM showed comparable response characteristics, with similar sensitivity patterns and isotherm shapes. Compared to the 9DT film, the 89%12T-9DT film sorbed a similar mass of toluene molecules but a significantly smaller mass of 1-propanol molecules. This observation underscores that a better swelling ability accounts for the high chemiresistive response amplitude, while the increased hydrophobicity of the organic matrix, resulting from the addition of the 12T ligand, prevents the film from sorbing large amounts of polar analytes. Furthermore, 1-propanol does not appear to condense on the film surface, resulting in consistent sensitivity patterns and response isotherm shapes for both chemiresistor and QCM data.

In contrast, GNP films incorporating ω -mercaptocarboxylic acids showed different sensitivity patterns for chemiresistors and QCM sensors. These films demonstrated overall higher mass uptake than those GNP films composed of hydrophobic organic matrices, particularly sorbing high amounts of toluene. However, despite the substantial mass uptake of toluene, this did not result in a substantial swelling of the organic matrix, since only small resistive response amplitudes were observed. Such deviations between chemiresistive and sorption characteristics have been observed in some previous studies as well. For example, a cross-linked GNP film prepared by Joseph et al. exhibited a high analyte uptake but showed almost no resistive response.[17] Similarly, in the case of GNP films prepared with MT ligands, Lu's group observed different response patterns when using them as chemiresistors or QCM sensors.[135] The reasons behind these differences may involve specific binding sites for different analytes, as described by Snow[177], or the distinct assembly structures of GNPs leading to chemically different regions with different ability to swell during analyte uptake.[135] Most likely, the polar analytes, water and 1-propanol, bind via

hydrogen-bonds to the sorption sites provided by the carboxylic acid groups of ω -mercaptocarboxylic acid ligands. Binding to these sites seems to cause a more effective swelling and, thereby, higher resistive responses than sorption of toluene to more hydrophobic moieties in the organic matrix.

Regarding the 95%3MPA-9DT films, their sorption isotherms extracted from QCM data exhibited a sensitivity pattern markedly different from the corresponding chemiresistive response isotherms. In the higher concentration range from 1000 ppm, the sensitivity order was toluene > 1-propanol \gg water (Figure 7.20c), whereas in the low concentration range between 50 to 1000 ppm, it shifted to 1-propanol \approx toluene \gg water (Figure 7.20h). However, the shape of the sorption isotherms remained consistent with a Langmuir-Henry type behavior, indicating a limited amount of sorption sites. In contrast, for the 95%8MOA-9DT GNP film-coated QCM, the sorption isotherms for both 1-propanol and water vapors closely resembled their chemiresistive response isotherms, showing a linear correlation over a range of up to 3000 ppm. With an even higher 8MOA fraction, the shape of the sorption isotherms of the 100%8MOA GNP film-coated QCM changed significantly for all three vapors compared to the shape of the corresponding chemiresistive response isotherms. Again, the sorption isotherm recorded with the corresponding QCM sensors revealed a similar mass uptake for 1-propanol and toluene (Figure 7.20e), despite the chemiresistor being much more sensitive to 1-propanol. This distinct performance between chemiresistive and sorption characteristics was even more significant in the high concentration range (> 500 ppm).

In conclusion, while GNP films prepared with hydrophobic 9DT linker and 12T ligand exhibited consistent sensitivity patterns in both chemiresistors and QCM sensors, those incorporating more hydrophilic ω -mercaptocarboxylic acids showed deviations between chemiresistive and sorption characteristics, particularly towards the toluene vapor. This discrepancy suggests that polar analytes such as 1-propanol likely bind to the carboxylic acid end groups, inducing effective swelling of the organic matrix, whereas nonpolar analytes such as toluene likely bind to regions where vapor-induced swelling is less pronounced.

In the in situ chemiresistor/QCM measurements, it became evident that the chemiresistive response characteristics of certain GNP films may differ from their sorption characteristics. Radar plots of sensor responses to toluene, 1-propanol, and water at a vapor concentration of 500 ppm (Figure 7.21) illustrate the tunable selectivities provided by ligand/linker mixtures and pure linkers. Notably, the response patterns of the chemiresistive sensors (Figure 7.21a-c) markedly differ from those of the corresponding QCM sensors (Figure 7.21d-f). Despite using only five types of GNP films, each analyte exhibits a unique response pattern, suggesting that these distinctive fingerprints could be utilized for vapor recognition. Multi-transducer sensors offer several advantages over single-transducer sensors in various applications. For instance, Lu's group combined chemiresistors and QCM sensors into an array, leading to improved accuracy in analyte identification compared to single-transducer setups.[135] Similarly, Zellers' group reported the capability of multi-transducer arrays for determining binary and ternary mixtures of VOCs, a task that single-transducer sensors cannot accomplish.[188–190] Therefore, further investigation into arrays composed of these dual-transducers is of great interest.

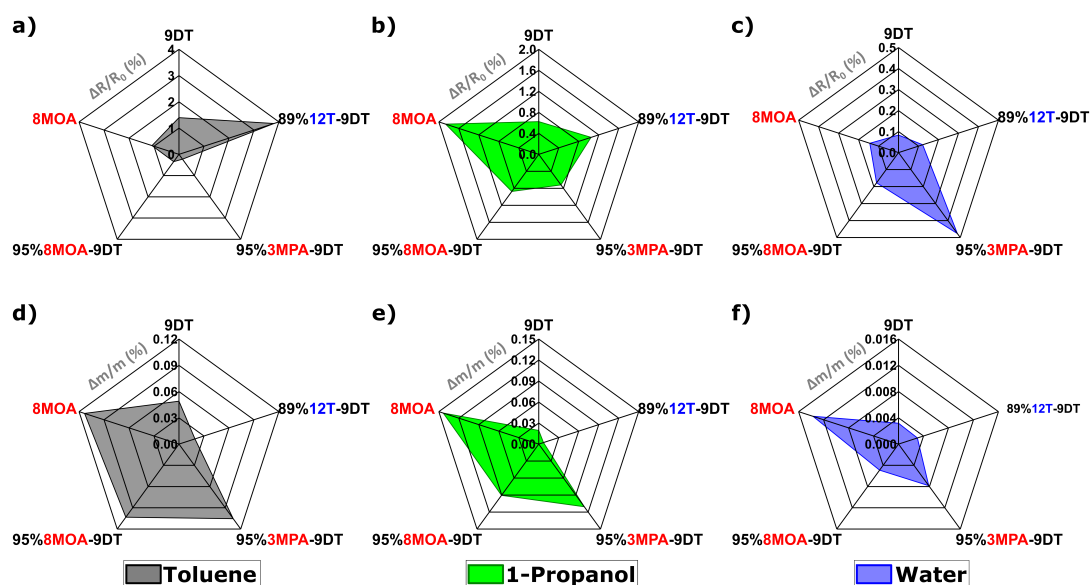


Figure 7.21: Radar plots of a)-c) chemiresistive response amplitudes and d)-e) relative mass uptakes extracted from QCM sensors. The results were obtained from in situ chemiresistor/QCM measurements. Five selected GNP films were exposed to three different vapors, toluene (black), 1-propanol (green), and water (blue), at 500 ppm in nitrogen.

7.3.5 Summary and Outlook

In this study, GNP films prepared with mixtures of ligand/linker molecules with tunable selectivity and high sensitivity were fabricated through a facile preparation process—the LbL-SC method, and the resulting films were systematically investigated. In situ GNP surface modifications were done during the LbL-SC deposition of partially cross-linked GNP films using mixtures of functionalized MT with 9DT. By utilizing hydrophobic alkyl- and hydrophilic carboxylic acid-functionalized MT ligands, we could easily adjust the chemical selectivity of the resulting films. Additionally, the 9DT linker molecules play a crucial role in cross-linking the GNPs and, thereby, enabling the LbL-SC method to accurately deposit uniform GNP films in a cost-effective manner.

The electrical and optical properties of studied GNP films are significantly influenced by the length and chemical nature of the MT ligands, as well as their mixing ratio with the 9DT linker. When comparing GNP films prepared with MT/9DT mixtures to those prepared with pure 9DT, a blue-shift in the LSPR band and a dramatic decrease in film conductivity are observed, particularly for the mixtures with longer MT ligands. The addition of hydrophobic AT ligands results in GNP films that selectively respond to nonpolar analytes. Especially when the AT ligands exceed the length of the 9DT molecule and at low 9DT fractions down to 11% or 5%, the sensitivity is significantly enhanced. GISAXS measurements suggest that the increasing interparticle distances in the films prepared with the long AT ligands primarily contribute to the blue-shift in the LSPR band and the decrease in film conductivity. Additionally, less cross-linked GNP films exhibit significantly enhanced chemiresistive sensitivity towards analyte vapors, and lead to a change in the shape of resistive response isotherms from Langmuir-Henry to Henry type. Furthermore, films consisting of hydrophobic organic matrices (e.g., the 9DT and 89%12T-9DT films) exhibit consistent sensitivity patterns when comparing their respective chemiresistors and QCM sensors, with similar characteristics of the response isotherms.

On the other hand, GNP films prepared with different ω -mercaptocarboxylic acids combined with the 9DT linker demonstrate similar trends in changes in film conductivity and optical properties with increasing length and fraction of the MT ligands. Unlike AT ligands, pure ω -mercaptocarboxylic acids without the addition of the 9DT linker are compatible with the LbL-SC film fabrication due to hydrogen bond formation via carboxylic acid groups of neighboring GNPs. Moreover, the hydrophilic carboxylic acid groups increase the polarity of the organic matrix, enhancing chemical selectivity towards more polar vapors with increasing MT fractions. Similar to the films prepared with long AT/9DT mixtures at high AT fractions, films consisting of high fraction of long ω -mercaptocarboxylic acids exhibit a change in the shape of response isotherms from Langmuir-Henry to Henry type. However, unlike the GNP films prepared with the hydrophobic AT/9DT mixtures, those comprising ω -mercaptocarboxylic acids show different sensitivity patterns of their chemiresistors and respective QCM sensors. Moreover, QCM data reveal that these films have overall higher analyte uptake, likely due to significant changes in the films' microstructure compared to the 9DT film and the presence of different regions for sorption of different analytes inducing effective or ineffective swelling of the organic matrix.

As multi-transducer arrays offer advantages over single-transducer arrays by providing more comprehensive and diverse information, future research could focus on developing an array that includes both GNP-based chemiresistors and QCM sensors. These arrays could be exposed to a broad variety of chemical vapors, with the selection of GNP films based on the findings discussed in this section. The responses from both transducers could then be fed into a classification algorithm, such as LDA, enabling the identification of different analyte vapors as well as binary or ternary mixtures of analyte vapors.

7.4 Gold Nanoparticle Films Composed of Mixed Organic Composites: Experimental Data vs. Simulation Data

The previous section highlighted the promising sensing capabilities of GNP films prepared with ligand/linker mixtures via the LbL-SC procedure. The fabricated GNP films with various organic composites exhibited tunable distinct optical and electrical properties. However, in Sections 7.3.2 and 7.3.3, the study was mainly focused on the preparation of only one film for each organic matrix composition to reveal the major trends as a function of the ligand/linker composition. So far, no additional experiments were conducted to assess the reproducibility of the results. Moreover, even though some films prepared with specific organic composites demonstrated outstanding sensing performance, the underlying mechanisms at the nanoscale—such as how the conformation of the ligand and linker molecules and the length of the added ligand molecules influence the sensor’s behavior—remained unidentified. Qualitatively, SEM data revealed that the order of the nanoparticle assembly increased when using a high molar fraction of long chained MT molecules (length longer than the 9DT molecule). Similarly, GISAXS measurements also suggested a general trend of increasing interparticle distance with increasing length of the added MTs. However, quantitative evidence is difficult to provide due to the limitations of experimental analysis techniques.

Molecular dynamics (MD) simulations can provide insights into detailed nanoscale properties, which are challenging to probe experimentally. MD simulations can model the interactions and motions of individual atoms and molecules, thus enabling researchers to understand structural and dynamic properties at the atomic level. Moreover, they offer the possibility to visualize the real-time dynamics of molecules. These detailed information is usually not available with experimental techniques due to limitations in resolution and sensitivity. Early studies reported by Luedtke and Landman presented simulation results of 3D GNP assemblies.[191, 192] Grest’s group carried out simulations of 2D non-cross-linked GNP assemblies, focusing on the stiffness of various GNP films. Their findings revealed that the stiffness of these films is significantly influenced by the terminal groups of the added ligands.[193, 194] Yeh et al. conducted MD simulations to investigate alkanedithiols cross-linked GNP assemblies to describe their exceptional mechanical properties.[42, 195] The simulation results were in good agreement with the experimental data and revealed estimations for the interparticle distances of GNPs, the ratio of cross-linking degree, and the conformations of the cross-linker molecules. Such important insights into molecules’ conformation and molecules’ interaction are very helpful for the design of GNP-based sensors.

To address the knowledge gap between the experimental results and the underlying mechanisms, such as charge transport and sensing properties, we conducted fundamental experiments in collaboration with Prof. Dr. Carmen Hermann’s group. Karen Schaefer (a PhD student in Prof. Dr. Carmen Hermann’s group, University of Hamburg) provided theoretical MD simulations to investigate the effects of different alkanethiol (AT) ligands with varying chain lengths and mixing ratios in combination with the 9DT cross-linker on the conformation of the ligand and linker molecules and interparticle distances within GNP assemblies. In this section, our group provided the results from laboratory experiments and K. Schaefer designed and conducted the MD simulations.

7.4.1 Molecular Dynamics Simulations

K. Schaefer used a MD program called LAMMPS[196]. A model of a sandwich structure was developed based on a recent publication by Schaefer et al. to emulate the non-cross-linked ligand and cross-linked linker molecules between two Au(111) surfaces, which consisted of three different regions, illustrated in Figure 7.22.[1] As shown in Figure 7.22, the top and bottom regions simulate the Au(111) surfaces of two neighboring GNPs, and the "mobile region" represents the organic matrix within GNP film. In addition, to avoid edge effects and artificially extend the size of the model system, periodic boundary conditions were applied to both of the x and y directions. A reactive force field (ReaxFF) was employed together with the parameters reported by Bae and Aikens[197] for Au-S-C-H systems. ReaxFF includes non-bonded and bonded interactions, and therefore enables to describe the ligand dissociation and association during MD simulations. In the simulations, the temperature was set to 300 K to mimic laboratory conditions.

In the sandwich structure depicted in Figure 7.22, a total of 8 molecules were positioned between the gold surfaces. Initially, all ligand and linker molecules were in an upright and all-trans conformation. Zero forces were assigned to atoms in the handle and fixed regions, with the velocities of atoms in the fixed region set to zero. Atoms in the mobile region were allowed to move freely. Throughout the simulations, atoms in the handle region exerted downward acceleration towards the bottom gold surface. The potential energy and the corresponding surface-to-surface distance were recorded. When the potential energy reached its minimum, the surface-to-surface distance was extracted and subsequently compared with the interparticle distances observed in experiments. Each ligand/linker mixture system underwent ten simulation iterations to obtain average values and standard deviations.

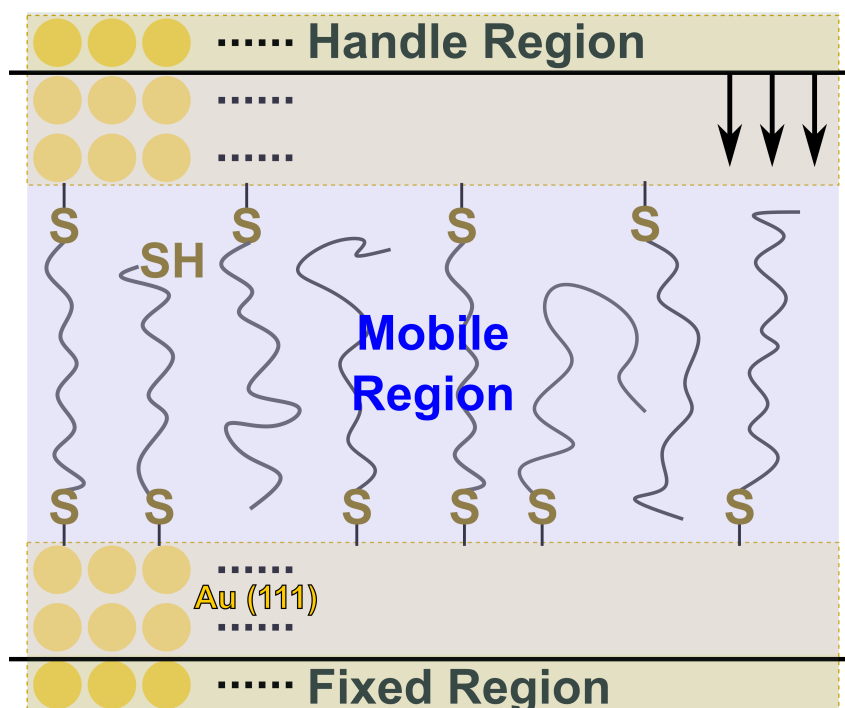


Figure 7.22: The sandwich structure model employed in MD simulations, outlining three distinct regions as indicated in the schematic representation. A total of eight ligand and linker molecules is situated between two gold surfaces. During the MD simulations, the handle region moves downwards towards the fixed region. The schematic design is inspired by the work of Schaefer et al.[1].

7.4.2 Fabrication of Gold Nanoparticle Films

GNP films were fabricated using batch GNP4 via the LbL-SC fabrication route described in Section 7.3.1. The LbL-SC method involved three to four deposition cycles to build up the GNP films. Film thickness of the resulting GNP films ranged from 20 to 35 nm, see Table A2 in the Appendix. Previous findings suggested that the shorter AT ligands (length shorter than the 9DT molecule) had negligible impact on the optical and electrical properties of the films, compared to the 9DT cross-linked GNP films. In contrast, longer AT ligands (length longer than the 9DT molecule) significantly influenced these properties of the resulting GNP films, with the extent of change increasing with higher AT fractions in the organic matrix. Herein, the AT ligands used in this study can be categorized into two groups based on their chain lengths relative to 9DT: i) 6T representing shorter ligand and ii) 11T and 12T representing longer ligands than the 9DT cross-linker (as listed in Table 7.3). In the previous section, most GNP films showed no or minor changes in their physical properties and chemiresistive responses when the AT molar fraction was applied at its lowest level (67%). However, when the AT molar fraction increased from 67% to 89%, drastic changes were observed. To obtain more insight into this transition and understand the role of added AT in altering the assembly order and microstructure of the films, different AT/9DT mixing ratios, where AT molar fractions were between 67% and 89%, were investigated using both experimental and MD simulation approaches.

Because the MD simulation model was designed to accommodate a total of eight molecules in the system, it was only possible to achieve mixing ratios of AT ligand to 9DT linker ranging from 7:1, 6:2, 5:3, to 4:4,

corresponding to AT molar fractions of 87.5%, 75%, 62.5%, and 50%, respectively. The highest molar fraction of AT used in this study was 87.5%, which is very close to the molar fraction of 89% used in Section 7.3. The films prepared with this AT molar fraction presented remarkable physical properties and sensing characteristics. For the experimental validation, four films were produced for each ligand/linker composition to ensure the data were reliable and representative. These films were characterized regarding their optical and electrical properties, as well as their chemiresistive responses to analyte vapor.

Table 7.3: Cross-linker and AT ligands used in this section, AT molar fractions for AT/9DT mixtures, and sensor notations.

Thiols	Alkanethiol Molar Fraction	Sensor
1,9-Nonanedithiol (9DT)	0%	9DT
	50%	50%6T-9DT
1-Hexanethiol (6T)	62.5%	62.5%6T-9DT
	75%	75%6T-9DT
	87.5%	87.5%6T-9DT
	50%	50%11T-9DT
1-Undecanethiol (11T)	62.5%	62.5%11T-9DT
	75%	75%11T-9DT
	87.5%	87.5%11T-9DT
	50%	50%12T-9DT
1-Dodecanethiol (12T)	62.5%	62.5%12T-9DT
	75%	75%12T-9DT
	87.5%	87.5%12T-9DT

7.4.3 Experimental Results

As outlined in Section 7.3.2, interparticle distance of GNP films can be roughly estimated through electrical measurement and UV/vis spectroscopy. To validate these findings, GISAXS measurements were conducted on the selected GNP films, providing further insights into relative changes in interparticle distance compared to those in the 9DT film. Additionally, SEM analysis was employed to examine the microstructures of these films at both microscale and nanoscale levels. Subsequently, the chemiresistive characteristics of the GNP films were evaluated under exposure to n-octane vapor at concentrations of 200 and 2000 ppm. Given the constraints of the MD simulations, which only accommodate single-bond and straight-chain molecules consisting of S, C, and H atoms, hydrophobic n-octane was chosen as the analyte vapor. This choice aligns with the composition of the GNP films' organic matrices, mainly consisting of hydrophobic AT ligand and 9DT linker molecules. Consequently, the chemiresistive response of the GNP films to this analyte is primarily governed by the swelling ability rather than polarity-based affinity differences.

Firstly, I-V measurements were conducted to examine the charge transport properties of the fabricated GNP films. All GNP films displayed linear behavior in their I-V characteristic curves in accordance with Ohm's law. The measured average conductivity of the fabricated 9DT cross-linked GNP films was comparable to that of the 9DT GNP film presented in Section 7.3.2, and fell within the same order of

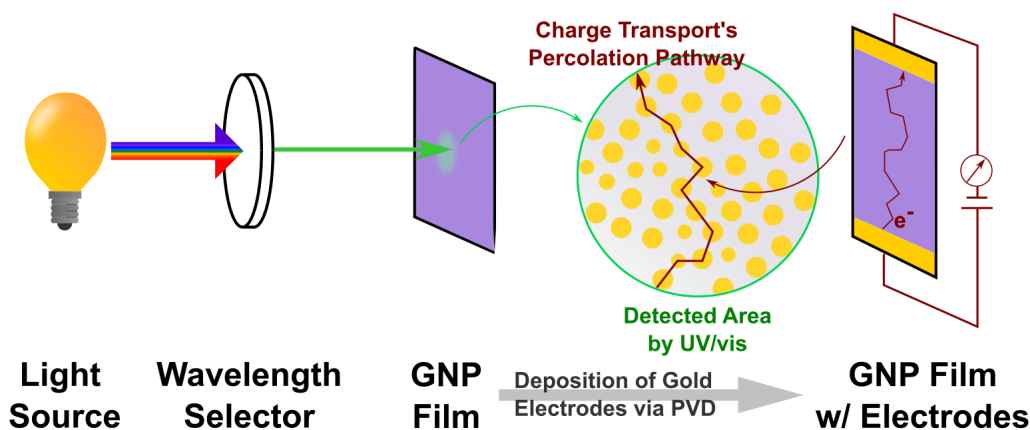


Figure 7.23: Schematic depicting the different estimates of interparticle distances obtained through electrical measurement (right) and UV/vis spectroscopy (left). The GNP films were fabricated using the LbL-SC procedure on a glass substrate and characterized by a UV/vis spectrophotometer at four different spots on the film. Subsequently, two gold electrode pads were deposited onto the same GNP film via physical vapor deposition (PVD), and its electrical conductivity was measured using a sourcemeter.

magnitude as the values reported in literature.[15, 119] Similarly, the resulting AT/9DT composite GNP films also exhibited conductivities similar to the values reported in Section 7.3.2. Despite the use of a different GNP batch, the electrical properties remained consistent.

The electrical conductivity of GNP films can be described by the tunneling and activation energy terms, as shown in Equation 5.3. In this section, it is important to note that all organic matrices used for the fabrication of GNP films comprised only hydrophobic molecules (9DT and ATs), resulting in minimal changes to the activation energy term. Consequently, variations in film conductivity were predominantly influenced by the tunneling distance between the nanoparticles. As discussed in Section 7.3.2, the conductivity exhibits an exponential decay with increasing interparticle distance. Figure 7.24 provides an overview of the conductivities obtained from all fabricated GNP films, indicating the trends of interparticle distances along the percolation pathway of charge transport (illustrated in Figure 7.23). Upon incorporating the shorter AT, 6T, into the GNP films, a gradual increase in film conductivity was observed. This increase correlated with the rising fraction of 6T. Compared with the 9DT cross-linked GNP film, the film conductivity doubled at 6T molar fractions of 75% and 87.5%, which indicates that the 6T molecules lead to a shorter average interparticle distance.

Pioneering works have reported the decay constant (β) of GNP assemblies consisting of ATs or alkanedithiols, typically falling within the range of 0.8 to 1.2 \AA^{-1} . [105, 106, 111] Assuming $\beta \sim 1 \text{ \AA}^{-1}$ and negligible difference in the activation energy of the different GNP films, the relative change in the interparticle distance ($\Delta\delta$) compared with that in the 9DT film can be estimated as follows:

$$\ln \frac{\sigma}{\sigma_{9DT}} \sim -\beta \cdot \Delta\delta \sim -1 \text{ \AA}^{-1} \cdot \Delta\delta \quad (7.2)$$

Here, σ represents the conductivity of the GNP film, compared to that of the 9DT film (σ_{9DT}). This equation facilitates the evaluation of changes in interparticle distance relative to the 9DT film. However, it is important to note that this value might be underestimated, as several factors, such as the effects of changes of the activation energy, different ligand conformations and packing densities, were not accounted

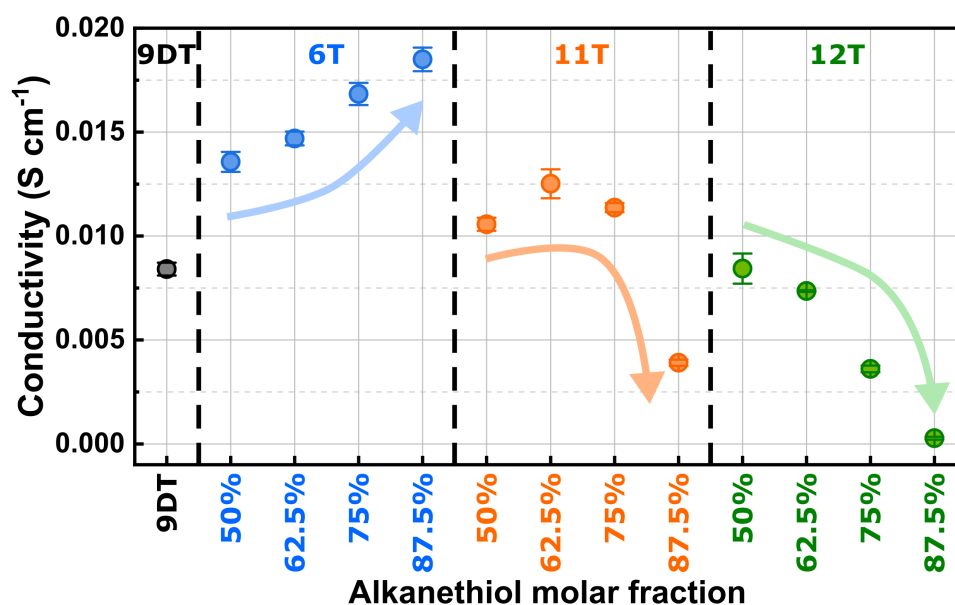


Figure 7.24: Room temperature conductivities of GNP films prepared with the pure 9DT linker and AT/9DT mixtures.

for. Additionally, the decay constant (β) could potentially be smaller due to these and other factors, such as variations in the electronic properties of the ligands or the presence of defects in the film. Nevertheless, compared to the 9DT film, the 87.5%6T-9DT film showed a relative decrease in interparticle distance of ~ 0.8 Å.

When applying the longer AT (11T) ligand at lower molar fractions (50%, 62.5% and 75%), the resulting GNP films exhibited the conductivity similar to the 9DT film. However, in the case of the 87.5%11T-9DT film, the conductivity decreased by approximately 50% compared to the 9DT film. According to Equation 7.2, the 87.5%11T-9DT film should possess an average interparticle distance roughly 0.8 Å longer than the 9DT film. Further, with the addition of an even longer AT (12T) ligand, the conductivity of the resulting films exhibited a progressively decreasing trend. A pronounced decrease in conductivity was observed for GNP films prepared with the mixtures of 12T/9DT at a 12T molar fraction of 75%, resulting in approximately a 50% reduction in the film's conductivity. At a even higher 12T molar fraction of 87.5%, the film's conductivity decreased by a factor of 30. Again, based on Equation 7.2, the average interparticle distance in this film is estimated to increase by 3.4 Å relative to that in the 9DT film.

In addition to electrical measurements, UV/vis spectroscopy provides valuable insights into the properties of GNP assemblies, as illustrated in Figure 7.23. The UV/vis absorbance spectra of all GNP films are shown in Figure A27 in the Appendix. Given that the organic matrices of GNP films possess comparable dielectric constants, the spectral position of the localized surface plasmon resonance (LSPR) band strongly correlates with the interparticle distance. As the interparticle distance increases, the coupling between the plasmonic fields of neighboring nanoparticles decreases. Consequently, less energy is transferred between the nanoparticles, resulting in a shift of the LSPR band towards shorter wavelengths (blueshift). It is worth emphasizing that the observed trend of interparticle distance obtained from UV/vis data represents the average value across the detected spot of the spectrometer (depicted in Figure 7.23).

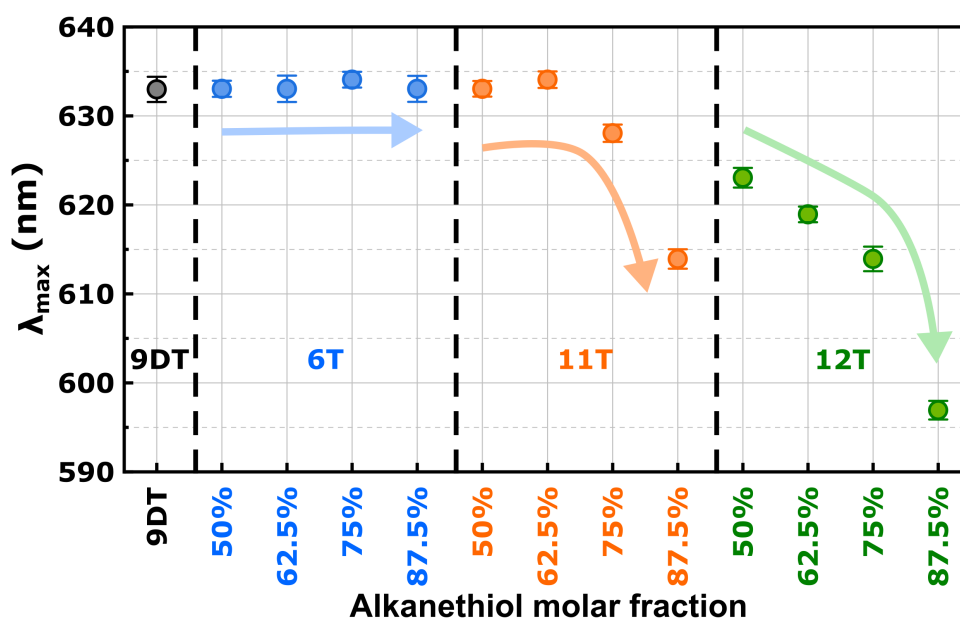


Figure 7.25: Spectral positions of the LSPR band of GNP films prepared with the pure 9DT linker and the mixtures of AT/9DT.

Figure 7.25 presents the spectral positions of the LSPR bands (λ_{\max}) of the fabricated GNP films. When using the mixtures of 6T/9DT, the LSPR bands of the resulting GNP films remained at the same spectral position as the 9DT film, indicating nearly no changes in the average interparticle distance between adjacent GNPs within the sampled spot size area. Similarly, when mixing the 11T ligand with the 9DT linker, at lower 11T fractions of 50% and 62.5%, λ_{\max} remained unchanged. However, at a higher 11T fraction of 75%, a slight blueshift in the LSPR band occurred, suggesting a subtle increase in the interparticle distance. A more pronounced blueshift was observed at a molar fraction of 87.5% for 11T, where the LSPR band blue-shifted by 20 nm, indicating a considerable increase in the interparticle distance. When using the longest ligand, 12T, in combination with 9DT, the resulting GNP film exhibited a blueshift even at a very low 12T fraction of 50%. For the GNP films prepared with mixtures of 12T/9DT, the extent of the LSPR band's blueshift gradually increased with an increasing 12T fraction. The LSPR bands shifted to shorter wavelengths, ranging from approximately 10 nm (12T molar fraction of 50%) to approximately 40 nm (12T molar fraction of 87.5%), indicating a progressive increase in the interparticle distance.

Both electrical and UV/vis measurements consistently demonstrate an increasing trend in interparticle distance with higher AT fractions for the mixtures of 11T/9DT and 12T/9DT in the GNP films. The slight discrepancy between the conductivity and UV/vis data for films prepared with the 6T/9DT mixtures may be attributed to the different experimental methods. Electrical measurements focus specifically on the total tunneling distances along the charge transport pathway, while UV/vis data offer a comprehensive view of the average interparticle distance across the entire GNP film within the sampled spot size (as illustrated in Figure 7.23). In the case of films prepared with the 6T/9DT mixtures, the improved charge transport is attributed to shorter tunneling distances along the percolation paths, while the average interparticle distance, observed by UV/vis measurements, may remain rather unchanged. On the other hand, the films prepared with a 50% molar fraction of 12T exhibited a noticeable shift in the LSPR band

position, yet displayed comparable conductivity to that of the 9DT film.

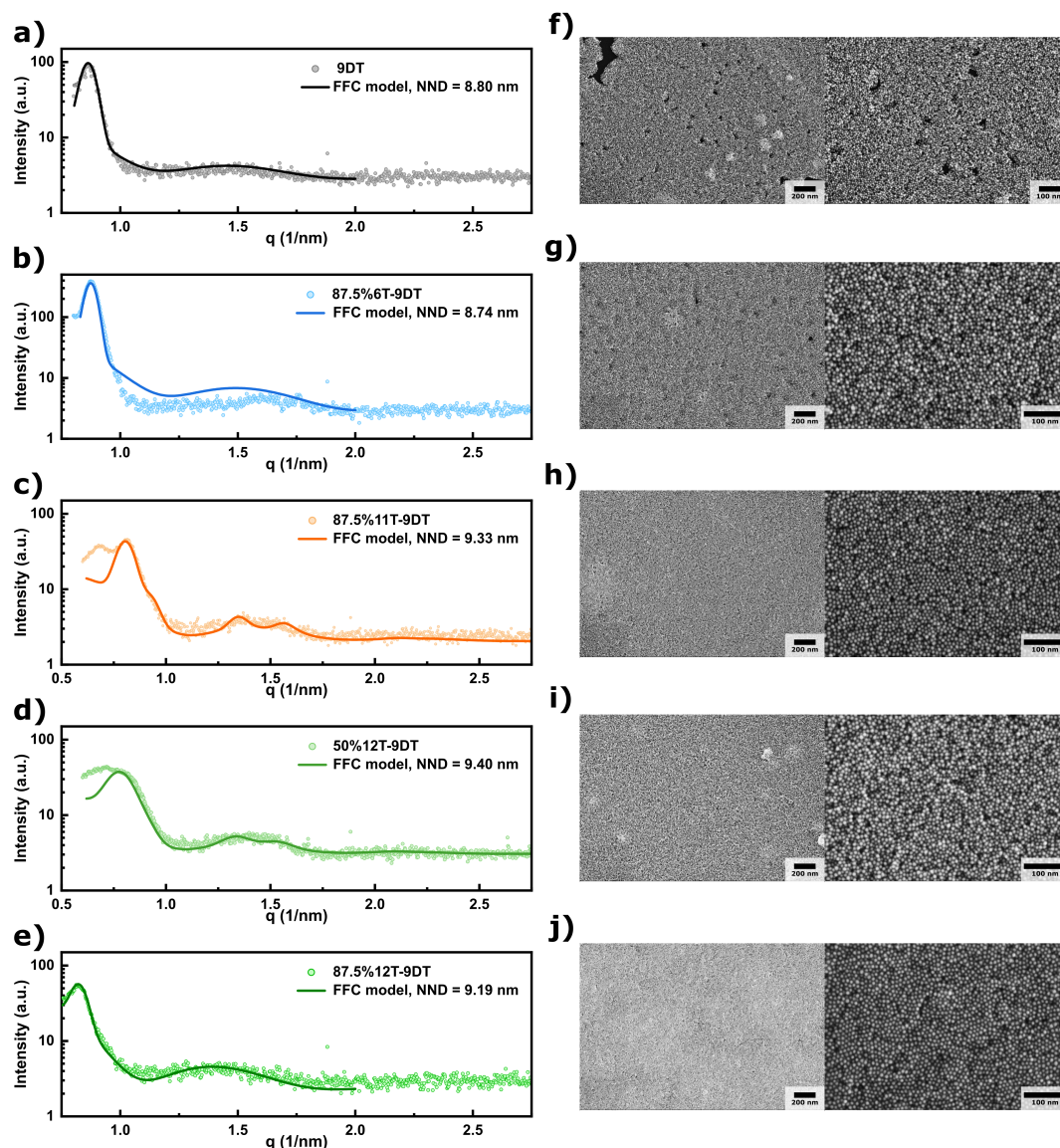


Figure 7.26: GISAXS intensity profiles of GNPs in thin films prepared with a) the 9DT and the mixtures of b) 87.5% 6T/9DT, c) 87.5% 11T/9DT, d) 50% 12T/9DT, and e) 87.5% 12T/9DT. Average nearest neighbor distances (NNDs) were computed from fits (solid lines) of an FCC model to the data. f)-j) SEM images of the GNP films prepared with the pure 9DT and the mixtures of 87.5% 6T/9DT, 87.5% 11T/9DT, 50% 12T/9DT, and 87.5% 12T/9DT, respectively. The left and right images have scale bars of 200 and 100 nm, respectively.

Given the slight divergence between the electrical and optical measurements, GISAXS measurements were conducted using five selected GNP films for further investigations. Figure 7.26a-e shows the intensity profiles of selected samples derived from the downward sections of the scattering patterns, with specular reflections not taken into account (cf. Figure 7.13a). The derived volume scatter signatures were attributed to the model of a 3D face-centered-cubic (FCC) lattice, and the average center-to-center nearest neighbor distance (NND) of the GNPs was calculated using the software Scatter.[162, 163] Qualitatively, the NNDs extracted from the GISAXS measurements were in good agreement with the conductivity and UV/vis data. It is worth noting that measurements of the 9DT, 87.5%6T-9DT, and 87.5%12T-9DT films

were performed on the same day, while those for the 87.5%11T-9DT and 50%12T-9DT GNP films were conducted on a different day. Therefore, minor variations in sample alignment between different experimental runs may have contributed to slight deviations in the determined average NND values. Moreover, assumptions such as uniform GNP size and the formation of an FCC superlattice structure may introduce errors into the GISAXS analysis.

From the GISAXS data, the average interparticle distance of the 87.5%6T-9DT film (extracted NND values shown in Figure 7.26, NND: ~ 8.74 nm) was found to be similar to or slightly smaller than that in the 9DT film (NND: ~ 8.80 nm). Even at the highest fraction of 6T, only a relative decrease of ~ 0.6 Å compared to the 9DT film was observed. This change in the relative interparticle distance is fairly comparable to that estimated by Equation 7.2. These minimal changes in the interparticle distance may explain why the UV/vis data showed nearly no shifts in the LSPR band's position, while the film conductivity data exhibited higher sensitivity to distance changes. In contrast, for the 87.5%12T-9DT film (NND: ~ 9.19 nm), a relative increase in interparticle distance of 3.9 Å compared to the 9DT film was measured by GISAXS, again aligning closely with the value estimated by conductivity data using Equation 7.2. The average edge-to-edge interparticle distances were calculated by subtracting the average GNP size determined by TEM (average core diameter of GNPs: ~ 7.48 nm, cf. Figure 7.1) from the GISAXS-measured average NND values. The GISAXS measurements demonstrated average edge-to-edge interparticle distances of ~ 1.32 nm, ~ 1.26 nm, and ~ 1.71 nm in the 9DT, 87.5%6T-9DT, and 87.5%12T-9DT films, respectively. These results are consistent with the values of ~ 1.2 nm, ~ 0.9 nm, and ~ 1.9 nm provided in Section 7.3.2 for the 9DT, 95%6T-9DT, and 89%12T-9DT films.

On the other hand, the 87.5%11-9DT (NND: ~ 9.33 nm and edge-to-edge interparticle distance: ~ 1.85 nm) and 50%12T-9DT (NND: ~ 9.40 nm, and edge-to-edge interparticle distance: ~ 1.92 nm) films, measured on a different day, both show significantly larger NNDs compared to the 9DT film. The average NND of the 50%12T-9DT film estimated by GISAXS measurements is slightly higher than that of the 87.5%12T-9DT film. However, both electrical and UV/vis data suggest a greater average interparticle distance for the 87.5%12T-9DT film. This disparity may be attributed to the different sample alignment discussed earlier, resulting in a deviation of the NND value and consequently an overall higher estimate of NNDs for the 87.5%11-9DT and 50%12T-9DT films. Nevertheless, an obvious trend emerged: shorter AT ligands led to a decrease in the interparticle distance, while longer AT ligands led to an increase in the interparticle distance.

Moreover, the orders of GNP assemblies can also be roughly inferred from the GISAXS data. The selected five GNP films exhibited disordered arrangements of GNPs, with the entire films believed to be composed of numerous small ordered domains. Among them, the 87.5%12T-9DT film has the highest degree of assembly order. The peak at ~ 0.75 nm $^{-1}$ (see Figure 7.26e) appeared to be relatively well-defined and sharper compared to the peaks observed in the other films, indicating better long-range order in the GNP assembly. This observation was confirmed by the SEM image (Figure 7.26j). In contrast, the GISAXS intensity profile of the 9DT film (Figure 7.26a) exhibited a broader and lower intensity peak, suggesting that the film had moderate assembly order and some short-range arrangement. The SEM images showed that the 9DT film displayed the most defective assembly of GNPs (see Figure 7.26f), with unevenly distributed GNPs, leaving voids, and some GNPs aggregated on the surface. The addition of the AT ligand molecules mitigated these defects, with films prepared with the mixtures of 87.5% 11T/9DT

and 87.5% 12T/9DT exhibiting many well-ordered regions (cf. Figure 7.26h and j).

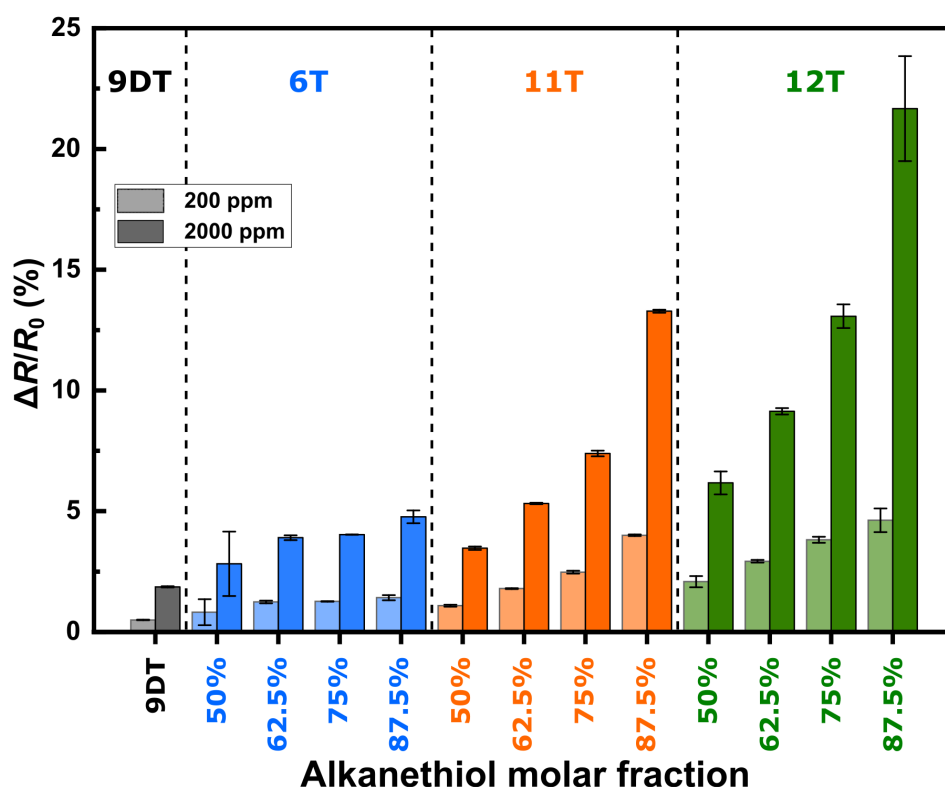


Figure 7.27: Average resistive response amplitudes of GNP films prepared with pure 9DT and the AT/9DT mixtures when exposed to n-octane vapor. Light-colored bars represent exposure to 200 ppm vapor, while dark-colored bars represent exposure to 2000 ppm vapor. Error bars indicate standard deviations of the response amplitudes of four GNP films.

All GNP films used in this project consisted of organic matrices with similar permittivity. Therefore, when exposed to vapors of n-octane, which has a similar permittivity as the organic matrices, differences in the sensitivity resulted mainly from differences in the swelling ability, corresponding to the degree of cross-linking within the film. Chemiresistor measurements were conducted at analyte concentrations of 200 and 2000 ppm. The average chemiresistive response amplitudes of all GNP films are presented in Figure 7.27, and their respective transient responses are presented in Figure A28 in the Appendix. A clear trend was observed in all GNP films prepared with the AT/9DT mixtures. As the fraction of 9DT linker molecules decreased, it is expected that the cross-linking degree of the resulting film also decreased. Consequently, as the film became more flexible, the swelling ability increased, leading to enhanced response amplitudes. Based on the conductivity, UV/vis, and GISAXS data, incorporating the 6T ligand shortened the interparticle distance. It is conceivable that due to the small size of the 6T ligands, the 9DT cross-linked GNP network remained intact to large extent, and therefore, no significant enhancement of the response amplitudes was observed. However, the cross-linking degree within the organic matrix was gradually reduced with increasing 6T fraction, as indicated by the slightly increasing response amplitudes. Conversely, when using longer AT ligands (11T and 12T), these ligands disrupted the 9DT cross-linked network more efficiently, resulting in a significant enhancement of response amplitudes. As the 12T ligand molecules are somewhat longer than 11T molecules, it is expected that an increase in the film's flexibility already occurred at a lower AT fraction. Therefore, with such long AT (12T), the

9DT's cross-linked network is most efficiently disrupted and, hence, the chemiresistors prepared with the 12T/9DT mixtures showed the highest response amplitudes at comparable AT fractions.

To summarize the results obtained from the conductivity, UV/vis, GISAXS, SEM, and chemiresistor measurements, a comprehensive understanding of the interparticle distance in the GNP films was achieved. The addition of AT ligands altered the interparticle distance and microstructure of the films, along with the cross-linking degree. Moreover, Van-der-Waals interactions between the interdigitated AT's alkyl chains improved the resulting films' quality with a higher assembly order. The short AT ligand may provide more free space, allowing the 9DT linkers easily cross-link neighboring GNPs. Consequently, adding the short AT ligand resulted in a slightly shorter interparticle distance, while the organic matrix remained mainly established by a cross-linked network. On the other hand, mixing the long AT ligands with the 9DT linker led to greater interparticle distances. The extent of the increase in the interparticle distance was found to depend significantly on the fraction of the long AT ligands. Previous findings demonstrated that a pure 12T ligand stabilized GNP film possessed approximately 1.8-2.3 nm spacing between neighboring GNPs[10, 14], which is similar to the interparticle distances of the 50%12T-9DT and 87.5%12T-9DT films determined by GISAXS in this project. Moreover, such large interparticle distance within films prepared with the long AT/9DT mixtures (87.5%11T-9DT, 50%12T-9DT, and 87.5%12T-9DT) exceeded the length of a fully extended 9DT molecule (~ 1.5 nm), suggesting that the cross-linkages cannot be formed under these circumstances. However, from the previous preliminary experiments regarding the LbL-SC fabrication of the GNP films (as described in Section 7.3.1), it is clear that without adding the 9DT cross-linkers, the GNPs could not be deposited in a layer-by-layer approach. In contrast, the LbL-SC deposition of films was feasible by using the AT/9DT mixtures. Hence, it is obvious that GNP cross-linking via 9DT molecules happened to some degree. Therefore, to explain the conditions mentioned above, the presence of two different domains within organic matrix of the film is proposed (as schematically depicted in Figure 7.28): a domain with a larger average interparticle distance established mainly by the long AT ligands (as "long AT controlled" domain), and a domain with a smaller average interparticle distance established mainly by the 9DT cross-linkers (as "9DT controlled" domain). The higher fraction of long AT ligands likely leads to a more frequent occurrence of "long AT controlled" domains, consequently resulting in larger average interparticle distances and increased flexibility of the resulting GNP films with more pronounced ability to swell during analyte sorption.

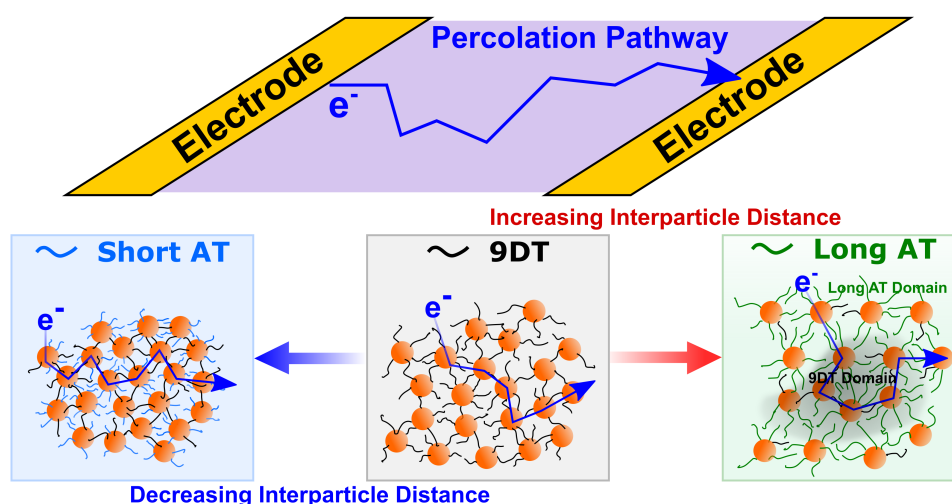


Figure 7.28: Schematic illustration of percolation pathways through GNP films consisting of different organic matrix compositions. When employing short AT ligands (blue panel), the cross-linked network within the film remains intact, leading to a decrease in the average interparticle distance compared to the 9DT film (grey panel). Conversely, when employing long AT ligands (green panel), two distinct domains emerge within the film: "long AT controlled" and "9DT controlled" domains. Electrons have to travel through both domains, contributing to the conductivity of the film.

7.4.4 Molecular Dynamics Simulation Results

In the preliminary simulations, we employed the sandwich structure depicted in Figure 7.22, involving a total of eight molecules. For the system with pure 9DT molecules, all eight 9DT molecules were initially bound to both the top and bottom gold surfaces, resulting in a 100% ligand coverage on the gold surface. In contrast, in the systems with pure AT ligands and mixtures of AT/9DT, initially, four molecules were attached to the top planar gold surface, while the remaining four were affixed to the bottom surface. Additionally, all molecules were bound to only one side of the gold surface, corresponding to a 50% ligand coverage. As the handle moved downwards towards the bottom surface, the potential energy of the system reached its minimum, which we referred to as the "lower-energy state" of the system. The surface-to-surface distance at this "lower-energy state" was derived as the preferred spacing of the Au-organic matrix-Au system, resembling the "interparticle distance" in GNP assemblies. To ensure robustness, all simulations were repeated ten times to obtain average values with standard deviations.

Figure 7.29 presents the "interparticle distance" extracted from the MD simulations. Remarkably, the trends observed in the simulations closely align with the experimental data. When employing short AT molecules like 6T in the system, the interparticle distance was smaller compared to the system with only the 9DT linkers. Increasing the molar fraction of 6T led to a gradual decrease in the interparticle distance. In contrast, the addition of long AT molecules, such as 11T and 12T, resulted in larger interparticle distances compared to the system with only the 9DT linkers. As the molar fraction of these longer AT molecules increased, the interparticle distance also slightly increased. However, the dependence on the AT fraction was less pronounced for the longer AT molecules (11T and 12T) compared to systems with shorter AT ligands (6T).

An average interparticle distance of ~ 12 Å was estimated from the MD simulations of the system with

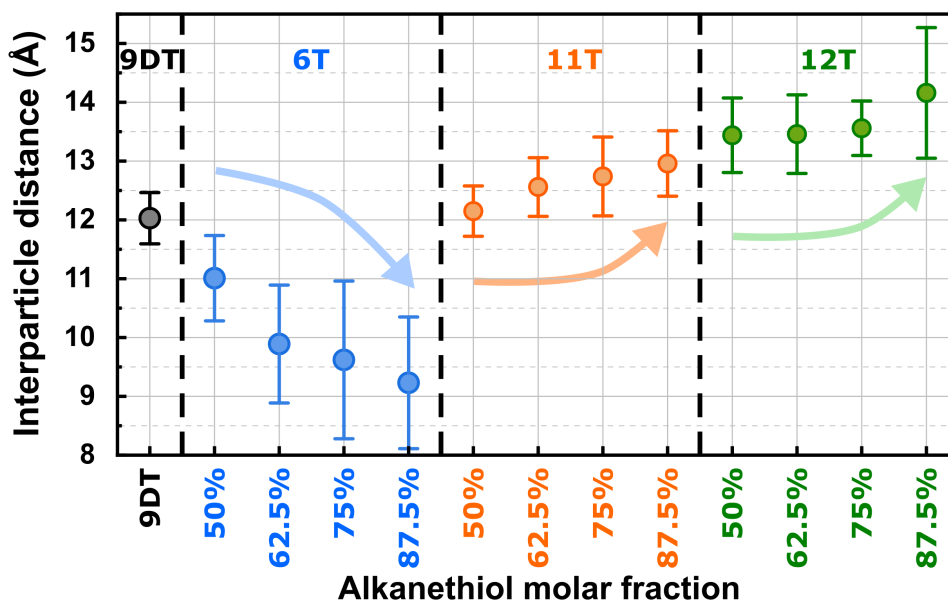


Figure 7.29: MD simulation results showing the average interparticle distances involving eight molecules of either pure 9DT or AT/9DT mixtures within the sandwich structure. The AT molar fraction is indicated on the x-axis. The average interparticle distances were obtained from 10 repeated MD simulations, with corresponding standard deviations shown as error bars.

pure 9DT molecules, which is in good agreement with the values determined by GISAXS measurements (~ 12 Å for the 9DT film prepared with batch GNP4 shown in Section 7.4.3 and ~ 13.2 Å for the 9DT film prepared with batch GNP3 shown in Section 7.3.2). However, for systems using mixtures of AT/9DT, the interparticle distances determined by the simulation model were significantly underestimated. A similar observation was reported in a recent simulation study, where the pure 6T-, 11T-, 12T-ligands systems gave interparticle distances of 7.47 ± 0.40 , 12.82 ± 0.97 , and 13.98 ± 0.67 Å, respectively.[1] In comparison, experimental data for assemblies comprised of 12T-stabilized GNPs provided average interparticle distances ranging from 18 to 23 Å.[10, 14] Bain et al. reported an empirical formula to calculate the length (L) of a fully extended AT molecule, expressed as $L(\text{Å}) = 2.5 + 1.27n$, where n represents the number of carbons in the alkyl chain.[198–200] Motte and Pileni[200] studied assemblies of silver sulfide nanoparticles stabilized with ATs of different lengths. When using the 12T ligands, the interparticle distance was approximately 17 Å, similar to the length of one 12T molecule. A similarity in the behavior of Au(111) and $\text{Ag}_2\text{S}(111)$ surfaces was reported, hence an average interparticle distance between 12T-stabilized GNPs was expected to be $\gtrsim 17$ Å. Recent studies suggest that the underestimation of nanoparticle distances in simulations can be attributed to an underestimated ligand coverage on the surface.[1, 198] Schaefer et al. reported an increase in the surface-to-surface spacing of 2.3 Å per 10% increase in thiol coverage.[1] However, the optimal coverage of the two opposite Au(111) surfaces with ligands and linker molecules is still under investigation.

Some preliminary simulations have been conducted to investigate the influence of ligand coverage on the interparticle distance. The interparticle distances in assemblies of gold nanocrystals (or GNPs) prepared using 12T ligands have been reported in earlier publications.[10, 14, 201] We compared these literature values with simulation results. Figure 7.30 presents the average interparticle distances obtained from MD simulations of systems with eight to sixteen 12T molecules (50 to 100% ligand coverage), demonstrating

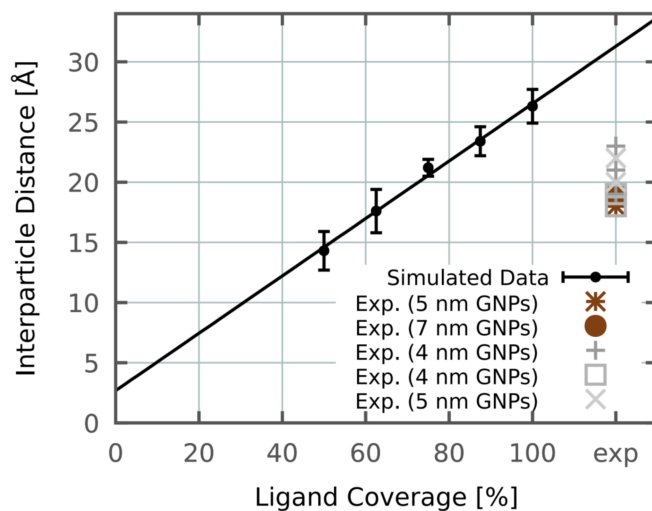


Figure 7.30: Average interparticle distances (black dots) extracted from the MD simulations of the systems with pure 12T ligands and varying ligand coverages on the gold surface. Error bars represent standard deviations from ten MD simulation runs. The average interparticle distances extracted from each system are fitted with a linear function (solid black line). Experimental data are also included: brown stars and dots represent supercrystals prepared using two different sizes of gold nanocrystals[10]; grey pluses and squares represent superlattices prepared by Olichwer et al. using two different batches of colloidal GNPs with similar average core diameters[14]; grey crosses represent the superlattice prepared using GNP colloid with an average diameter of approximately 5 nm[201].

that the estimated interparticle distances strongly depends on the ligand coverage on the gold surface. At a ligand coverage of 75%, the obtained interparticle distance was approximately 21 Å, which aligns well with the experimental values reported in the literature.[10, 14, 201] In comparison to the GNP films with a higher 12T fraction (87.5%12T-9DT film) discussed in Section 7.4.3, this value is slightly larger than the interparticle distance determined by the GISAXS measurement (17.1 Å). Nevertheless, our simulations suggest a ligand coverage of ~75% in the experimentally studied GNP assemblies. In our simulations, this corresponds to six ligands on each side of the gold surface, totaling twelve ligands in the simulation for systems with pure AT molecules or mixtures of AT/9DT molecules. The results for the systems with pure 6T and 11T ligands are shown in Figures A30 and A31 in the Appendix, revealing interparticle distances of approximately 14 Å and 20 Å, respectively, at a ligand coverage of 75% on the gold surface. These values are comparable to, but slightly higher than, the interparticle distances determined by the GISAXS measurements for the GNP films prepared with high fractions of 6T and 11T ligands, which were 12.6 Å and 18.5 Å for the 87.5%6T-9DT and 87.5%11T-9DT films, respectively.

In conclusion, the simulation data qualitatively mirrored the results obtained from the experimental measurements. Figure 7.31 shows snapshots of MD simulations of the systems at "lowest-energy structures" with mixtures of AT/9DT (systems with pure 9DT and 12T molecules are shown in Figure A29 in the Appendix). Consistent with the experimental findings, systems comprised of 6T/9DT mixtures maintained cross-linkages (see Figure 7.31a), and an increase in the 6T fraction on the GNP surface resulted in more free space for 9DT to form a cross-linked network, leading to a shorter interparticle distance. It is worth noting that while the ligand coverage on the gold surface was likely underestimated, resulting in a significant deviation in the interparticle distance values obtained from MD simulations, the overall trends in changes in interparticle distances are still discernible. When using eight 6T ligands in the simulation

system, an average interparticle distance of approximately 7.47 Å[1] was obtained, which differs significantly from the values obtained from systems using both 6T and 9DT molecules (9-11 Å). This suggests that the 6T ligand/9DT linker system behaves differently from the pure 6T ligands system. Conversely, when using long AT ligands such as 12T, the simulation system with 87.5% molar fraction of 12T ligands showed a similar spacing (~ 14.15 Å) to that of the pure 12T system (~ 13.98 Å[1]). Similarly, the system containing 11T ligands also showed an interparticle distance (approximately 12.96 Å for 87.5%11T-9DT) comparable to that of the pure 11T system (approximately 12.82 Å[1]). For long ATs 11T and 12T, these ligands dominate the spacing between neighboring GNPs, while the 9DT linker molecules barely form cross-linkages during the simulation runs (cf. Figure 7.31b and c). For systems containing an 87.5% molar fraction of 11T or 12T molecules, the distance between the two gold surfaces was too large for the 9DT molecule to bind to both sides, resulting in binding to only one surface. These findings from MD simulations indirectly confirm the high possibility of the presence of two different domains. This "two-domain" hypothesis was suggested earlier in the discussion of the experimental results. Moreover, in the simulation system containing AT ligands, the interparticle distances obtained at 50% ligand coverage tend to be underestimated compared to the experimental values. In contrast, when the ligand coverage is 75%, the interparticle distances obtained by MD simulations are closer to the experimental results.

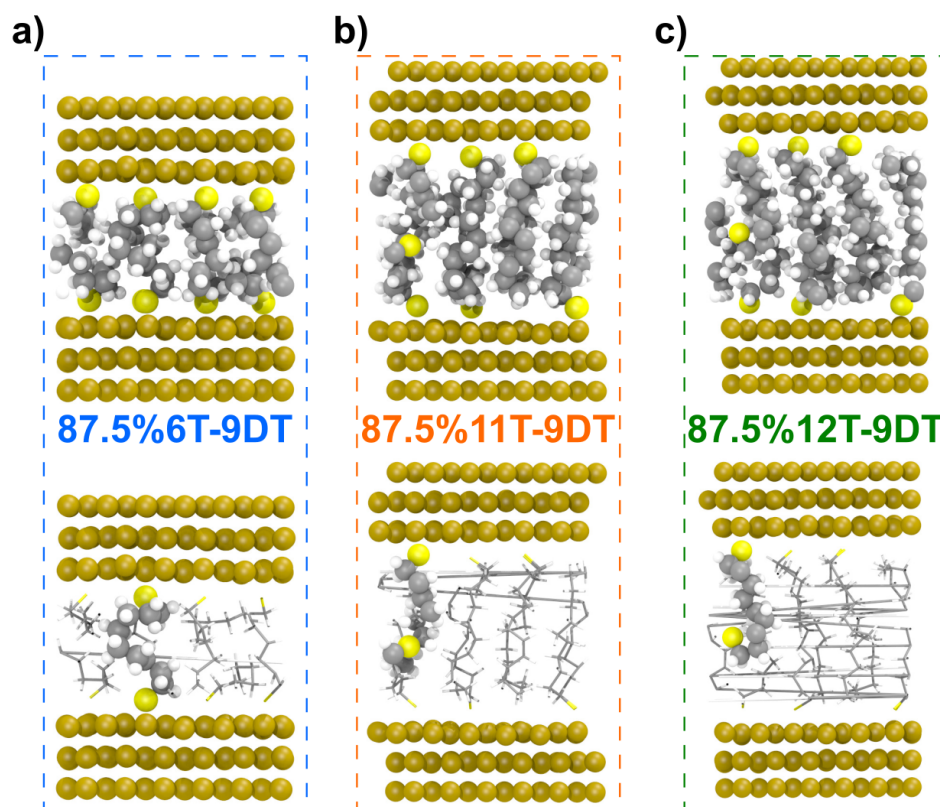


Figure 7.31: Snapshots of MD simulations of the systems at "lowest-energy structures", with 50% coverage of the surface by ligand/linker molecules include: a) seven 6T ligands and one 9DT linker, representing the 87.5%6T-9DT GNP film, b) seven 11T ligands and one 9DT linker, representing the 87.5%11T-9DT GNP film, and c) seven 12T ligands and one 9DT linker, representing the 87.5%12T-9DT GNP film. In the top part of each snapshot, all molecules are displayed using the ball-and-stick model, showing both atoms and bonds. In the bottom part, the alkanethiol (AT) ligands are displayed in stick model, while the 9DT molecule is represented in the same manner as in the top snapshots.

According to the "two-domain" hypothesis, a linear combination model can describe the interparticle

distance (D) using weighting factors A and B , ideally reflecting the relative molar fraction of 9DT and long AT ligands, respectively. Here, D_{9DT} and D_{longAT} represent the surface-to-surface spacing obtained from simulations of the pure 9DT (a ligand coverage of 100% in the MD simulation system) and pure long AT (a ligand coverage of 75% in the MD simulation system) systems, respectively.

$$D = A \cdot D_{9DT} + B \cdot D_{longAT} \quad (7.3)$$

Schaefer et al. reported an average interparticle distance of 1.2 nm from MD simulations of the system containing pure 9DT molecules (with ligand coverage of 100%).^[1] Preliminary simulations of the systems with pure 11T and 12T ligands, discussed above, yielded interparticle distances of 1.85 nm and 2.1 nm, respectively (with ligand coverage of 75%). Using Equation 7.3, the calculated interparticle distances for the simulated systems containing 87.5% molar fractions of 11T and 12T ligands were 1.77 nm and 1.99 nm, respectively. These values are very close to the interparticle distances determined from GISAXS measurements, which were 1.85 nm and 1.71 nm for the 87.5%11T-9DT and 87.5%12T-9DT films, respectively. This equation enables a more accurate representation of the interparticle distance averaged across the two domains in mixed long l ligand/linker systems.

7.4.5 Summary and Outlook

The experimental investigations, including electrical measurements, UV/Vis spectroscopy, GISAXS analysis, chemiresistor measurements, and SEM analysis, provided valuable insights into the influence of differently long AT ligands and AT/9DT mixing ratios on the properties of the resulting GNP films. Electrical measurements revealed that the conductivity is affected by the type and fraction of AT ligands, with shorter ligands (length shorter than the 9DT molecule) leading to higher conductivity due to shorter tunneling distances. UV/Vis spectroscopy showed minimal shifts in the LSPR band position, indicating only small changes in interparticle distance. Long AT ligands (length longer than the 9DT molecule), however, lead to a significant decrease in the charge transport, indicating longer interparticle distances, which is confirmed by pronounced blueshifts in the UV/vis data. As shown by GISAXS data, trends in interparticle distance changes are consistent with the electrical and UV/Vis data. Besides changes in interparticle distances, chemiresistor measurements highlight changes in the swelling ability of different organic matrices. Films prepared with longer AT ligands (11T and 12T) are more flexible as they have a lower degree of GNP cross-linking via 9DT molecules. Hence, they show significantly stronger chemiresistive responses, due to a pronounced ability to swell during analyte sorption.

The MD simulations further support these experimental findings, showing the trends in interparticle distance consistent with changes in ligand type and fraction. Short ligands (e.g., 6T) lead to shorter interparticle distances, while long ligands (e.g., 11T and 12T) result in larger distances. However, the simulation results indicate that the interparticle distance of systems containing the 6T ligand strongly depends on the AT molar fraction, whereas the dependence on AT fraction is weaker for systems containing long AT ligands. Moreover, the estimated interparticle distances obtained from systems with the 11T/9DT and 12T/9DT mixtures are comparable to the values determined from the systems with the pure 11T and 12T ligands, respectively (systems with ligand coverage of 50%). During MD simulations,

cross-linkage formation by the 9DT linker was still observed even at the lowest 9DT molar fraction of 12.5% in systems containing mixtures of 6T and 9DT molecules. However, in systems consisting of long AT ligands (11T or 12T), the 9DT molecules could not cross-link both sides of the gold surfaces. Consequently, it is believed that in long AT/9DT systems, the long AT may predominate the spacing between particles. This observation indirectly confirms the formation of two distinct domains within the organic matrix, dominated by long AT ligands and 9DT linkers.

Overall, the combined experimental and computational approach provides a comprehensive understanding of how the type and fraction of AT ligands influence the cross-linking degree, microstructure and properties of GNP films. These findings offer valuable insights for the design and optimization of GNP-based materials for various applications, including sensors.

As the interparticle distances determined by the MD simulations were significantly underestimated due to low ligand coverage of the Au surfaces, a more comprehensive investigation should be conducted, and re-analysis of the surface-to-surface spacing will be crucial to obtain more accurate results. In the preliminary experiments, an optimized ligand coverage of 75% on the gold surface for the pure AT ligand systems was found. Future research should focus on recalculating the interparticle distance based on this optimized ligand coverage, which corresponds to a total of twelve molecules in the system. Moreover, the influence of different ratios of AT and 9DT molecules on the ligand coverage on the gold surface should also be studied.

Two methods have been proposed to obtain the interparticle distance from MD simulations:

1. Direct Extraction Method: Interparticle distance is directly extracted from MD simulations using mixed AT and 9DT molecules in the system.
2. Linear Combination Model: Interparticle distance is calculated based on Equation 7.3. This involves using the interparticle distances extracted from systems with pure AT ligands and 9DT linkers, weighted by their respective fractions.

A deeper investigation is required to evaluate which method provides more accurate results. Subsequently, the obtained interparticle distances can serve as input parameters for calculating charge transport properties utilizing a density functional tight binding approach (DFTB electronic structure calculations) in conjunction with a Landauer coherent tunneling approach employing Green's functions, as implemented in DFTB+[202]. This approach, as described in a recent study by Schaefer et al.[1], allows for the prediction of the electrical characteristics of GNP films composed of mixtures of ligands and linkers. Furthermore, different compositions of the organic matrix demonstrate distinct sensing characteristics, as shown in Figure 7.27. However, the interaction between analyte molecules and the organic matrix remains unknown. Future research should also focus on simulating the swelling phenomenon of organic matrices and the interaction between analyte molecules and ligands/linkers. This could significantly advance the design of GNP-based sensors and provide insights into the sensing mechanism at the molecular scale. Previously, a multitude of GNP films needed to be produced and tested with target analytes, with the selection of the films of interest occurring afterward. By leveraging MD simulations, the screening of sensors can be facilitated, streamlining the sensor development process in a more efficient manner.

7.5 Chemiresistor Array

In Section 7.3, GNP films prepared with MT/9DT mixtures showed tunable selectivity and sensitivity enhancement, and a further investigation of such GNP composites was conducted with the help of MD simulations in Section 7.4. As demands for real-time target analyte sensing grow across various applications including health diagnosis, environmental monitoring, and explosives detection, gas sensor arrays, also known as electronic noses, have attracted increased attention. The mixed ligand/linker strategy offers an effective technique for the fabrication of sensor arrays with diverse response patterns, serving as a fingerprint for each specific analyte. To leverage these findings in real-world applications, two monolithic chemiresistor arrays based on previous studies were fabricated using the LbL-SC procedure combined with lithographic patterning[23] approaches. In this presented section, the batch GNP5 was used to prepare the chemiresistor arrays, and the fabricated chemiresistor arrays were used to discriminate a wide variety of volatile analytes using linear discriminant analysis (LDA).

This section contains a summary of results that were published in the following journal article: C.-Y. Liu, S. C. Bittinger, A. Bose, A. Meyer, H. Schlicke, T. Vossmeier, "Tuning the Interfacial Chemistry of Nanoparticle Assemblies via Spin-Coating: From Single Sensors to Monolithic Sensor Arrays", *Advanced Materials Interfaces*, **2024**, 2301058.[2]

7.5.1 Fabrication of Monolithic Chemiresistor Arrays

Figure 7.32 illustrates the key steps of the fabrication process.[23] Initially, a silicon substrate with four pairs of interdigitated electrode (IDE) structures was coated with a thin layer of poly(methyl methacrylate) (PMMA) using a spin-coating (SC) method. Next, PMMA-coated areas with two IDEs were selectively exposed to deep ultraviolet (DUV) radiation, and the irradiated regions of the PMMA layer were removed by immersing the substrate in a mixture of 4-methyl-2-pentanone (4M2P) and 2-propanol solution, creating a patterned PMMA layer. Subsequently, the first GNP film was deposited onto the patterned PMMA using the LbL-SC method as described in Section 7.3.1. The GNP film on the PMMA-covered sections was removed via lift-off by dissolving the PMMA layer with acetone. This process was repeated three times, resulting in an array consisting of four pairs of IDEs, each covered with a different type of GNP film.

The pure 9DT cross-linkers, the mixtures of 89% 12T/9DT and 95% 3MPA/9DT, and the pure 8MOA ligand were applied based on previous findings (in Section 7.3.4) to create varying response characteristics and selectivities for the different sensing elements. Figure 7.32b shows the photograph of the fabricated sensor array consisting of the above-mentioned four types of GNP films mounted on a printed circuit board (PCB).

During the lithographic patterning procedure, careful attention was paid to the sequence in which the four different GNP films were manufactured. As shown in Figure 7.33a, the GNP films of this sensor array were deposited in the following order: 9DT, 89%12T-9DT, 100%8MOA, and 95%3MPA-9DT films. On the other hand, in the case of the sensor array shown in Figure 7.33b, the GNP films were deposited in the following order: 9DT, 89%12T-9DT, 95%3MPA-9DT, and 100%8MOA films. The 9DT GNP film was

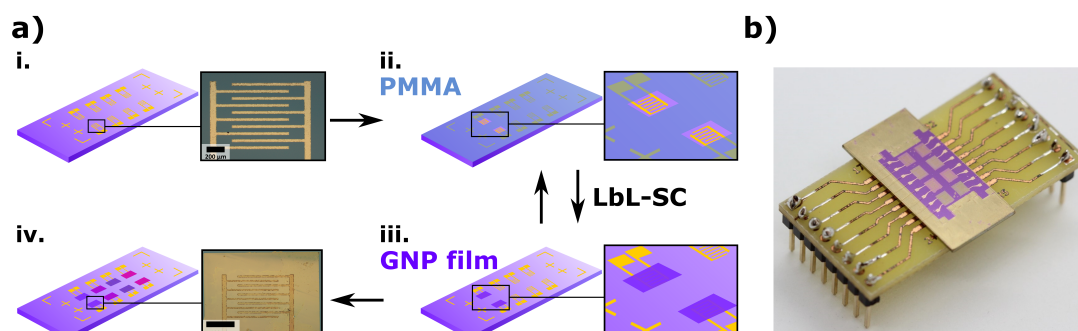


Figure 7.32: a) Lift-off-based lithographic patterning for GNP based sensor array fabrication: i) a silicon chip with 4 pairs of interdigitated electrode structures, ii) depositing a PMMA layer and opening one pair of electrode structures with DUV patterning, iii) spin-coating the GNP film onto the PMMA mask covered silicon chip, and repeating the procedure three times to cover all interdigitated electrodes, iv) the fabricated sensor array comprising four types of GNP films. b) Photograph of the sensor array mounted on a PCB. Reprinted with permission from Ref. [2]. ©2024 The Authors. *Advanced Materials Interfaces* published by Wiley-VCH GmbH.

selected as the first to be fabricated, as it was considered to be the most robust one due to its high degree of cross-linking. Although the 95%3MPA-9DT film also consists of a cross-linked network, it was found to be less stable in preliminary tests, e.g., partial removal from the substrate after sequential PMMA coating and lift-off steps was observed (as shown in Figure 7.33 a). This instability is possibly due to the affinity between the carbonyl groups of PMMA and the carboxylic acid groups of 3MPA. Therefore, the GNP film with the 12T ligand was deliberately chosen to be fabricated before depositing the 95%3MPA-9DT film. Finally, the 100% 8MOA film was fabricated because this film was assumed to be the less stable one, as it contains only the long flexible 8MOA ligands without covalent 9DT cross-linking.

In addition, care must be taken when removing the certain areas of the GNP film, which were unexposed to DUV. To ensure complete removal of these unexposed areas of the GNP film, the PMMA layer was stripped using an acetone bath. Immersing the entire substrate in acetone and gently rinsing it may cause some of the detached GNP film flakes to re-attach to the substrate, as shown in Figure 7.33b. To prevent this re-attachment, a 50 mL syringe with a cannula (diameter of 2 mm) was used to generate a stronger acetone rinse, and the as-fabricated sensor array is shown in Figure 7.32b.

The successfully fabricated array of sensors is shown in Figure 7.32b, and the baseline resistances of the sensors were measured after each deposition of the GNP films and are presented in Figure 7.33c. The cross-linked 9DT and partially cross-linked 95%3MPA-9DT films exhibited high stability throughout the sensor array fabrication process. On the other hand, the resistance of the 89%12T-9DT film increased drastically after depositing the 95%3MPA-9DT film. This effect is possibly due to damages caused by the PMMA layer in lift-off step, resulting in partial removal of the 89%12T-9DT film (within the sensor array shown in Figure 7.32b) and the formation of cracks within the film, cf. Figure 7.33d. Despite these damages, the film maintained sufficient conductance, allowing it to function effectively in sensing chemical analytes.

To evaluate the consistency of the sensor responses, the two sensing films within each sensor pair (corresponding to the sensor array shown in Figure 7.32b) were exposed to toluene, 1-propanol, and water vapors at the concentration of 1000 ppm. Figure 7.34 demonstrates highly reproducible responses of the

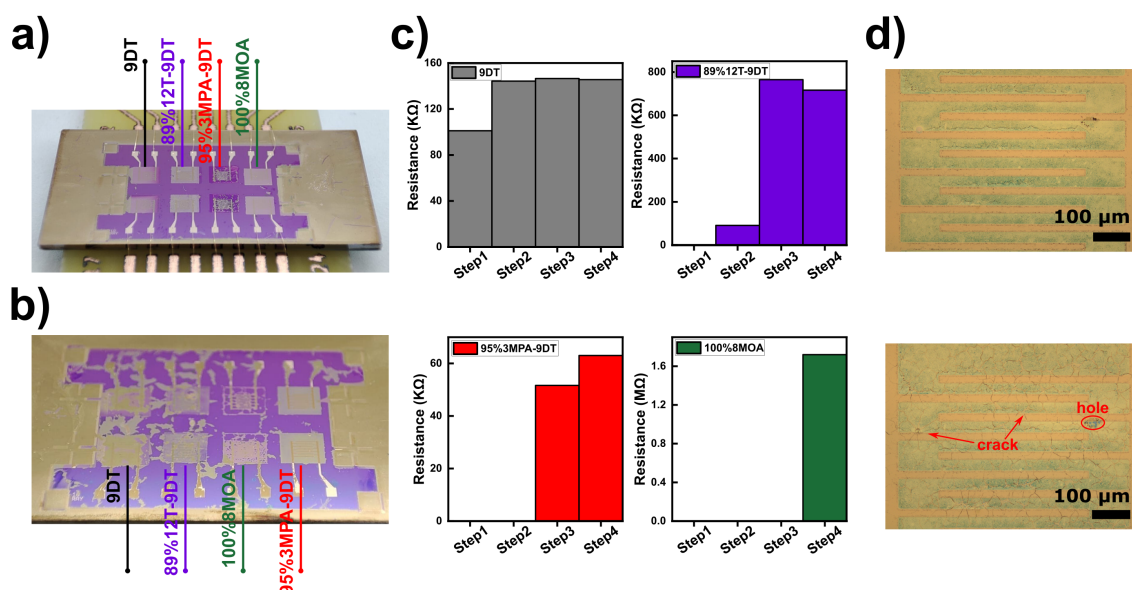


Figure 7.33: Photography of exemplary failures encountered during the fabrication of monolithic sensor arrays. a) The GNP films of the sensor array were deposited in the following order: 9DT, 89%12T-9DT, 95%3MPA-9DT, and 100%8MOA films. The 100%8MOA film was torn off the substrate after the PMMA removal step. b) The GNP films of the sensor array were deposited in the following order: 9DT, 89%12T-9DT, 100%8MOA, and 95%3MPA-9DT films. The floating GNP film was accidentally re-attached to the substrate during the lift-off step while immersed in acetone to dissolve the PMMA layer. c) Baseline resistances of the LbL-SC GNP films after each deposition of GNP films (corresponding to the sensor array shown in Figure 7.32b). The films were deposited in the following order: 9DT, 89%12T-9DT, 95%3MPA-9DT, and 100%8MOA films. d) Microscopic images of the 89%12T-9DT film of the sensor array shown in Figure 7.32b right after the LbL-SC procedure (step 2, top) and after the subsequent LbL-SC of another GNP film (step 3, bottom).

sensor pairs. While the majority of sensors of the array displayed similar selectivity patterns as their counterparts deposited on individual glass substrates (as illustrated in Section 7.3.4, Figure 7.18), some variations were noted. Once again, the 89%12T-9DT and 100%8MOA films exhibited notably higher sensitivities to toluene and 1-propanol compared to the 9DT and 95%3MPA-9DT films, consistent with previous observations. However, slight variations in the relative response amplitudes to the different analyte vapors were observed among the GNP films. These differences in relative response amplitudes are attributed to differences in the fabrication procedures, whether individual sensors were produced on single substrates or as part of an array on a monolithic substrate. Fabricating the sensor array involved multiple steps, including the repeated deposition and removal of the PMMA layer, multiple treatments with GNP solutions and ligand/linker mixtures, and extensive washing with various solvents. These steps can potentially cause subtle changes in the composition of the GNP films. Nonetheless, the results confirm that the selectivity and sensitivity of the sensors of an array can be adjusted by utilizing different ligand/linker mixtures during fabrication.

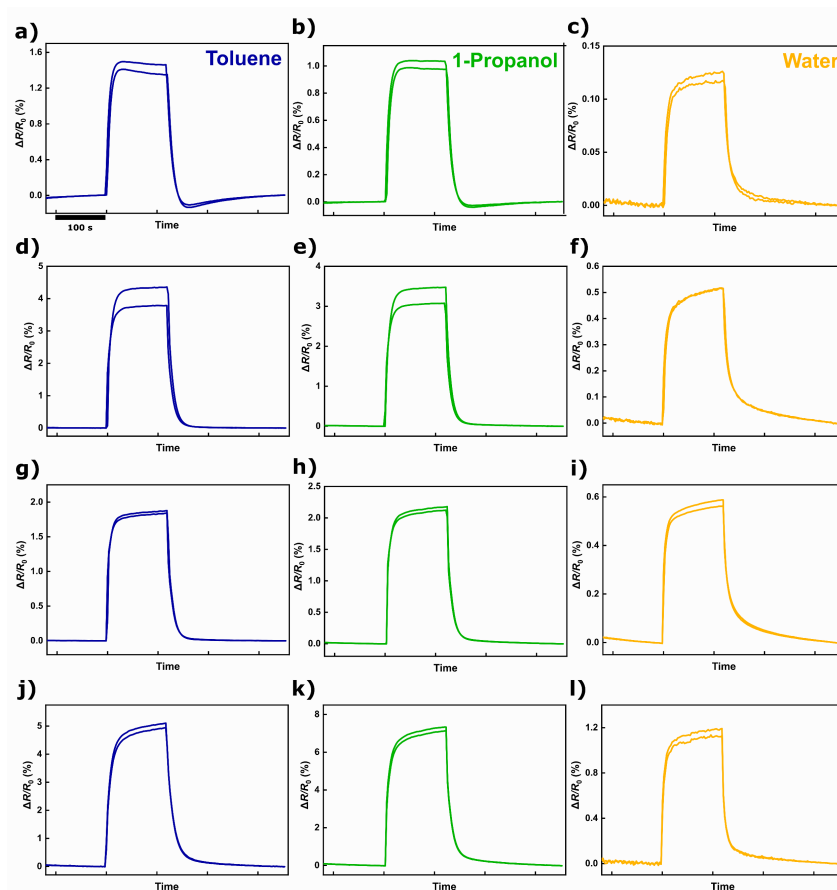


Figure 7.34: Transient responses of a monolithic GNP chemiresistor array (corresponding to the one shown in Figure 7.32b), consisting of four sensor pairs: a-c) 9DT d-f) 89%12T-9DT g-i) 95%3MPA-9DT j-l) 100%8MOA. The chemiresistor array was exposed to toluene (blue), 1-propanol (green), and water (orange) vapors at a concentration of 1000 ppm, with nitrogen serving as the carrier gas. Each panel exhibits the transient responses of the two sensors within the corresponding sensor pair. Reprinted with permission from the Supporting Information of Ref. [2]. ©2024 The Authors. Advanced Materials Interfaces published by Wiley-VCH GmbH.

7.5.2 Array Consisting of Four Types of Gold Nanoparticle Chemiresistors

To evaluate the analyte classification capability of the array consisting four types of GNP chemiresistors (9DT, 89%12T-9DT, 95%3MPA-9DT, and 100%8MOA films, Figure 7.32b), 17 different analyte vapors were tested. These tested analyte vapors vary in dielectric constant, vapor pressure, and molecular size. During the measurements, analyte vapors in the concentration range from 50 to 1000 ppm were supplied using nitrogen as carrier gas, and nitrogen zero gas (ZG) and analyte gas (AG) were periodically introduced into the test-cell (~ 16 mL), alternating between 4 minutes of ZG followed by 2 minutes of AG. In addition, the gas flow through the test cell was maintained at a rate of 500 mL/min using a pump.

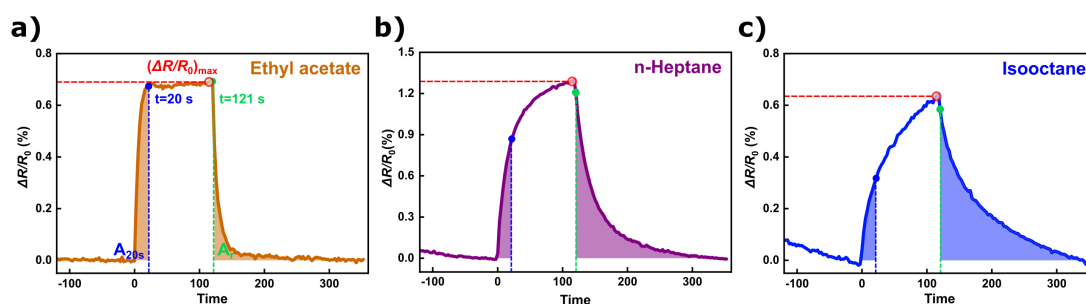


Figure 7.35: Transient responses of the 100%8MOA GNP film exposed to vapors at the concentration of 500 ppm: a) ethyl acetate, b) n-heptane, and c) isooctane. Maximum resistive response amplitude $(\Delta R/R_0)_{\max}$, the area under the transient curve during the first 20 seconds of vapor exposure A_{20s} , and the area under the recovery transient curve from 121th to 360th second A_r are indicated in part a). Adapted and reproduced with permission from Ref. [2]. ©2024 The Authors. Advanced Materials Interfaces published by Wiley-VCH GmbH.

Figure 7.35 presents the response transients of the 100%8MOA film upon exposure to ethyl acetate, n-heptane, and isooctane vapors at the concentration of 500 ppm. As the sensor was exposed to different vapors, the maximum response amplitudes and transient shapes changed. Previous studies have described strategies to improve the sensor array performance by optimizing sensing elements, extracting effective response features, and applying suitable classification algorithms. The investigation in Section 7.3 already identified the optimized GNP films, and some researchers have suggested using LDA rather than principal component analysis (PCA) to achieve better classification capability.[203, 204] Here, the selection of response features was deeply investigated. Generally, response features can be categorized into "steady-state" and "transient-state" response features.[205, 206] The "steady-state" denotes a phase where the response curve reaches its saturation, and the response amplitude stabilizes. The most common "steady-state" feature is the maximum response amplitude measured after a certain time of exposure to the analyte. However, drawbacks of using "steady-state" features, such as response drifts caused by aging and concentration-dependent response amplitudes, have to be addressed. Moreover, chemically and structurally similar compounds may result in similar response amplitudes. Some publications have pointed out the advantages of employing "transient-state" response features to overcome this problem.[205–209] As shown in Figure 7.35, the quasi-rectangular shape of the transient indicates a rapid response during exposure to ethyl acetate. In contrast, the transients during exposures to n-heptane and isooctane reveal slow kinetics of the vapor/sensor interaction. Such differences in response kinetics can be helpful in advancing analyte identification, as the maximum amplitudes of the responses to both ethyl acetate and isooctane were similar but their transient characteristics exhibited significant differences. As shown by this example, features extracted from the transient behavior of GNP sensor arrays can be widely used as

input dataset to enable the classification and recognition of analytes via appropriate pattern analyses.[18, 25, 30, 156, 210]

In a preliminary test, "transient-state" features such as rise time, recovery time, area under the transient curve during the entire period of vapor exposure, area under the transient curve during the initial period of vapor exposure, and area under the transient curve during the recovery phase after vapor exposure, were used as training data for LDA feature selection. The obtained feature weights ranked their importance for analyte classification.[211] As a result, using the areas under the transient during the initial period of vapor exposure and during the recovery phase yielded the best results. Following this finding, three features were extracted from the single signal readout, and LDA was applied for analyte classification:

1. The response amplitude $(\Delta R/R_0)_{\max}$ recorded at the end of analyte exposure (average value over the interval 110-115 s).
2. The area A_{20s} beneath the transient curve during the first 20 seconds of analyte exposures (response region).
3. The area A_r below the recovery transient curve from the 121th second until the 360th second (recovery region).

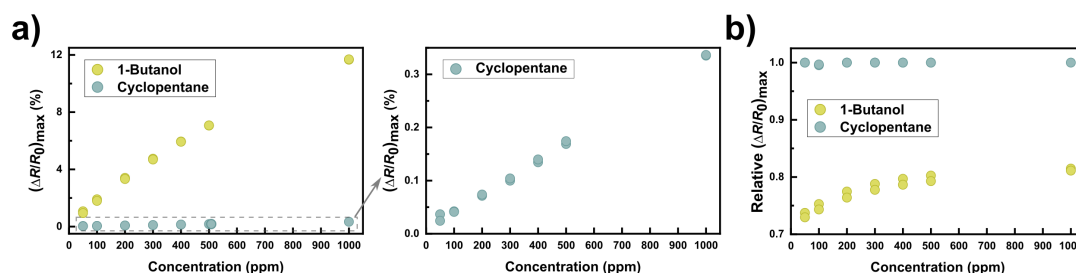


Figure 7.36: The 89%12T-9DT film's a) maximum response amplitudes $(\Delta R/R_0)_{\max}$ and b) relative maximum response with normalization process for vapor exposures to 1-butanol (yellow) and cyclopentane (cyan) at concentrations ranging from 50 to 1000 ppm. The presented data was obtained from one of the 89%12T-9DT films of the sensor array. The tested concentration profile was 50, 100, 200, 300, 400, 500, 1000, 1000, 500, 400, 300, 200, 100, and 50 ppm.

Figure 7.36a shows $(\Delta R/R_0)_{\max}$ values directly extracted from the responses of the 89%12T-9DT sensor when exposed to 1-butanol and cyclopentane vapors in the concentration range from 50 to 1000 ppm. Notably, 1-butanol and cyclopentane possess vapor pressures of ~ 7 and ~ 316 mmHg at 25 °C[170], respectively. Due to the relatively low vapor pressure of 1-butanol (high partition coefficient), the sensor exhibited a significantly higher response amplitude than for cyclopentane. Specifically, the response amplitude to cyclopentane is less than 3% of that to 1-butanol. Furthermore, it is evident that the response amplitudes to both vapors were highly dependent on the analyte's concentrations. In this case, the "steady-state" feature, $(\Delta R/R_0)_{\max}$, may be primarily driven by the vapor pressure and concentration of the compounds rather than their structural and chemical differences, potentially resulting in erroneous clustering of the analyte vapors in the LDA plot. To prevent extremely high "steady-state" feature values caused by low-vapor-pressure compounds, the $(\Delta R/R_0)_{\max}$ value was square rooted. This adjustment ensures that the feature values of analytes with very different vapor pressures are within a comparable range (cf. Figure 7.36b). Additionally, for each exposure, the "steady-state" features obtained from individual sensors were normalized by dividing each value by the highest value observed

among all eight sensors. This normalization process minimized the feature's concentration dependency. Within the tested concentration range (50-1000 ppm), the normalized "steady-state" feature values (relative $(\Delta R/R_0)_{\max}$) for cyclopentane exhibited nearly no change, while for 1-butanol, the normalized values (relative $(\Delta R/R_0)_{\max}$) varied only by approximately 10% as the vapor concentration increased from 50 to 1000 ppm (without normalization, the "steady-state" feature values, $(\Delta R/R_0)_{\max}$, increased by 1200% with increasing analyte concentrations from 50 to 1000 ppm). Regarding the two "transient-state" features (A_{20s} and A_r), they were first normalized by dividing themselves by their corresponding $(\Delta R/R_0)_{\max}$ value for each exposure to mitigate variations caused by the varying analyte concentrations. Subsequently, similar to the normalization process for maximum response amplitude features, each "transient-state" feature value was divided by the highest feature value among all sensors for each exposure to further eliminate concentration-dependent effects. After this two-step normalization process, the resulting normalized values are defined as the relative A_{20s} and the relative A_r .

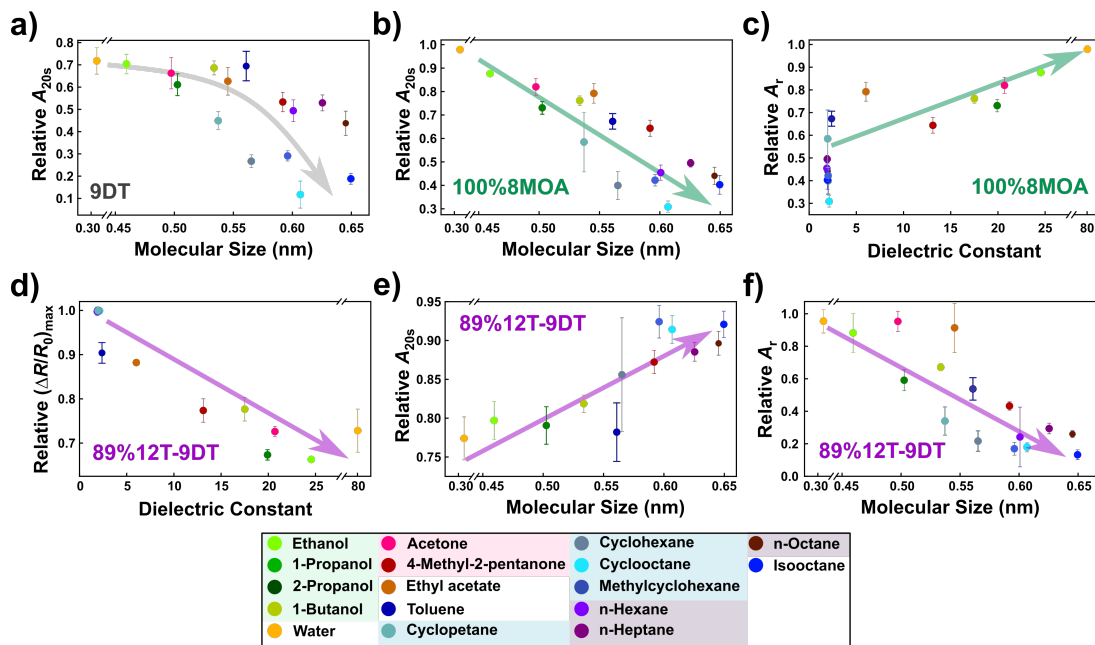


Figure 7.37: Three normalized "steady-state" and "transient-state" features are plotted against either the dielectric constants or the estimated molecular spaces (S_a) of the analytes. Each data point represents the average feature value for the analyte at concentrations ranging from 50 to 1000 ppm. The three features underwent the normalization process as described earlier, and are indicated as relative $(\Delta R/R_0)_{\max}$, relative A_{20s} , and relative A_r . Panel a) illustrates the relative A_{20s} feature value vs. S_a for the 9DT film, while b) displays the same correlation for the 100%8MOA film. In panel c), the relative A_r feature value vs. the relative dielectric constant is plotted for the 100%8MOA film. Panels d), e), and f) depict the correlation between the relative $(\Delta R/R_0)_{\max}$ and the relative dielectric constant of analytes, the relative A_{20s} feature value and S_a , and the relative A_r feature value and S_a , respectively, for the 89%12T-9DT film.

Figure 7.37 illustrates examples where certain features of the selected GNP films exhibited a high dependence on either the molecular size or the relative dielectric constant of the analytes. These features can effectively discriminate between different analytes. The "steady-state" feature (relative $(\Delta R/R_0)_{\max}$) values of most GNP films composed of hydrophobic ligand or linker molecules within the organic matrix are primarily influenced by the vapor pressures and concentrations of analyte gases.[15, 18, 109] Consistent with this observation, for the 9DT film investigated in this study, even after normalization, its relative $(\Delta R/R_0)_{\max}$ feature values still depended on both vapor pressure and concentration of the analytes, but appeared to be independent of the molecular size and the relative dielectric constant of the

analytes. However, in striking contrast, for the GNP film consisting of the mixture of 89% 12T/9DT, the relative $(\Delta R/R_0)_{\max}$ feature effectively differentiated between analyte vapors based on their polarity (cf. Figure 7.37d).

"Transient-state" features are considered to offer a more effective means for discriminating analyte vapors based on their structural and chemical properties. In terms of chemistry, the higher affinity between analyte molecules and the organic matrix may lead to rapid interactions, resulting in faster response kinetics (larger values of A_{20s}). Additionally, the size of the analyte may also influence the response kinetics.[18] The space occupied by a single analyte molecule (S_a) can be estimated from its volume in the liquid phase using the equation: $S_a = \sqrt[3]{M_w \cdot N_A^{-1} \cdot \rho_a^{-1}}$, where M_w is the molecular weight of the analyte, N_A is the Avogadro constant, and ρ_a is the mass density of the analyte. The calculated volume occupied by the analyte molecules applied in this study range from 0.3 to 0.65 nm, and the average interparticle distances within the applied GNP films range from ~ 1 nm to ~ 2 nm according to the previous section (cf. Figure 7.13).

Figure 7.37a, b, and e present the correlation between the relative A_{20s} feature and the estimated volume occupied by a single analyte molecule. As anticipated based on previous findings[18], the films, 9DT and 100%8MOA, exhibited faster reactions to smaller size of analytes. This phenomenon can be attributed to the quicker diffusion and easier transfer of smaller analyte molecules to sorption sites within the organic matrix, leading to rapid chemiresistive responses.[18] However, contrary to expectations, the 89%12T-9DT films showed rapid responses to larger analytes, and slower responses to the smaller analytes. This contrasting observation of the correlation between response time and analyte molecular volume may be attributed to the different microstructures within the films. The 9DT film possesses a highly cross-linked network, while the 89%12T-9DT film has relatively low cross-linkage within the film. This difference in structure leads to completely opposite response kinetics.

"Transient-state" features extracted from the sensor's recovery phase (A_r) also proved to be useful. For example, in the case of the 100%8MOA film, the relative A_r values were below 0.6 (except for toluene) for nonpolar analytes (cf. Figure 7.37c). Similarly, in the case of the 89%12T-9DT film, such features can also be applied to distinguish the sizes of analyte molecules (cf. Figure 7.37f). In summary, both "steady-state" and "transient-state" features enable discrimination of analyte compounds based on their sizes and dielectric constants. These extracted normalized features were used as input dataset into the classification algorithm, LDA. Utilizing both "steady-state" and "transient-state" features aids LDA in identifying the optimal subspace to minimize variations within the same class and maximize separation between different classes.

As indicated in previous studies, GNP films, particularly prepared with the MT ligands functionalized with groups such as hydroxyl and carboxylic acid, exhibit aging phenomena.[22, 144] To track the extent of aging, the baseline resistances of the eight GNP films were recorded in a period of 40 days, as illustrated in Figure 7.38. The resistances of the 9DT and 95%3MPA-9DT films remained similar throughout the measurement period. Both 89%12T-9DT films experienced a significant resistance decrease in the first week and the films' resistances stabilized afterwards. In contrast, the 100%8MOA films' resistances fluctuated over time. Nevertheless, despite these variations, GNP films generally stabilized one or two weeks post-fabrication. Therefore, the chemiresistor data measured three weeks after fabrication was attentively applied as the training dataset in the LDA plot (cf. Figure 7.39). LDA was performed using a

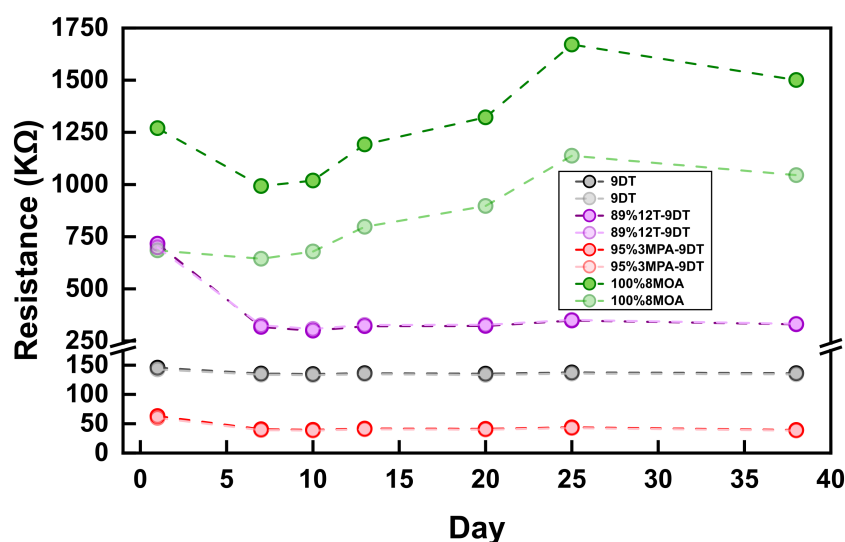


Figure 7.38: Baseline resistance of four pairs of GNP films (corresponding to the sensor array shown in Figure 7.32b) plotted over a period of 40 days. Day 0 is defined as the day when the first GNP film was deposited. Note that, except for the 100%8MOA films, the baseline resistances of each pair of films remained consistent throughout the 40-day period, with their data points overlapping each other.

python script with the "discriminant_analysis.LinearDiscriminantAnalysis" class from the scikit-learn library (version 0.24.2) with the eigen-solver algorithm. The sensor array was exposed to 17 analyte vapors at concentrations ranging from 50 to 1000 ppm. The features were extracted from the response transients shown in Figures A32-A48, excluding the second set of 400 ppm response transients. Each exposure in the training dataset is represented by the filled circles, with different shade gradients indicating tested concentrations (light to dark: 50-1000 ppm). Despite the varying vapor concentrations, data points related to different analyte grouped in distinct clusters. Roughly, polar analyte vapors' data points are located at the upper right of the LDA plot. Moreover, chemicals sharing the same functional groups fall into nearby areas, for examples, the alcohols and ketones. Remarkably, even structural isomers, such as 1-propanol and 2-propanol, can be distinguished clearly. On the other hand, nonpolar vapors fall in the left side of the LDA plot. Again, similar compounds, such as n-hexane and cyclohexane, and n-octane and cyclooctane, form clearly separated clusters. However, some overlap occurs between the straight-chain alkanes and cycloalkanes (e.g., methylcyclohexane vs. n-octane, and n-hexane vs. cyclopentane).

To further evaluate the LDA performance, each analyte vapor exposure measured at 400 ppm on the same day as the training data was used as the test dataset (extracted from the second set of 400 ppm response transients shown in Figures A32-A48 in the Appendix). The test data matrix was first transformed linearly with the LDA model and projected on the LDA plot, represented by hollow circles (see Figure 7.39). All projected data points were assigned to their corresponding cluster location. Further, Bayes Theorem was applied to estimate the probability for classification, and this prediction method provided 100% classification accuracy for all 17 analyte vapors (cross markers).

As shown in Figure 7.38, some fluctuations in the resistance of GNP films were observed, which may relate to the rearrangement of GNP assemblies, oxidation of functional groups, and irreversible changes in the films upon vapor exposures. To examine the influence of the aging phenomenon, the sensor array

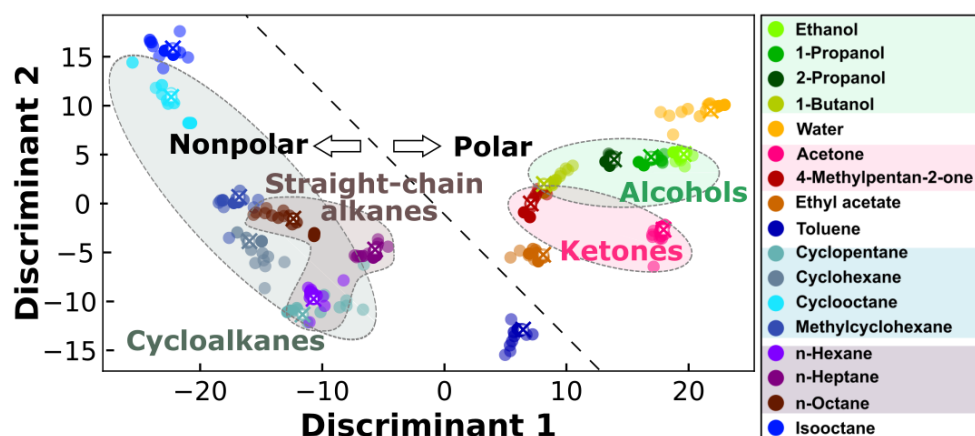


Figure 7.39: Linear discriminate analysis (LDA) performed with datasets obtained from a monolithic sensor array (as shown in Figure 7.32b) consisting of four pairs of GNP chemiresistors: 9DT, 89%12T-9DT, 95%3MPA-9DT, and 100%8MOA. Analyte concentrations ranged from 50 to 1000 ppm. Filled circles represent data points utilized for fitting the model, while empty circles denote test data projected onto the discriminant coordinate system. Colored crosses indicate predictions of the test data. Reprinted with permission from Ref. [2]. ©2024 The Authors. Advanced Materials Interfaces published by Wiley-VCH GmbH.

was also tested with some of the analyte vapors after different time intervals. In the first week after the fabrication (week 1, shown in Figure 7.40b), the sensor array was exposed to two concentrations of the analyte vapors (200 and 400 ppm, with two replicates). Compared with the relative $(\Delta R/R_0)_{\max}$ used in the training data (measured in week 3, shown in Figure 7.40a), the response patterns of different analyte vapors (measured in week 1) showed only slight variations but were overall similar. The "transient-state" features, the relative A_{20s} and A_r , showed more pronounced variations compared to the "steady-state" features, see Figures A49 and A50. These significant changes in the response kinetics can be attributed to the rearrangement of the GNP assembly as well as the changes in the ligand conformation and packing, which affect the sorption and desorption dynamics of analyte molecules by the organic matrix. In week 4, some of the analyte vapors were tested again at four different concentrations (200, 400, 600 and 800 ppm with one replicate each), as shown in Figures 7.40c, A49c, and A50c. Compared to the data obtained in the first week, the responses measured in week 4 showed even greater similarity to those from week 3. The extracted "steady-state" (the relative $(\Delta R/R_0)_{\max}$) and "transient-state" (the relative A_{20s} and A_r) features were consistent with those measured in week 3, see Figure 7.40 and Figures A49 and A50 in the Appendix. Nevertheless, since the response patterns of the features did not change dramatically over time, the 400 ppm exposures from week 1 and 4 were used as the test datasets to examine the classification accuracy of the LDA, as shown in Figures A53 and A54 in the Appendix.

Figure 7.41 depicts the response patterns of the "steady-state" features extracted from the sensor array's responses measured in week 1, 3, and 4, corresponding to parts b, a, and c of the figure, respectively. The response patterns of both the "steady-state" (cf. Figure 7.41a) and "transient-state" (cf. Figures A51a and A52a in the Appendix) features for alcohol analytes, including ethanol, 1-propanol, 2-propanol, and 1-butanol, exhibited notable similarities. Consequently, the data corresponding to these analytes were projected into close areas in the LDA plot, as shown in Figure 7.39. On the other hand, this close clustering made it difficult for the LDA algorithm to clearly distinguish between these analytes, and may incorrectly assign them to similar clusters.

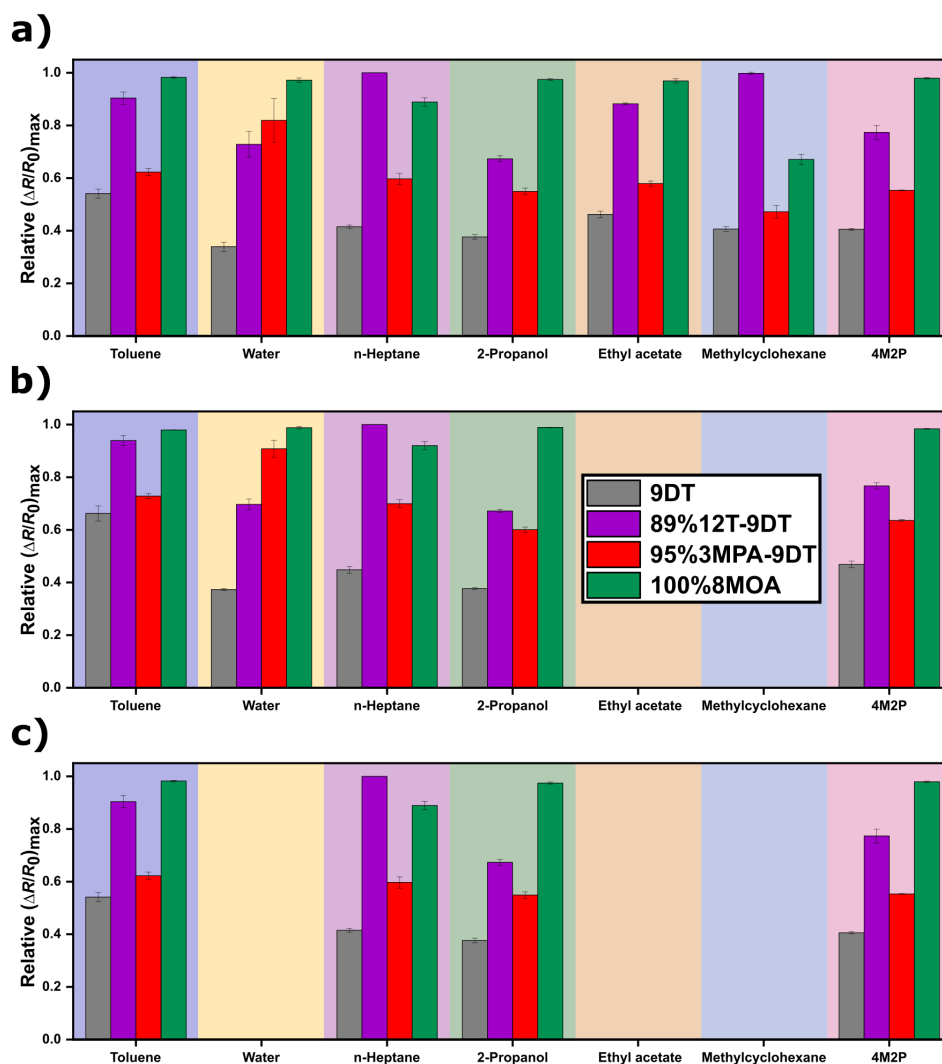


Figure 7.40: Average relative ($\Delta R/R_0$)_{max} features of four GNP films: 9DT (black), 89%12T-9DT (purple), 95%3MPA-9DT (red), and 100%8MOA (green). The sensors were exposed to different analyte vapors (indicated on the x-axis). The responses were measured in a) week 3 (in the concentration range of 50 to 1000 ppm), b) week 1 (in the concentration range of 200 to 400 ppm), and c) week 4 (in the concentration range of 50 to 1000 ppm). Error bars were calculated as the standard deviation of the relative ($\Delta R/R_0$)_{max} features of each GNP chemiresistor within the array, exposed to analyte vapors in the tested concentration range.

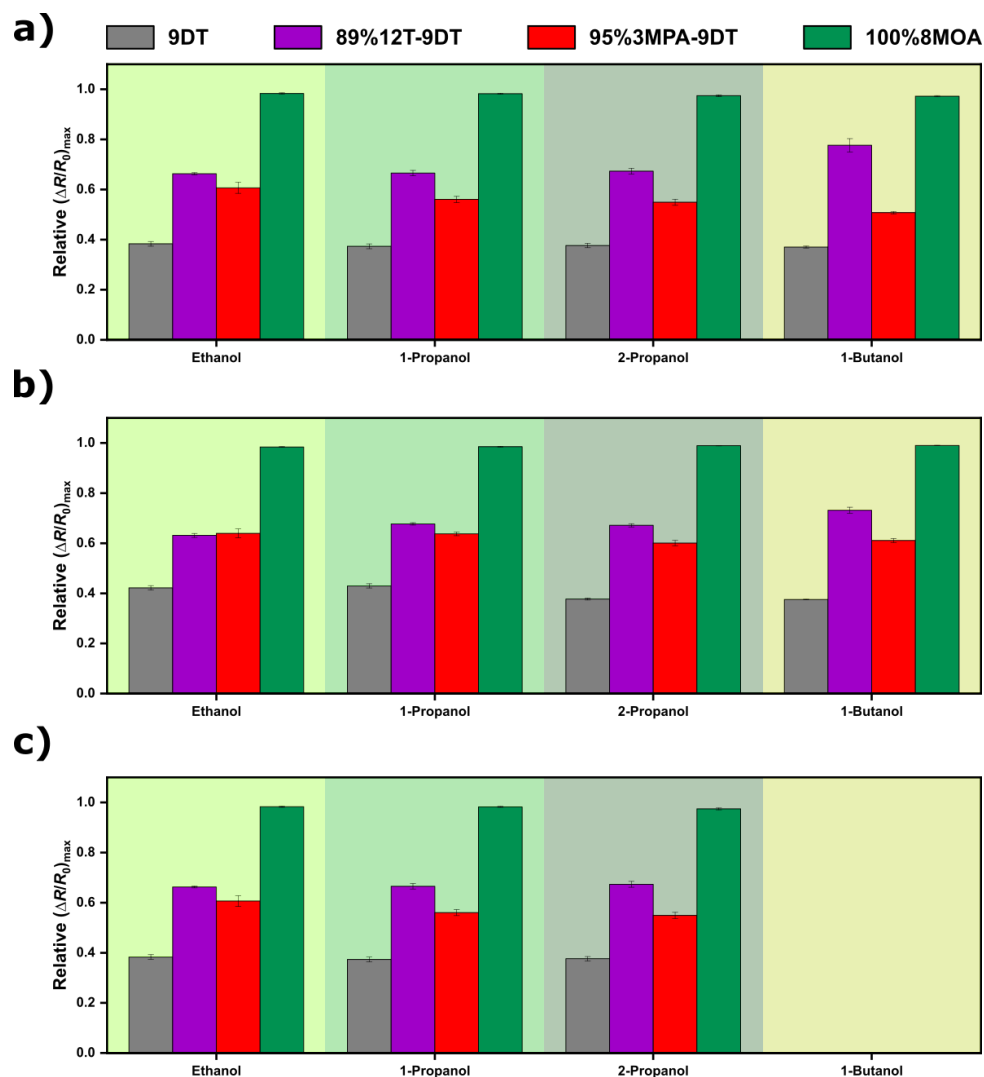


Figure 7.41: Average relative $(\Delta R/R_0)_{\max}$ features of four GNP films: 9DT (black), 89%12T-9DT (purple), 95%3MPA-9DT (red), and 100%8MOA (green). The sensors were exposed to alcohol analytes, ethanol, 1-propanol, 2-propanol, and 1-butanol. The responses were measured in a) week 3 (in the concentration range of 50 to 1000 ppm), b) week 1 (in the concentration range of 200 to 400 ppm), and c) week 4 (in the concentration range of 50 to 1000 ppm). Error bars were calculated as the standard deviation of the relative $(\Delta R/R_0)_{\max}$ features of each GNP chemiresistor within the array, exposed to analyte vapors in the tested concentration range.

Table 7.4 presents the results of the LDA prediction using 400 ppm analyte exposures as the test dataset. Based on the data extracted from the responses measured in week 1, 7 out of 14 analytes were correctly classified into their respective groups, yielding a 50% accuracy. The "transient-state" features extracted from the responses measured in week 1 showed subtle differences from those measured in week 3, and the projected data appeared slightly displaced from their respective clusters, cf. Figure A53. For example, in the case of alcohol analytes, 2-propanol and 1-butanol were misclassified, though they remained within the alcohol group. The response pattern of the relative $(\Delta R/R_0)_{\max}$ collected in week 1 for 2-propanol was highly similar to that collect in week 3, while both the "transient-state" features showed subtle deviations from those measured in week 3. Similarly, compared the response patterns of both the "steady-state" and "transient-state" features collected in week 1 with those in week 3, small variations were observed. Consequently, these subtle differences were significant enough to impact how the test data projected onto the LDA plot. For the test data, 2-propanol and 1-butanol exposures were projected into the 1-propanol and 2-propanol clusters, respectively, in the LDA plot, resulting in misclassifications. On the other hand, even though the response patterns of features extracted from the responses to toluene exhibited more significant changes, it was still correctly classified by LDA. This can be attributed to the fact that the toluene cluster was significantly distant from other clusters in the LDA plot. Therefore, even though the test data was not projected closely to its respective cluster in the LDA plot, the LDA classification could still perform correctly. Similarly, the response patterns from week 4 exhibited visually comparable to those from week 3, however, the slight variations in both the "steady-state" and "transient-state" features were observed. As a result, all six analytes were assigned incorrectly, leading to a 0% accuracy of the classification with this LDA model.

Table 7.4: The array comprised four types of GNP chemiresistors, and LDA was used for classification. The data collected in week 3 served as the training dataset. Features extracted from response transients exposed to 400 ppm analyte vapors on different measurement dates were used as the test dataset, and the projected test data in the LDA plot are shown in Figures A53 and A54. A check mark indicates a correct predicted classification, a cross mark represents a wrong prediction (the wrongly assigned cluster is indicated in the parentheses), and a dash symbol is an untested analyte.

Analyte Vapor	Test Data Set(Week 1)	Test Data Set(Week 4)
Ethanol	✓	× (1-Butanol)
1-Propanol	✓	× (1-Butanol)
2-Propanol	× (1-Propanol)	× (1-Butanol)
1-Butanol	× (2-Propanol)	-
Water	✓	-
Acetone	× (Ethanol)	-
4M2P	✓	× (n-Heptane)
Ethyl acetate	-	-
Toluene	✓	× (Cyclopentane)
Cyclopentane	-	-
Cyclohexane	× (n-Heptane)	-
Cyclooctane	× (Methylcyclohexane)	-
Methylcyclohexane	-	-
n-Hexane	× (Toluene)	-
n-Heptane	✓	× (n-Octane)
n-Octane	✓	-
Isooctane	× (Cyclooctane)	-

In conclusion, the sensor array, consisting of four types of GNP chemiresistors, demonstrated efficient discrimination of 17 volatile compounds. The LDA model successfully assigned analytes with similar

functional groups to neighboring clusters in the LDA plot and accurately classified them into their corresponding groups. However, the accuracy of the LDA model was influenced by aging of the sensors, which caused subtle changes in the features used for LDA and reduced classification accuracy over time. Despite this, the overall stability and response patterns suggest that such GNP chemiresistor array holds promise for reliable and effective vapor discrimination. However, further optimization, such as improvements of the pattern recognition algorithm, is necessary to avoid the effects of the sensor's aging and enhance long-term performance.

7.5.3 Array Consisting of Eight Types of Gold Nanoparticle Chemiresistors

In Section 7.5.2, the high efficiency in differentiating a variety of volatile chemical compounds was achieved by our fabricated sensor array. The sensor array, which utilized four types of GNP chemiresistors, demonstrated efficient discrimination of 17 analytes. However, despite the overall effectiveness, there were some notable limitations. For instance, slight overlap of different clusters were observed in the LDA plot, indicating that it may not be possible to classify certain analytes reliably. Moreover, the classification accuracy was significantly influenced by the aging of the sensor films. These disadvantages highlight the challenges of using this current sensor array configuration for real-world applications, where consistent and precise differentiation of volatile analytes is crucial. To address these issues and further improve the performance of the sensor array, an array comprised of a broader variety of sensors was designed. This new design involved the preparation of two monolithic sensor chips, each incorporating four distinct GNP films. Based on the previously reported sensing capabilities, three additional MTs with different functional groups were selected for the sensor array: 6-mercapto-3-pyridinecarboxylic acid (6MNA), 4-nitrothiophenol (4NTP), and 8-mercapto-1-octanol (8MOO).[23, 41, 212–214] These three MT ligands were chosen due to their unique functional groups and molecular structure, which may contribute to different interaction mechanisms with the analyte molecules, thus improving the overall discriminatory power of the sensor array. Further, earlier findings of our studies into GNP films prepared with a mixed ligand/9DT system showed that the optimal mixing condition was identified as a 95% molar fraction of functionalized MT ligands. This proportion was found to maximize the unique sensing characteristics of the modified organic matrix contributed by the added MTs.

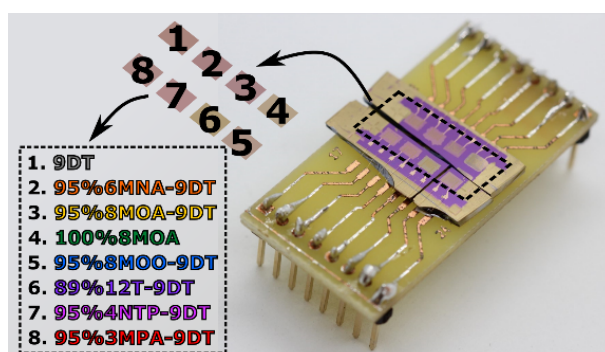


Figure 7.42: A Photograph depicting the assembled chemiresistor array consisting of eight distinct GNP films, labeled as follows: 9DT, 95%6MNA-9DT, 95%8MOA-9DT, 100%8MOA, 95%8MOO-9DT, 89%12T-9DT, 95%4NTP-9DT, and 95%3MPA-9DT GNP films. Reprinted with permission from the Supporting Information of Ref. [2]. ©2024 The Authors. Advanced Materials Interfaces published by Wiley-VCH GmbH.

Taking into account aging effects and the potential of film degradation due to multiple PMMA layer-deposition and -removal steps, the fabrication procedure was optimized to make it as simple as possible and to shorten the time required for preparation. Therefore, two monolithic sensor chips, each equipped with 4 different GNP films, were prepared in parallel within two days. Previous results showed that the higher the degree of cross-linking, the more stable the film is, and generally, the organic matrices composed of shorter MTs maintain a highly cross-linked network. Two chips, A and B, were coated with the GNP films in the following order, chip A: 9DT, 95%6MNA-9DT, 95%8MOA-9DT and 100%8MOA; chip B: 95%4NTP-9DT, 95%3MPA-9DT, 95%8MOO-9DT and 89%12T-9DT. These two chips were then split in half and halves from each were combined on a PCB as shown in Figure 7.42.

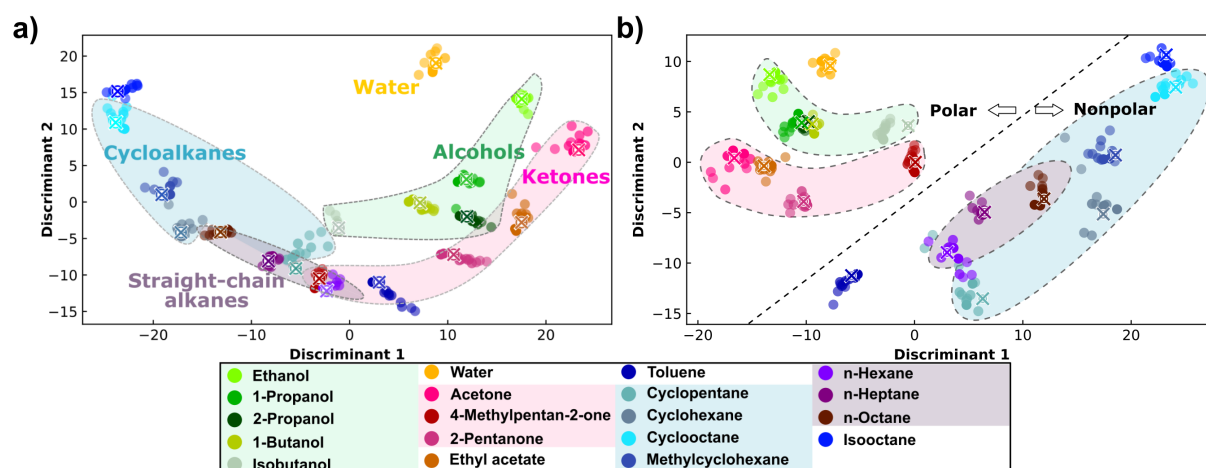


Figure 7.43: LDA plot for the responses extracted from the chemiresistor array consisting of 8 different GNP films exposed to 19 different analyte vapors in the concentration range of 100 to 1000 ppm, which were measured in a) week 1, and b) week 5. Filled circles represent data points (training dataset) used for fitting the model, hollow circles denote data points from the test dataset projected onto the discriminant coordinate system. The colored crosses indicate predictions of data points from the test dataset. a) Reprinted with permission from Ref. [2]. ©2024 The Authors. Advanced Materials Interfaces published by Wiley-VCH GmbH.

To validate the classification performance, the 8-sensor array was exposed to 19 different volatile compounds at concentrations ranging between 100 to 1000 ppm. Three normalized "steady-state" and "transient-state" features, as applied for the 4-sensor array, were used as the input dataset for LDA. All baseline-corrected transient responses measured in week 1 (week 0 refers to as the week when the two chips were prepared) in the concentration range of 100 to 1000 ppm can be found in the Appendix (Figures A55-A73). In a preliminary test, three features were extracted from the response transients of the eight sensing elements measured in week 1 and used as training dataset (including vapor concentrations of 100, 200, 300, 400, 500, and 1000 ppm), as presented in Figure 7.43a. As anticipated, compared to the 4-sensor array, LDA for the 8-sensor array resulted in better clustering of different analyte vapors. Chemically and structurally similar analyte compounds were assigned to neighboring regions, but still remain well-separated from each other. For example, the class of straight-chain alkanes is encircled by a purple ellipse, falling in the similar area of the LDA plot. However, three clusters of n-hexane, n-heptane, and n-octane are still well-separated from each other, allowing for easy identification of different lengths of straight-chain alkanes.

"Discriminate 1" effectively differentiates analytes based on intrinsic differences in dielectric constants, with most nonpolar analytes located at the negative coordinates and polar analytes at the positive

coordinates of "Discriminate 1". To evaluate the generalization performance of the model, analyte vapors at a concentration of 600 ppm were used as the test dataset, a concentration not included in the training data. The training data were transformed by the LDA algorithm, and projected to the discriminant coordinate system. Further, the prediction algorithm was used to estimate the probability of the training dataset belonging to the predicted cluster (colored crosses). Even though exposures of 600 ppm analyte vapors had not been used for the LDA model training, the test data of all 19 analyte vapors were assigned 100% accurately to their respective clusters.

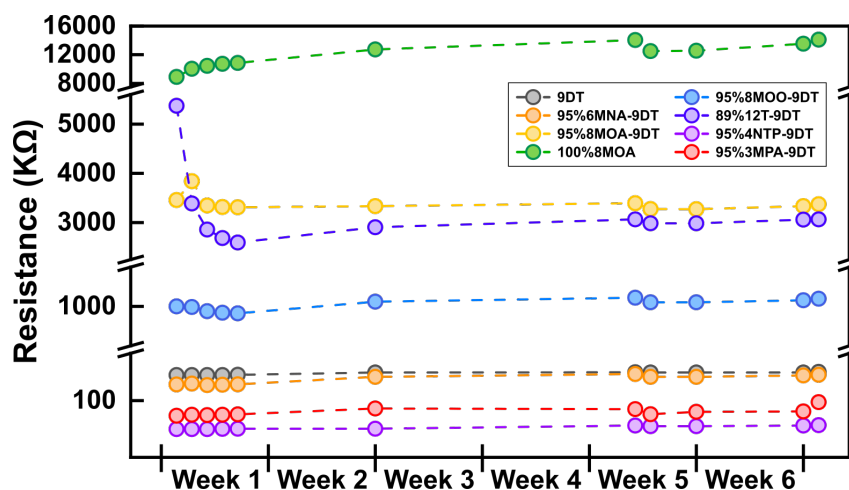


Figure 7.44: Variations in the baseline resistance of the eight sensors over a period of 7 weeks (~43 days). Week 0 refers to as the week when the two sensor chips were prepared.

Figure 7.44 shows the variations in baseline resistance of the 8 sensing elements within the array. Similar to the 4-sensor array, notable changes were observed only in case of the 89%12T-9DT and 100%8MOA films. Specifically, the baseline resistance of the 89%12T-9DT film decreased significantly in week 1, and then stabilized from week 2 on. In contrast, the baseline resistance of the 100%8MOA film gradually increased over the duration of the measurements. When the test data (responses to 600 ppm analytes) extracted from the measurements conducted in week 3 were fitted into the LDA model, which was trained with data measured in week 1, the classification accuracy on the test data was only ~47%, and the results of the assigned cluster of these 19 exposures are listed in Table A3 in the Appendix. The poor accuracy can be attributed to unexpected drastic changes in the response patterns for the analyte vapors, as illustrated in Figure 7.45a and b (respective "transient-state" features are shown in Figures A74 and A75 in the Appendix). Despite these changes, the response patterns for toluene, water, and methylcyclohexane vapors remained relatively similar in the 8-sensor array, enabling correct classification into their respective clusters. However, the response patterns for n-heptane, 2-propanol, ethyl acetate, and 2-pentanone vapors exhibited noticeable variations, leading to misclassification of test exposures into incorrect clusters. Again, this can be attributed to the position of the clusters in the LDA plot. When few clusters are crowded in a nearby area in the LDA plot, small variations in their features may lead to the projected data to deviate from its respective cluster and be closer to the neighboring clusters, resulting in misclassification.

To further study aging effects of the 8-sensor array, additional measurements were conducted five weeks after fabrication (week 5). By this time, the baseline resistance of all 8 GNP films appeared to have stabilized, indicating consistent sensor performance. Additionally, the response patterns for different

analyte vapors remained preserved across all 8 GNP sensors (cf. Figure 7.45c and Figures A74c and A75c in the Appendix). Following this stabilization, the 8-sensor array was once again exposed to 19 analyte vapors, with each analyte measured with 13 exposures at concentrations ranging from 100 to 1000 ppm (concentration profile: 100, 200, 300, 400, 500, 1000, 1000, 600, 500, 400, 300, 200 and 100 ppm). A new LDA model was then trained using the data extracted from the responses measured in week 5 (excluding the responses to 600 ppm analytes), resulting in the LDA plot shown in Figure 7.43b. In the new LDA plot, clusters of polar analytes are observed in the upper left area, while clusters of nonpolar analytes are located in the lower right area. The same classes of analytes (e.g., classes of alcohol, ketone, and straight-chain alkane) appear closer together, yet remain well-separated. Although the alcohols exhibit clear clustering, the clusters of 1-propanol, 2-propanol, and 1-butanol vapors are slightly squeezed into the same area and overlap. To test the new LDA model (training data extracted from the responses measured in week 5), the sensor responses to analytes at a concentration of 600 ppm were excluded from the training data, and projected onto the LDA plot (Figure 7.43b). The LDA model accurately classified the test dataset with 100% accuracy.

Based on previous findings, the aging phenomenon strongly influences the classification accuracy of a sensor array. However, for practical application purposes, it is important that a sensor array provides reliable information over time. To evaluate the stability of the 8-sensor array, it was exposed to 19 analytes at vapor concentrations of 600, 800, and 2000 ppm 45 days after the fabrication (considered as week 7). These exposures were measured 8 to 11 days apart from those used as the training dataset for LDA. The projected test data of these three concentrations of analytes in the LDA plot (trained with the data measured in week 5) are shown in Figures A76-A78 in the Appendix. When applying the responses measured under exposure to 600 ppm and 800 ppm analyte vapors (exposures within the concentration range used for the training dataset) as the test dataset, the new LDA model (based on the training data from week 5) achieved remarkable results and correctly assigning all analytes at these concentrations to their corresponding clusters with 100% accuracy. Further, the 8-sensor array was tested with exposures to 19 analyte vapors at 2000 ppm, a concentration beyond the range used to train the LDA model. Surprisingly, only 2-propanol vapor was misclassified into the 1-butanol cluster, likely due to the very close positions in the LDA plot. Nevertheless, the remaining 18 analytes were classified correctly, yielding an accuracy of 94.7%. These results demonstrate the robustness and reliability of the sensor array for the detection and classification of various volatile analytes.

When two similar test analytes are located close to each other in the LDA plot, the likelihood of misclassification increases. To address this, a multiple-layered LDA classification approach was employed in a preliminary experiment to evaluate the ability of cluster separation. As depicted in the upper LDA plot (the LDA trained with dataset measured in week 5, as shown in Figure 7.43b) in Figure 7.46, a dash line can serve as a boundary to distinguish between polar and nonpolar analytes. Following this, two sequential LDA models were trained using responses from exposures to either polar or nonpolar analytes exclusively, as illustrated in the bottom LDA plots. This approach improved clustering and separation of the analytes. In practical applications, if a test exposure is assigned to a cluster in the polar region, a sequential polar LDA model can be employed to classify the analyte more accurately, and similarly for test exposures assigned to the nonpolar region. This double-layered LDA classification approach appears to reduce the probability of misclassification. Adding further layers to discriminate between specific classes, such as alcohols, ketones, and alkanes, could potentially enhance the capability to separate individual

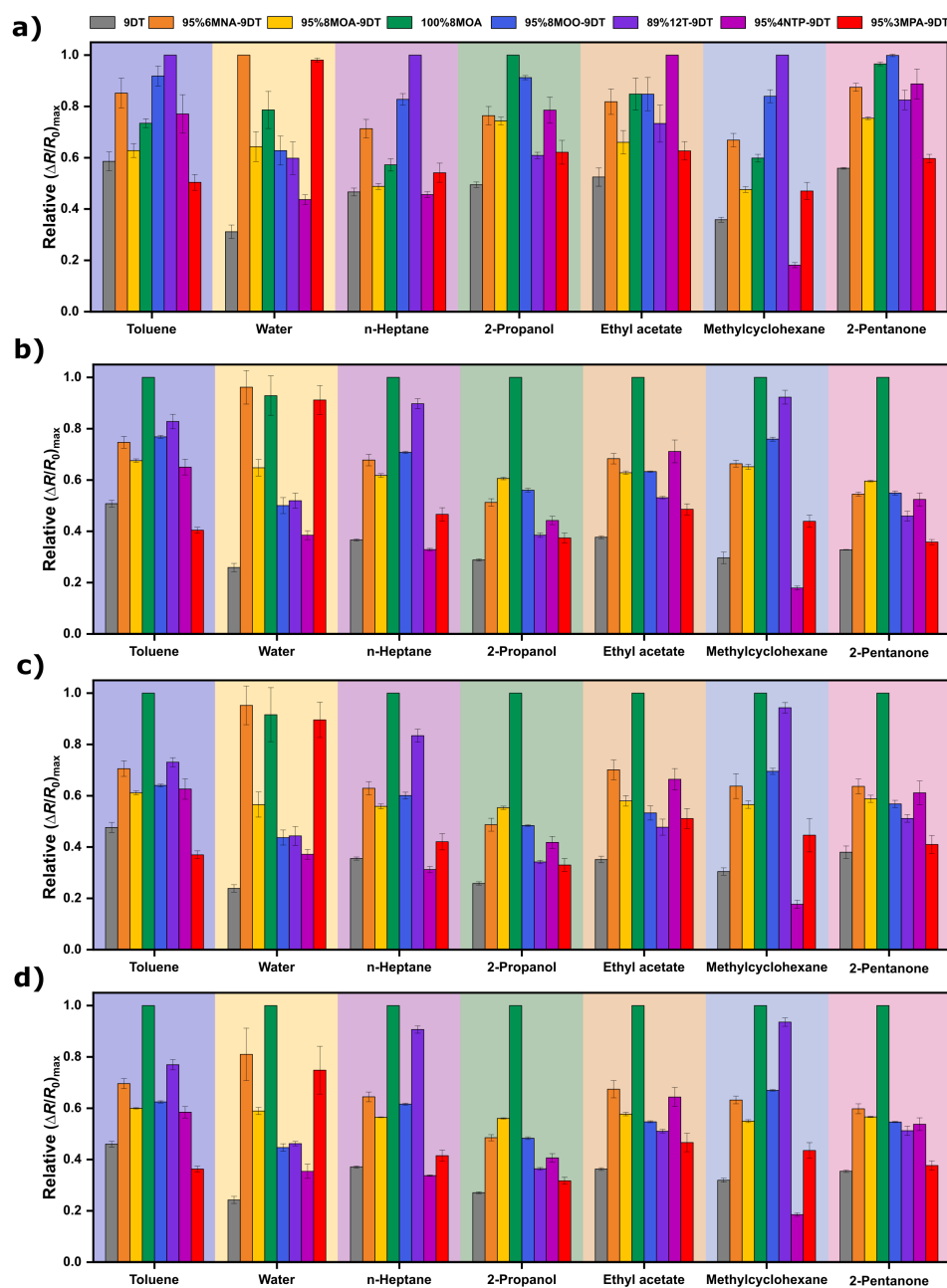


Figure 7.45: Average relative $(\Delta R/R_0)_{\max}$ for 8 GNP sensors (indicated by different bar colors) exposed to 7 analyte vapors in a) week 1 (in the concentration range of 100-1000 ppm), b) week 3 (in the concentration range of 100-1000 ppm), c) week 5 (in the concentration range of 100-1000 ppm), and d) week 7 (in the concentration range of 600-2000 ppm).

clusters.

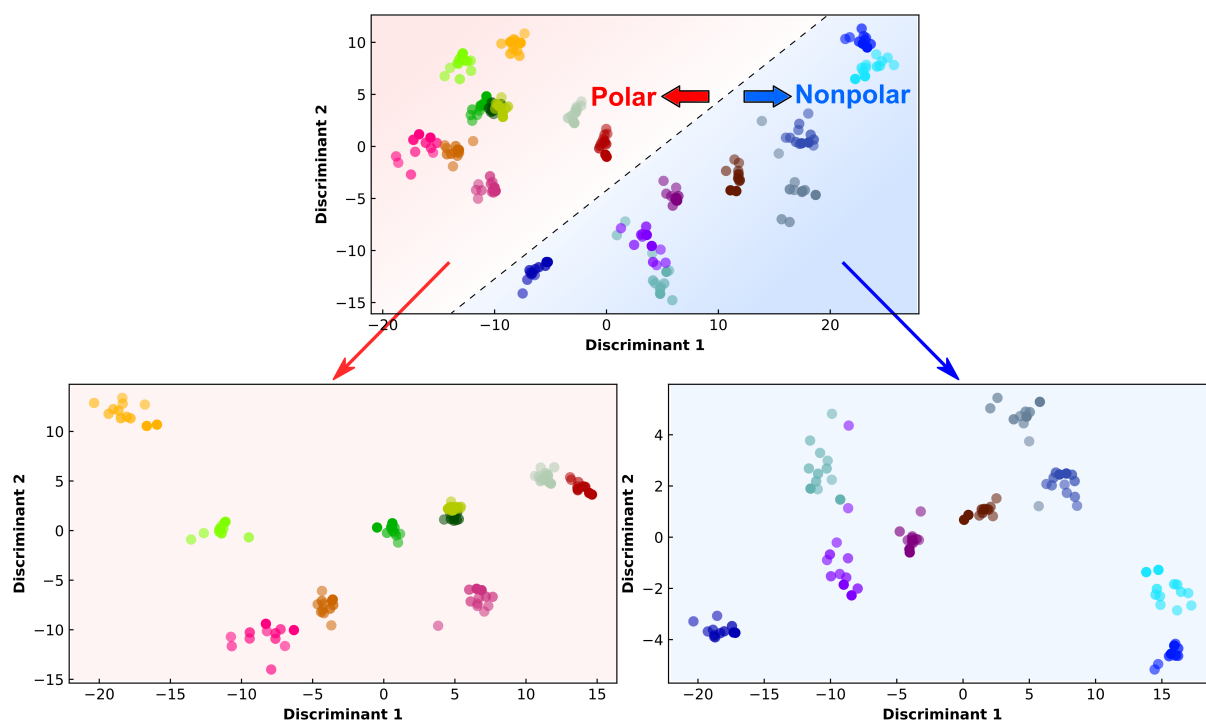


Figure 7.46: LDA plots of the 8-sensor array responses measured in week 5, corresponding to Figure 7.43b. The bottom left LDA plot is trained solely with responses from exposures to 10 polar analytes, and the bottom right LDA plot is trained solely with responses from exposures to 9 nonpolar analytes. (Vapor concentration range: 100-1000 ppm)

7.5.4 Summary and Outlook

This study focused on the development and characterization of monolithic chemiresistor arrays for the classification of volatile chemical compounds. To this end, a facile fabrication pathway was proposed, combining straightforward GNP film fabrication via the LbL-SC process[85] with DUV-lithographic patterning[23] of the GNP films. This approach allows for the fabrication of a sensor array consisting of various GNP films using the ligand/linker mixture strategy outlined in Section 7.3.

In preliminary experiments, an array comprising four pairs of GNP films was exposed to 17 different analyte vapors. An LDA model was trained using three features extracted from the transient responses, including one "steady-state" feature and two "transient-state" features. After normalization, it was shown that some of the features were sensitive to the molecular volume and dielectric constant of the analytes, facilitating effective classification of different analytes, including isomers like 1-propanol and 2-propanol. All analytes were correctly assigned to their respective clusters when the training and test datasets were derived from responses measured on the same day. However, this 4-sensor array experienced aging issues, which led to significantly decreased classification accuracy over time.

To improve stability and classification-capability for an even more diverse range of volatile chemical compounds, a sensor array comprised of 8 different GNP films was fabricated, and exposed to 19 different

analytes. These efforts resulted in improved cluster separation in the LDA plot compared to the 4-sensor array. After a stabilization period, the 8-sensor array exhibited remarkable stability and classification accuracy of 100% over time (the training data and the test data were measured approximately 8 to 11 days apart) when tested with exposures within the concentration range of the training data (results as shown in Figures A76 and A77 in the Appendix). Even when tested with analyte vapors at 2000 ppm, beyond the concentration range of training data, the array still demonstrated high accuracy, with only one misclassification. As shown in Figure A78 in the Appendix, the data point corresponding to the 2000 ppm 2-propanol exposure was projected onto the area of the LDA plot where the alcohols, 1-propanol, 2-propanol, and 1-butanol, were located. However, similar to the results discussed in Section 7.5.2, when the response patterns of features are highly similar within a group of analytes, LDA may struggle to distinguish them. Thus, even though the 2000 ppm 2-propanol exposure was projected close to the 2-propanol cluster in the LDA plot, it was still assigned to the 1-butanol cluster. Overall, this study highlights the importance of stability and reliability in chemiresistor arrays for practical applications. The results demonstrate the effectiveness of the developed array in accurately detecting and classifying volatile chemical compounds, even over time and at varying concentrations. However, since the response characteristics of the sensors change over time due to aging, periodic re-training of the LDA model may be required to maintain the reliability of analyte classification.

Moving forward, future research endeavors could focus on enhancing the performance of sensor arrays in two key directions: i) expanding the diversity of the GNP films applied in the array, and ii) optimizing data analysis using machine learning models. While this study explored four types of functional groups of the MT ligands, there is potential to investigate additional groups, such as alkoxy compounds and amines, which have shown effectiveness in controlling the selectivity in gas sensing applications. The development of a highly versatile sensor array could lead to broad applications in breath diagnosis, environmental monitoring, and toxic gas detection.

As shown in Figure 7.46, the multiple-layered LDA classification approach can enhance the separation of different analyte clusters. However, the boundary used to assign test analytes to either polar or nonpolar regions remains unclear. Therefore, a broader variety of both polar and nonpolar compounds should be tested and included in the training dataset for the LDA model to obtain a clearer understanding of where the boundary lies. Additionally, considering the use of neural networks could further enhance classification capabilities. Unlike simpler algorithms, such as LDA, neural networks can leverage deep learning techniques, enabling them to analyze entire response transient datasets rather than specific data points. Neural networks excel at handling non-linear relationships and large datasets effectively. This capability allows them to process complex datasets more efficiently, and may potentially outperform traditional LDA models.[215, 216]

Chapter 8

Bibliography

- [1] K. Schaefer, C.-Y. Liu, A. Meyer, H. Schlicke, T. Vossmeier, C. Herrmann, *The Journal of Physical Chemistry C* **2023**, *128*, 3994–4008.
- [2] C.-Y. Liu, S. C. Bittinger, A. Bose, A. Meyer, H. Schlicke, T. Vossmeier, *Advanced Materials Interfaces* **2024**, *11*, 2301058.
- [3] J. Langer, S. M. Novikov, L. M. Liz-Marzán, *Nanotechnology* **2015**, *26*, 322001.
- [4] J. Sun, Y. Lu, L. He, J. Pang, F. Yang, Y. Liu, *TrAC Trends in Analytical Chemistry* **2020**, *122*, 115754.
- [5] R. Elghanian, J. J. Storhoff, R. C. Mucic, R. L. Letsinger, C. A. Mirkin, *Science* **1997**, *277*, 1078–1081.
- [6] P. K. Jain, K. S. Lee, I. H. El-Sayed, M. A. El-Sayed, *The journal of Physical Chemistry B* **2006**, *110*, 7238–7248.
- [7] A. Zabet-Khosousi, A.-A. Dhirani, *Chemical Reviews* **2008**, *108*, 4072–4124.
- [8] F. J. Ibanez, F. P. Zamborini, *Acs Nano* **2008**, *2*, 1543–1552.
- [9] F. J. Ibañez, F. P. Zamborini, *Small* **2012**, *8*, 174–202.
- [10] M. Gauvin, Y. Wan, I. Arfaoui, M.-P. Pileni, *The Journal of Physical Chemistry C* **2014**, *118*, 5005–5012.
- [11] H. Schlicke, E. W. Leib, A. Petrov, J. H. Schröder, T. Vossmeier, *The Journal of Physical Chemistry C* **2014**, *118*, 4386–4395.
- [12] H. Schlicke, S. Kunze, M. Finsel, E. W. Leib, C. J. Schröter, M. Blankenburg, H. Noei, T. Vossmeier, *The Journal of Physical Chemistry C* **2019**, *123*, 19165–19174.
- [13] H. Wohltjen, A. W. Snow, *Analytical Chemistry* **1998**, *70*, 2856–2859.
- [14] N. Olichwer, A. Meyer, M. Yesilmen, T. Vossmeier, *Journal of Materials Chemistry C* **2016**, *4*, 8214–8225.
- [15] N. Olichwer, E. W. Leib, A. H. Halfar, A. Petrov, T. Vossmeier, *ACS Applied Materials & Interfaces* **2012**, *4*, 6151–6161.

- [16] Y. Joseph, I. Besnard, M. Rosenberger, B. Guse, H.-G. Nothofer, J. M. Wessels, U. Wild, A. Knop-Gericke, D. Su, R. Schlögl, et al., *The Journal of Physical Chemistry B* **2003**, *107*, 7406–7413.
- [17] Y. Joseph, A. Peić, X. Chen, J. Michl, T. Vossmeier, A. Yasuda, *The Journal of Physical Chemistry C* **2007**, *111*, 12855–12859.
- [18] H. Schlicke, S. C. Bittinger, H. Noei, T. Vossmeier, *ACS Applied Nano Materials* **2021**, *4*, 10399–10408.
- [19] T. Vossmeier, Y. Joseph, I. Besnard, O. Harnack, N. Krasteva, B. Guse, H.-G. Nothofer, A. Yasuda in *Physical Chemistry of Interfaces and Nanomaterials III, Vol. 5513*, SPIE, **2004**, pp. 202–212.
- [20] N. Krasteva, I. Besnard, B. Guse, R. E. Bauer, K. Müllen, A. Yasuda, T. Vossmeier, *Nano Letters* **2002**, *2*, 551–555.
- [21] N. Krasteva, B. Guse, I. Besnard, A. Yasuda, T. Vossmeier, *Sensors and Actuators B: Chemical* **2003**, *92*, 137–143.
- [22] F. J. Ibañez, U. Gowrishetty, M. M. Crain, K. M. Walsh, F. P. Zamborini, *Analytical Chemistry* **2006**, *78*, 753–761.
- [23] H. Schlicke, S. C. Bittinger, T. Vossmeier, *ACS Applied Electronic Materials* **2020**, *2*, 3741–3748.
- [24] B. Ketelsen, P. P. Tjarks, H. Schlicke, Y.-C. Liao, T. Vossmeier, *Chemosensors* **2020**, *8*, 116.
- [25] L. Wang, L. Wang, X. Shi, N. N. Kariuki, M. Schadt, G. R. Wang, Q. Rendeng, J. Choi, J. Luo, S. Lu, et al., *Journal of the American Chemical Society* **2007**, *129*, 2161–2170.
- [26] M. K. Nakhleh, Y. Y. Broza, H. Haick, *Nanomedicine* **2014**, *9*, 1991–2002.
- [27] Y. Y. Broza, X. Zhou, M. Yuan, D. Qu, Y. Zheng, R. Vishinkin, M. Khatib, W. Wu, H. Haick, *Chemical Reviews* **2019**, *119*, 11761–11817.
- [28] U. Tisch, I. Schlesinger, R. Ionescu, M. Nassar, N. Axelrod, D. Robertman, Y. Tessler, F. Azar, A. Marmur, J. Aharon-Peretz, et al., *Nanomedicine* **2013**, *8*, 43–56.
- [29] N. Kahn, O. Lavie, M. Paz, Y. Segev, H. Haick, *Nano Letters* **2015**, *15*, 7023–7028.
- [30] W. Zhao, L. F. Al-Nasser, S. Shan, J. Li, Z. Skeete, N. Kang, J. Luo, S. Lu, C.-J. Zhong, C. J. Grausgruber, et al., *Sensors and Actuators B: Chemical* **2016**, *232*, 292–299.
- [31] G. Shang, D. Dinh, T. Mercer, S. Yan, S. Wang, B. Malaei, J. Luo, S. Lu, C.-J. Zhong, *ACS Sensors* **2023**, *8*, 1328–1338.
- [32] G. Peng, U. Tisch, O. Adams, M. Hakim, N. Shehada, Y. Y. Broza, S. Billan, R. Abdah-Bortnyak, A. Kuten, H. Haick, *Nature Nanotechnology* **2009**, *4*, 669–673.
- [33] G. Peng, M. Hakim, Y. Broza, S. Billan, R. Abdah-Bortnyak, A. Kuten, U. Tisch, H. Haick, *British Journal of Cancer* **2010**, *103*, 542–551.
- [34] B. Shan, Y. Y. Broza, W. Li, Y. Wang, S. Wu, Z. Liu, J. Wang, S. Gui, L. Wang, Z. Zhang, et al., *ACS Nano* **2020**, *14*, 12125–12132.
- [35] M. S. Webster, J. S. Cooper, E. Chow, L. J. Hubble, A. Sosa-Pintos, L. Wieczorek, B. Raguse, *Sensors and Actuators B: Chemical* **2015**, *220*, 895–902.
- [36] L. Wright, E. Zellers, *Analyst* **2013**, *138*, 6860–6868.

- [37] T. Gao, C. Zhang, Y. Wang, J. A. Diaz, J. Zhao, B. G. Willis, *IEEE Sensors Journal* **2020**, *20*, 14016–14023.
- [38] T. Gao, Y. Wang, K. Fu, C. Zhang, Z. A. Pittman, J. Zhao, B. G. Willis in 2019 IEEE SENSORS, IEEE, **2019**, pp. 1–4.
- [39] T. Gao, Y. Wang, C. Zhang, Z. A. Pittman, A. M. Oliveira, K. Fu, J. Zhao, R. Srivastava, B. G. Willis, *Sensors* **2019**, *19*, 2547.
- [40] M. Ancona, A. Snow, F. Perkins, B. Pate, D. Park, *Sensors and Actuators B: Chemical* **2013**, *177*, 936–946.
- [41] L. J. Hubble, J. S. Cooper, A. Sosa-Pintos, H. Kiiveri, E. Chow, M. S. Webster, L. Wieczorek, B. Raguse, *ACS Combinatorial Science* **2015**, *17*, 120–129.
- [42] K.-C. Yeh, Y.-Y. Tsai, S.-W. Chang, *The Journal of Physical Chemistry C* **2022**, *126*, 6456–6464.
- [43] D. J. Barber, I. C. Freestone, *Archaeometry* **1990**, *32*, 33–45.
- [44] U. Leonhardt, *Nature Photonics* **2007**, *1*, 207–208.
- [45] M. Faraday, *Philosophical transactions of the Royal Society of London* **1857**, 145–181.
- [46] J. Turkevich, P. C. Stevenson, J. Hillier, *Discussions of the Faraday Society* **1951**, *11*, 55–75.
- [47] M. Brust, M. Walker, D. Bethell, D. J. Schiffrin, R. Whyman, *Journal of the Chemical Society Chemical Communications* **1994**, 801–802.
- [48] T. Mappes, N. Jahr, A. Csaki, N. Vogler, J. Popp, W. Fritzsche, *Angewandte Chemie International Edition* **2012**, *51*, 11208–11212.
- [49] H. Siedentopf, R. Zsigmondy, *Annalen der Physik* **1902**, *315*, 1–39.
- [50] G. Mie, *Annalen der Physik* **1908**, *330*, 377–445.
- [51] S. K. Ghosh, T. Pal, *Chemical Reviews* **2007**, *107*, 4797–4862.
- [52] S. Link, M. A. El-Sayed, *The Journal of Physical Chemistry B* **1999**, *103*, 8410–8426.
- [53] K. L. Kelly, E. Coronado, L. L. Zhao, G. C. Schatz, *The Journal of Physical Chemistry B* **2003**, *107*, 668–677.
- [54] V. Amendola, R. Pilot, M. Frascioni, O. M. Maragò, M. A. Iatì, *Journal of Physics: Condensed Matter* **2017**, *29*, 203002.
- [55] J. C. Maxwell-Garnett, *Philosophical Transactions of the Royal Society of London. Series A Containing Papers of a Mathematical or Physical Character* **1904**, *203*, 385–420.
- [56] J. C. Maxwell-Garnett, *Philosophical Transactions of the Royal Society of London. Series A Containing Papers of a Mathematical or Physical Character* **1906**, *205*, 237–288.
- [57] T. Ung, L. M. Liz-Marzán, P. Mulvaney, *The Journal of Physical Chemistry B* **2001**, *105*, 3441–3452.
- [58] G. Frens, *Nature Physical Science* **1973**, *241*, 20–22.
- [59] I. Ojea-Jiménez, N. G. Bastús, V. Puentes, *The Journal of Physical Chemistry C* **2011**, *115*, 15752–15757.
- [60] F. Schulz, T. Homolka, N. G. Bastus, V. Puentes, H. Weller, T. Vossmeier, *Langmuir* **2014**, *30*, 10779–10784.

- [61] D. V. Leff, L. Brandt, J. R. Heath, *Langmuir* **1996**, *12*, 4723–4730.
- [62] N. Zheng, J. Fan, G. D. Stucky, *Journal of the American Chemical Society* **2006**, *128*, 6550–6551.
- [63] C. R. Patra, R. Bhattacharya, E. Wang, A. Katarya, J. S. Lau, S. Dutta, M. Muders, S. Wang, S. A. Buhrow, S. L. Safgren, et al., *Cancer Research* **2008**, *68*, 1970–1978.
- [64] P. Baptista, E. Pereira, P. Eaton, G. Doria, A. Miranda, I. Gomes, P. Quaresma, R. Franco, *Analytical and Bioanalytical Chemistry* **2008**, *391*, 943–950.
- [65] A. Corma, H. Garcia, *Chemical Society Reviews* **2008**, *37*, 2096–2126.
- [66] Z. Wang, L. Ma, *Coordination Chemistry Reviews* **2009**, *253*, 1607–1618.
- [67] C. S. Thaxton, D. G. Georganopoulou, C. A. Mirkin, *Clinica Chimica Acta* **2006**, *363*, 120–126.
- [68] J. Wang, L. Liu, J. Guo, X. Zhao, Y. Zhang, Y. Yan, *Advanced Functional Materials* **2023**, 2309531.
- [69] K. Saha, S. S. Agasti, C. Kim, X. Li, V. M. Rotello, *Chemical Reviews* **2012**, *112*, 2739–2779.
- [70] R. A. Potyrailo, *Chemical Reviews* **2016**, *116*, 11877–11923.
- [71] S. Huang, K. Minami, H. Sakaue, S. Shingubara, T. Takahagi, *Langmuir* **2004**, *20*, 2274–2276.
- [72] A. Gharra, Y. Y. Broza, G. Yu, W. Mao, D. Shen, L. Deng, C. Wu, Q. Wang, X. Sun, J. Huang, et al., *Cancer Communications* **2020**, *40*, 273.
- [73] Y. Milyutin, M. Abud-Hawa, V. Kloper-Weidenfeld, E. Mansour, Y. Y. Broza, G. Shani, H. Haick, *Nature Protocols* **2021**, *16*, 2968–2990.
- [74] C.-Y. Yang, C.-L. Li, C.-J. Lu, *Analytica Chimica Acta* **2006**, *565*, 17–26.
- [75] S. Johnson, S. Evans, R. Brydson, *Langmuir* **1998**, *14*, 6639–6647.
- [76] K. Fu, S. Chen, J. Zhao, B. G. Willis, *ACS Sensors* **2016**, *1*, 444–450.
- [77] T. Degousee, W. G. Neal, Z. Edwards, S. Singh, J. Selvarajah, T. S. Talha-Dean, M. Palma, B. C. Schroeder, J. Mol, *Journal of Materials Chemistry C* **2023**, *11*, 16518–16526.
- [78] L. Han, D. R. Daniel, M. M. Maye, C.-J. Zhong, *Analytical Chemistry* **2001**, *73*, 4441–4449.
- [79] F. L. Leibowitz, W. Zheng, M. M. Maye, C.-J. Zhong, *Analytical Chemistry* **1999**, *71*, 5076–5083.
- [80] M. N. Martin, J. I. Basham, P. Chando, S.-K. Eah, *Langmuir* **2010**, *26*, 7410–7417.
- [81] F. P. Zamborini, M. C. Leopold, J. F. Hicks, P. J. Kulesza, M. A. Malik, R. W. Murray, *Journal of the American Chemical Society* **2002**, *124*, 8958–8964.
- [82] Y. Yang, L. B. Cornwell, F. J. Ibañez, F. P. Zamborini, *ChemElectroChem* **2016**, *3*, 1230–1236.
- [83] D. Bethell, M. Brust, D. Schiffrin, C. Kiely, *Journal of Electroanalytical Chemistry* **1996**, *409*, 137–143.
- [84] Y. Joseph, N. Krasteva, I. Besnard, B. Guse, M. Rosenberger, U. Wild, A. Knop-Gericke, R. Schlögl, R. Krustev, A. Yasuda, et al., *Faraday Discussions* **2004**, *125*, 77–97.
- [85] H. Schlicke, J. H. Schröder, M. Trebbin, A. Petrov, M. Ijeh, H. Weller, T. Vossmeier, *Nanotechnology* **2011**, *22*, 305303.
- [86] E. Chow, T. R. Gengenbach, L. Wiczorek, B. Raguse, *Sensors and Actuators B: Chemical* **2010**, *143*, 704–711.

- [87] R.-S. Jian, C.-J. Tsai, L.-Y. Sung, C.-J. Lu in *SENSORS*, 2011 IEEE, IEEE, **2011**, pp. 732–735.
- [88] E. Garcia-Berrios, T. Gao, J. C. Theriot, M. D. Woodka, B. S. Bruntschwig, N. S. Lewis, *The Journal of Physical Chemistry C* **2011**, *115*, 6208–6217.
- [89] Y. Joseph, B. Guse, T. Vossmeier, A. Yasuda, *The Journal of Physical Chemistry C* **2008**, *112*, 12507–12514.
- [90] B. Ketelsen, M. Yesilmen, H. Schlicke, H. Noei, C.-H. Su, Y.-C. Liao, T. Vossmeier, *ACS Applied Materials & Interfaces* **2018**, *10*, 37374–37385.
- [91] R. Elmqvist, Measuring instrument of the recording type, US Patent 2,566,443, **1951**.
- [92] S. E. Evans, T. Harrington, M. C. R. Rivero, E. Rognin, T. Tuladhar, R. Daly, *International Journal of Pharmaceutics* **2021**, *599*, 120443.
- [93] J. Perelaer, P. Kröber, J. Delaney, U. Schubert in *NIP & Digital Fabrication Conference, Vol. 2009*, Society for Imaging Science and Technology, **2009**, pp. 791–794.
- [94] A. A. Khalate, X. Bombois, R. Babuška, H. Wijshoff, R. Waarsing, *Control Engineering Practice* **2011**, *19*, 771–781.
- [95] C.-H. Wu, W.-S. Hwang, *Microelectronics Reliability* **2015**, *55*, 630–636.
- [96] P. Drude, *Annalen der Physik* **1900**, *306*, 566–613.
- [97] N. W. Ashcroft, N. Mermin, *Solid State Physics*, **1976**.
- [98] H. Lorentz in *KNAW, proceedings, Vol. 7*, **1905**, pp. 438–453.
- [99] P. Atkins, J. De Paula, *Physical Chemistry, Vol. 1*, Macmillan, **2006**.
- [100] G. Schmid, *Journal of the Chemical Society Dalton Transactions* **1998**, 1077–1082.
- [101] C. Neugebauer, M. Webb, *Journal of Applied Physics* **1962**, *33*, 74–82.
- [102] B. Barwiński, *Thin Solid Films* **1985**, *128*, 1–9.
- [103] M. Brust, D. J. Schiffrin, D. Bethell, C. J. Kiely, *Advanced Materials* **1995**, *7*, 795–797.
- [104] M. Brust, D. Bethell, C. J. Kiely, D. J. Schiffrin, *Langmuir* **1998**, *14*, 5425–5429.
- [105] R. H. Terrill, T. A. Postlethwaite, C.-H. Chen, C.-D. Poon, A. Terzis, A. Chen, J. E. Hutchison, M. R. Clark, G. Wignall, *Journal of the American Chemical Society* **1995**, *117*, 12537–12548.
- [106] W. P. Wueling, S. J. Green, J. J. Pietron, D. E. Cliffl, R. W. Murray, *Journal of the American Chemical Society* **2000**, *122*, 11465–11472.
- [107] M. Van Staveren, H. Brom, L. De Jongh, G. Schmid, *Solid State Communications* **1986**, *60*, 319–322.
- [108] G.-F. Hohl, S. Baranovskii, J. Becker, F. Hensel, S. Quaiser, M. Reetz, *Journal of Applied Physics* **1995**, *78*, 7130–7136.
- [109] W. H. Steinecker, M. P. Rowe, E. T. Zellers, *Analytical Chemistry* **2007**, *79*, 4977–4986.
- [110] E. W. Cowell, S. W. Muir, D. A. Keszler, J. F. Wager, *Journal of Applied Physics* **2013**, *114*.
- [111] J. M. Wessels, H.-G. Nothofer, W. E. Ford, F. von Wrochem, F. Scholz, T. Vossmeier, A. Schroedter, H. Weller, A. Yasuda, *Journal of the American Chemical Society* **2004**, *126*, 3349–3356.
- [112] N. J. Tao, *Nature Nanotechnology* **2006**, *1*, 173–181.

- [113] X. Cui, A. Primak, X. Zarate, J. Tomfohr, O. Sankey, A. Moore, T. Moore, D. Gust, L. Nagahara, S. Lindsay, *The Journal of Physical Chemistry B* **2002**, *106*, 8609–8614.
- [114] B. Abeles in *Applied Solid State Science*, Vol. 6, Elsevier, **1976**, pp. 1–117.
- [115] R. A. Marcus, N. Sutin, *Biochimica et Biophysica Acta (BBA)-Reviews on Bioenergetics* **1985**, *811*, 265–322.
- [116] R. A. Marcus, *Angewandte Chemie International Edition in English* **1993**, *32*, 1111–1121.
- [117] V. Montes-Garcia, R. F. de Oliveira, Y. Wang, A. Berezin, P. Fanjul-Bolado, M. B. Gonzalez Garcia, T. M. Hermans, D. Bonifazi, S. Casalini, P. Samori, *Advanced Functional Materials* **2021**, *31*, 2008554.
- [118] B. Raguse, E. Chow, C. S. Barton, L. Wieczorek, *Analytical Chemistry* **2007**, *79*, 7333–7339.
- [119] H. Schlicke, S. Kunze, M. Rebber, N. Schulz, S. Riekeberg, H. K. Trieu, T. Vossmeier, *Advanced Functional Materials* **2020**, *30*, 2003381.
- [120] B. Ketelsen, H. Schlicke, V. R. Schulze, S. C. Bittinger, S.-D. Wu, S.-h. Hsu, T. Vossmeier, *Advanced Functional Materials* **2023**, *33*, 2210065.
- [121] S.-D. Wu, S.-h. Hsu, B. Ketelsen, S. C. Bittinger, H. Schlicke, H. Weller, T. Vossmeier, *Small Methods* **2023**, 2300170.
- [122] J. Curie, P. Curie, *Bulletin de Minéralogie* **1880**, *3*, 90–93.
- [123] S. Katzir in *The Beginnings of Piezoelectricity: A Study in Mundane Physics*, Springer, **2006**, pp. 15–64.
- [124] J. Janata, J. Janata, *Principles of Chemical Sensors* **2009**, 63–98.
- [125] P. Sharma, A. Ghosh, B. Tudu, S. Sabhapondit, B. D. Baruah, P. Tamuly, N. Bhattacharyya, R. Bandyopadhyay, *Sensors and Actuators B: Chemical* **2015**, *219*, 146–157.
- [126] C. Barthet, P. Montméat, N. Eloy, P. Prené, *Procedia Engineering* **2010**, *5*, 472–475.
- [127] F. Parret, P. Montméat, P. Prené in *SENSORS, 2007 IEEE*, IEEE, **2007**, pp. 248–251.
- [128] Y. Zhihua, Z. Liang, S. Kaixin, H. Weiwei, *Procedia Engineering* **2012**, *29*, 2448–2452.
- [129] V. Van Quang, V. N. Hung, V. N. Phan, T. Q. Huy, N. Van Quy, et al., *Thin Solid Films* **2014**, *568*, 6–12.
- [130] Y. Jin, Y. Huang, G. Liu, R. Zhao, *Analyst* **2013**, *138*, 5479–5485.
- [131] J. Ortega-Valencia, J. Oliva-Ramirez, O. Garcia-Barradas, M. Jiménez-Fernández, G. Rosas-Saito, J. Oseguera-Peña, D. Melo-Máximo, *Materials Letters* **2022**, *314*, 131885.
- [132] G. Sauerbrey, *Zeitschrift für Physik* **1959**, *155*, 206–222.
- [133] F.-G. Banica, *Chemical Sensors and Biosensors: Fundamentals and Applications*, John Wiley & Sons, **2012**.
- [134] A. Janshoff, H.-J. Galla, C. Steinem, *Angewandte Chemie International Edition* **2000**, *39*, 4004–4032.
- [135] C.-L. Li, Y.-F. Chen, M.-H. Liu, C.-J. Lu, *Sensors and Actuators B: Chemical* **2012**, *169*, 349–359.
- [136] J. W. Grate, D. A. Nelson, R. Skaggs, *Analytical Chemistry* **2003**, *75*, 1868–1879.

- [137] Y. Joseph, B. Guse, A. Yasuda, T. Vossmeier, *Sensors and Actuators B: Chemical* **2004**, *98*, 188–195.
- [138] Y. Li, J. Huang, R. T. McIver Jr, J. C. Hemminger, *Journal of the American Chemical Society* **1992**, *114*, 2428–2432.
- [139] J. Huang, J. C. Hemminger, *Journal of the American Chemical Society* **1993**, *115*, 3342–3343.
- [140] D. A. Hutt, G. J. Leggett, *The Journal of Physical Chemistry* **1996**, *100*, 6657–6662.
- [141] M. H. Schoenfish, J. E. Pemberton, *Journal of the American Chemical Society* **1998**, *120*, 4502–4513.
- [142] N. J. Brewer, R. E. Rawsterne, S. Kothari, G. J. Leggett, *Journal of the American Chemical Society* **2001**, *123*, 4089–4090.
- [143] T. M. Willey, A. L. Vance, T. Van Buuren, C. Bostedt, L. Terminello, C. Fadley, *Surface Science* **2005**, *576*, 188–196.
- [144] J. Maciel, M. C. L. Martins, M. A. Barbosa, *Journal of Biomedical Materials Research Part A* **2010**, *94*, 833–843.
- [145] J. Im, S. K. Sengupta, M. F. Baruch, C. D. Granz, S. Ammu, S. K. Manohar, J. E. Whitten, *Sensors and Actuators B: Chemical* **2011**, *156*, 715–722.
- [146] N. Garg, A. Mohanty, N. Lazarus, L. Schultz, T. R. Rozzi, S. Santhanam, L. Weiss, J. L. Snyder, G. K. Fedder, R. Jin, *Nanotechnology* **2010**, *21*, 405501.
- [147] Y. Joseph, B. Guse, G. Nelles, *Chemistry of Materials* **2009**, *21*, 1670–1676.
- [148] B. Ketelsen, Available at https://ediss.sub.uni-hamburg.de/bitstream/ediss/9949/1/Dissertation_Bendix_Ketelsen_final_publication.compressed.pdf, PhD thesis, University of Hamburg, Hamburg, Germany, **2022**.
- [149] Z. Xie, M. V. R. Raju, A. C. Stewart, M. H. Nantz, X.-A. Fu, *RSC Advances* **2018**, *8*, 35618–35624.
- [150] Z. Xie, M. V. Ramakrishnam Raju, P. K. Adihetty, X.-A. Fu, M. H. Nantz, *Sensors* **2020**, *20*, 7024.
- [151] K. Persaud, G. Dodd, *Nature* **1982**, *299*, 352–355.
- [152] P. Gouma, G. Sberveglieri, *MRS Bulletin* **2004**, *29*, 697–702.
- [153] J. S. Cooper, B. Raguse, E. Chow, L. Hubble, K.-H. Müller, L. Wieczorek, *Analytical Chemistry* **2010**, *82*, 3788–3795.
- [154] O. Marom, F. Nakhoul, U. Tisch, A. Shiban, Z. Abassi, H. Haick, *Nanomedicine* **2012**, *7*, 639–650.
- [155] Z. Li, Y. Liu, O. Hossain, R. Paul, S. Yao, S. Wu, J. B. Ristaino, Y. Zhu, Q. Wei, *Matter* **2021**, *4*, 2553–2570.
- [156] J. Luo, J. Luo, L. Wang, X. Shi, J. Yin, E. Crew, S. Lu, L. M. Lesperance, C.-J. Zhong, *Sensors and Actuators B: Chemical* **2012**, *161*, 845–854.
- [157] C. D. Natale, E. Martinelli, G. Pennazza, A. Orsini, M. Santonico in *Advances in Sensing with Security Applications*, Springer, **2006**, pp. 147–169.

- [158] S. K. Vungarala, PCA vs LDA — No more confusion!, **2023**, <https://medium.com/@seshu8hachi/pca-vs-lda-no-more-confusion-fc21fb8d06e9#:~:text=PCA%20is%20an%20unsupervised%20method%20that%20aims%20to%20find%20the,the%20characteristics%20of%20the%20dataset>. (visited on 01/31/2024).
- [159] A. Tharwat, T. Gaber, A. Ibrahim, A. E. Hassanien, *AI Communications* **2017**, *30*, 169–190.
- [160] S. Peng, Y. Lee, C. Wang, H. Yin, S. Dai, S. Sun, *Nano Research* **2008**, *1*, 229–234.
- [161] W. Haiss, N. T. Thanh, J. Aveyard, D. G. Fernig, *Analytical Chemistry* **2007**, *79*, 4215–4221.
- [162] S. Förster, A. Timmann, M. Konrad, C. Schellbach, A. Meyer, S. Funari, P. Mulvaney, R. Knott, *The Journal of Physical Chemistry B* **2005**, *109*, 1347–1360.
- [163] S. Förster, L. Apostol, W. Bras, *Journal of Applied Crystallography* **2010**, *43*, 639–646.
- [164] A. Technologies, Agilent E5100A/B Network Analyzer Programming Manual, Agilent Technologies, 373 pp.
- [165] S.-D. Wu, B. Ketelsen, S.-h. Hsu, T. Vossmeier in Proceedings, Vol. 56, MDPI, **2020**, p. 17.
- [166] E. Song, T. H. da Costa, J.-W. Choi, *Microsystem Technologies* **2017**, *23*, 3505–3511.
- [167] C.-H. Su, H.-L. Chiu, Y.-C. Chen, M. Yesilmen, F. Schulz, B. Ketelsen, T. Vossmeier, Y.-C. Liao, *Langmuir* **2019**, *35*, 3256–3264.
- [168] Y. Li, Q. Yang, M. Li, Y. Song, *Scientific Reports* **2016**, *6*, 24628.
- [169] E. Skotadis, J. Tang, V. Tsouti, D. Tsoukalas, *Microelectronic engineering* **2010**, *87*, 2258–2263.
- [170] C. L. Yaws, *The Yaws Handbook of Vapor Pressure: Antoine Coefficients*, Gulf Professional Publishing, **2015**.
- [171] K. Musa-Veloso, S. S. Likhodii, S. C. Cunnane, *The American Journal of Clinical Nutrition* **2002**, *76*, 65–70.
- [172] V. Ruzsányi, M. P. Kalapos, *Journal of Breath Research* **2017**, *11*, 024002.
- [173] Z. Wang, C. Wang, *Journal of Breath Research* **2013**, *7*, 037109.
- [174] O. B. Crofford, R. E. Mallard, R. Winton, N. L. Rogers, J. C. Jackson, U. Keller, *Transactions of the American Clinical and Climatological Association* **1977**, *88*, 128.
- [175] X.-D. Zhao, W.-F. Sun, H. Zhao, *Polymers* **2019**, *11*, 592.
- [176] M. Singh, N. Kaur, G. Drera, A. Casotto, L. Sangaletti, E. Comini, *Advanced Functional Materials* **2020**, *30*, 2003217.
- [177] A. W. Snow, M. G. Ancona, D. Park, *Langmuir* **2012**, *28*, 15438–15443.
- [178] R.-X. Huang, C.-J. Lu, W.-C. Tian, *Chemosensors* **2014**, *2*, 85–96.
- [179] L. Han, J. Luo, N. N. Kariuki, M. M. Maye, V. W. Jones, C. J. Zhong, *Chemistry of Materials* **2003**, *15*, 29–37.
- [180] L. Han, X. Shi, W. Wu, F. L. Kirk, J. Luo, L. Wang, D. Mott, L. Cousineau, I. Stephanie, I. Lim, et al., *Sensors and Actuators B: Chemical* **2005**, *106*, 431–441.
- [181] J. Yin, P. Hu, J. Luo, L. Wang, M. F. Cohen, C.-J. Zhong, *ACS Nano* **2011**, *5*, 6516–6526.
- [182] R. S. Andre, L. A. Mercante, M. H. Facure, R. C. Sanfelice, L. Fugikawa-Santos, T. M. Swager, D. S. Correa, *ACS sensors* **2022**, *7*, 2104–2131.

- [183] V. Kumar, P. Guleria, S. K. Mehta, *Nanoscience in Food and Agriculture 3* **2016**, 145–181.
- [184] J. W. Erisman, R. Otjes, A. Hensen, P. Jongejan, P. Van Den Bulk, A. Khlystov, H. Möls, S. Slanina, *Atmospheric Environment* **2001**, *35*, 1913–1922.
- [185] D. J. Kearney, T. Hubbard, D. Putnam, *Digestive Diseases and Sciences* **2002**, *47*, 2523–2530.
- [186] N. C. for Biotechnology Information (US), PubChem Annotation Record for , N-BUTYLAMINE, Source: Hazardous Substances Data Bank (HSDB), **2024**, <http://web.archive.org/web/20080207010024/http://www.808multimedia.com/winnt/kernel.htm> (visited on 07/24/2024).
- [187] J. M. Garnett, *Philosophical Transactions of the Royal Society of London. Series A Containing Papers of a Mathematical or Physical Character* **1904**, *203*, 385–420.
- [188] C. Jin, E. T. Zellers, P. Kurzawski, A. Hierlemann in *SENSORS*, 2007 IEEE, IEEE, **2007**, pp. 1217–1220.
- [189] C. Jin, P. Kurzawski, A. Hierlemann, E. T. Zellers, *Analytical Chemistry* **2008**, *80*, 227–236.
- [190] C. Jin, E. T. Zellers, *Analytical Chemistry* **2008**, *80*, 7283–7293.
- [191] W. Luedtke, U. Landman, *The Journal of Physical Chemistry* **1996**, *100*, 13323–13329.
- [192] W. Luedtke, U. Landman, *The Journal of Physical Chemistry B* **1998**, *102*, 6566–6572.
- [193] K. M. Salerno, D. S. Bolintineanu, J. M. D. Lane, G. S. Grest, *Physical Review Letters* **2014**, *113*, 258301.
- [194] K. M. Salerno, D. S. Bolintineanu, J. M. D. Lane, G. S. Grest, *Physical Review E* **2015**, *91*, 062403.
- [195] K.-C. Yeh, Y. Chiang, S.-W. Chang, *Multiscale Science and Engineering* **2020**, *2*, 242–251.
- [196] A. P. Thompson, H. M. Aktulga, R. Berger, D. S. Bolintineanu, W. M. Brown, P. S. Crozier, P. J. in 't Veld, A. Kohlmeyer, S. G. Moore, T. D. Nguyen, R. Shan, M. J. Stevens, J. Tranchida, C. Trott, S. J. Plimpton, *Comp. Phys. Comm.* **2022**, *271*, 108171.
- [197] G.-T. Bae, C. M. Aikens, *The Journal of Physical Chemistry A* **2013**, *117*, 10438–10446.
- [198] M. Reik, M. Calabro, S. Griesemer, E. Barry, W. Bu, B. Lin, S. A. Rice, *Soft Matter* **2019**, *15*, 8800–8807.
- [199] C. D. Bain, E. B. Troughton, Y. T. Tao, J. Evall, G. M. Whitesides, R. G. Nuzzo, *Journal of the American Chemical Society* **1989**, *111*, 321–335.
- [200] L. Motte, M. Pileni, *The Journal of Physical Chemistry B* **1998**, *102*, 4104–4109.
- [201] N. Olichwer, T. Koschine, A. Meyer, W. Egger, K. Rätzke, T. Vossmeier, *RSC Advances* **2016**, *6*, 113163–113172.
- [202] B. Hourahine, B. Aradi, V. Blum, F. Bonafé, A. Buccheri, C. Camacho, C. Cevallos, M. Deshayé, T. Dumitrică, A. Dominguez, et al., *The Journal of Chemical Physics* **2020**, *152*.
- [203] S. Huang, A. Croy, L. A. Panes-Ruiz, V. Khavrus, V. Bezugly, B. Ibarlucea, G. Cuniberti, *Advanced Intelligent Systems* **2022**, *4*, 2200016.
- [204] A. Sharma, K. K. Paliwal, *International Journal of Machine Learning and Cybernetics* **2015**, *6*, 443–454.
- [205] E. Llobet, J. Brezmes, X. Vilanova, J. E. Sueiras, X. Correig, *Sensors and Actuators B: Chemical* **1997**, *41*, 13–21.

- [206] N. Joshi, V. Kushvaha, P. Madhushri, *Machine Learning for Advanced Functional Materials*, Springer, **2023**.
- [207] H. Yuan, C. Xiao, W. Zhan, Y. Wang, C. Shi, H. Ye, K. Jiang, Z. Ye, C. Zhou, Y. Wen, et al., *Journal of Intelligent & Robotic Systems* **2019**, *94*, 871–882.
- [208] K. A. Ngo, P. Lauque, K. Aguir, *Sensors and Materials* **2006**, *18*, 251–260.
- [209] E. C. Nallon, V. P. Schnee, C. J. Bright, M. P. Polcha, Q. Li, *Analytical Chemistry* **2016**, *88*, 1401–1406.
- [210] X. Shi, S. Lu, L. Wang, J. Luo, C.-J. Zhong, G. Wang in IIE Annual Conference. Proceedings, Institute of Industrial and Systems Engineers (IIE), **2006**, p. 1.
- [211] Z. Lei, S. Liao, S. Z. Li in Proceedings of the 21st International Conference on Pattern Recognition (ICPR2012), IEEE, **2012**, pp. 1136–1139.
- [212] Y. Xue, H. Zhao, Z. Wu, X. Li, Y. He, Z. Yuan, *Analyst* **2011**, *136*, 3725–3730.
- [213] R. Bharadwaj, S. Mukherji, S. Mukherji in 2012 International Conference on Fiber Optics and Photonics (PHOTONICS), IEEE, **2012**, pp. 1–3.
- [214] B. Zientek, H. Wang, J. Indacochea, Y. Liu, M. Wang in Sensors and Smart Structures Technologies for Civil, Mechanical, and Aerospace Systems 2010, *Vol. 7647*, SPIE, **2010**, pp. 908–915.
- [215] K. Bertels, J.-M. Jacques, L. Neuberg, L. Gatot, *European Journal of Operational Research* **1999**, *115*, 608–615.
- [216] G. P. Georgiou, *Scientific Reports* **2023**, *13*, 15594.
- [217] S. Aldrich, Sigma Aldrich Online Database, US Patent 2,566,443, **1951**.

Appendix A

Supplementary Data

A.1 Printed Gold Nanoparticle-Based Sensors

In this section, all gold nanoparticle (GNP)-based sensors were prepared using batch GNP1 via printing technologies. The organic inks used to produce the GNP films were prepared using differently functionalized monothiols (MTs) mixed with 1,9-nonanedithiol (9DT) linker molecules, and the used MT ligands are listed as follows: 1-thioglycerol (TG), 11-mercapto-1-undecanol (11MUO), 4-mercaptophenol (4MPO), 11-mercapto-1-undecanoic acid (11MUA), 4-mercaptobenzoic acid (4MBA), and 2-aminothiophenol (2ATP). The notations of the as-fabricated GNP-based chemiresistor discussed in this section are 9DT (prepared using pure 9DT linker), TG-9DT, 11MUO-9DT, 4MPO-9DT, 11MUA-9DT, 4MBA-9DT, and 2ATP-9DT, as listed in Table 7.1. These GNP-based chemiresistors were exposed to six different analyte vapors at concentrations ranging from 50 to 1000 ppm, specifically at 50, 100, 150, 200, 300, 400, 500, and 1000 ppm. Figures A1 to A7 present the baseline-corrected timetraces of the seven GNP chemiresistors upon exposure to six different analyte vapors. Figures A8 to A14 present the response isotherms at lower concentrations (50-500 ppm). Within this concentration range, the response isotherms were fitted with linear functions, and these linear functions did not pass through the origin. The slope of the linear function was extracted to determine the sensitivity. The calculated sensitivities are summarized in the bar plot as shown in Figure 7.6 in Section 7.2.4.

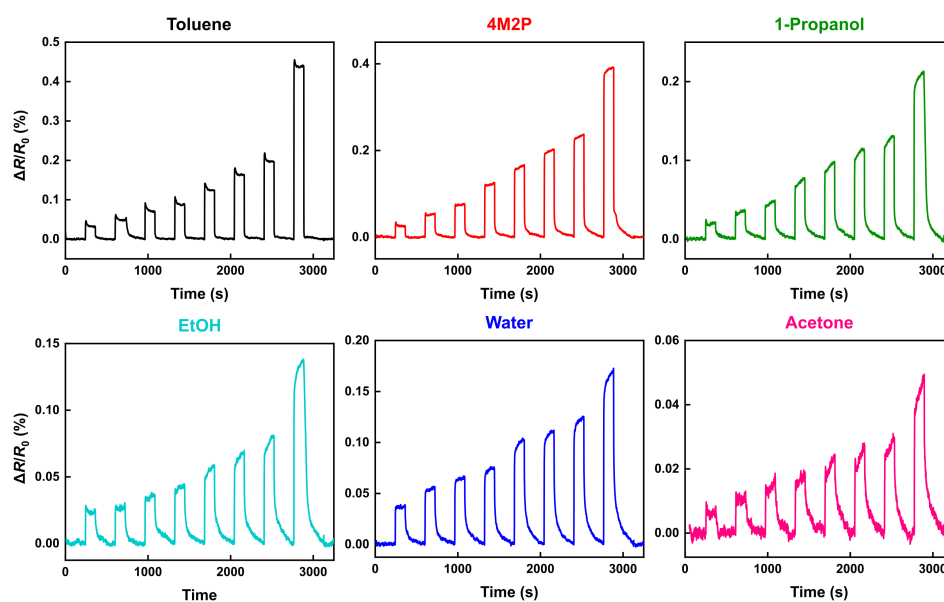


Figure A1: Baseline-corrected resistive responses of the 9DT sensor when exposed to six different analyte vapors are presented, with the specific types of analytes indicated in the caption of each subplot.

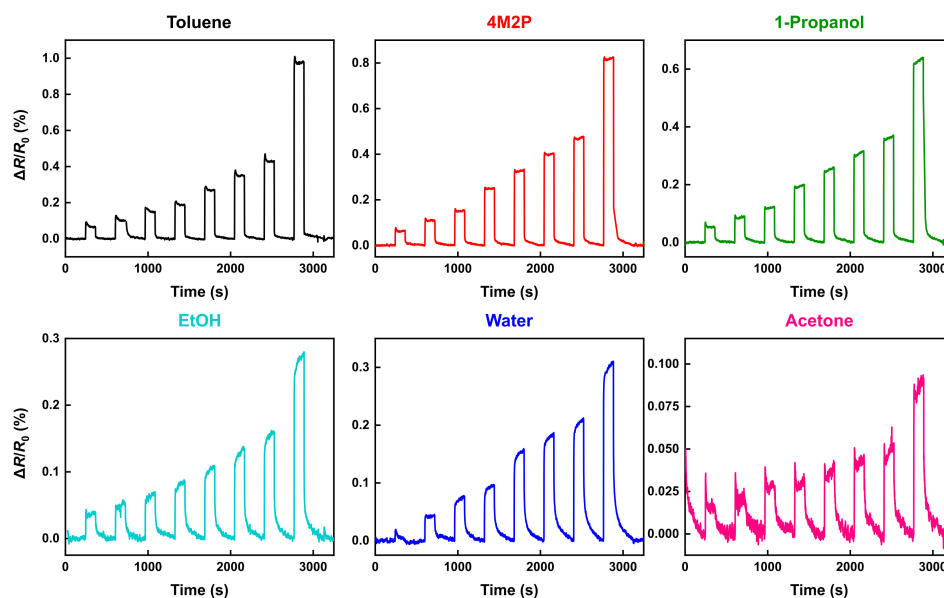


Figure A2: Baseline-corrected resistive responses of the 11MUO-9DT sensor when exposed to six different analyte vapors are presented, with the specific types of analytes indicated in the caption of each subplot.

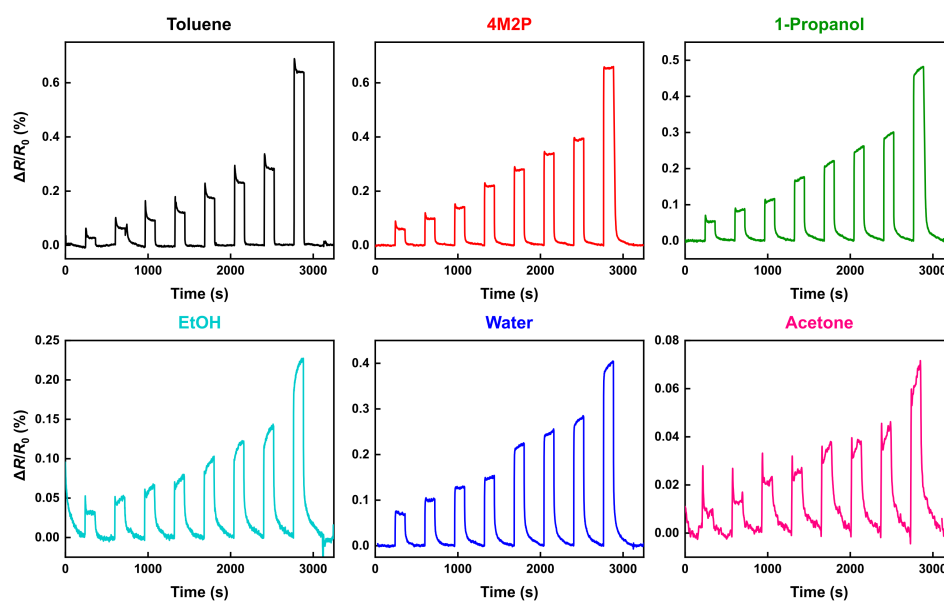


Figure A3: Baseline-corrected resistive responses of the TG-9DT sensor when exposed to six different analyte vapors are presented, with the specific types of analytes indicated in the caption of each subplot.

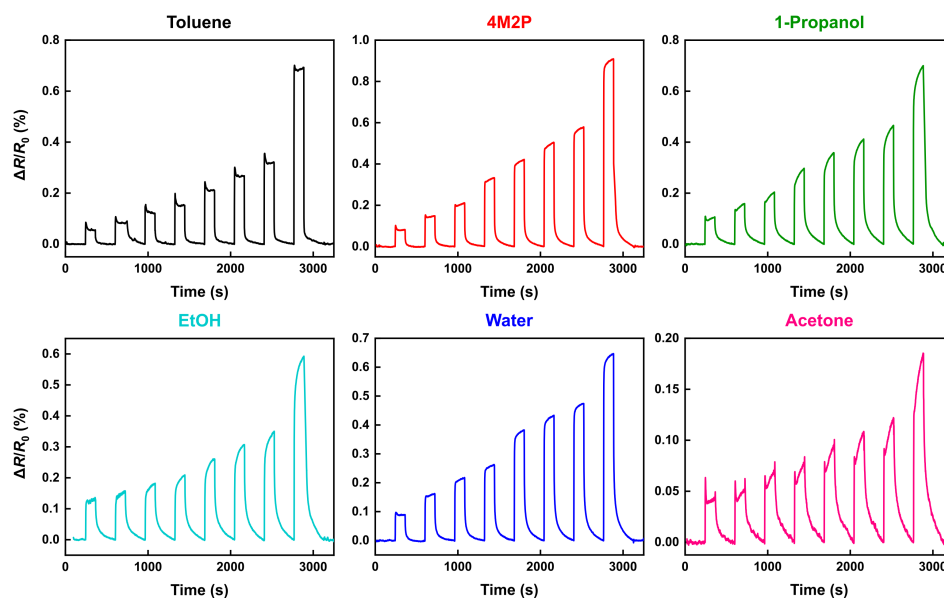


Figure A4: Baseline-corrected resistive responses of the 4MPO-9DT sensor when exposed to six different analyte vapors are presented, with the specific types of analytes indicated in the caption of each subplot.

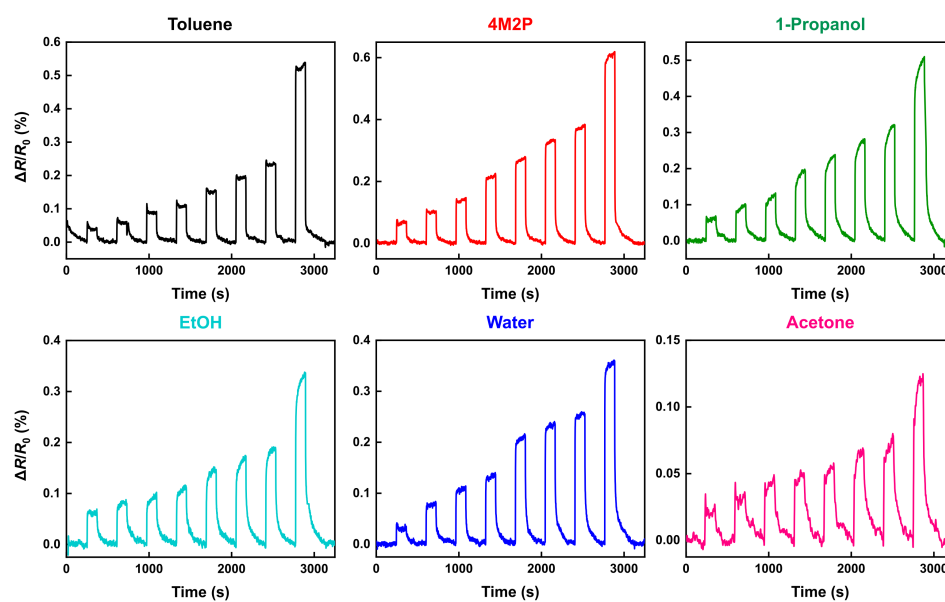


Figure A5: Baseline-corrected resistive responses of the 11MUA-9DT sensor when exposed to six different analyte vapors are presented, with the specific types of analytes indicated in the caption of each subplot.

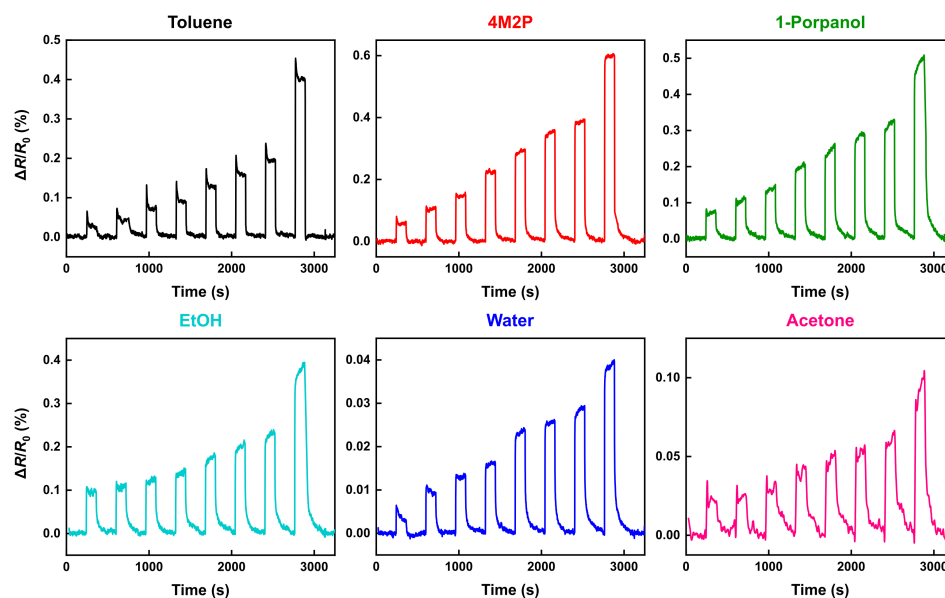


Figure A6: Baseline-corrected resistive responses of the 4MBA-9DT sensor when exposed to six different analyte vapors are presented, with the specific types of analytes indicated in the caption of each subplot.

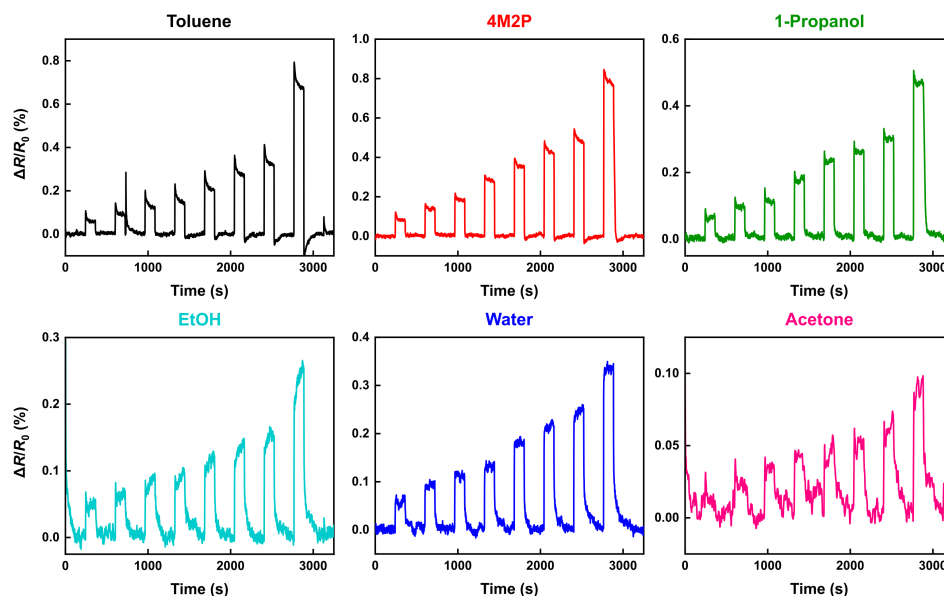


Figure A7: Baseline-corrected resistive responses of the 2ATP-9DT sensor when exposed to six different analyte vapors are presented, with the specific types of analytes indicated in the caption of each subplot.

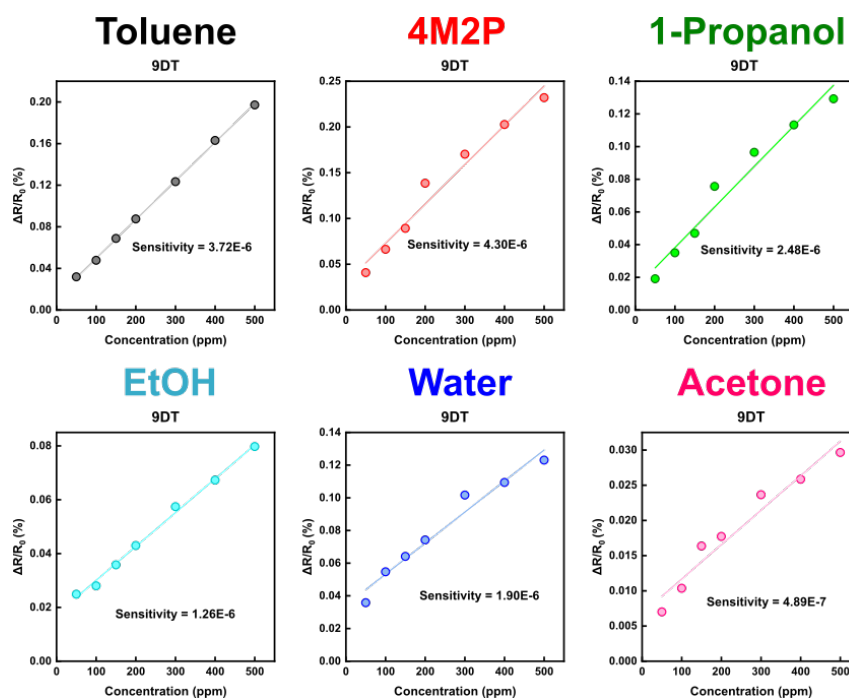


Figure A8: Response isotherms of the printed 9DT film when exposed to six different analyte vapors at concentrations ranging from 50 to 500 ppm, the maximum response amplitudes were extracted from the responses shown in Figure A1. Linear functions were fitted to the response isotherms (solid lines), and sensitivities were determined from the slopes of these fits.

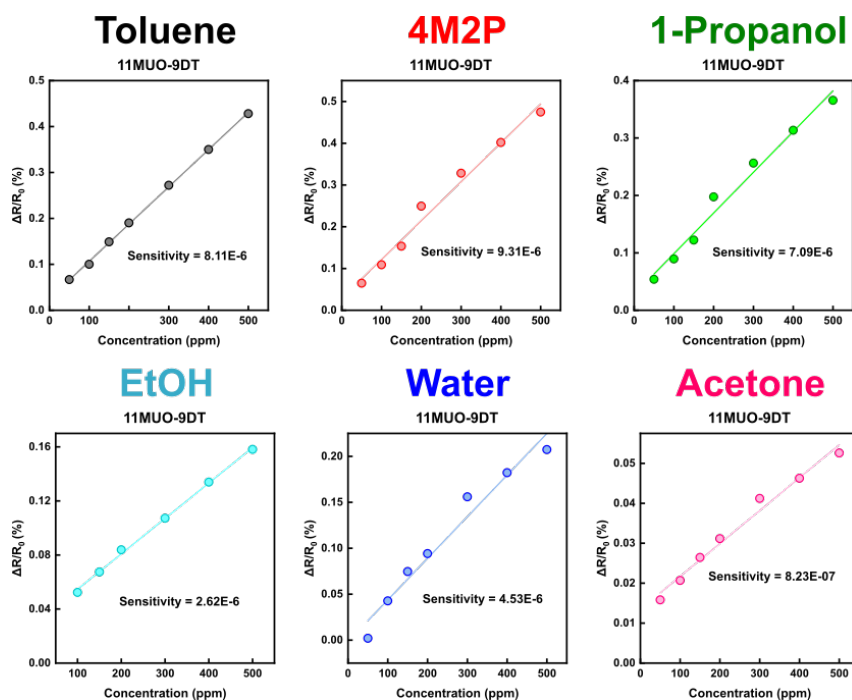


Figure A9: Response isotherms of the printed 11MUO-9DT film when exposed to six different analyte vapors at concentrations ranging from 50 to 500 ppm, the maximum response amplitudes were extracted from the responses shown in Figure A2. Linear functions were fitted to the response isotherms (solid lines), and sensitivities were determined from the slopes of these fits.

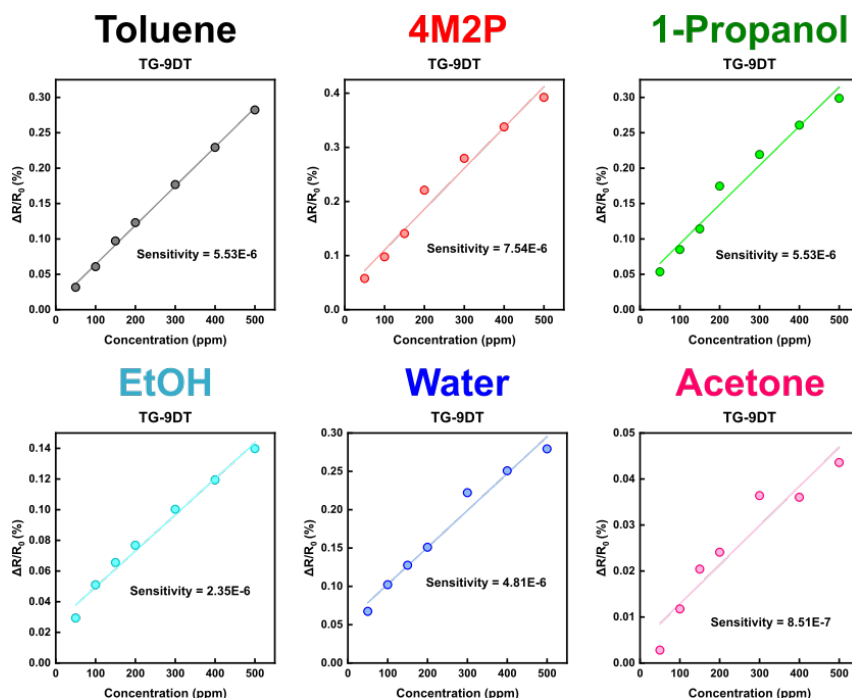


Figure A10: Response isotherms of the printed TG-9DT film when exposed to six different analyte vapors at concentrations ranging from 50 to 500 ppm, the maximum response amplitudes were extracted from the responses shown in Figure A3. Linear functions were fitted to the response isotherms (solid lines), and sensitivities were determined from the slopes of these fits.

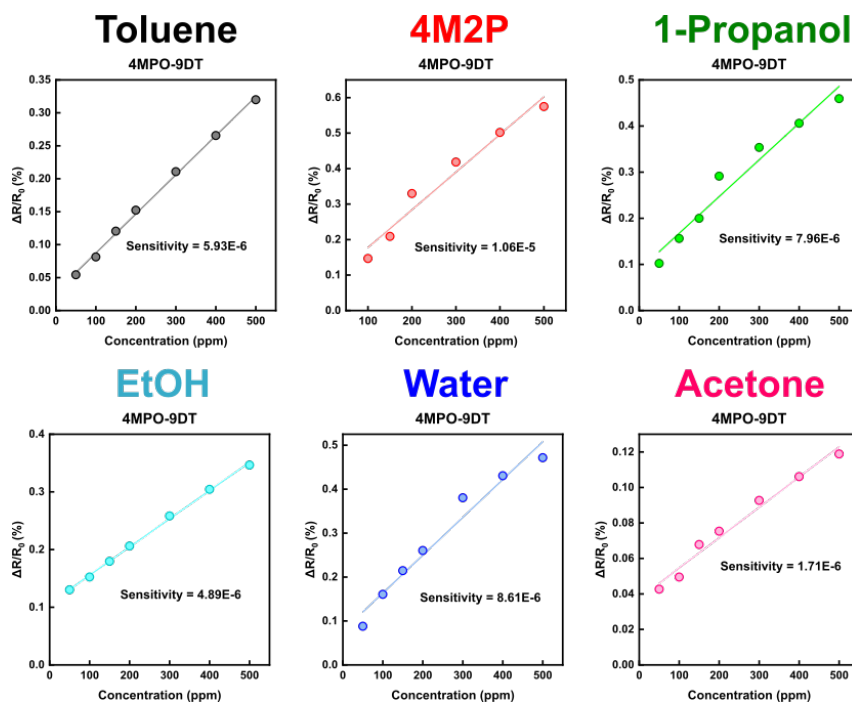


Figure A11: Response isotherms of the printed 4MPO-9DT film when exposed to six different analyte vapors at concentrations ranging from 50 to 500 ppm, the maximum response amplitudes were extracted from the responses shown in Figure A4. Linear functions were fitted to the response isotherms (solid lines), and sensitivities were determined from the slopes of these fits.

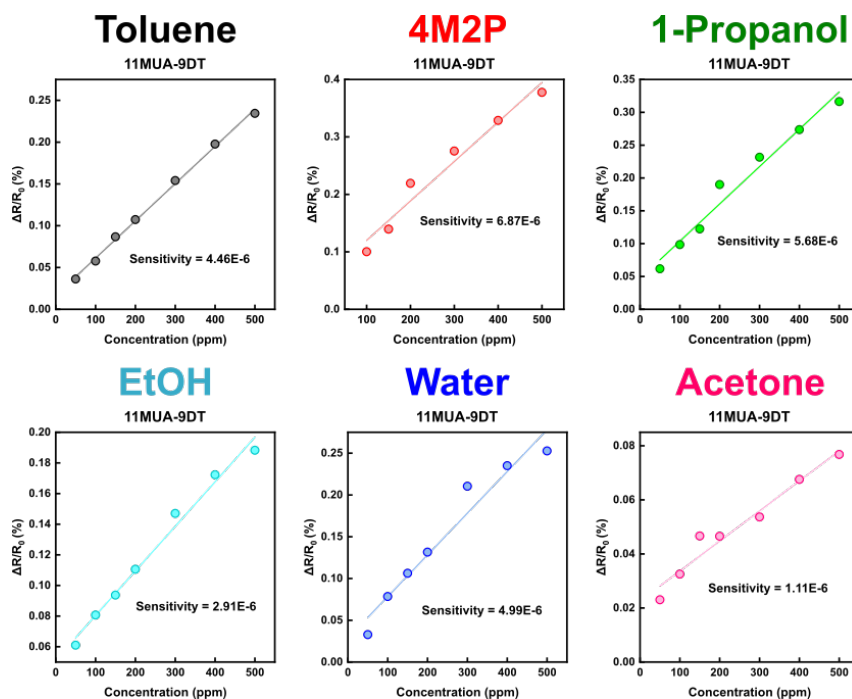


Figure A12: Response isotherms of the printed 11MUA-9DT film when exposed to six different analyte vapors at concentrations ranging from 50 to 500 ppm, the maximum response amplitudes were extracted from the responses shown in Figure A5. Linear functions were fitted to the response isotherms (solid lines), and sensitivities were determined from the slopes of these fits.

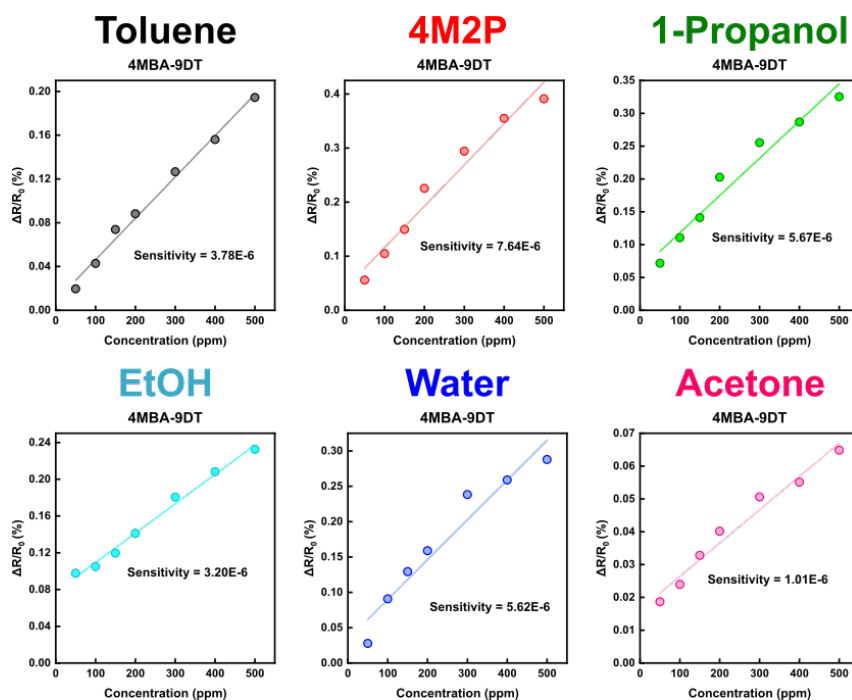


Figure A13: Response isotherms of the printed 4MBA-9DT film when exposed to six different analyte vapors at concentrations ranging from 50 to 500 ppm, the maximum response amplitudes were extracted from the responses shown in Figure A6. Linear functions were fitted to the response isotherms (solid lines), and sensitivities were determined from the slopes of these fits.

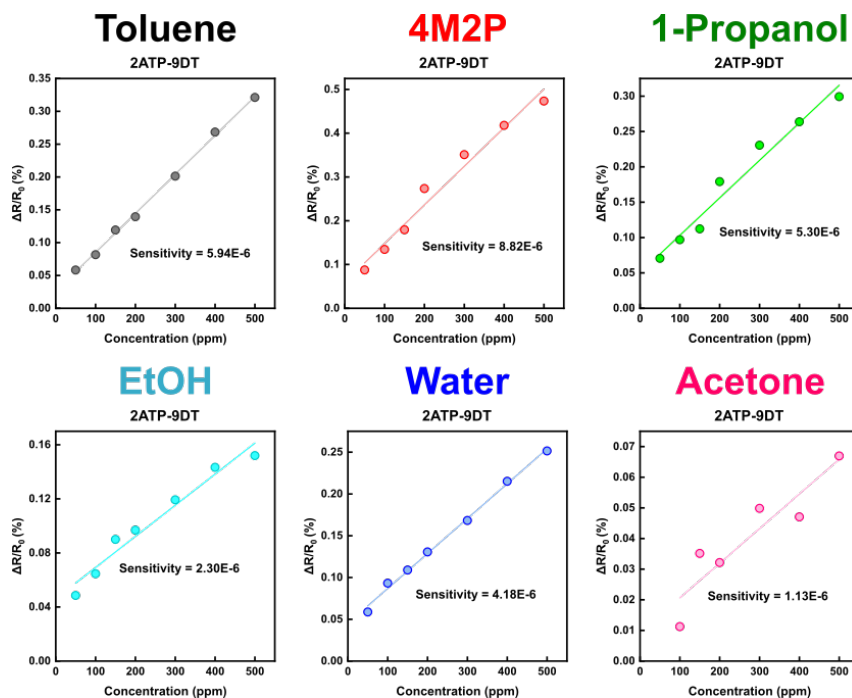


Figure A14: Response isotherms of the printed 2ATP-9DT film when exposed to six different analyte vapors at concentrations ranging from 50 to 500 ppm, the maximum response amplitudes were extracted from the responses shown in Figure A7. Due to signal noises and baseline fluctuations in the response to acetone vapor at 50 ppm, this data was not included. Linear functions were fitted to the response isotherms (solid lines), and sensitivities were determined from the slopes of these fits.

A.2 Glass-Supported Gold Nanoparticle Films via Layer-by-Layer Spin-Coating

In this section, GNP batches, GNP2 and GNP3, were used to prepare the GNP films. Figure A15 shows the small angle X-ray scattering (SAXS) intensity profile of the GNP batch, GNP3. The mean particle size was determined using a fit of a core/shell spherical form-factor model, yielding an average core diameter of approximate 7.44 nm, which is in good agreement with the result measured via transmission electron microscopy (TEM) (approximately 7.25 nm as shown in Figure 7.1).

To produce GNP films with different organic compositions, different alkanethiols (ATs) and ω -mercaptocarboxylic acids were used in the combination with the 9DT as follows: 1-hexanethiol (6T), 1-octanethiol (8T), 1-decanethiol (10T), 1-undecanethiol (11T), 1-dodecanethiol (12T), 1-tetradecanethiol (14T), 3-mercaptopropionic acid (3MPA), 6-mercaptohexanoic acid (6MHA), 8-mercaptooctanoic acid (8MOA), 11-mercaptoundecanoic acid (11MUA), and 4-mercaptobenzoic acid (4MBA). The figures and table presented in this section are based on the results obtained from the GNP films with the organic matrices composed of different functionalized MT/9DT mixtures, which were prepared using the layer-by-layer spin-coating (LbL-SC)[85] method. These results include atomic force microscopy (AFM) images, UV/vis absorption spectra, and chemiresistor measurements, providing comprehensive insights into the structural and functional properties of the resulting GNP films. The notations of the GNP sensors are listed in Table 7.2.

Figure A15 is reprinted with permission from the Supporting Information of Ref. [1] (©2024 The Authors. Published by American Chemical Society).

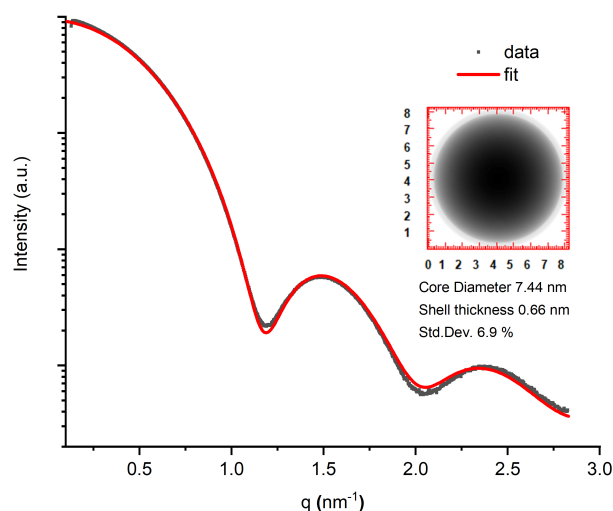


Figure A15: SAXS intensity profile of batch GNP3 and fitted with a model of a core/shell spherical form-factor.

A.2.1 Characterizations of Gold Nanoparticle Films

Five exemplary GNP films were prepared using batch GNP2, as shown in Figure A16 with their respective photographs, SEM images, and AFM images. For SEM measurements, GNP films were deposited

on silicon substrates via the LbL-SC method applying 3-4 deposition cycles. The scanning electron microscopy (SEM) samples were placed under vacuum conditions overnight before the measurements. AFM measurements were conducted to determine the film thickness. For AFM measurement, GNP films were deposited on glass substrates via the LbL-SC method with 5-6 deposition cycles.

To compare the film quality between the 89%12T-9DT and 95%12T-9DT films, Figure A19 shows the photographic and microscopic images of both films. The GNP film prepared with the 95% 12T/9DT mixture displayed an inhomogeneous morphology as some GNP aggregated on the surface, which can be observed in the microscopic image as shown in Figure A19e. Moreover, Figure A19c reveals that the 95%12T-9DT film was less robust, since it partially came off during the washing step of the film fabrication. Some exemplary AFM images of selected GNP films are shown in Figure A16, and the thicknesses of all resulting films used in UV/vis, and I-V characterizations and chemiresistor measurements presented in Section 7.3 are listed in Table A1. These glass-supported GNP films were scanned at the edge of the scratched film by AFM in tapping mode with scan area of $5 \times 20 \mu\text{m}^2$.

Figures A17 and A18 depict the average UV/vis absorbance spectra of the GNP films recorded from 4 different spots on a film. The GNP films were deposited on the glass substrates via the LbL-SC method with 5-6 deposition cycles. While the 100%3MPA and 100%8MOA films were prepared with batch GNP3, the remaining GNP films were prepared with batch GNP2. The localized surface plasmon resonance (LSPR) band's position of each GNP film shown in Figure 7.12 was summarized from these UV/vis data.

Figures A16-A18 are reprinted with permission from the Supporting Information of Ref. [2] (©2024 The Authors. Advanced Materials Interfaces published by Wiley-VCH GmbH). Table A1 is adapted and reproduced with permission from the Supporting Information of Ref. [2] (©2024 The Authors. Advanced Materials Interfaces published by Wiley-VCH GmbH).

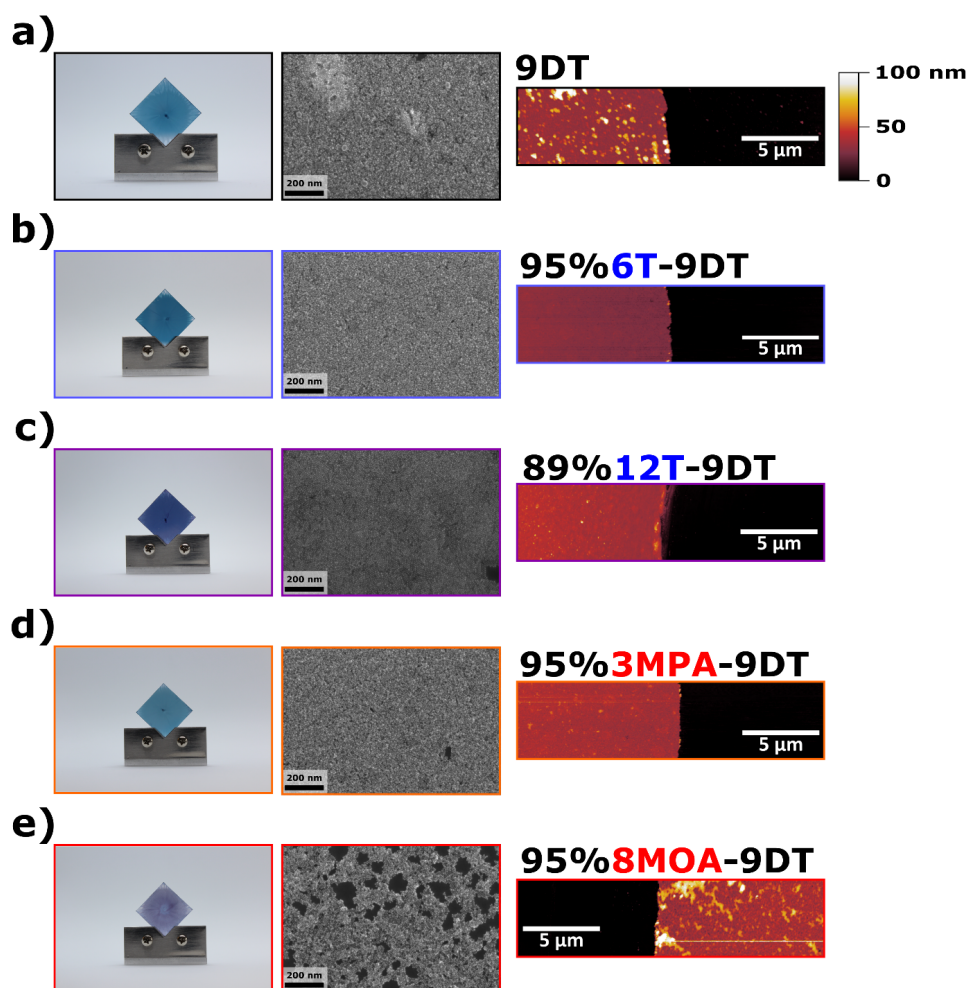


Figure A16: Photographs, SEM images (scale bar: 200 nm), and AFM images (scale bar: 5 μm) of exemplary GNP films prepared using batch GNP2, and their respective organic matrices, were prepared with: a) pure 9DT, and the b) 95% 6T/9DT, c) 89% 12T/9DT, d) 95% 3MPA/9DT, and e) 95% 8MOA/9DT mixtures.

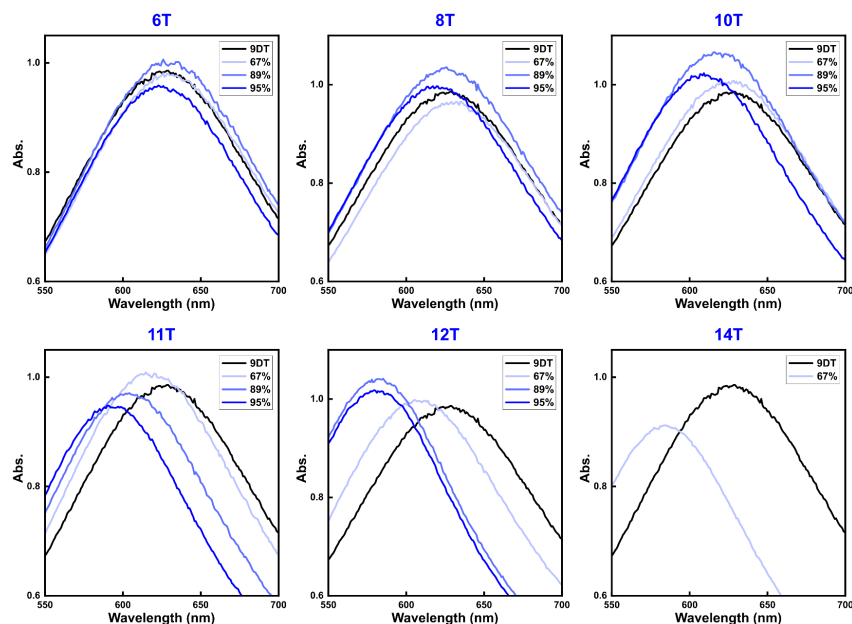


Figure A17: UV/vis absorbance spectra of GNP films on glass substrates prepared using batch GNP2 and different mixtures of AT/9DT (blue lines) and pure 9DT (black line). The molar fractions of the ATs (6T, 8T, 10T, 11T, 12T, 14T) are indicated in the legend.

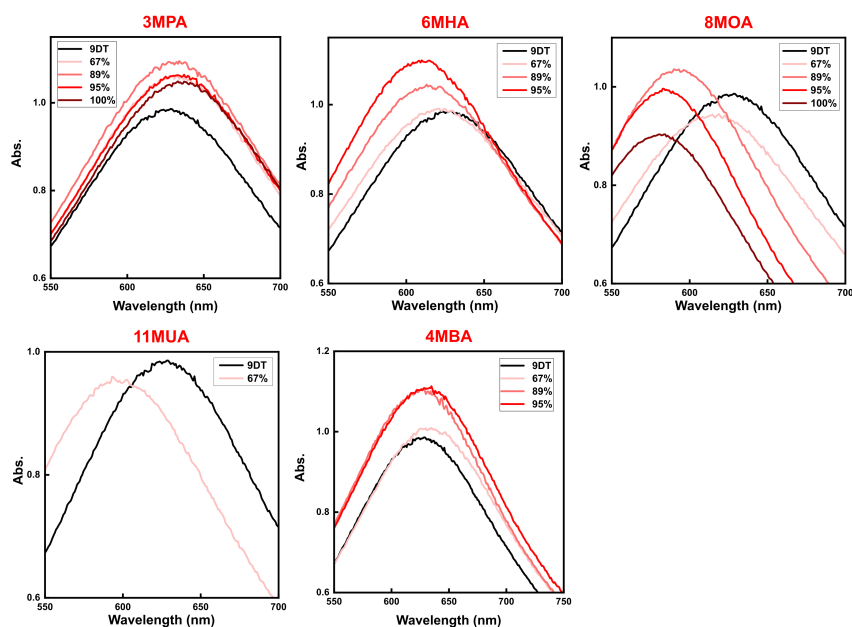


Figure A18: UV/vis absorbance spectra of GNP films on glass substrates prepared using batches GNP2 and GNP3, and different mixtures of ω -mercaptopcarboxylic acid/9DT (red lines) and pure 9DT (black line). The 100%3MPA and 100%8MOA GNP films were prepared using batch GNP3, while the remaining films were prepared with batch GNP2. The molar fractions of the ω -mercaptopcarboxylic acids (3MPA, 6MHA, 8MOA, 11MUA, 4MBA) are indicated in the legend.

Table A1: Thicknesses of GNP films determined by AFM with the standard deviation.

GNP film	GNP batch	Thickness (nm)
9DT	GNP2	38.07±1.66
67%6T-9DT	GNP2	37.92±2.09
89%6T-9DT	GNP2	36.72±1.18
95%6T-9DT	GNP2	34.65±1.29
67%8T-9DT	GNP2	38.16±1.93
89%8T-9DT	GNP2	37.14±3.92
95%8T-9DT	GNP2	36.75±1.74
67%10T-9DT	GNP2	35.89±2.32
89%10T-9DT	GNP2	35.26±1.70
95%10T-9DT	GNP2	39.43±2.12
67%11T-9DT	GNP2	35.48±1.16
89%11T-9DT	GNP2	36.80±1.45
95%11T-9DT	GNP2	37.02±0.98
67%12T-9DT	GNP2	34.44±1.35
89%12T-9DT	GNP2	43.74±1.22
95%12T-9DT	GNP2	41.77±3.76
67%14T-9DT	GNP2	44.42±3.64
67%3MPA-9DT	GNP2	36.91±1.87
89%3MPA-9DT	GNP2	36.18±1.23
95%3MPA-9DT	GNP2	41.28±1.54
100%3MPA	GNP3	34.41±1.88
67%6MHA-9DT	GNP2	39.90±2.55
89%6MHA-9DT	GNP2	45.27±2.90
95%6MHA-9DT	GNP2	35.42±3.04
67%8MOA-9DT	GNP2	36.25±3.92
89%8MOA-9DT	GNP2	45.45±3.06
95%8MOA-9DT	GNP2	40.63±1.43
100%8MOA	GNP3	38.89±1.90
67%11MUA-9DT	GNP2	43.68±2.97
67%4MBA-9DT	GNP2	41.63±4.52
89%4MBA-9DT	GNP2	43.09±3.48
95%4MBA-9DT	GNP2	41.50±3.93

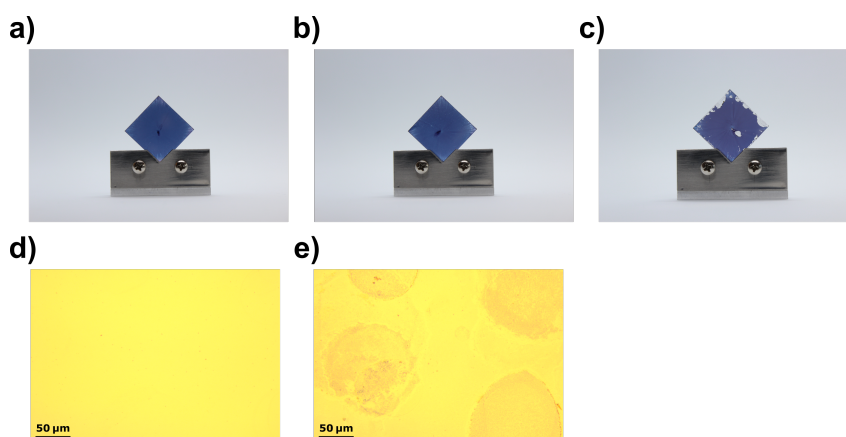


Figure A19: Photographs of GNP films prepared with a) the 89% 12T/9DT mixture and both b) and c) prepared with the 95% 12T/9DT mixture. The films shown in parts b and c are two different 95%12T-9DT films. In part c, the film was damaged during the washing step of the film preparation (as indicated in Figure 7.11a, step v), suggesting that when the molar fraction of 12T is as high as 95%, the resulting GNP film is less robust. Microscopic images of GNP films prepared with the d) 89% 12T/9DT and e) 95% 12T/9DT mixtures corresponding to the films shown in parts a and b, respectively.

A.2.2 Chemiresistor Screening Tests

The same glass-supported GNP films discussed in Section A.2.1 were further subjected to the chemiresistor screening tests. The GNP films were exposed to toluene and 1-propanol vapors at concentrations of 200 (Figures A20 and A21) and 2000 ppm (Figures 7.14 and 7.15). The results of the chemiresistor screening tests presented in Section 7.3.3 were extracted from the transient responses shown in Figures A22 and A23. Figures A22 and A23 are reprinted from the Supporting Information of Ref. [2] (©2024 The Authors. Advanced Materials Interfaces published by Wiley-VCH GmbH).

Contrary to the results shown in Section 7.3.3, when the GNP films prepared with pure 9DT or hydrophobic MT/9DT mixtures were exposed to analyte vapors at 200 ppm, the amplitudes of the resistive responses to 1-propanol were higher than that to toluene for most of the GNP films. However, the enhanced response amplitudes to toluene vapor were still observed when the longer and higher fractions of alkanethiol (AT) ligands were used. It is noteworthy that the GNP films prepared using the 12T/9DT mixtures showed higher responses to toluene vapor than to 1-propanol vapor. On the other hand, when the GNP films were prepared using the ω -mercaptocarboxylic acids/9DT mixtures, the trends of the chemiresistor screening tests for 200 ppm analyte vapors were consistent with those shown in Figure 7.15.

Moreover, comparing the results shown in Figure A20 (GNP films prepared with batch GNP2) to those shown in Figures 7.18 and 7.19 (GNP films prepared with batch GNP3), the sensitivity patterns for toluene and 1-propanol vapors showed slight deviations. This can be attributed to several factors, including the aging effect (in Sections 7.3.3 and A.2.1, all GNP films were measured one day after the film fabrication, while in Section 7.3.4, measurements were conducted three days after the film fabrication) and the use of different GNP batches. Nevertheless, a general trend of changes in the sensing properties of the GNP films with the addition of the AT ligands was observed in the screening tests.

Figure A24 shows the chemiresistive response isotherms of four 9DT GNP films, two of which were prepared with batch GNP2 and the other two with batch GNP3. In parts a and b, both films were prepared with GNP2, and the sensitivity to toluene and 1-propanol vapors deviated slightly, but the overall sensitivity pattern remained consistent. However, in parts c and d, where both films were prepared with GNP3, a significant change in sensitivity to toluene vapor was observed. The deviation between the sensors may be due to the difference in film preparation conditions and different degrees of aging of GNP films, causing a different GNP assembly. Moreover, although the average particle size and concentration of GNP2 and GNP3 were similar, subtle differences in particle size potentially contributed to the batch-to-batch deviations, resulting in the differences in sensitivity patterns observed in the four 9DT GNP films.

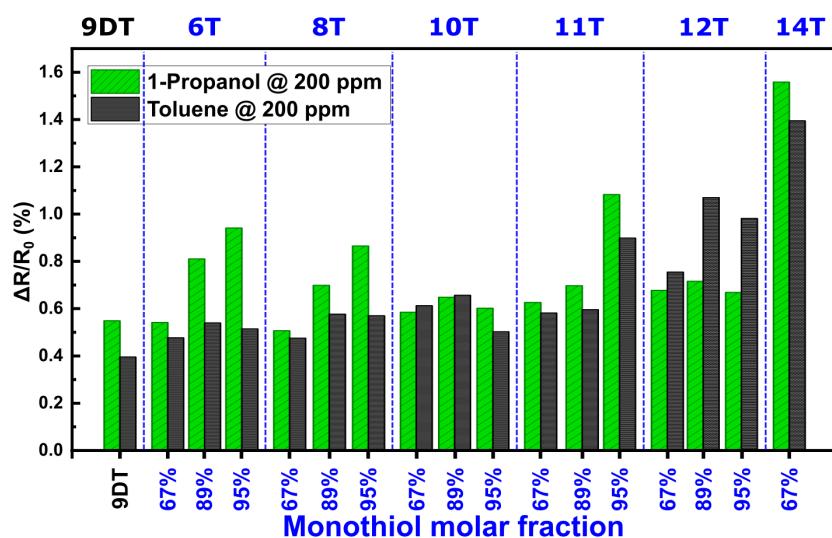


Figure A20: Resistive response amplitudes of GNP films used in the screening tests presented in Section 7.3.3. The films were prepared using pure 9DT and AT/9DT mixtures. Toluene vapor (black bars) and 1-propanol vapor (green bars) were applied at the concentration of 200 ppm in nitrogen. All films were prepared using batch GNP2.

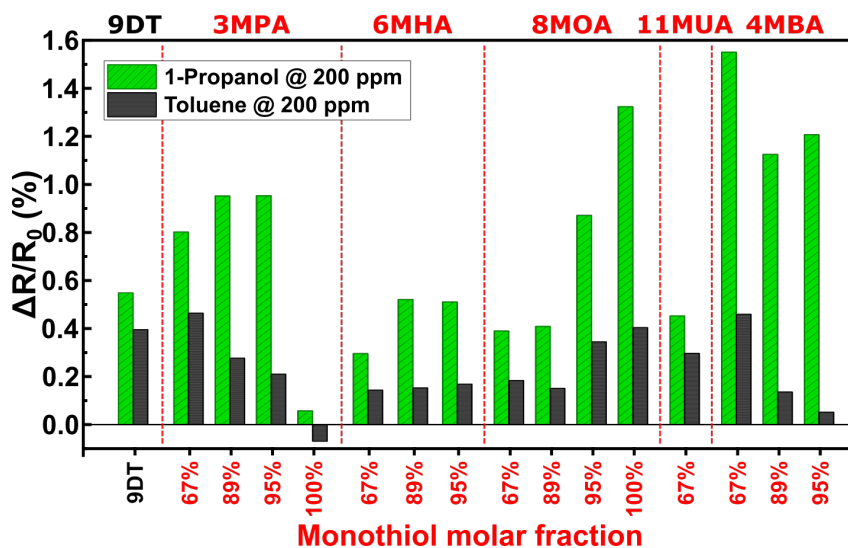


Figure A21: Resistive response amplitudes of GNP films used in the screening tests presented in Section 7.3.3. The films were prepared using pure 9DT and ω -mercaptocarboxylic acid/9DT mixtures. Toluene vapor (black bars) and 1-propanol vapor (green bars) were applied at the concentration of 200 ppm in nitrogen. The 100%3MPA and 100%8MOA films were prepared using batch GNP3, while the remaining films were prepared using batch GNP2.

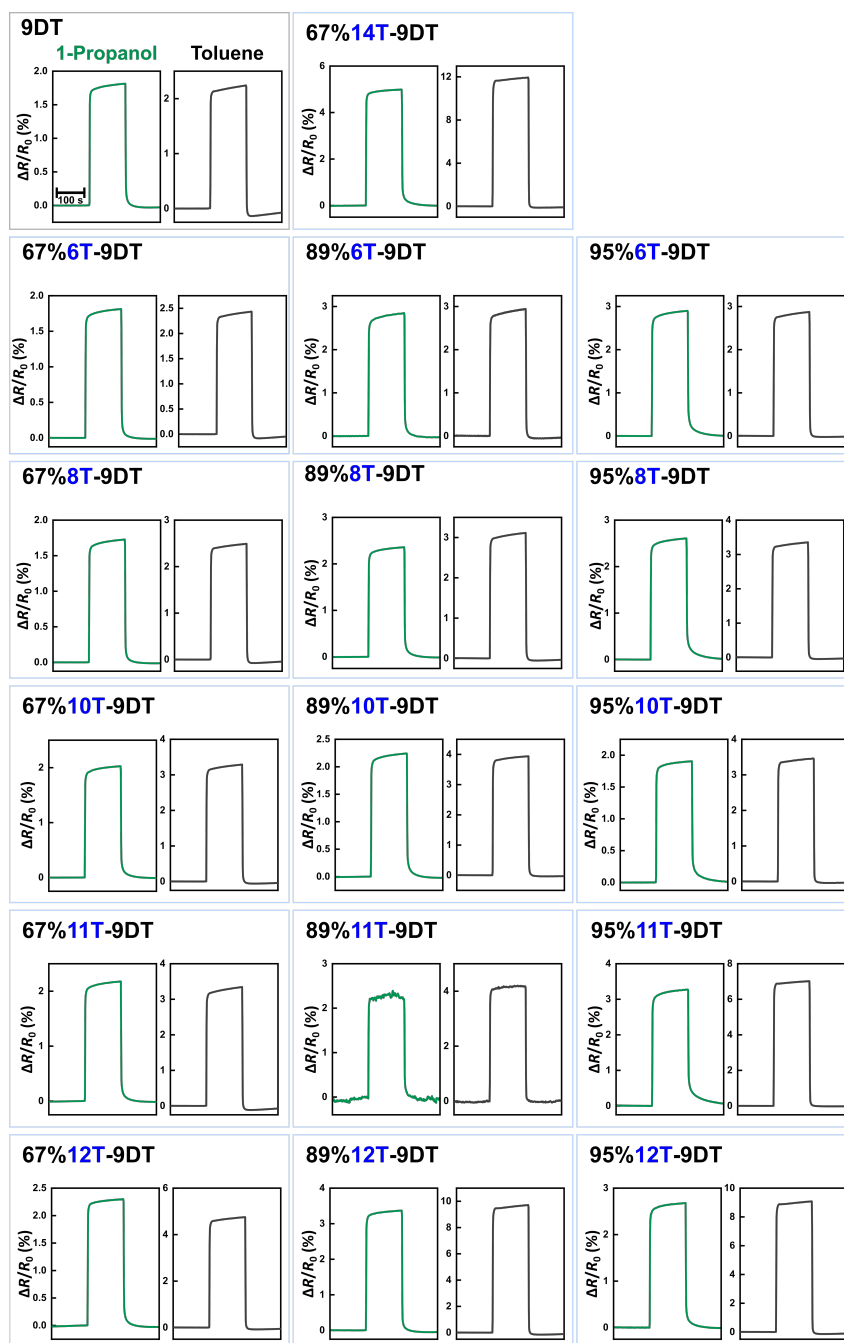


Figure A22: Transient resistive responses of chemiresistors prepared with pure 9DT and the AT/9DT mixtures to 1-propanol (green) and toluene (black) vapors at 2000 ppm. All films were prepared using batch GNP2.

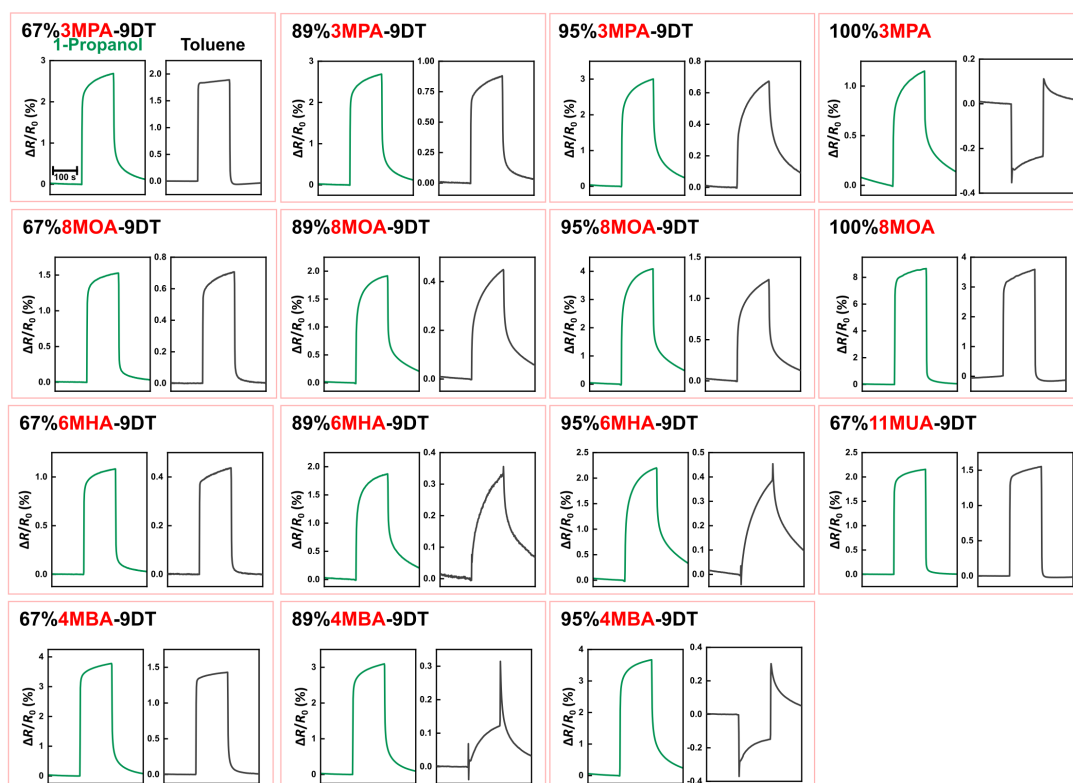


Figure A23: Transient resistive responses of chemiresistors prepared with the ω -mercaptocarboxylic acid/9DT mixtures to 1-propanol (green) and toluene (black) vapors at 2000 ppm. The 100%3MPA and 100%8MOA films were prepared with batch GNP3, while the remaining films were prepared using batch GNP2.

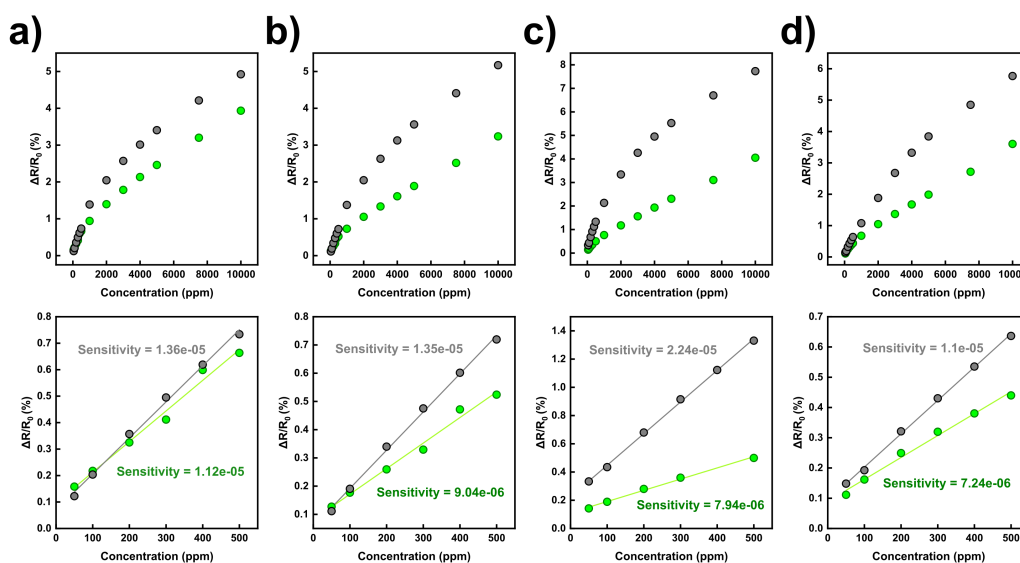


Figure A24: Chemiresistive response isotherms of the 9DT cross-linked GNP films. These films were exposed to toluene (black) and 1-propanol (green) vapors at concentrations ranging from 50 to 10000 ppm (shown in upper part), and at concentrations ranging from 50 to 500 ppm (shown in lower part). The response isotherms in the concentration range of 50 to 500 ppm were fitted with a linear function to determine the sensitivity. a) and b) are two individual 9DT GNP films, which were prepared using batch GNP2. In part a, this film was also used in the chemiresistor screening tests as described in Section 7.3.3. The chemiresistive response isotherms for toluene and 1-propanol vapors, in the concentration range of 50 to 10000 ppm, were measured a few days after the screening tests. c) and d) are two individual 9DT GNP films, which were prepared using batch GNP3. In part c, this film was used in the response isotherms investigation in Section 7.3.4, with its response isotherms presented in Figure 7.18a and f.

A.2.3 Aging of Gold Nanoparticle Films

The selected GNP films, which were prepared using batch GNP2, were investigated for the changes in their chemiresistor characteristics over a period of time. These films were exposed to toluene and 1-propanol in the concentration range of 50 to 10000 ppm to access their chemiresistive response isotherms, cf. Figure A24a. Day 0 is defined as the date when the film was deposited on the glass substrate, and week 0 is defined as the week when the film was fabricated. The response isotherms of three selected GNP films shown in Figure A25 were measured in a period of 4 weeks. On the other hand, the 100%3MPA film was tested in a period of 1 week. It is well-known that GNP-based sensors are severely affected by aging effects within the first week of the fabrication. Therefore, the deviations observed in the response amplitude can be attributed to the aging of the film.

Furthermore, the 100%3MPA film prepared using batch GNP3 was exposed to toluene and 1-propanol at concentrations ranging from 50-1000 ppm and measured on different days. Figures A25 and A26 show the results of the aging tests. The GNP films prepared with ω -mercaptocarboxylic acids experienced severe aging compared to those prepared with hydrophobic ligands and linkers.

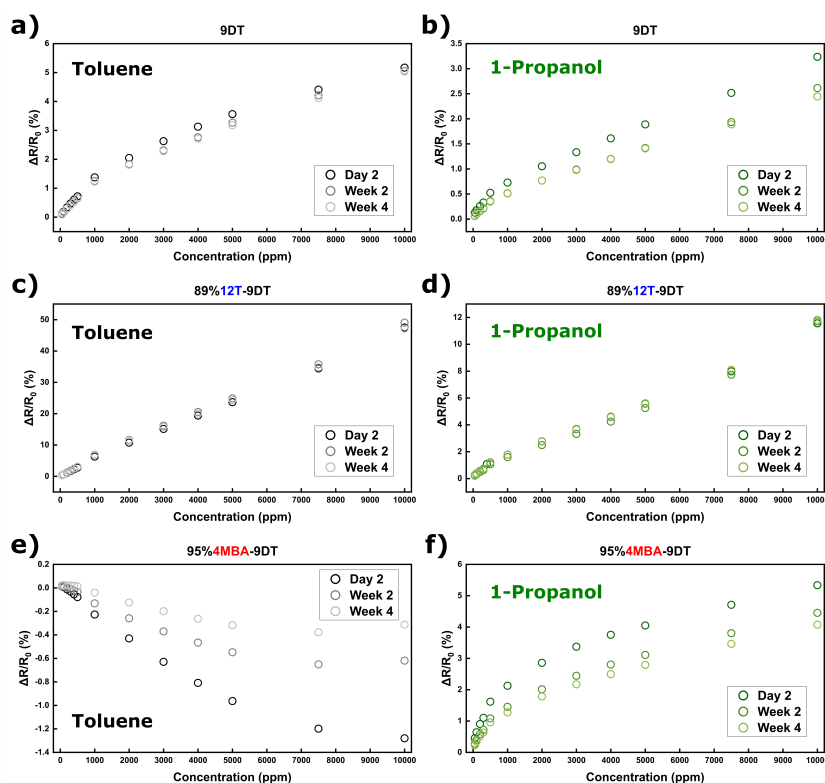


Figure A25: Chemiresistive response isotherms of the GNP films prepared with a)-b) pure 9DT and the mixtures of c)-d) 89% 12T/9DT and e)-f) 95% 4MBA/9DT to toluene (black) and 1-propanol (green) at vapor concentrations ranging from 50 to 10000 ppm. The chemiresistor measurements were conducted on three different days.

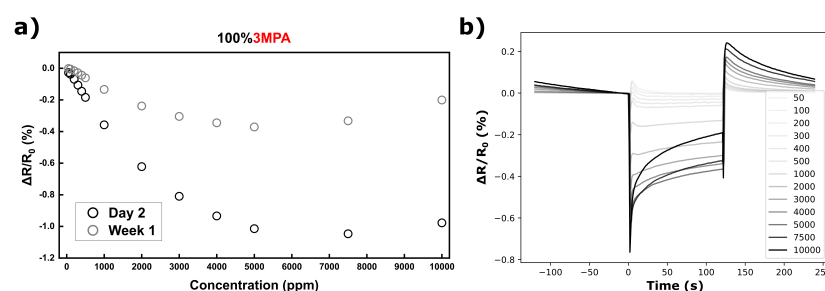


Figure A26: a) Chemiresistive response isotherms of the GNP film prepared with pure 3MPA to toluene at vapor concentrations ranging from 50 to 10000 ppm. These chemiresistor measurements were conducted on two different days. b) Transient responses of the 100%3MPA chemiresistor measured one week after film fabrication (week 1). The toluene vapor concentrations are indicated in the legend.

A.3 Glass-Supported Gold Nanoparticle Films for Comparison with Simulation Data

All GNP films were prepared using batch GNP4 and different alkanethiol (AT)/9DT mixtures via the LbL-SC procedure. The applied AT ligands were 1-hexanethiol (6T), 1-undecanethiol (11T), and 1-dodecanethiol (12T). The notations of GNP films are listed in Table 7.3. The resulting GNP films were compared with the results obtained from molecular dynamics (MD) simulations. The following figures and table show the UV/vis absorbance spectra, the chemiresistive characteristics, and the thickness of the resulting films as well as the results obtained from MD simulations.

A.3.1 Characterizations of Gold Nanoparticle Films

Figure A27 depicts the average UV/vis absorbance spectra of four GNP films for each organic matrix composition. For determination of film thickness, the glass-supported GNP films were scanned at the edge of the scratched film by AFM in tapping mode with scan area of $5 \times 20 \mu\text{m}^2$. The thicknesses of the GNP films are listed in Table A2.

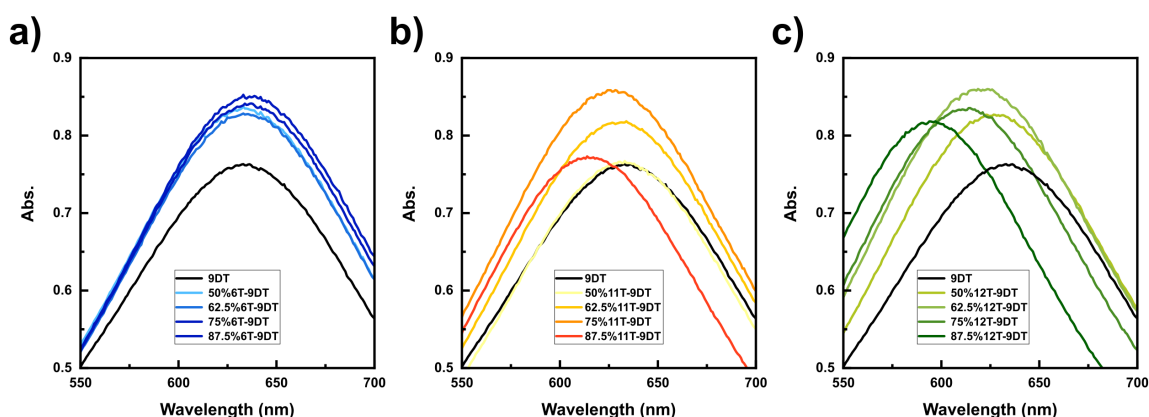


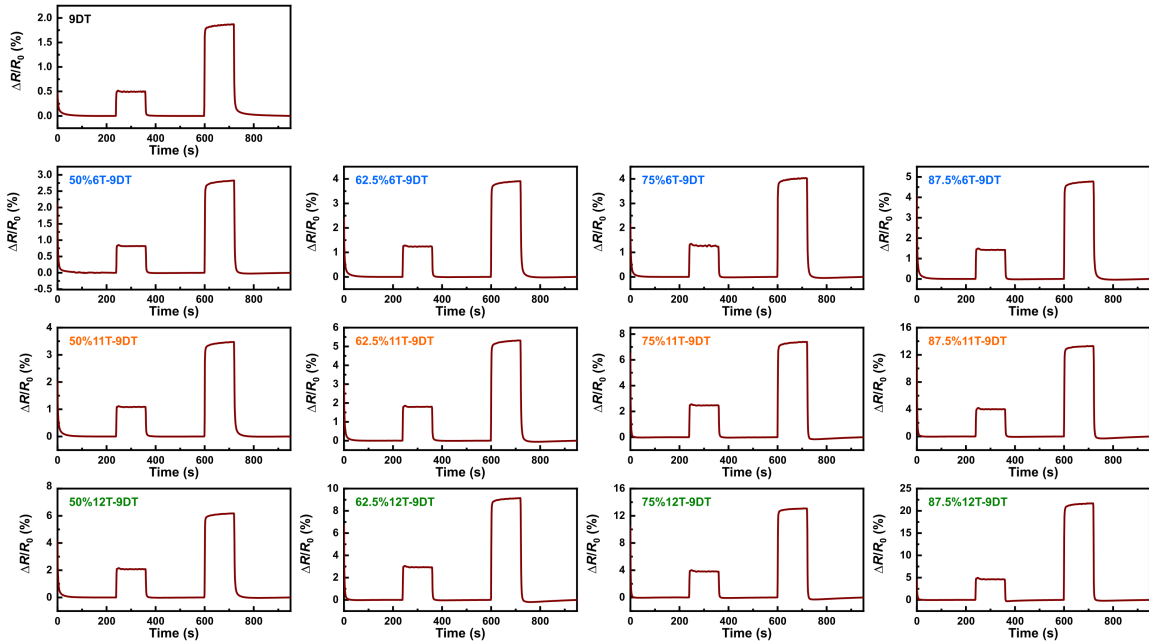
Figure A27: UV/vis absorbance spectra of GNP films on glass substrates prepared using different AT/9DT mixtures and pure 9DT (black line). Three different lengths of AT were applied: a) 6T (in blue), b) 11T (in orange), and c) 12T (in green). The molar fractions of the AT ligands are provided in the legend.

Table A2: GNP film thicknesses determined by AFM. GNP films were prepared using batch GNP4 and investigated in Section 7.4.

GNP film	Thickness (nm)
9DT	34.05±2.61
50%6T-9DT	31.01±0.59
62.5%6T-9DT	29.46±1.34
75%6T-9DT	29.04±1.26
87.5%6T-9DT	30.27±1.16
50%11T-9DT	23.97±1.95
62.5%11T-9DT	20.08±3.70
75%11T-9DT	27.25±1.59
87.5%11T-9DT	23.54±2.64
50%12T-9DT	24.77±3.54
62.5%12T-9DT	29.95±1.43
75%12T-9DT	27.60±1.19
87.5%12T-9DT	30.75±3.04

A.3.2 Chemiresistor Measurements

For the chemiresistor measurements, all GNP films were exposed to n-octane vapor at concentrations of 200 and 2000 ppm in nitrogen, and the measurements were conducted two days after the film fabrication. Figure A28 shows the average transient responses of four GNP films for each organic matrix composition. These average transient responses were used to extract the average resistive response amplitudes presented in Figure 7.27.

**Figure A28:** Baseline-corrected transient responses of GNP films to n-octane vapor at concentrations of 200 and 2000 ppm. The GNP films were prepared with different mixtures of AT/9DT and the pure 9DT, as indicated in the legend.

A.3.3 Molecular Dynamics Simulations

Figures A29, A30, and A31 were provided by K. Schaefer. Figure A29 presents snapshots of MD simulations of the systems with pure 9DT and 12T molecules (a total of 8 molecules in the simulation system, corresponding to 100% ligand coverage for 9DT system and 50% ligand coverage for 12T system). In the system with pure 9DT linkers, all 9DT molecules cross-linked both sides of the gold surfaces. Conversely, in the system with pure 12T ligands, the 12T molecules intercalated with the neighboring molecules. On both top and bottom gold surfaces, four 12T molecules bonded to each surface. To determine the optimal ligand coverage on the gold surface to estimate the interparticle distance, some preliminary simulations were conducted. Figures A30 (simulation systems with pure 6T ligands) and A31 (simulation systems with pure 11T ligands) illustrate the correlation between the estimated interparticle distance and the ligand coverage on the gold surface.

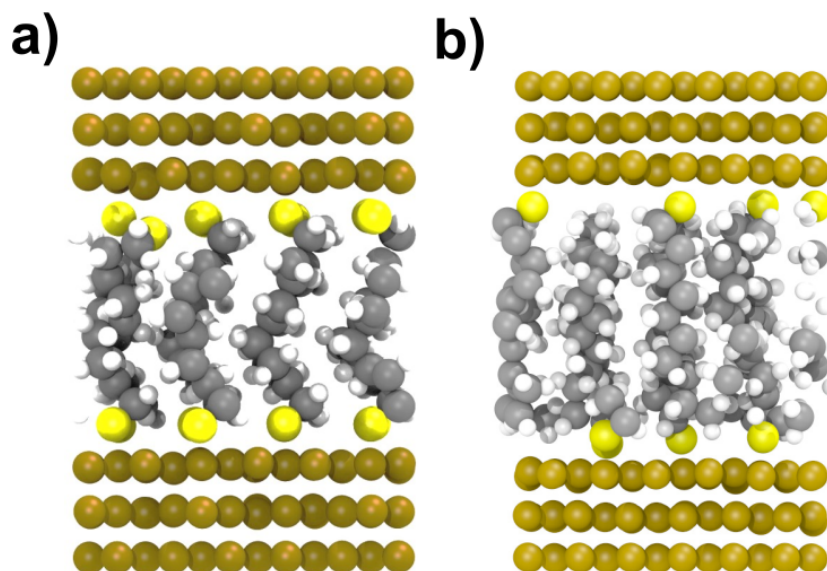


Figure A29: Snapshots of MD simulations of the systems at "lowest-energy structures" containing: a) eight 9DT molecules (corresponding to 100% ligand coverage in the simulation system), and b) eight 12T molecules (corresponding to 50% ligand coverage in the simulation system).

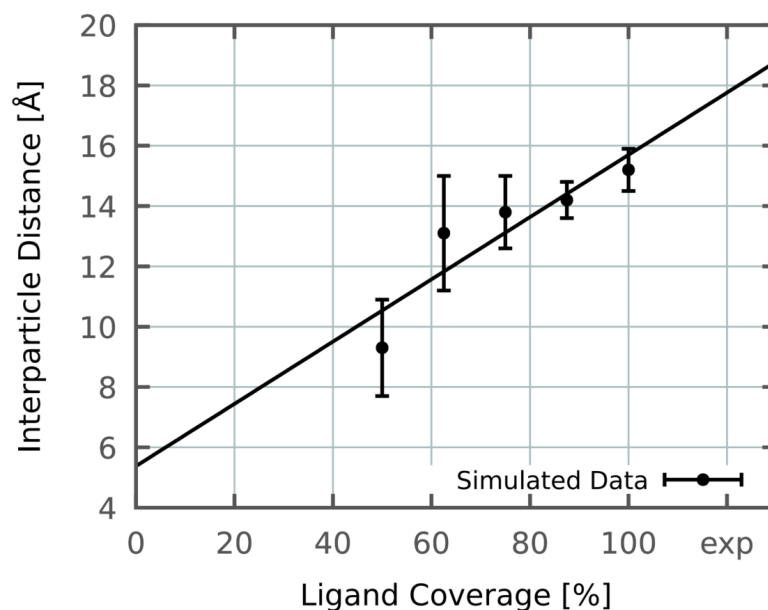


Figure A30: Average interparticle distances extracted from the MD simulations of the systems with pure 6T ligands and varying ligand coverages on the gold surface. Error bars represent standard deviations from ten MD simulation runs. The average interparticle distances extracted from each system are fitted with a linear function (solid black line).

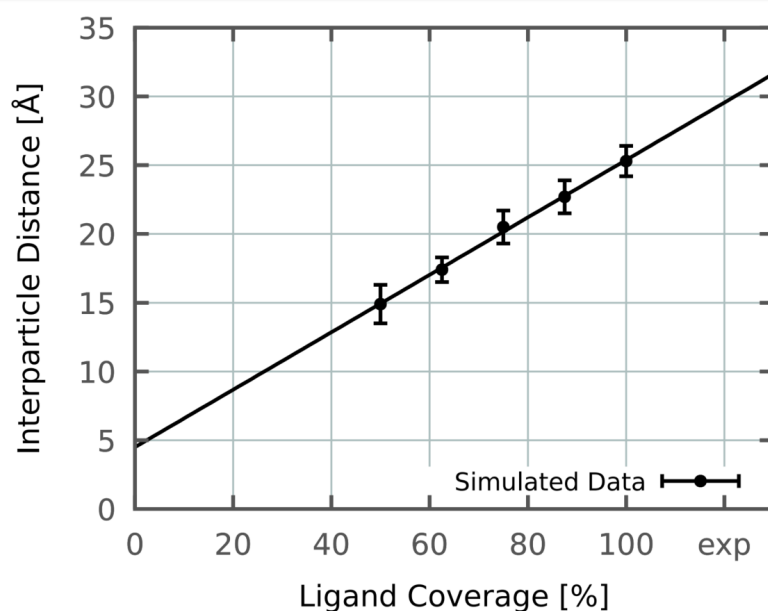


Figure A31: Average interparticle distances extracted from the MD simulations of the systems with pure 11T ligands and varying ligand coverages on the gold surface. Error bars represent standard deviations from ten MD simulation runs. The average interparticle distances extracted from each system are fitted with a linear function (solid black line).

A.4 Gold Nanoparticle-Based Chemiresistor Arrays

Monolithic sensor arrays consisting of different kinds of GNP films were fabricated through the LbL-SC procedure[85] in combination with DUV lithographic patterning[23]. All GNP films were prepared using batch GNP5. To produce GNP films with different organic matrix compositions, different functionalized MT ligands were used as follows: 1-dodecanethiol (12T), 3-mercaptopropionic acid (3MPA), 8-mercaptooctanoic acid (8MOA), 6-mercapto-3-pyridinecarboxylic acid (6MNA), 4-nitrothiophenol (4NTP), and 8-mercapto-1-octanol (8MOO).

A.4.1 4-Sensor Array

A monolithic chemiresistor array was produced, consisting of four pairs of different GNP films (9DT, 89%12T-9DT, 95%3MPA-9DT, and 100%8MOA), cf Figure 7.32b. The baseline resistance of the GNP films of this sensor array showed some variations (see Figure 7.38) after the film fabrication, the chemiresistor measurements were conducted three times in the period of one month. Week 0 is defined as the week when the 4-sensor array was fabricated. In week 1 (one week after fabrication), the 4-sensor array was exposed to 14 different analyte vapors in the concentration range of 200 to 400 ppm, with 14 exposures for each analyte. In week 3, the 4-sensor array was exposed to 17 different analytes in the concentration range of 50 to 1000 ppm, with each analyte dosing with 14 exposures. In week 4, the 4-sensor array was exposed to 6 different analyte vapors at concentrations of 200, 400, 600, and 800 ppm. Figures A32-A48 present the baseline-corrected timetraces measured in week 3, which were used to extract the three features as the training dataset for linear discriminant analysis (LDA), and the resulting LDA plot is shown in Figure 7.39.

The average response patterns of the "transient-state" features of the 4-sensor array to 7 different types of analytes are shown in Figures A49 and A50, and the average "transient-state" features to alcohol vapors are shown in Figures A51 and A52.

To evaluate the classification affected by aging effects of the GNP films, the responses to 400-ppm analytes measured in week 1 were used as the test dataset. This test dataset was transformed and projected onto the LDA plot, which was trained with the dataset collected from the responses measured in week 3. The resulting LDA is shown in Figure A53, and these results are summarized and presented in Table 7.4. In addition, the responses to 400-ppm analytes measured in week 4 were also used as the test dataset, and the data were projected onto the LDA plot, as shown in Figure A54. The classification results are presented in Table 7.4.

Figures A32-A48 are reprinted with permission from the Supporting Information of Ref. [2] (©2024 The Authors. Advanced Materials Interfaces published by Wiley-VCH GmbH).

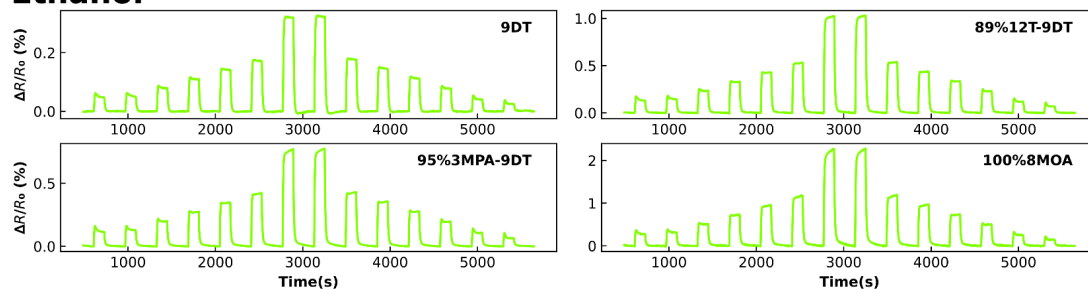
Ethanol

Figure A32: Baseline-corrected resistive responses of four GNP films of 4-sensor array to ethanol vapor at concentrations of 50, 100, 200, 300, 400, 500, 1000, 1000, 500, 400, 300, 200, 100 and 50 ppm.

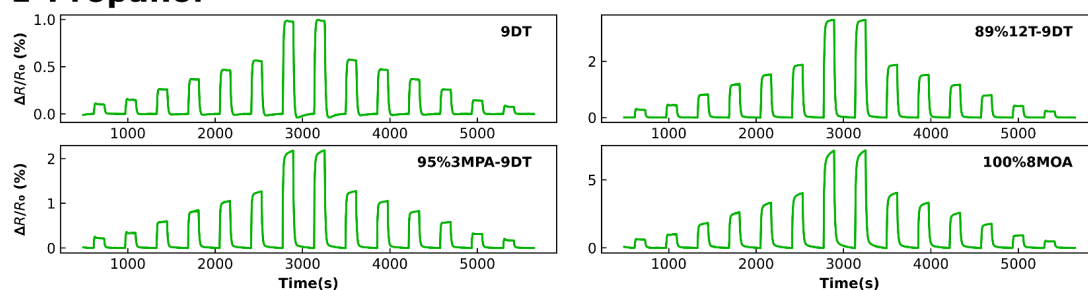
1-Propanol

Figure A33: Baseline-corrected resistive responses of four GNP films of 4-sensor array to 1-propanol vapor at concentrations of 50, 100, 200, 300, 400, 500, 1000, 1000, 500, 400, 300, 200, 100 and 50 ppm.

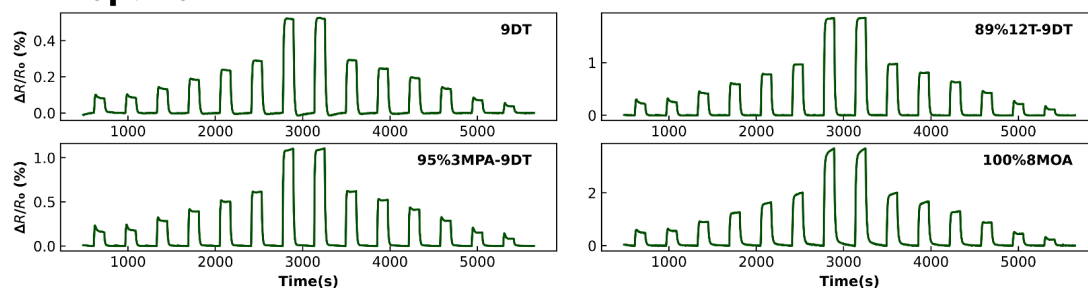
2-Propanol

Figure A34: Baseline-corrected resistive responses of four GNP films of 4-sensor array to 2-propanol vapor at concentrations of 50, 100, 200, 300, 400, 500, 1000, 1000, 500, 400, 300, 200, 100 and 50 ppm.

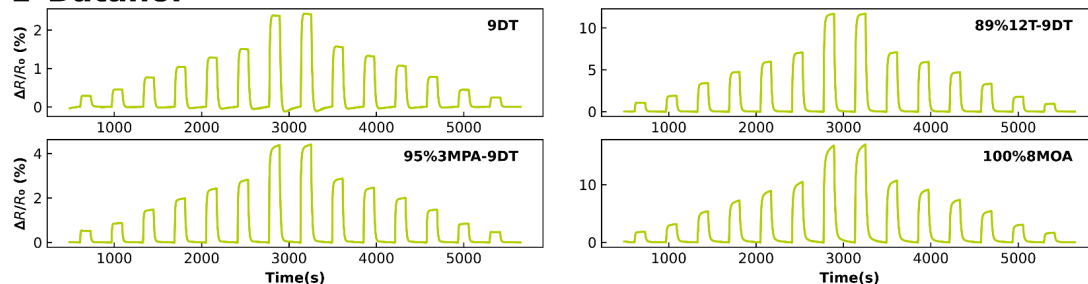
1-Butanol

Figure A35: Baseline-corrected resistive responses of four GNP films of 4-sensor array to 1-butanol vapor at concentrations of 50, 100, 200, 300, 400, 500, 1000, 1000, 500, 400, 300, 200, 100 and 50 ppm.

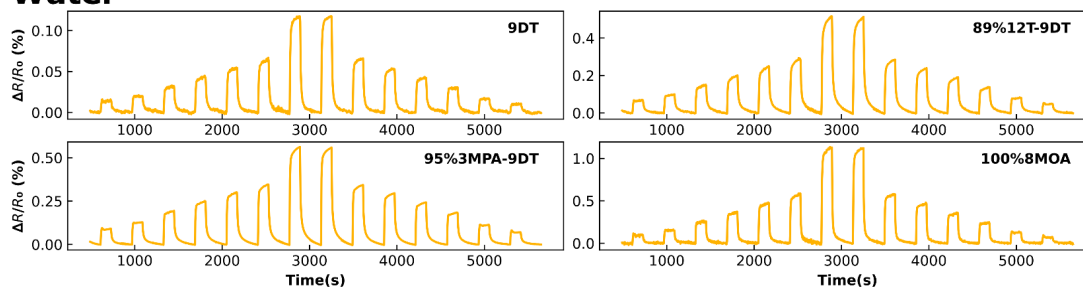
Water

Figure A36: Baseline-corrected resistive responses of four GNP films of 4-sensor array to water vapor at concentrations of 50, 100, 200, 300, 400, 500, 1000, 1000, 500, 400, 300, 200, 100 and 50 ppm.

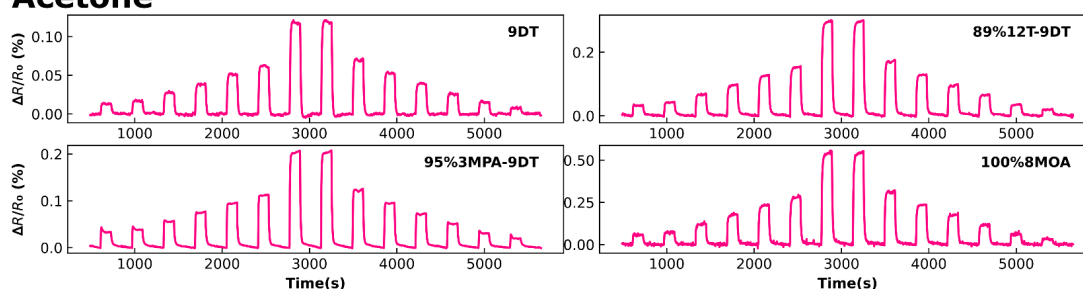
Acetone

Figure A37: Baseline-corrected resistive responses of four GNP films of 4-sensor array to acetone vapor at concentrations of 50, 100, 200, 300, 400, 500, 1000, 1000, 500, 400, 300, 200, 100 and 50 ppm.

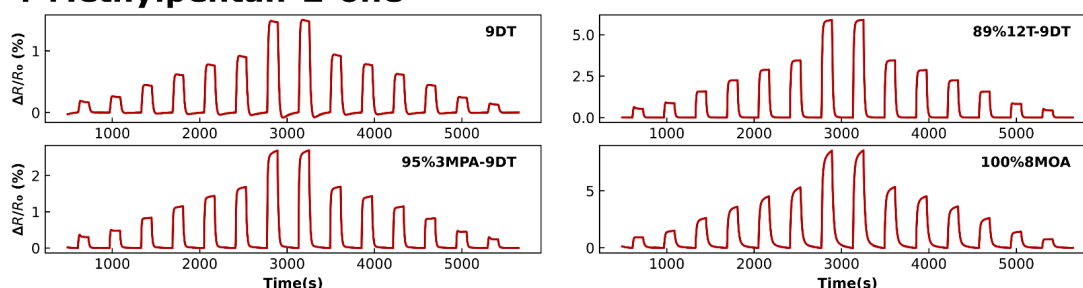
4-Methylpentan-2-one

Figure A38: Baseline-corrected resistive responses of four GNP films of 4-sensor array to 4-methylpentan-2-one vapor at concentrations of 50, 100, 200, 300, 400, 500, 1000, 1000, 500, 400, 300, 200, 100 and 50 ppm.

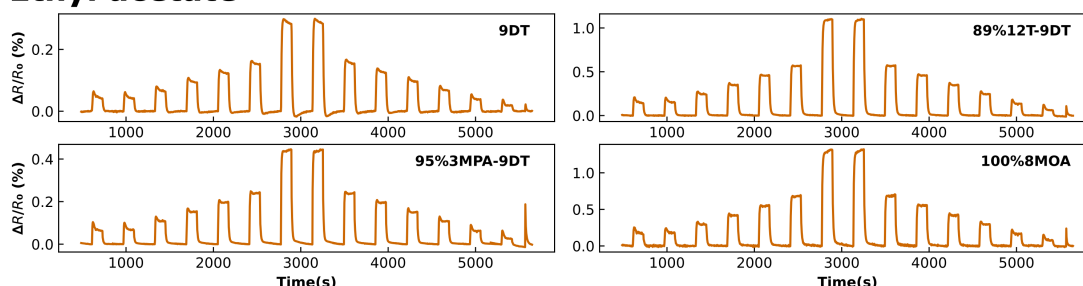
Ethyl acetate

Figure A39: Baseline-corrected resistive responses of four GNP films of 4-sensor array to ethyl acetate vapor at concentrations of 50, 100, 200, 300, 400, 500, 1000, 1000, 500, 400, 300, 200, 100 and 50 ppm.

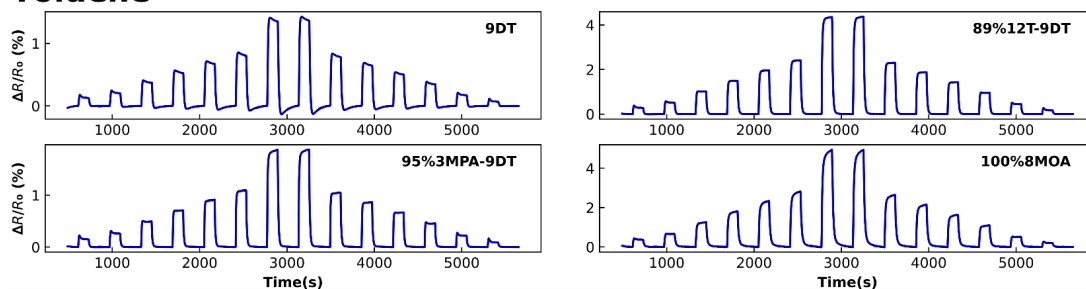
Toluene

Figure A40: Baseline-corrected resistive responses of four GNP films of 4-sensor array to toluene vapor at concentrations of 50, 100, 200, 300, 400, 500, 1000, 1000, 500, 400, 300, 200, 100 and 50 ppm.

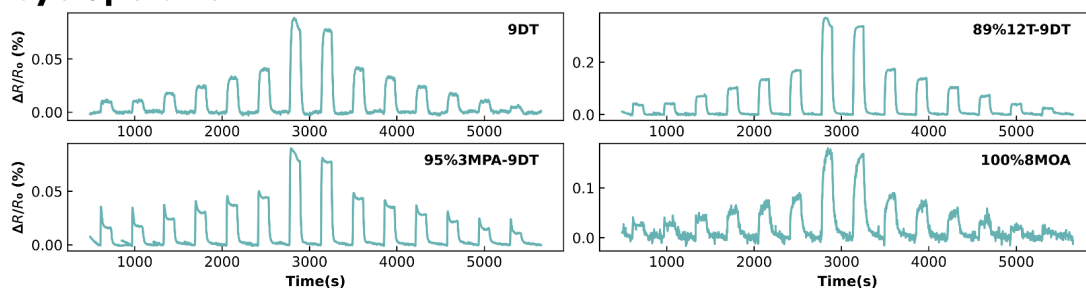
Cyclopentane

Figure A41: Baseline-corrected resistive responses of four GNP films of 4-sensor array to cyclopentane vapor at concentrations of 50, 100, 200, 300, 400, 500, 1000, 1000, 500, 400, 300, 200, 100 and 50 ppm.

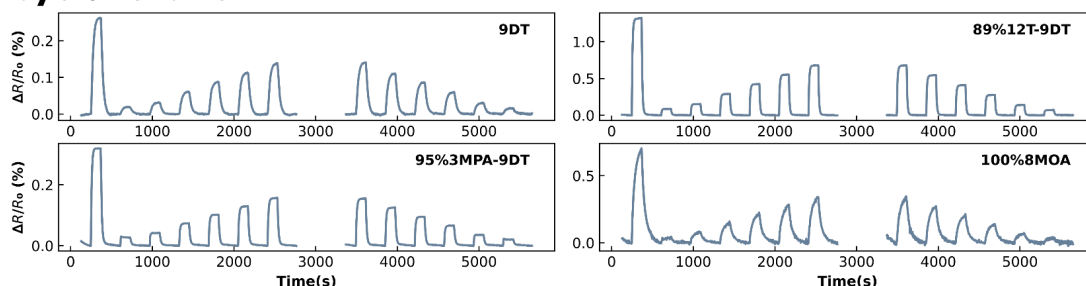
Cyclohexane

Figure A42: Baseline-corrected resistive responses of four GNP films of 4-sensor array to cyclohexane vapor at concentrations of 1000, 50, 100, 200, 300, 400, 500, 500, 400, 300, 200, 100 and 50 ppm.

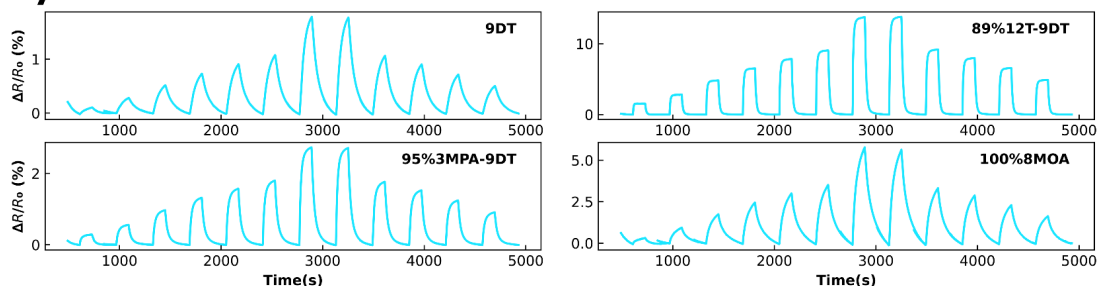
Cyclooctane

Figure A43: Baseline-corrected resistive responses of four GNP films of 4-sensor array to cyclooctane vapor at concentrations of 50, 100, 200, 300, 400, 500, 1000, 1000, 500, 400, 300, 200, 100 and 50 ppm.

Methylcyclohexane

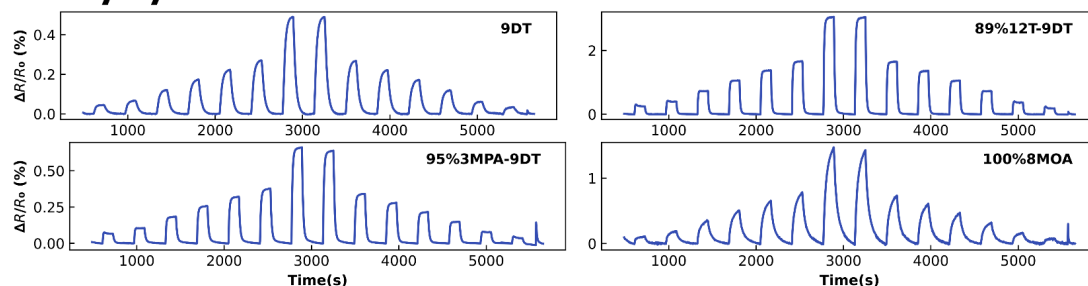


Figure A44: Baseline-corrected resistive responses of four GNP films of 4-sensor array to methylcyclohexane vapor at concentrations of 50, 100, 200, 300, 400, 500, 1000, 1000, 500, 400, 300, 200, 100 and 50 ppm.

n-Hexane

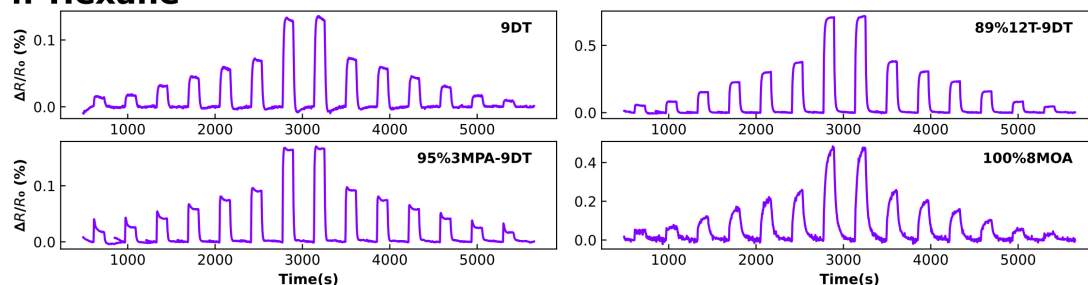


Figure A45: Baseline-corrected resistive responses of four GNP films of 4-sensor array to n-hexane vapor at concentrations of 50, 100, 200, 300, 400, 500, 1000, 1000, 500, 400, 300, 200, 100 and 50 ppm.

n-Heptane

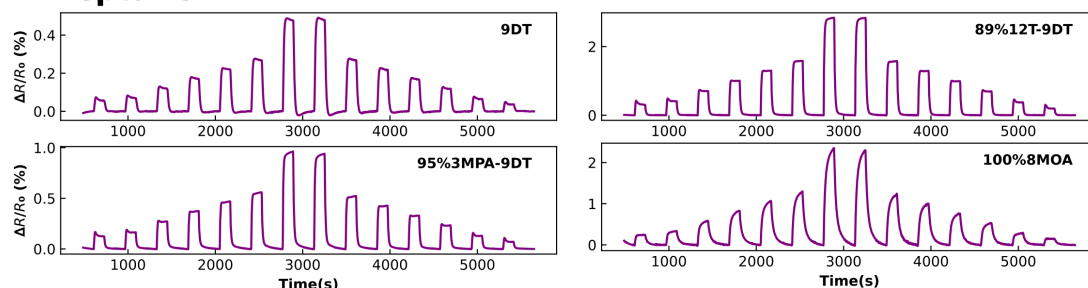


Figure A46: Baseline-corrected resistive responses of four GNP films of 4-sensor array to n-heptane vapor at concentrations of 50, 100, 200, 300, 400, 500, 1000, 1000, 500, 400, 300, 200, 100 and 50 ppm.

n-Octane

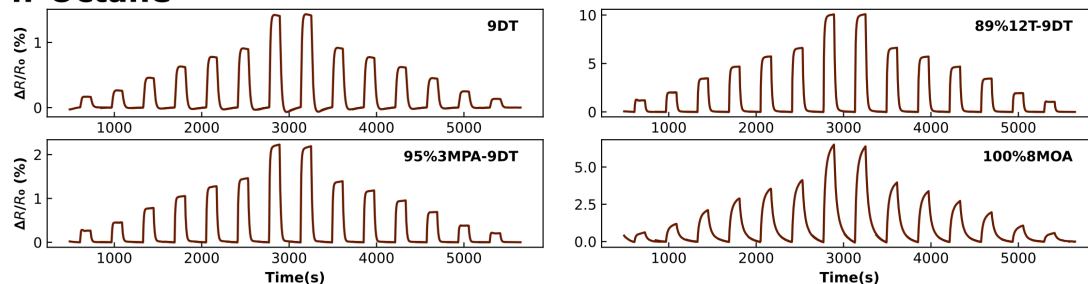


Figure A47: Baseline-corrected resistive responses of four GNP films of 4-sensor array to n-octane vapor at concentrations of 50, 100, 200, 300, 400, 500, 1000, 1000, 500, 400, 300, 200, 100 and 50 ppm.

Isooctane

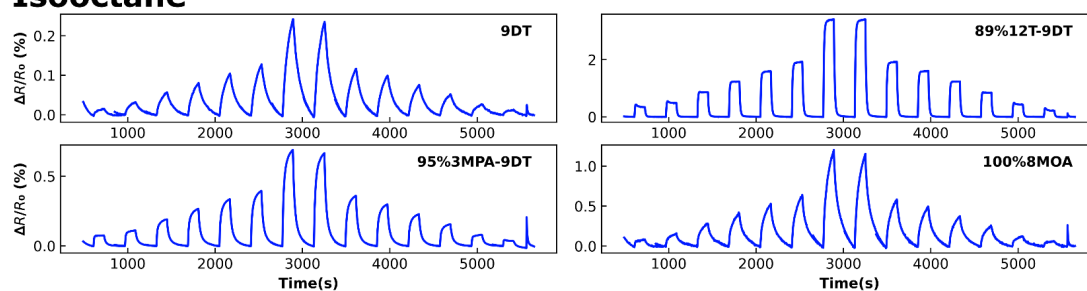


Figure A48: Baseline-corrected resistive responses of four GNP films of 4-sensor array to isooctane vapor at concentrations of 50, 100, 200, 300, 400, 500, 1000, 1000, 500, 400, 300, 200, 100 and 50 ppm.

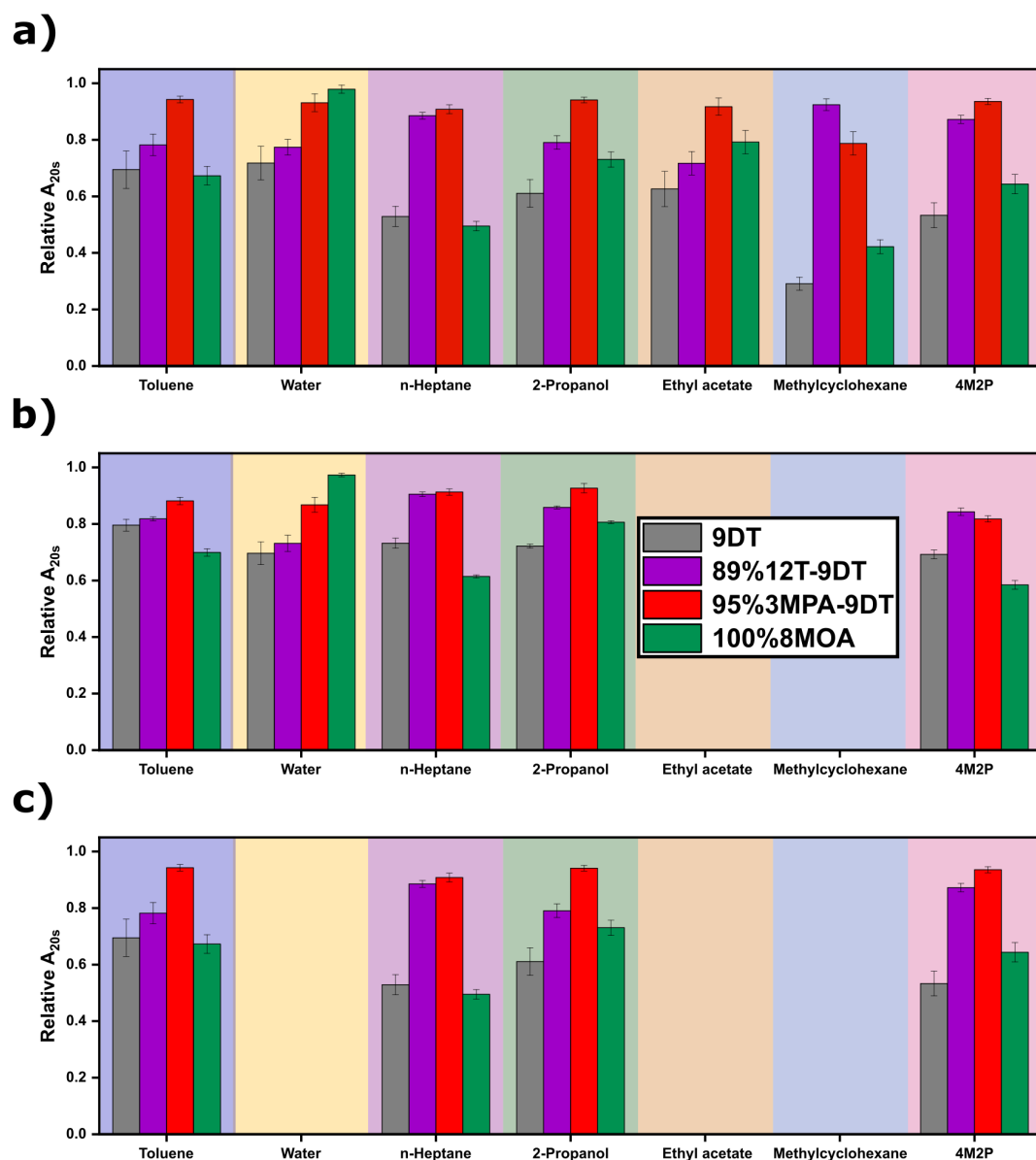


Figure A49: Average relative A_{20s} features of four GNP films: 9DT (black), 89%12T-9DT (purple), 95%3MPA-9DT (red), and 100%8MOA (green). The sensors were exposed to different analyte vapors (indicated on the x-axis). The responses were measured in a) week 3 (in the concentration range of 50 to 1000 ppm), b) week 1 (in the concentration range of 200 to 400 ppm), and c) week 4 (in the concentration range of 50 to 1000 ppm). Error bars were calculated as the standard deviation of the relative A_{20s} features of each GNP chemiresistor within the array, exposed to analyte vapors in the tested concentration range.

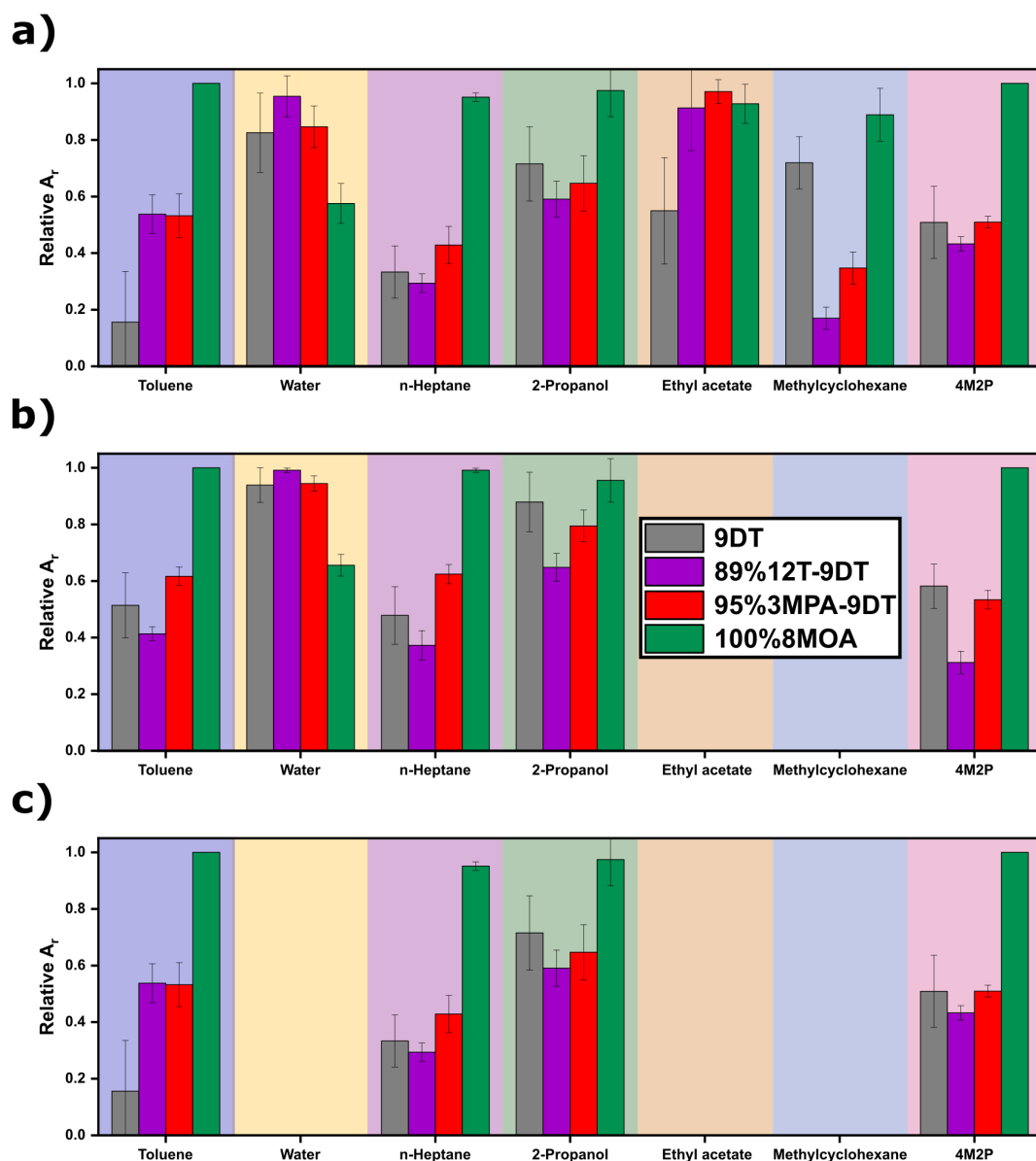


Figure A50: Average relative A_r features of four GNP films: 9DT (black), 89%12T-9DT (purple), 95%3MPA-9DT (red), and 100%8MOA (green). The sensors were exposed to different analyte vapors (indicated on the x-axis). The responses were measured in a) week 3 (in the concentration range of 50 to 1000 ppm), b) week 1 (in the concentration range of 200 to 400 ppm), and c) week 4 (in the concentration range of 50 to 1000 ppm). Error bars were calculated as the standard deviation of the relative A_r features of each GNP chemiresistor within the array, exposed to analyte vapors in the tested concentration range.

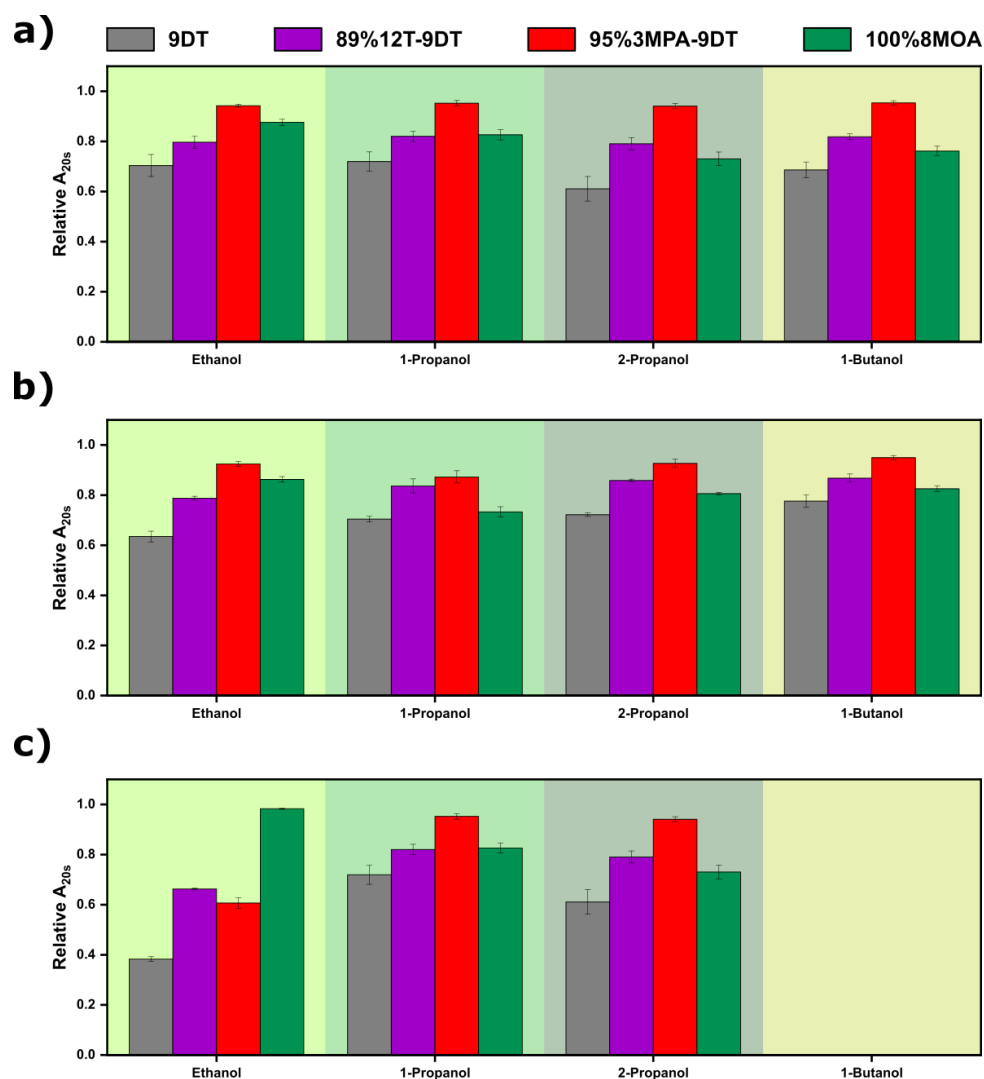


Figure A51: Average relative (A_{20s} features of four GNP films: 9DT (black), 89%12T-9DT (purple), 95%3MPA-9DT (red), and 100%8MOA (green). The sensors were exposed to alcohol vapors, ethanol, 1-propanol, 2-propanol, and 1-butanol. The responses were measured in a) week 3 (in the concentration range of 50 to 1000 ppm), b) week 1 (in the concentration range of 200 to 400 ppm), and c) week 4 (in the concentration range of 50 to 1000 ppm). Error bars were calculated as the standard deviation of the relative (A_{20s} features of each GNP chemiresistor within the array, exposed to analyte vapors in the tested concentration range.

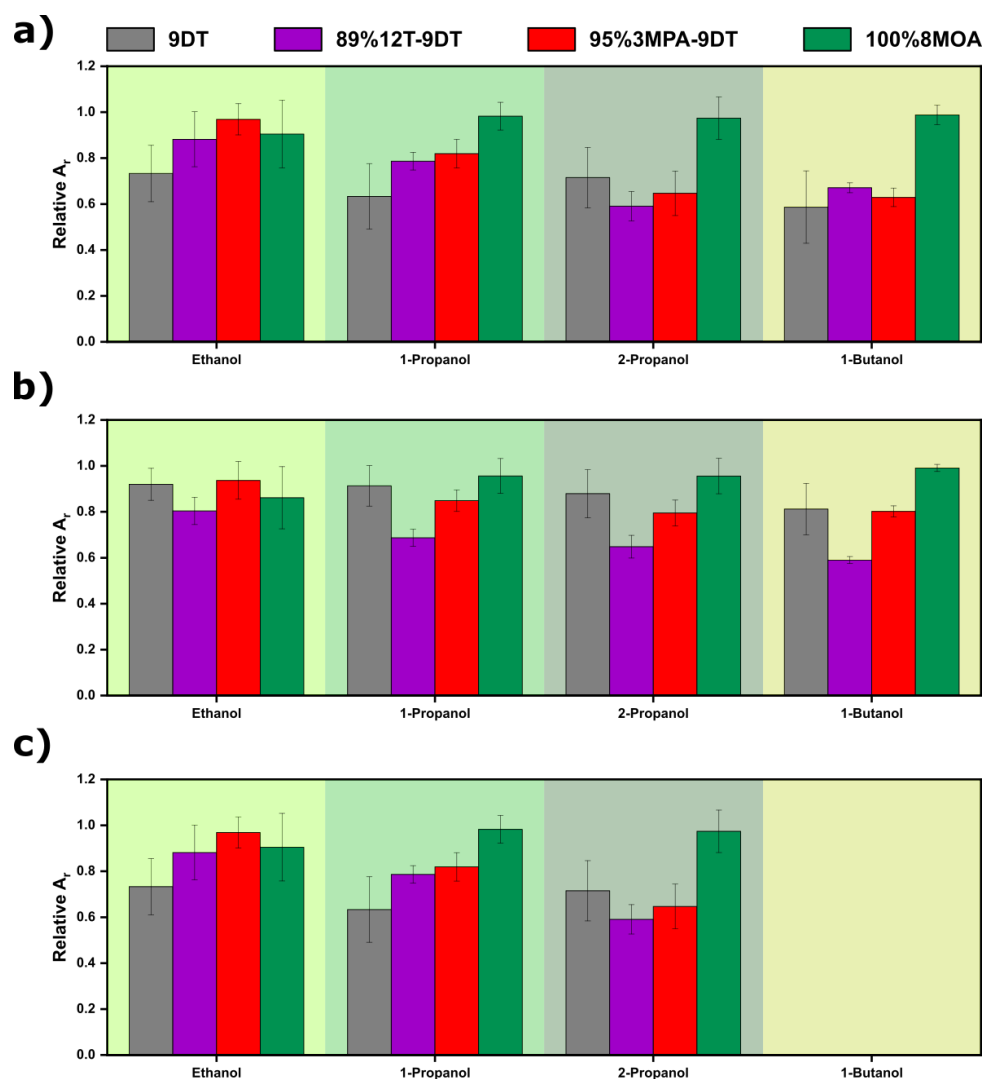


Figure A52: Average relative (A_r) features of four GNP films: 9DT (black), 89%12T-9DT (purple), 95%3MPA-9DT (red), and 100%8MOA (green). The sensors were exposed to alcohol vapors, ethanol, 1-propanol, 2-propanol, and 1-butanol. The responses were measured in a) week 3 (in the concentration range of 50 to 1000 ppm), b) week 1 (in the concentration range of 200 to 400 ppm), and c) week 4 (in the concentration range of 50 to 1000 ppm). Error bars were calculated as the standard deviation of the relative (A_r) features of each GNP chemiresistor within the array, exposed to analyte vapors in the tested concentration range.

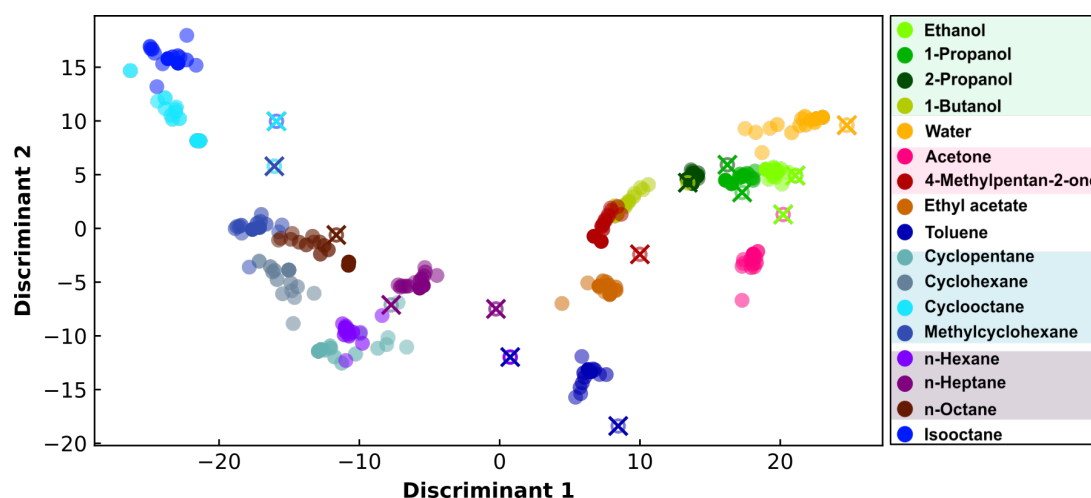


Figure A53: LDA plot trained using the dataset of the 4-sensor array (shown in Figure 7.32b) based on both "steady-state" and "transient-state" features (extracted from the responses measured in week 3), when exposed to 17 different analytes at concentrations ranging from 50 to 1000 ppm (indicated by different shades of color). Filled circles represent data points used to fit the LDA model. The responses to 14 different analytes at 400 ppm, measured in week 1, were used as the test dataset, and were projected onto the LDA plot as empty circles. Colored crosses indicate the model's predictions for the test dataset.

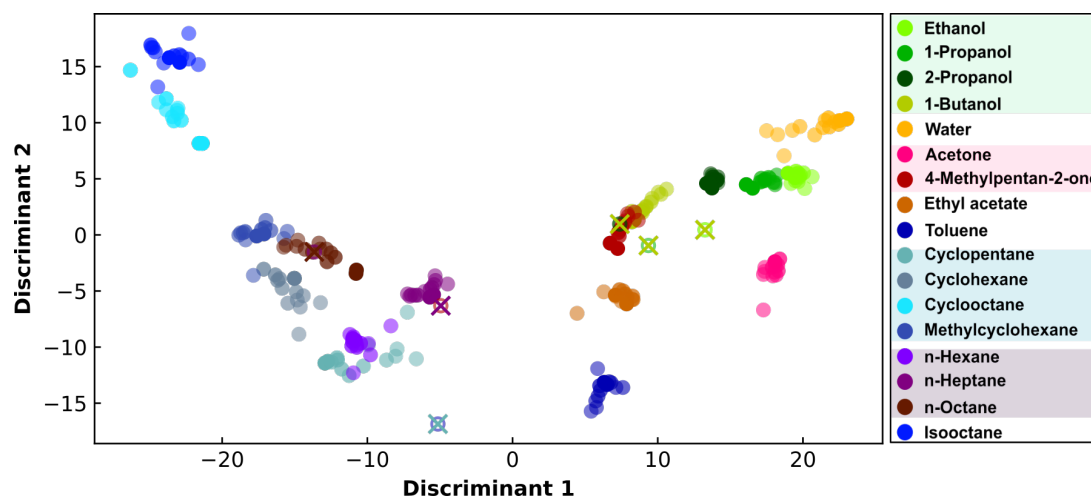


Figure A54: LDA plot trained using the dataset of the 4-sensor array (shown in Figure 7.32b) based on both "steady-state" and "transient-state" features (extracted from the responses measured in week 3), when exposed to 17 different analytes at concentrations ranging from 50 to 1000 ppm (indicated by different shades of color). Filled circles represent data points used to fit the LDA model. The responses to 6 different analytes at 400 ppm, measured in week 4, were used as the test dataset, and were projected onto the LDA plot as empty circles. Colored crosses indicate the model's predictions for the test dataset.

A.4.2 8-Sensor Array

In addition to 4-sensor array, another sensor array was fabricated by combining two monolithic sensor arrays, comprising eight different GNP films (9DT, 95%6MNA-9DT, 95%8MOA-9DT, 100%8MOA, 95%8MOO-9DT, 89%12T-9DT, 95%4NTP-9DT, and 95%3MPA-9DT). The resulting 8-sensor array is shown in Figure 7.42. This 8-sensor array was exposed to 19 different analyte vapors at concentrations ranging from 100 to 2000 ppm over a seven-week period. The average relative "transient-state" features extracted from the responses measured in four different times are shown in Figures A74 and A75.

Figures A55-A73 present the baseline-corrected response timetraces measured in week 1, which were used to extract the three features as the training dataset for LDA, and the resulting LDA plot is shown in Figure 7.43a. The tested analyte concentrations ranged from 100 to 1000 ppm. The 8-sensor array was exposed to the same 19 analytes at the concentration of 600 ppm for 11 to 17 days (week 3) after the first chemiresistor measurements. These measured responses were used as the test dataset, and the data of each exposure were classified by the LDA, which was trained with the dataset collected from week 1. The classification results are presented in Table A3.

Due to aging-induced changes of the sensors' response characteristics over time, re-training of the LDA model is necessary from time to time to maintain the reliability of analyte classification. Therefore, the responses of the 8-sensor array to 19 analyte vapors (in the concentration range of 100 to 1000 ppm in nitrogen) were measured again in week 5, and three features extracted from these responses were used as the training dataset for LDA. The resulting LDA is shown in Figure 7.43b. To evaluate the classification of this new LDA affected by the aging of the GNP films, the 8-sensor array were exposed to the analyte vapors at concentrations of 600, 800, and 2000 ppm. The responses upon exposures of analytes at these three different concentrations were used as the test dataset, and the data were projected onto the LDA plot (trained by the dataset collected in week 5), the resulting LDA plots are shown in Figures A76, A77, and A78. When the test analyte vapors in the concentration range of the training data, all analytes were classified correctly, cf. Figures A76 and A77. However, when the test analyte vapors beyond the concentration range of the training data, 2-propanol was misclassified, and assigned to its neighboring cluster, 1-butanol, as shown in Figure A78.

Figures A55-A73 are reprinted with permission from the Supporting Information of Ref. [2] (©2024 The Authors. Advanced Materials Interfaces published by Wiley-VCH GmbH).

Ethanol

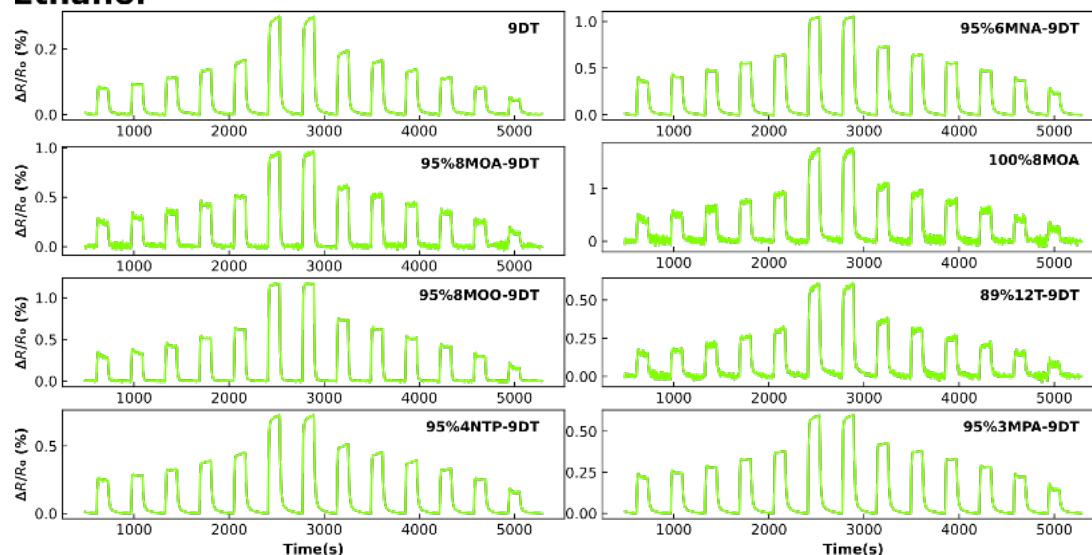


Figure A55: Baseline-corrected resistive responses of eight GNP films of the 8-sensor array to ethanol vapor at concentrations of 100, 200, 300, 400, 500, 1000, 1000, 600, 500, 400, 300, 200 and 100 ppm.

1-Propanol

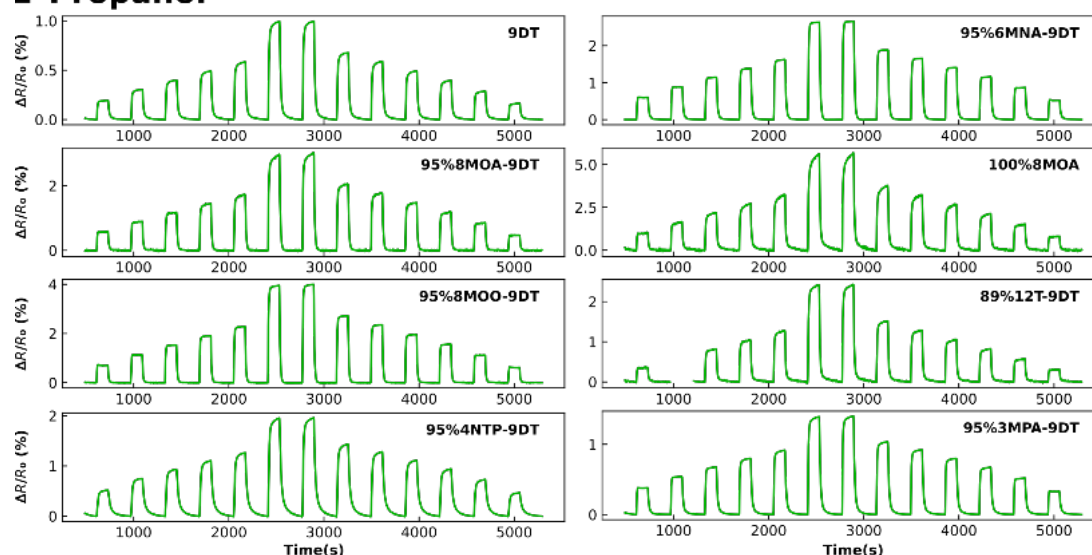


Figure A56: Baseline-corrected resistive responses of eight GNP films of the 8-sensor array to 1-propanol vapor at concentrations of 100, 200, 300, 400, 500, 1000, 1000, 600, 500, 400, 300, 200 and 100 ppm. The first 200-ppm exposure was deficient in 89%12T-9DT GNP film due to the technical issue.

2-Propanol

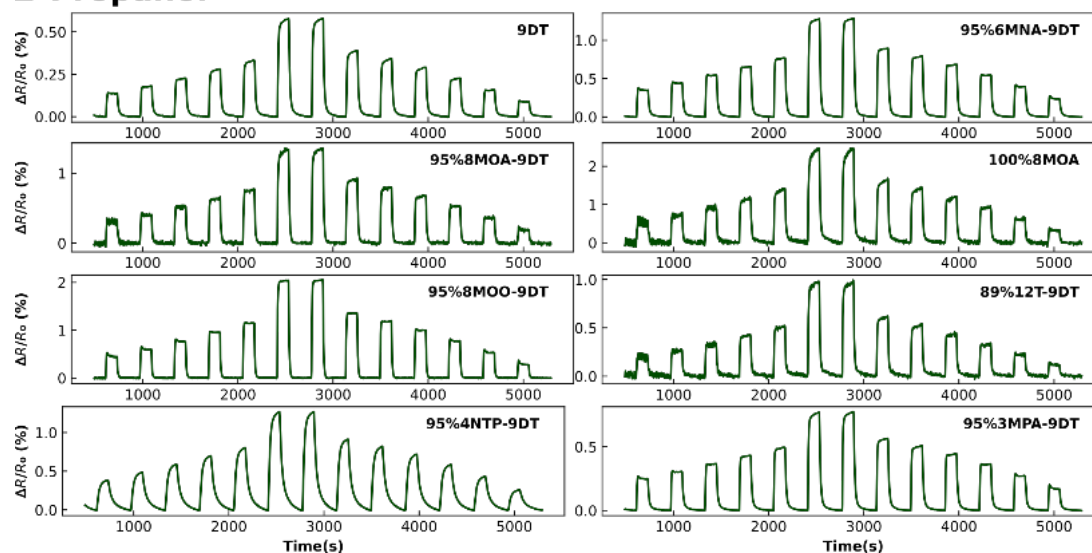


Figure A57: Baseline-corrected resistive responses of eight GNP films of the 8-sensor array to 2-propanol vapor at concentrations of 100, 200, 300, 400, 500, 1000, 1000, 600, 500, 400, 300, 200 and 100 ppm.

1-Butanol

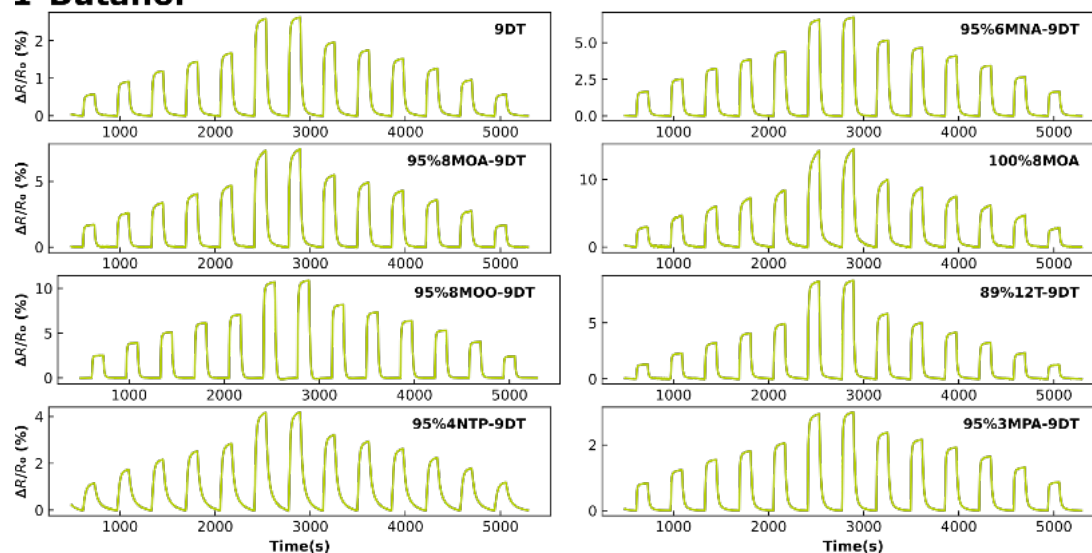


Figure A58: Baseline-corrected resistive responses of eight GNP films of the 8-sensor array to 1-butanol vapor at concentrations of 100, 200, 300, 400, 500, 1000, 1000, 600, 500, 400, 300, 200 and 100 ppm.

2-Butanol

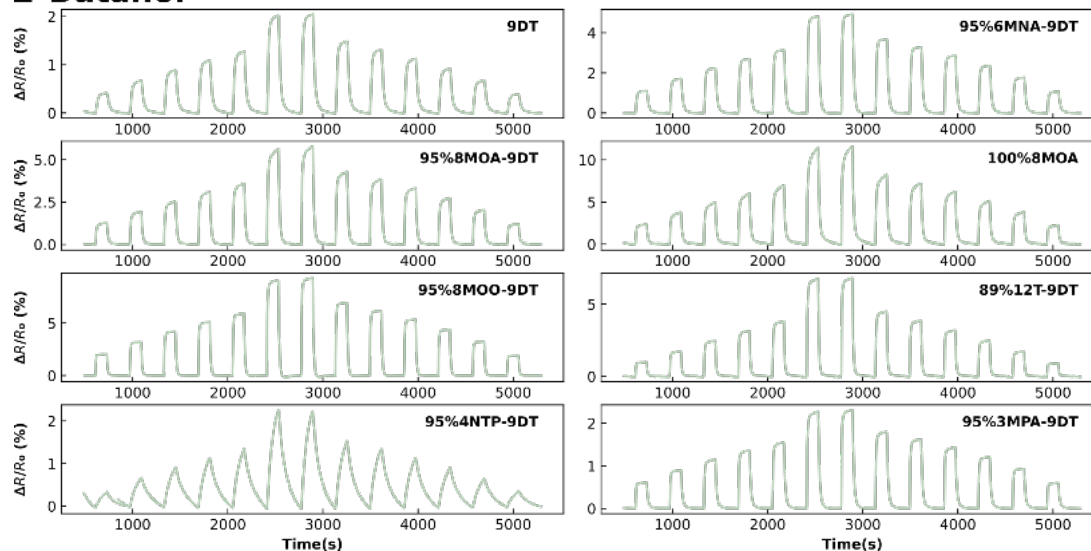


Figure A59: Baseline-corrected resistive responses of eight GNP films of the 8-sensor array to 2-butanol vapor at concentrations of 100, 200, 300, 400, 500, 1000, 1000, 600, 500, 400, 300, 200 and 100 ppm.

Water

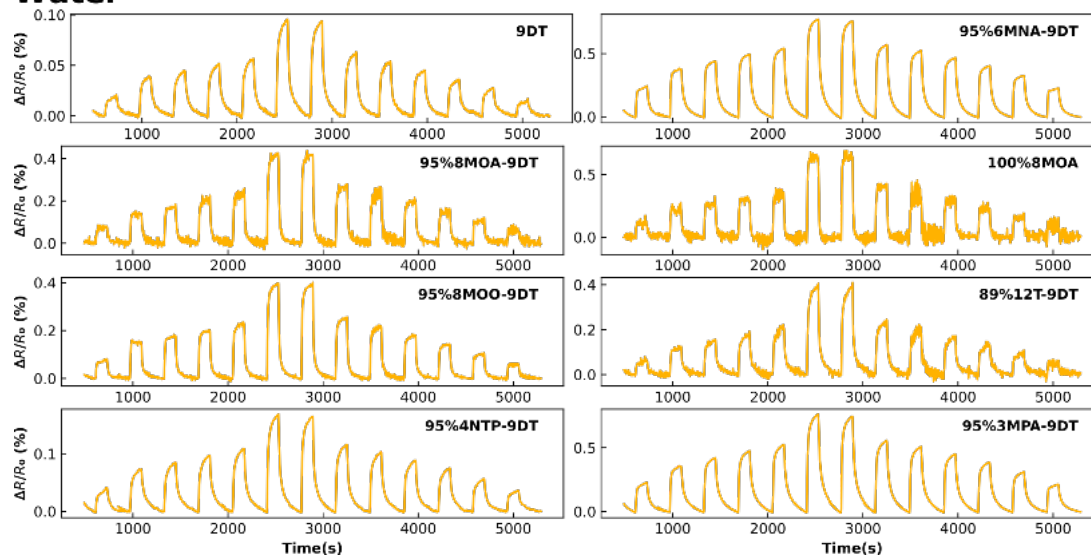


Figure A60: Baseline-corrected resistive responses of eight GNP films of the 8-sensor array to water vapor at concentrations of 100, 200, 300, 400, 500, 1000, 1000, 600, 500, 400, 300, 200 and 100 ppm.

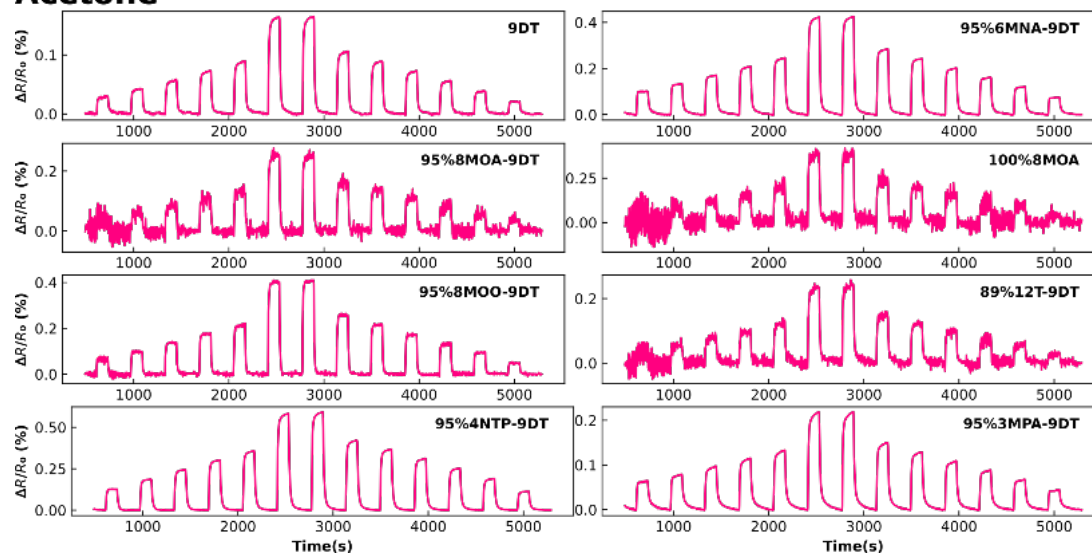
Acetone

Figure A61: Baseline-corrected resistive responses of eight GNP films of the 8-sensor array to acetone vapor at concentrations of 100, 200, 300, 400, 500, 1000, 1000, 600, 500, 400, 300, 200 and 100 ppm.

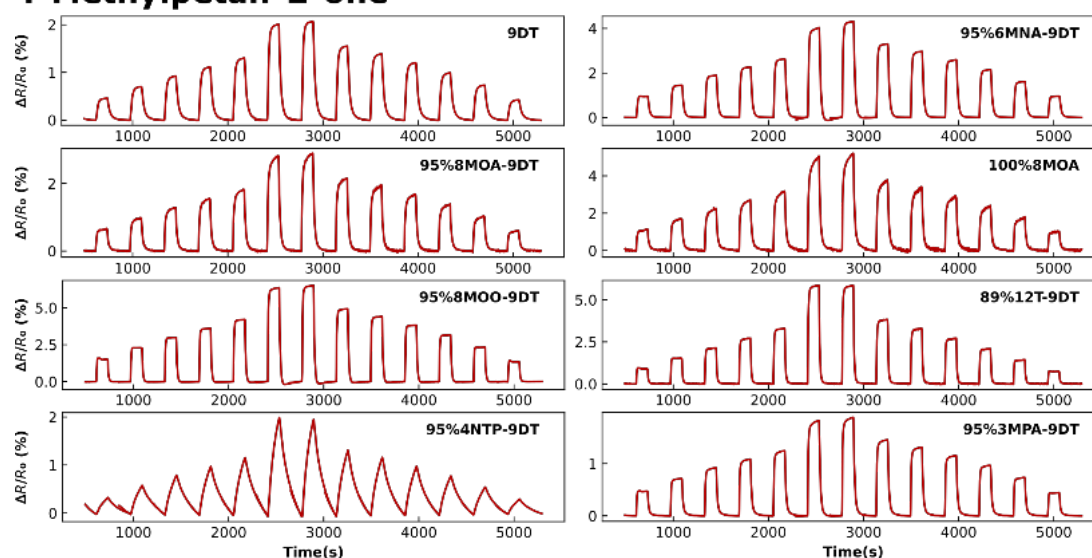
4-Methylpentan-2-one

Figure A62: Baseline-corrected resistive responses of eight GNP films of the 8-sensor array to 4-methylpentan-2-one vapor at concentrations of 100, 200, 300, 400, 500, 1000, 1000, 600, 500, 400, 300, 200 and 100 ppm.

2-Pentanone

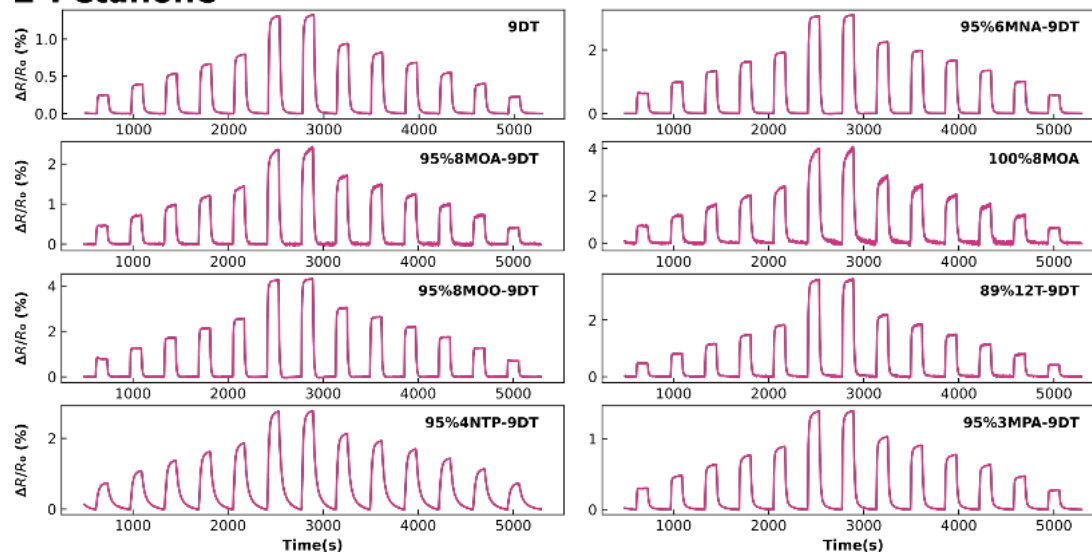


Figure A63: Baseline-corrected resistive responses of eight GNP films of the 8-sensor array to 2-pentanone vapor at concentrations of 100, 200, 300, 400, 500, 1000, 1000, 600, 500, 400, 300, 200 and 100 ppm.

Ethyl acetate

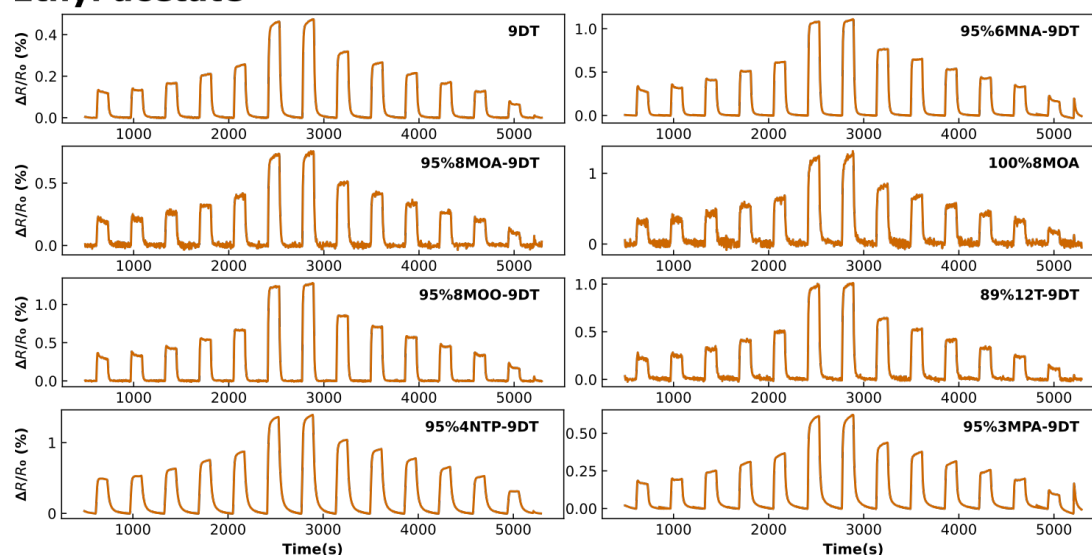


Figure A64: Baseline-corrected resistive responses of eight GNP films of the 8-sensor array to ethyl acetate vapor at concentrations of 100, 200, 300, 400, 500, 1000, 1000, 600, 500, 400, 300, 200 and 100 ppm.

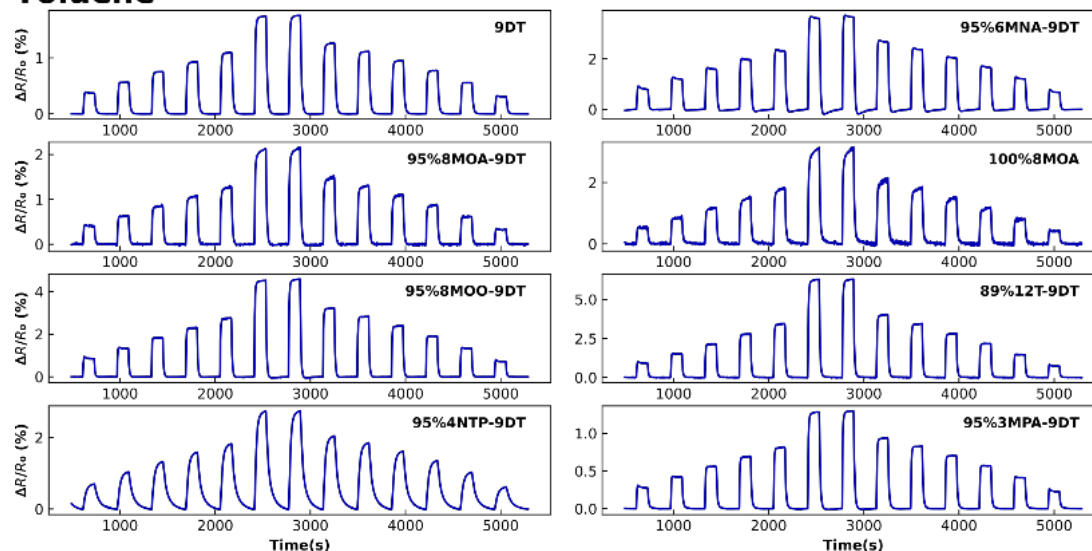
Toluene

Figure A65: Baseline-corrected resistive responses of eight GNP films of the 8-sensor array to toluene vapor at concentrations of 100, 200, 300, 400, 500, 1000, 1000, 600, 500, 400, 300, 200 and 100 ppm.

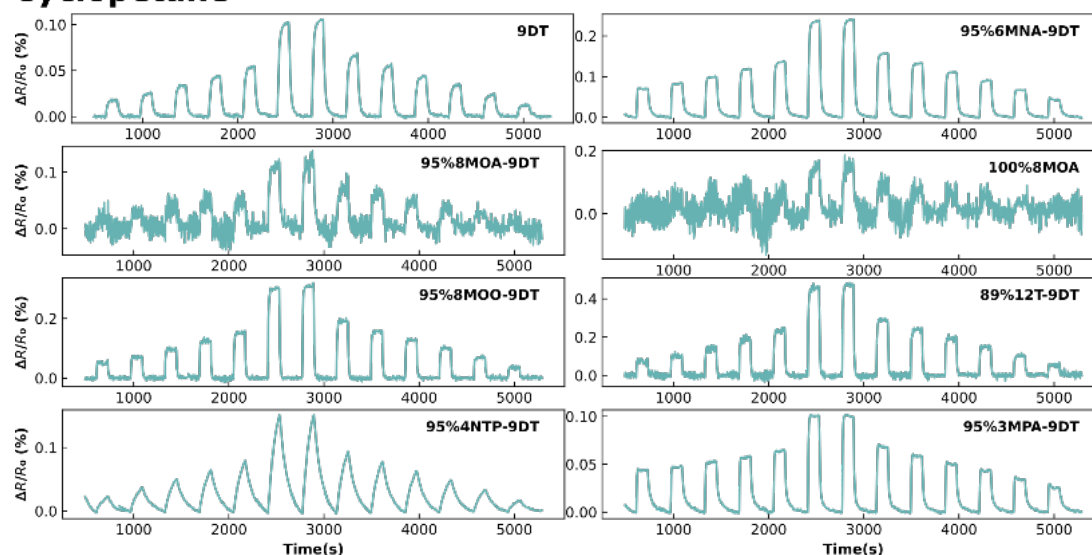
Cyclopentane

Figure A66: Baseline-corrected resistive responses of eight GNP films of the 8-sensor array to cyclopentane vapor at concentrations of 100, 200, 300, 400, 500, 1000, 1000, 600, 500, 400, 300, 200 and 100 ppm.

Cyclohexane

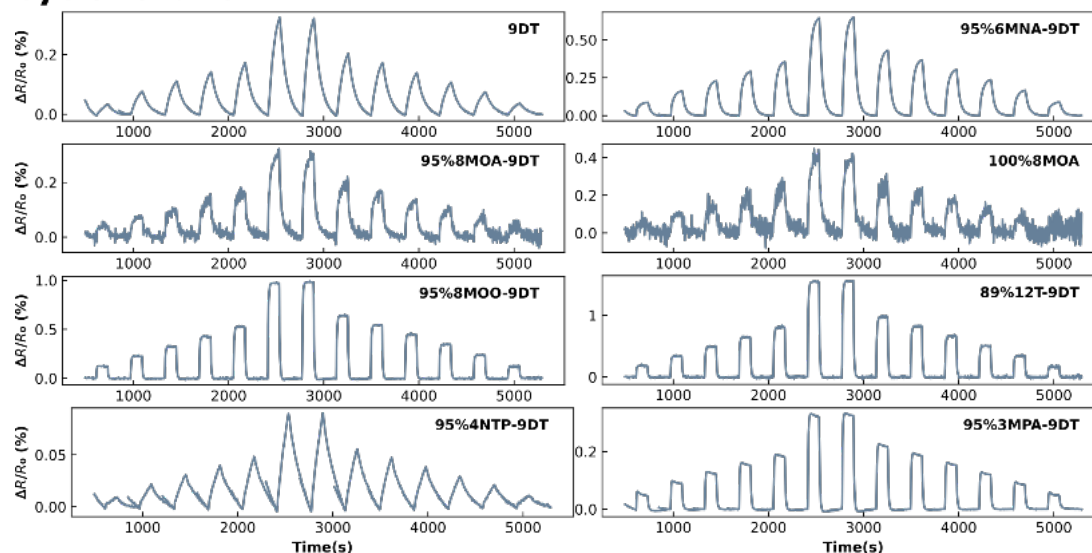


Figure A67: Baseline-corrected resistive responses of eight GNP films of the 8-sensor array to cyclohexane vapor at concentrations of 100, 200, 300, 400, 500, 1000, 1000, 600, 500, 400, 300, 200 and 100 ppm.

Cyclooctane

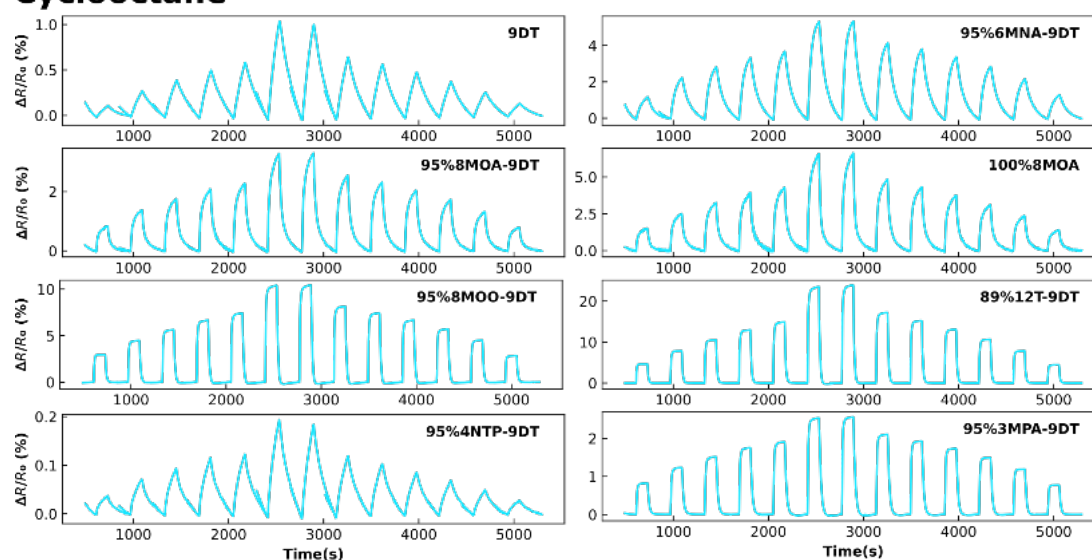


Figure A68: Baseline-corrected resistive responses of eight GNP films of the 8-sensor array to cyclooctane vapor at concentrations of 100, 200, 300, 400, 500, 1000, 1000, 600, 500, 400, 300, 200 and 100 ppm.

Methylcyclohexane

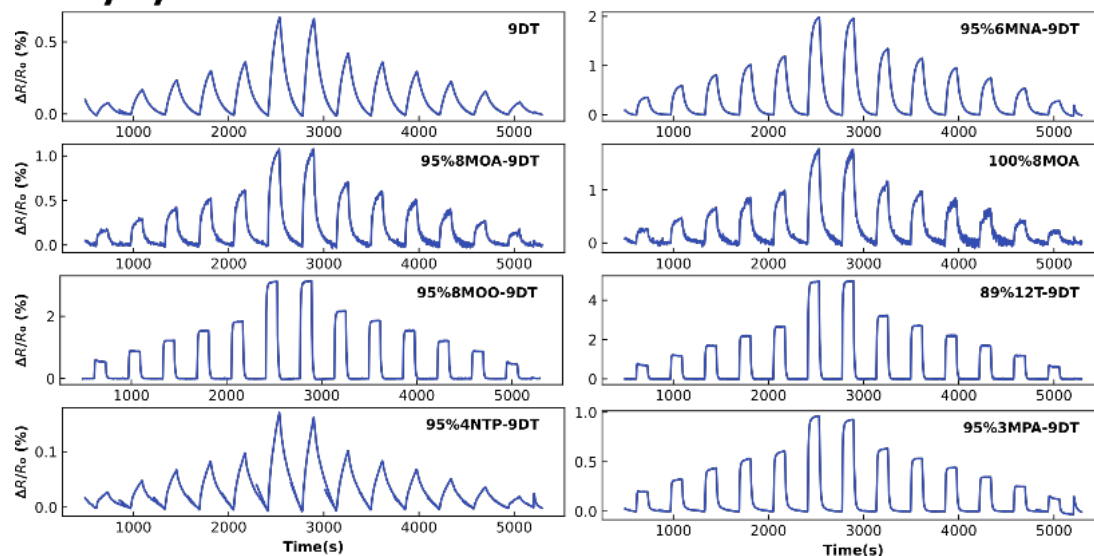


Figure A69: Baseline-corrected resistive responses of eight GNP films of the 8-sensor array to methylcyclohexane vapor at concentrations of 100, 200, 300, 400, 500, 1000, 1000, 600, 500, 400, 300, 200 and 100 ppm.

n-Hexane

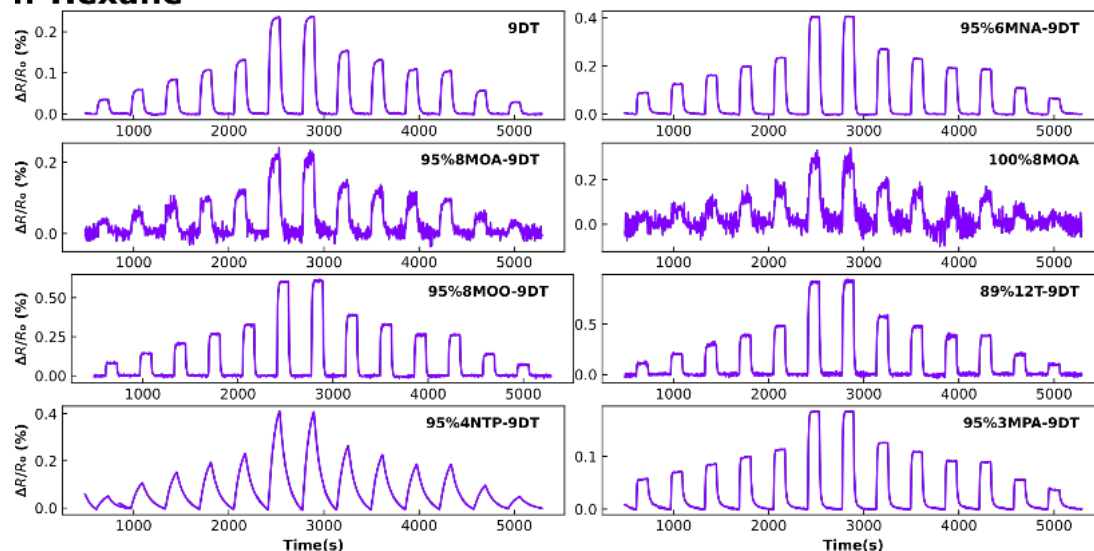


Figure A70: Baseline-corrected resistive responses of eight GNP films of the 8-sensor array to n-hexane vapor at concentrations of 100, 200, 300, 400, 500, 1000, 1000, 600, 500, 400, 300, 200 and 100 ppm.

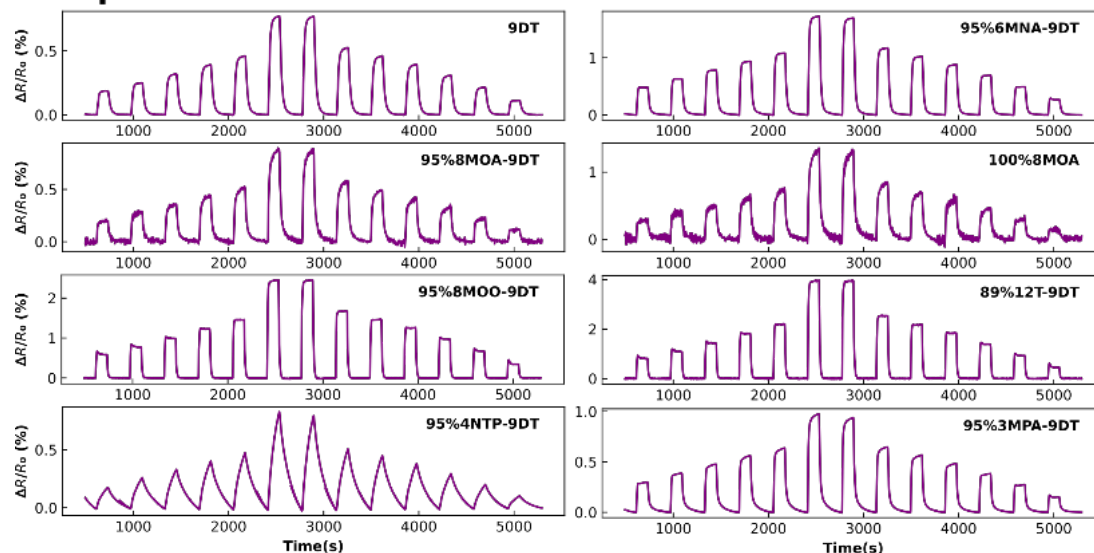
n-Heptane

Figure A71: Baseline-corrected resistive responses of eight GNP films of the 8-sensor array to n-heptane vapor at concentrations of 100, 200, 300, 400, 500, 1000, 1000, 600, 500, 400, 300, 200 and 100 ppm.

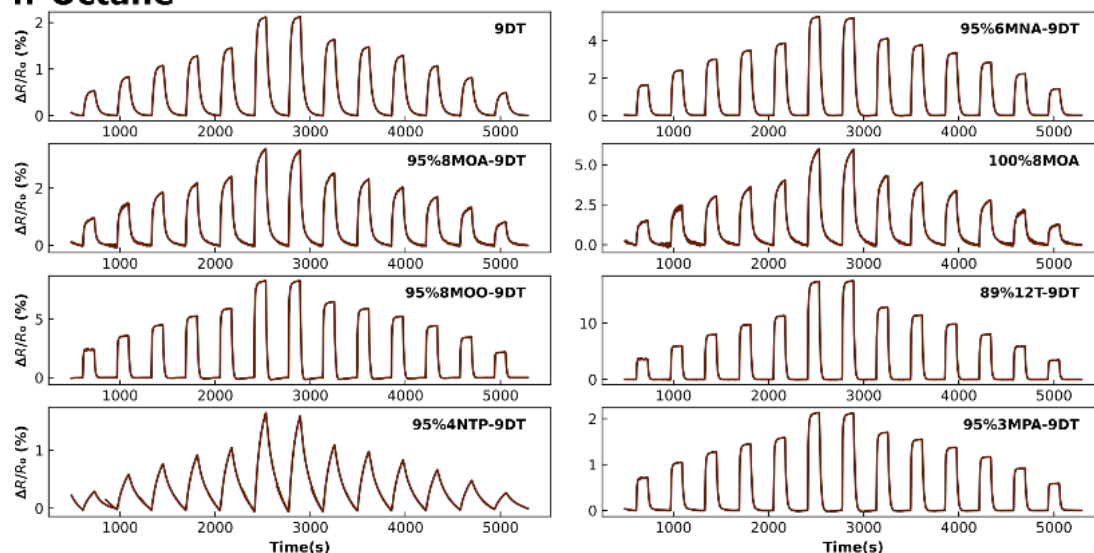
n-Octane

Figure A72: Baseline-corrected resistive responses of eight GNP films of the 8-sensor array to n-octane vapor at concentrations of 100, 200, 300, 400, 500, 1000, 1000, 600, 500, 400, 300, 200 and 100 ppm.

Isooctane

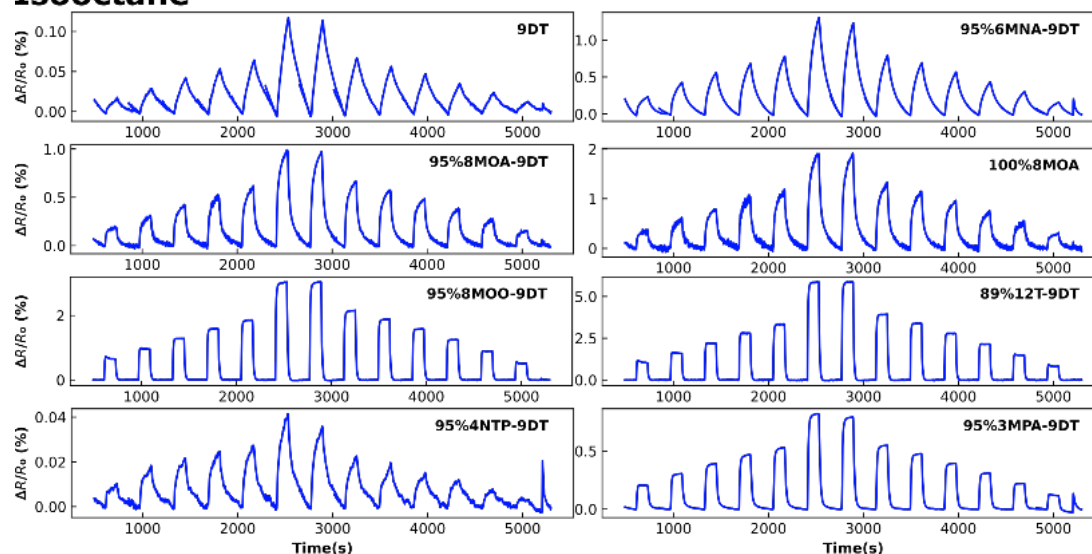


Figure A73: Baseline-corrected resistive responses of eight GNP films of the 8-sensor array to isooctane vapor at concentrations of 100, 200, 300, 400, 500, 1000, 1000, 600, 500, 400, 300, 200 and 100 ppm.

Table A3: The array comprised 8 types of GNP chemiresistors, and LDA was used for classification. The data collected in week 1 served as the training dataset. Features extracted from the response transients exposed to 600 ppm analyte vapors in week 3 were used as the test dataset. A check mark indicates a correct predicted classification, a cross mark represents a wrong prediction (the wrongly assigned cluster is indicated in the parentheses).

Analyte Vapor	Test Dataset(Week 3)
Ethanol	✓
1-Propanol	✓
2-Propanol	× (1-Propanol)
1-Butanol	× (1-Propanol)
Isobutanol	✓
Water	✓
Acetone	✓
4M2P	× (Isobutanol)
2-Pentanone	× (1-Propanol)
Ethyl acetate	× (1-Propanol)
Toluene	✓
Cyclopentane	× (n-Octane)
Cyclohexane	× (Methylcyclohexane)
Cyclooctane	✓
Methylcyclohexane	✓
n-Hexane	× (Isobutanol)
n-Heptane	× (n-Hexane)
n-Octane	× (Isobutanol)
Isooctane	✓

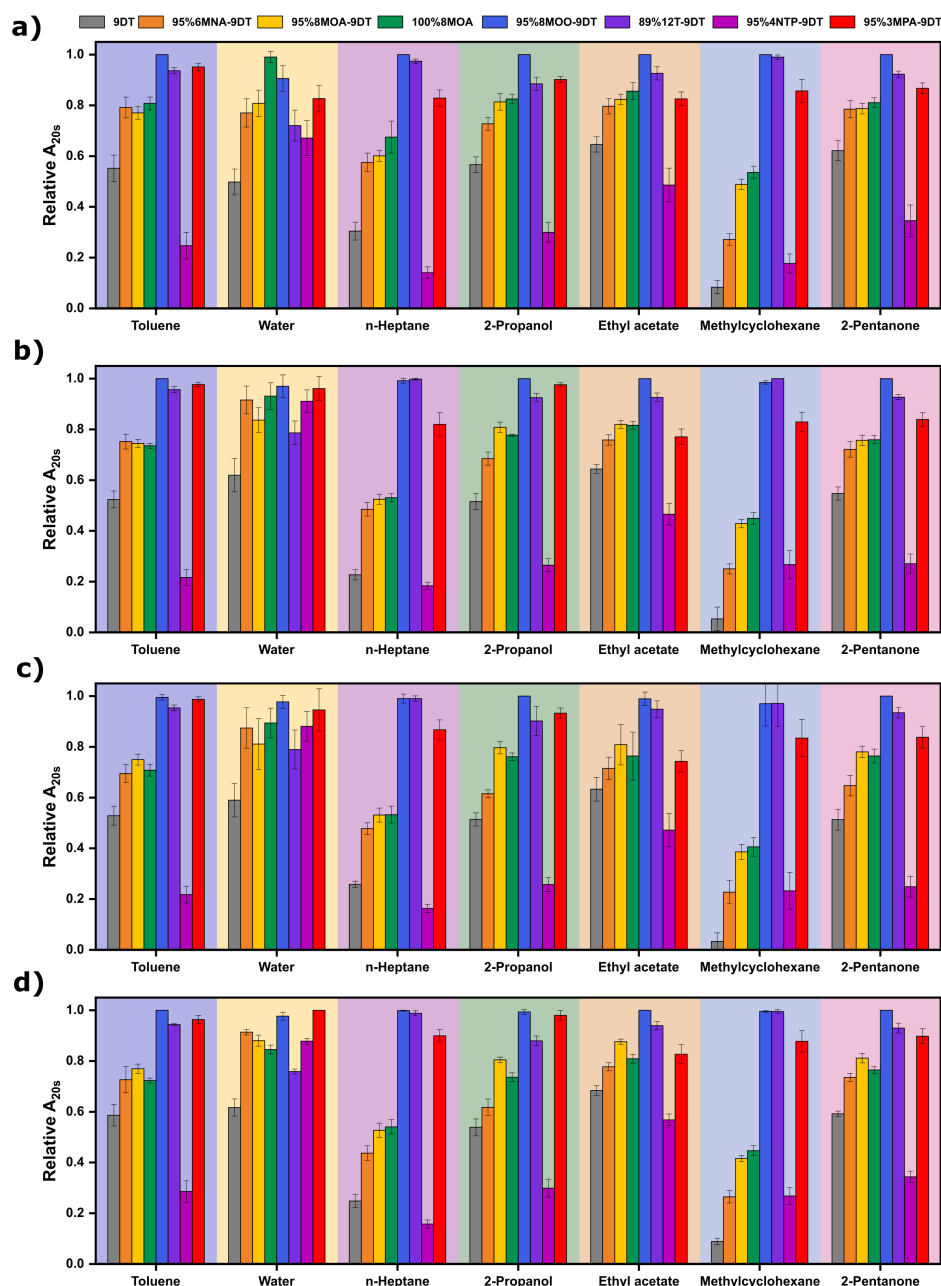


Figure A74: Average relative A_{20s} of eight GNP sensors (indicated by different bar colors) exposed to 7 analyte vapors in a) week 1 (in the concentration range of 100-1000 ppm), b) week 3 (in the concentration range of 100-1000 ppm), c) week 5 (in the concentration range of 100-1000 ppm), and d) week 7 (in the concentration range of 600-2000 ppm). Error bars were calculated as the standard deviation of the relative A_{20s} features of each GNP chemiresistor of the 8-sensor array, exposed to analyte vapors in the tested concentration range.

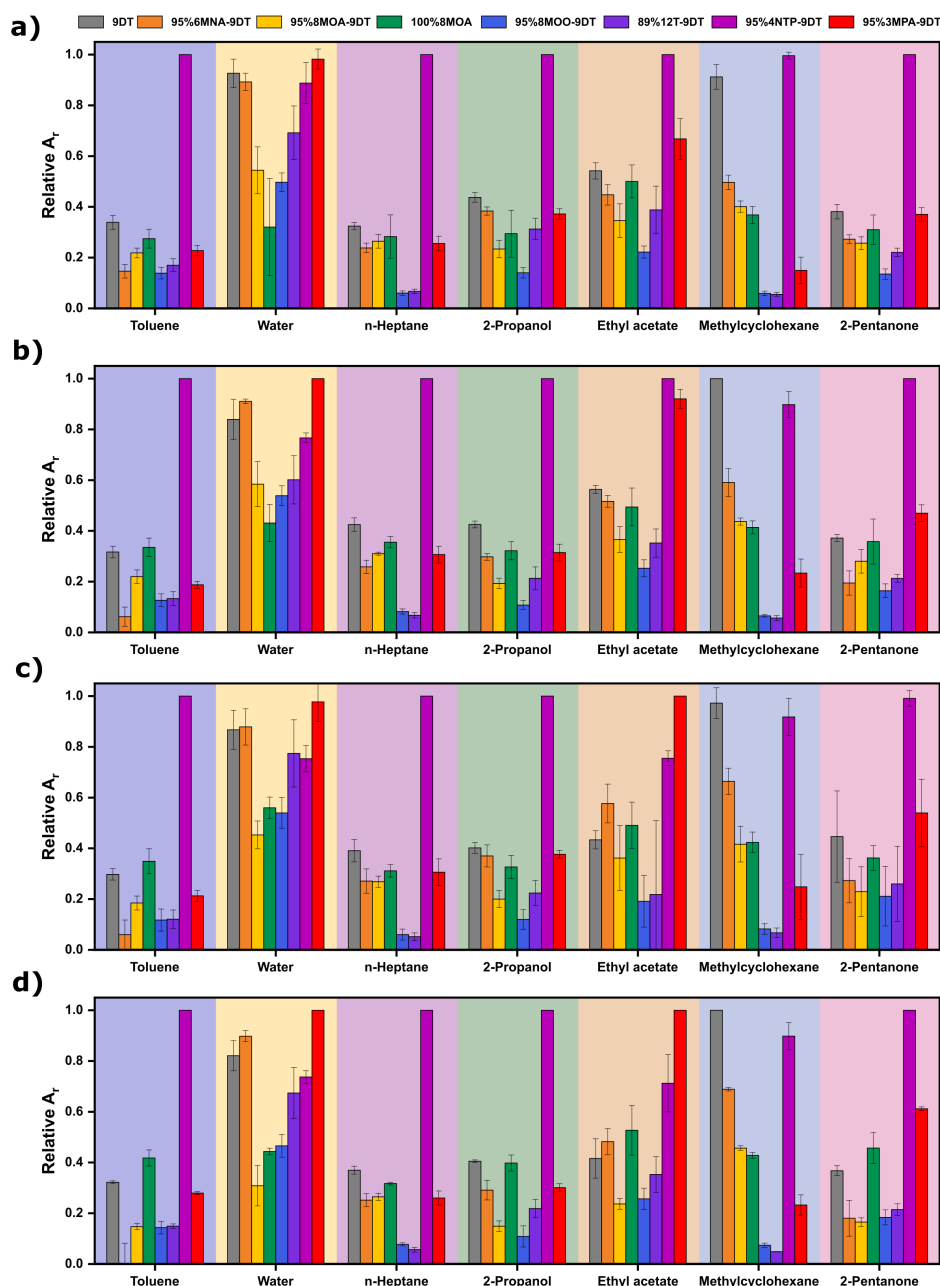


Figure A75: Average relative A_r of eight GNP sensors (indicated by different bar colors) exposed to 7 analyte vapors in a) week 1 (in the concentration range of 100-1000 ppm), b) week 3 (in the concentration range of 100-1000 ppm), c) week 5 (in the concentration range of 100-1000 ppm), and d) week 7 (in the concentration range of 600-2000 ppm). Error bars were calculated as the standard deviation of the relative A_r features of each GNP chemiresistor of the 8-sensor array, exposed to analyte vapors in the tested concentration range

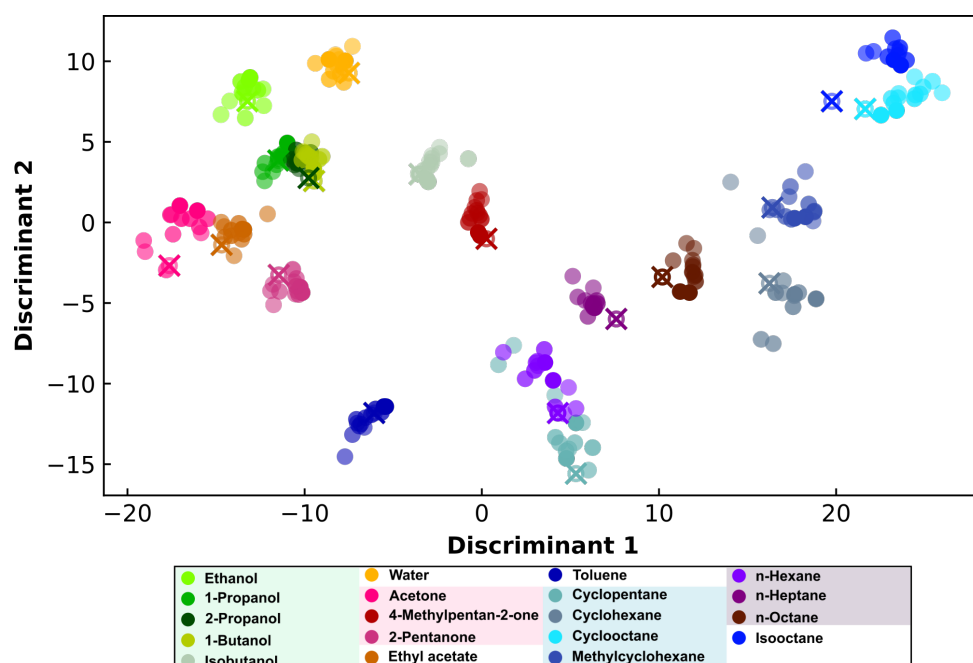


Figure A76: LDA plot of the 8-sensor array (as shown in Figure 7.42) when exposed to 19 different analyte vapors. The responses measured in week 5 to the analyte concentrations ranged from 100 to 1000 ppm were used as the training dataset for LDA. Filled circles represent data points (training data extracted from the responses measured in week 5) utilized for fitting the LDA model, while empty circles denote test data (extracted from the responses measured in week 7 exposed to 600 ppm analytes) projected onto the discriminant coordinate system. Colored crosses indicate predictions of the test data.

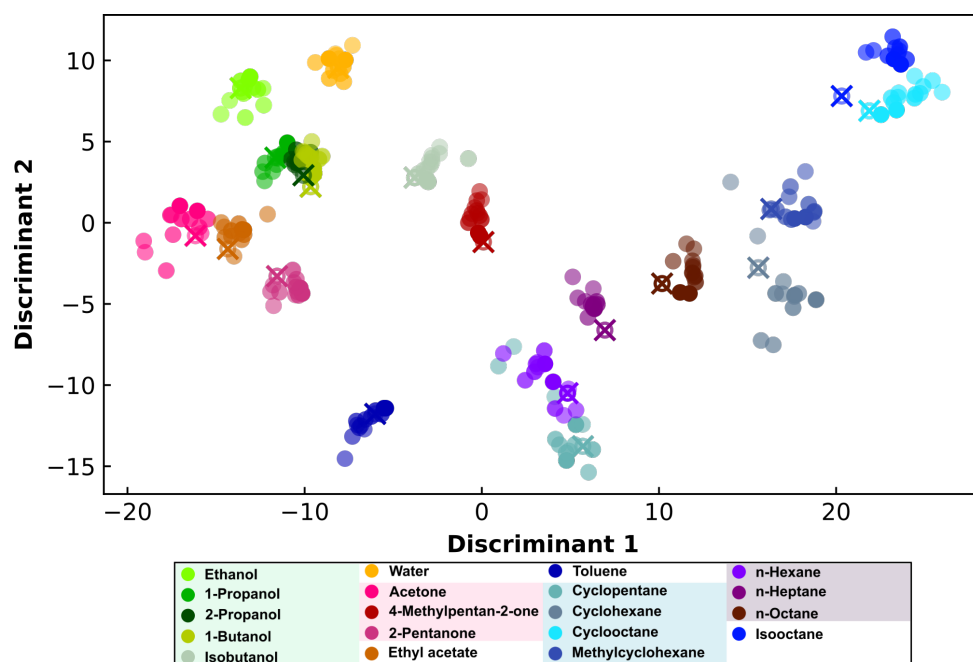


Figure A77: LDA plot of the 8-sensor array (as shown in Figure 7.42) when exposed to 19 different analyte vapors. The responses measured in week 5 to the analyte concentrations ranged from 100 to 1000 ppm were used as the training dataset for LDA. Filled circles represent data points (training data extracted from the responses measured in week 5) utilized for fitting the LDA model, while empty circles denote test data (extracted from the responses measured in week 7 exposed to 800 ppm analytes) projected onto the discriminant coordinate system. Colored crosses indicate predictions of the test data.

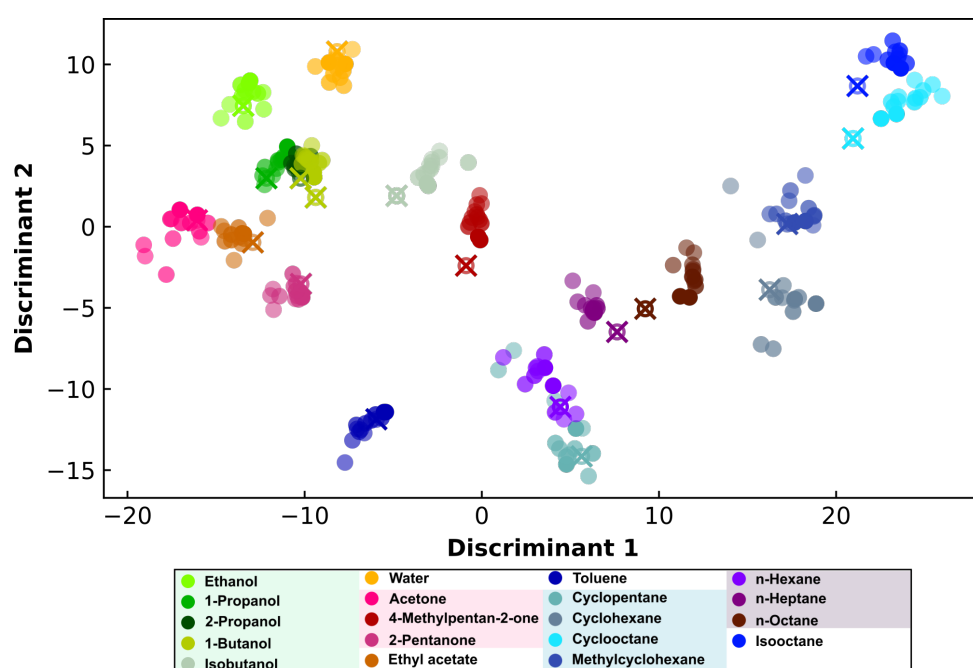









Figure A78: LDA plot of the 8-sensor array (as shown in Figure 7.42) when exposed to 19 different analyte vapors. The responses measured in week 5 to the analyte concentrations ranged from 100 to 1000 ppm were used as the training dataset for LDA. Filled circles represent data points (training data extracted from the responses measured in week 5) utilized for fitting the LDA model, while empty circles denote test data (extracted from the responses measured in week 7 exposed to 2000 ppm analytes) projected onto the discriminant coordinate system. Colored crosses indicate predictions of the test data.















Appendix B























Safety

The following table lists the chemicals used in this study with their GHS symbols as well as hazard and precautionary statements. If not indicated differently, safety information was obtained from the Sigma Aldrich online database.[217]

Chemical	GHS pictograms	hazard statements	precautionary statements
Acetone		H225, H319, H336	P210, P261, P305 + P351 + P338
3-Aminopropyl(dimethylethoxy)silane		H225, H315, H319, H335	P261, P305 + P351 + P338
2-Aminothiophenol		H302, H314, H400	P273, P280, P301 + P312, P303 + P361 + P353, P304 + P340, P305 + P351 + P338
AZ351B		H319	P264, P280, P305 + P351 + P338
AZ ECI 3000		H226, H318, H336, H280	P305 + P351 + P338, P313
1-Butanol		H226, H302, H315, H318, H335, H336	P210, P233, P280, P301 + P312, P303 + P361 + P353, P305 + P351 + P338
n-Butylamine		H302, H351	P202, P264, P280, P301 + P312, P308 + P313, P405

Chlorobenzene		H226, H315, H332, H411	P210, P233, P240, P273, P303 + P361 + P353, P304 + P340
Cyclohexane		H225, H304, H315, H336, H410	P210, P233, P273, P301 + P310, P303 + P361 + P353, P331
Cyclooctane		H226, H304	P210, P233, P240, P241, P301 + P310, P331
Cyclopentane		H225, H304, H336, H412	P210, P233, P240, P273, P301 + P310, P331
1-Decanethiol		H315, H319, H335	P261, P264, P271, P280, P302 + P352, P305 + P351 + P338
1-Dodecanethiol		H314, H317, H410	P261, P272, P273, P280, P303 + P361 + P353, P305 + P351 + P338
1-Dodecylamine		H302, H314, H410	P273, P280, P305 + P351 + P338, P310, P501
Ethyl acetate		H225, H319, H336	P210, P233, P240, P241, P242, P305 + P351 + P338
Ethanol		H225, H302, H371	P261, P305 + P351 + P338
n-Heptane		H225, H304, H315, H336, H410	P210, P261, P273, P301 + P310, P331, P501
n-Hexane		H225, H304, H315, H336, H361f, H373, H411	P201, P210, P273, P301 + P310, P303 + P361 + P353, P331
1-Hexadecanethiol	-	-	-
1-Hexanethiol		H226, H302	P210, P233, P240, P241, P242, P301 + P312, P501
Hydrogen peroxide		H318, H412	P273, P280, P305 + P351 + P338, P501
Isobutanol		H226, H302, H315, H318, H335, H336	P210, P233, P240, P280, P303 + P361 + P353, P305 + P351 + P338
Isooctane		H225, H304, H315, H336, H410	P210, P233, P273, P301 + P310, P303 + P361 + P353, P331
4-Mercaptobenzoic acid		H315, H319, H335	P261, P264, P271, P280, P302 + P352, P305 + P351 + P338

3-Mercaptopropionic acid		H290, H301, H314, H332	P234, P261, P280, P303 + P361 + P353, P305 + P351 + P338
6-Mercaptohexanoic acid		H315, H319, H335	P261, P264, P271, P280, P302 + P352, P305 + P351 + P338
8-Mercaptooctanoic acid		H315, H319, H335	P261, P264, P271, P280, P302 + P352, P305 + P351 + P338
8-Mercapto-1-octanol		H302, H315, H318, H335	P261, P264, P280, P301 + P312, P302 + P352, P305 + P351 + P338
4-Mercaptophenol		H315, H319, H335	P261, P264, P271, P280, P302 + P352, P305 + P351 + P338
6-Mercapto-3-pyridinecarboxylic acid		H315, H319, H335	P261, P264, P271, P280, P302 + P352, P305 + P351 + P338
11-Mercaptoundecanoic acid		H315, H319, H335	P261, P264, P271, P280, P302 + P352, P305 + P351 + P338
Methanol		H225, H301+H311+H331, H370	P210, P233, P280, P301 + P310, P303 + P361 + P353, P304 + P340
Methylcyclohexane		H225, H304, H315, H336, H410	P210, P233, P273, P301 + P310, P303 + P361 + P353, P331
4-Nitrothiophenol		H315, H319, H335	P261, P264, P271, P280, P302 + P352 P305 + P351 + P338
4-Methyl-2-pentanone		H225, H319, H332, H336, H351	P202, P210, P233, P305 + P351 + P338, P308 + P313
1,9-Nonanedithiol		H315, H319, H335	P261, P305 + P351 + P338
n-Octane		H225, H304, H315, H336, H410	P210, P233, P273, P301 + P310, P303 + P361 + P353, P331
1-Octanethiol		H317, H335, H410	P261, P271, P272, P273, P280, P302 + P352

2-Pentanone	 	H225, H302, H319	P210, P233, P240, P241, P301 + P312, P305 + P351 + P338
PMMA	-	-	-
1-Propanol	  	H225, H318, H336	P210, P261, P280, P305 + P351 + P338
2-Propanol	 	H225, H319, H336	P210, P261, P305 + P351 + P338
Potassium iodide		H372	P260, P264, P270, P314, P501
TechniStrip NI555	-	H302, H312	-
1-Tetradecanethiol	 	H317, H318	P280, P302 + P352, P305 + P351 + P338, P310
Tert-butylamine borane complex	 	H301, H311, H315, H319, H411	P264, P273, P301 + P310, P302 + P352, P305 + P351 + P338
Tetrachloroauric(III) acid trihydrate	   	H290, H302, H314, H373, H411	P260, P273, P280, P303 + P361 + P353, P305 + P351 + P338, P314
1-Thioglycerol		H302, H311, H314, H315, H317	P261, P264, P280, P301 + P312, P302 + P352, P304 + P340
Toluene	  	H225, H304, H315, H336, H361d, H373, H412	P202, P210, P273, P301 + P310, P303 + P361 + P353, P331
Triammonium citrate		H319	P264, P280, P305 + P351 + P338, P337 + P313
1-Undecanethiol		H315, H319, H335	P261, P264, P271, P280, P302 + P352, P305 + P351 + P338

Appendix C

Declaration On Oath

I hereby declare and affirm that this doctoral dissertation is my own work and that I have not used any aids and sources other than those indicated.

If electronic resources based on generative artificial intelligence (gAI) were used in the course of writing this dissertation, I confirm that my own work was the main and value-adding contribution and that complete documentation of all resources used is available in accordance with good scientific practice. I am responsible for any erroneous or distorted content, incorrect references, violations of data protection and copyright law or plagiarism that may have been generated by the gAI.

Chih-Yin Liu
10.January.2025